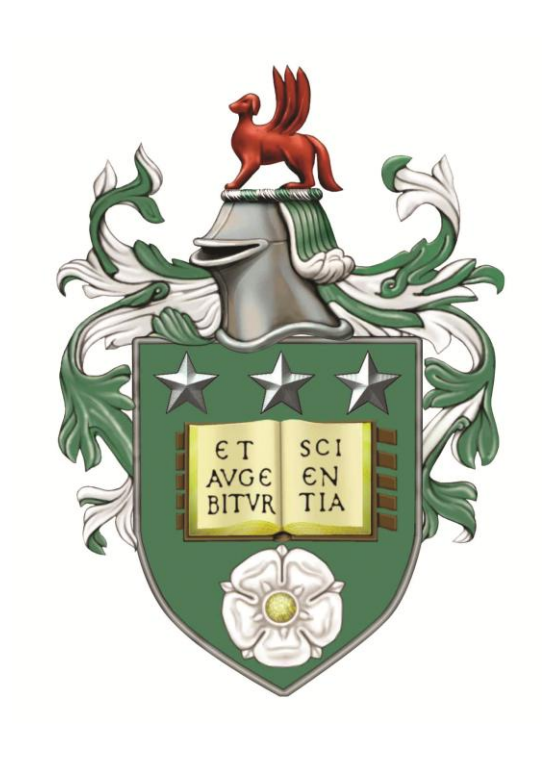
The Impact of Physicochemical Properties of Formulation Ingredients on Drug Product Flow and Compaction



Bridgit Anima EtbonSubmitted in accordance with the requirements for the degree of

DOCTOR OF PHILOSOPHY

Centre for Doctoral Training in Complex Particulate Products and Processes (CP3)

THE UNIVERSITY OF LEEDS
School of Chemical and Process Engineering

April 2025

Acknowledgments

A special thanks goes to my supervisory team, Professor Kevin J. Roberts and Dr Ali Hassanpour. Thank you for all your support throughout my PhD journey with continued guidance, advice and encouragement. I am forever grateful for your help in pushing me through the finish line despite life's challenges. I also extend my deepest gratitude to our CP3 CDT manager, Anoushka Kulikowski and the Graduate School Officer Victoria Masters for their support throughout the years.

I would also like to thank my CP3 CDT colleagues, who have contributed through discussions and the exchange of knowledge and expertise. Notably, I would like to thank Bethan Evans, Alex Moldovan, Thokozile Kathyola and Laksha Parameswaran. All have, in various ways, helped and encouraged me academically, as well as finding some study/life balance during this PhD.

A big thanks also goes to my dear friends outside of the CDT, Therese, Pamela, Ngonie, Phyllis, Sammra, and Amoie. Distance has not affected our friendship. Thank you for believing in me and standing by me when things were tough. To Geraldine and the rest of our Life Group, thank you for your consistency in support and prayer.

To my beloved Prince, I am beyond grateful for your encouragement and prayers, which have been a great anchor for me these last few months of writing. Thank you for your consistent, unwavering love and support.

Last but certainly not least, my dear family. Thank you, Dad, for pushing me to reach my highest academic level and always reminding me that: "Where determination exists, no amount of fear can dismantle the flag of success". And indeed, you were right. My dear mother, your prayers have not been in vain. Thank you for faithfully standing in the gap. To my sister Esther, thank you for your support and encouragement.

Abstract

Successful tablet manufacturing is greatly dependent on good flow and compaction behaviour of the active pharmaceutical ingredient (API) and excipients. These are governed by the physicochemical and mechanical properties of the materials. Like most organic crystalline materials, APIs are highly anisotropic, with weak van der Waals interactions often yielding needle-like, brittle crystals with poor flow and compaction. Additionally, the API-excipient ratio further impacts the processability and quality of the final tablet. Studying multi-component systems can prove challenging as API-excipient interactions are complex, and decoupling interparticle cohesion-adhesion and their impact on flow and compaction can be difficult to determine. This is especially true for modern formulations with low-dose excipients. Robust predictive models for formulation optimisation and processability remain limited. Thus, the need to utilise tools which enhance the understanding of how composition affects tabletability, ultimately optimising the manufacturing process.

This PhD combines computational and experimental methods to investigate the interplay between physicochemical and mechanical properties of the drug mefenamic acid (MA) and excipient d-mannitol (DM), and their impact on flow and compaction.

Molecular modelling successfully predicted the thin platy morphology of MA, driven by its anisotropic hydrogen bonding at its capping faces, and the columnar prismatic particles of DM, due to its homogenous distribution of -OH interactions. Predictions of their surface interactions revealed MA to have stronger cohesivity driven by strong dispersive interactions (93.53 %) and DM stronger adhesivity, displaying a better balance of dispersive to polar interactions (75.29 % and 24.71 % respectively). Prediction of their mechanical properties revealed both compounds to be brittle in nature; however, DM's extensive h-bond network allows for the occurrence of plastic deformation.

The predictions correlated well with experimental results. MA displayed poor flow (HR: 1.37, AOR: 44.55°), no plasticity (P_y : 357.14 MPa), high porosity (E: 0.22) and low tensile strength (0.095 MPa). On the contrary, DM displayed good flow (HR:1.13, AOR 39.20), good compressibility (E: 0.03) and plasticity (P_y : 65.79 MPa) and high tensile strength (1.07 MPa). Binary mixtures of 50-50, 65-35 and

75-25 MA to DM were examined in the same manner. The 50-50 blend provided the best balance between flow, compressibility and tensile strength. Whilst increasing the amount of MA, the blend's properties increasingly resembled those of pure MA. The findings were further validated through X-ray computed tomography (XCT), where powder flow, consolidation patterns, tablet compressibility and particle orientation were examined.

The work presented aids in the development of predictive models for formulation optimisation, enhancing processing efficiency. Two key research outputs are anticipated from this thesis: i) a study on "Predicting Cohesive and Adhesive Interactions and Mechanical Deformation of Mefenamic acid and D-mannitol" and ii) "Investigating Powder Flow and Tablet Properties of Mefenamic acid and D-mannitol using X-ray Computed Tomography".

Table of Contents

1	Intro	oduction	2
	1.1	Research Background	2
	1.2	Research Aims and Objectives	6
	1.3	Selection of Model System	7
	1.4	Project Management	8
	1.5	Thesis Structure	9
2	Cry	stal Science of Pharmaceutical Materials	13
	2.1	Basic Crystallography	13
	2.1.	1 Lattices, Unit Cells, and Crystal Systems	14
	2.2	Crystal Lattice Defects	17
	2.2.	Point, Plane and Volume Defects	18
	2.2.	2 Linear Defects	20
	2.3	Polymorphism	22
	2.4	Intermolecular Interactions & Crystal Lattice Energetics	25
	2.4.	1 Interaction Types	26
	2.4.	2 Predicting Intermolecular Interactions	27
	2.5	Crystal Morphology & Modelling of Organic Crystals	28
	2.6	Conclusion	32
3	Dru	g Powder Properties Influencing Tabletability	35
	3.1	Pre-Formulation	35
	3.2	Route of Administration	35
	3.2.	1 Drug Pathways	37

3.	2.2	Bioavailability	37
3.	2.3	Biopharmaceutical Classification System	38
3.3	Pow	vder Properties for Downstream Processing	40
3.	3.1	Particle Size Reduction	40
3.	3.2	Blending	40
3.	3.3	Tablet Manufacturing Routes	42
3.	3.4	Compaction	45
3.	3.5	Advantages and Disadvantages of the Tablet Manufacturing Routes	54
3.	3.6	Importance of Powder Flow and Compressibility	56
3.4	X-ra	ay Computed Tomography (XCT)	60
3.5	Pred	licting Mechanical Behaviour	61
3.6	Mod	del System – Mefenamic acid and D-mannitol	65
3.	6.1	Mefenamic acid (MA)	65
3.	6.2	D-mannitol (D-M)	67
3.7	Con	clusion	68
M	Iaterials	s and Methods	71
4.1	Mat	erials	71
4.	1.1	Chemical Powders	71
4.	1.2	Molecular Structure	71
4.2	Mol	ecular Modelling Methods	72
4.	2.1	Lattice Energy and Habit Prediction	72
4.	2.2	API-Excipient Interactions	74
4.	2.3	Slip-Plane Identification	75

4

4.3 Ch	aracterisation of Powders	76
4.3.1	Powder X-Ray Diffraction (PXRD)	76
4.3.2	Thermal Analysis	76
4.3.3	Morphological examination	78
4.3.4	Particle Size Distribution	78
4.3.5	Flowability	79
4.3.6	Powder Compression	80
4.4 X-	Ray Computed Tomography (XCT)	81
4.4.1	Sample Preparation	82
4.4.2	Data Analysis	84
4.5 Co	nclusion	89
5 Surface	and Solid-State Study and Prediction of Molecular Interactions of Mefenam	ic Acid and
D-mannitol u	using Molecular Modelling	91
5.1 Int	roduction	91
5.2 Mo	blecular Structure and Descriptors	91
5.3 So	lid-Sate Properties	92
5.3.1	Force-Field and Fractional Charges	96
5.3.2	Lattice Energies and their Convergence	100
5.3.3	Relative Contributions of the Molecular Fragments to the Lattice Energy	102
5.3.4	Intrinsic Synthon Chemistry	103
5.4 Su:	rface Properties	106
5.4.1	Crystal Morphology and Surface Chemistry of Mefenamic Acid	106
5.4.2	Crystal Morphology and Surface Chemistry of D-mannitol	110

	5.5 AP	I-Excipient Interactions – Prediction of cohesive/adhesive Interactions	116
	5.6 Pre-	diction of Mechanical Properties	122
	5.6.1	Mefenamic acid - Slip Plane Characterisation	122
	5.6.2	Mefenamic acid - Slip Direction and Slip System	124
	5.6.3	D-mannitol - Slip Plane Characterisation	126
	5.6.4	D-mannitol - Slip Direction and Slip System	128
	5.7 Cor	nclusions	129
6	Influence	e of Surface, Solid-State and Bulk Powder Properties on Compactibility	133
	6.1 Sol	id-State and Stability Characterisation	133
	6.1.1	Determination of Solid-State	133
	6.1.2	Material Stability	135
	6.2 Infl	uence of Particle Morphology, Size and Flow on Compaction	137
	6.2.1	Morphology and Particle Size	138
	6.2.2	Powder Flowability	140
	6.2.3	Powder Compactibility	143
	6.2.4	Summary of Bulk Powder Properties	148
	6.3 Cor	nclusions	150
7	Investiga	ating Powder and Tablet Properties using X-ray Computed Tomography	152
	7.1 Intr	oduction	152
	7.2 Pov	vder Packing Analysis of Mefenamic acid and D-mannitol	152
	7.2.1	Consolidation Pattern and Orientation Analysis of Mefenamic acid and D-mannito	ol 154
	7.3 Pov	yder Packing Analysis of Mefenamic acid-D-mannitol mixtures	157

7.3.1	Consolidation Pattern and Orientation Analysis of Mefenamic acid-D-mannito	l mixtures
	160	
7.4 Tal	blet Analysis of Mefenamic acid and D-mannitol	164
7.4.1	Mefenamic acid tablet	164
7.4.2	D-mannitol	166
7.4.3	Orientation Analysis of Mefenamic acid and D-mannitol Tablet	167
7.5 Tab	blet Analysis of Mefenamic acid and D-mannitol binary mixtures	169
7.5.1	50-50 tablet	170
7.5.2	65-35 tablet	171
7.5.3	75-25 Tablet	172
7.5.4	Comparison of Porosity	172
7.5.5	Orientation Analysis of Mefenamic acid-D-mannitol mixtures	174
7.6 Dis	scussion	176
7.6.1	Cohesive vs. Adhesive Interactions	176
7.6.2	Crystal Morphology and Powder Behaviour	177
7.6.3	XCT Analysis and Microstructural Insights	178
Conclus	sions and Future Work	182
8.1 Rev	visiting Initial Aims and Objectives	182
8.2 Sug	ggestions for Future Work	184
Referen	ices	186

List of Figures

Figure 1-1. The Material Science Tetrahedron ¹²
Figure 1-2. Unit operations for the three main pharmaceutical processing routes
Figure 1-3. Pharmaceutical powder mass adhered to the upper punch ²⁴
Figure 1-4. The molecular structure of mefenamic acid and d-mannitol
Figure 1-5. Outline of thesis structure
Figure 2-1. Two-dimensional depiction of a crystal lattice arrangement
Figure 2-2. Example of crystallographic Miller indices for directions ³⁴
Figure 2-3. Example of crystallographic Miller indices for planes ³⁵
Figure 2-4 Point defects in crystal structures ⁴¹
Figure 2-5. Perfect and faulted stacking sequence for a face-centred cubic crystal ⁴³
Figure 2-6 Grains and grain boundaries in a polycrystal. ⁴⁰
Figure 2-7. Example of (a) a closed Burgers circuit in a {100} plane of a cubic crystal and (b) an open,
failed circuit needing vector b to close it ⁴⁴
Figure 2-8. The movement of edge (top) and screw (bottom) dislocations during slip ⁴⁹
Figure 2-9. Structure of a) crystalline and b) amorphous (without impurities) silicon dioxide silica ⁵⁰ 23
Figure 2-10. A systematic scheme for classification of pharmaceutical solids ⁵⁵ . Key: ▲=API molecule,
•= co-crystal/salt, S = solvent molecule
Figure 2-11. The difference between intermolecular interactions and intramolecular interactions25
Figure 2-12. Examples of crystals of the a) same morphology but different habits and b) same habit
(isometric habit) but different morphologies ⁶⁷
Figure 2-13. Schematic outline of the SystSearch prediction, illustrating the movement of the probe
molecule on the grid over the slab ¹⁷
Figure 2-14. RS-ibuprofen crystals grown from a) ethanol, b) ethyl acetate, c) acetonitrile and d)
toluene ⁸⁰
Figure 3-1. Pre-formulation research areas ⁸³
Figure 3-2. Schematics of a) a high-shear mixer and b) a v-blender 98

Figure 3-3. Schematic of the three main tablet manufacturing routes
Figure 3-4. Stages of wet granulation (reconstructed) ¹⁰¹
Figure 3-5. Schematic of steps in tablet compaction
Figure 3-6. Schematic image of a rotary tablet press mechanism ¹⁰⁷
Figure 3-7. A typical stress vs. strain curve
Figure 3-8. Tablet defects: a) Capping, b) Lamination ¹²⁰
Figure 3-9. Schematic of punch-sticking highlighting the deformed tablet
Figure 3-10. Causes of punch-sticking, highlighting powder properties
Figure 3-11. Effect of morphology on the sticking tendency of needles and plates to tablet punches
during compression ²⁶
Figure 3-12. Schematic of the model describing Type I sticking (monolayer filming) and Type II severe
sticking ²³
Figure 3-13. Illustration of angle of repose experiment 116
Figure 3-14. X-ray computed tomography set-up 3D inhale ¹⁵⁴
Figure 3-15. Diagram illustrating two different types of interfaces during slip, a) a highly corrugated
plane with no interpenetration of layers, thus no obstruction to slip, and b) interpenetrated layers of a
less corrugated plane, obstructing slip ¹⁵⁷ .
Figure 3-16. Illustration of a highly corrugated system displaying potential slip in a specific direction
157
Figure 3-17. Mechanical Deformation Prediction Workflow ¹⁵⁹
Figure 3-18. Fenamate chemical structures: a) parent structure-fenamic acid, b) mefenamic acid, c)
tolfenamic acid, d) meclofenamic acid, e) flufenamic
Figure 3-19. Molecular structure of d-mannitol
Figure 4-1. a) The 2D molecular structure of mefenamic acid depicting its atom types and b) its 3D
packing within a unit cell
Figure 4-2. a) The 2D molecular structure of d-mannitol depicting its atom types and b) its 3D packing
within a unit cell

Figure 4-3. Schematic outline of the SystSearch prediction, illustrating the movement of the probe
molecule on the grid over the slab ¹⁷
Figure 4-4. Schematic of DVS instrumental set-up ¹⁷⁸
Figure 4-5. Example of differences between a) backscattered image, b) secondary electron image and
c) mixed image ¹⁷⁹
Figure 4-6. Angle of repose test on d-mannitol
Figure 4-7. Intron Mechanical Tester
Figure 4-8. Tooling used for powder compression: a) A) 5 mm die, B) die base, C) piston ("punch")
head and D) tool used to push out compacts from die, and b) optimised piston also used for better
ejection80
Figure 4-9. Tablet before and after diametric stress test
Figure 4-10. X-ray computed tomography set-up 3D inhale ¹⁵⁴
Figure 4-11. Sample preparations for the X-ray computed tomography experiments: a) free-flowing d-
mannitol in a polyamide tube, b) 5 mm d-mannitol compact
Figure 4-12. a) A 3D rendering of the mefenamic acid powder bed at 20 taps, revealing the powder in
the tube, b) a horizontal slice through the powder bed with a cylinder analysis mask overlayed as the
analysis region, c) the extracted analysis region with applied 'bilateral filtering' for better thresholding
and d) the same slice with the particles identified through thresholding
Figure 4-13. a) a horizontal slice through the 50-50 tablet with an analysis mask overlayed, b) the
extracted analysis region with the mefenamic acid (red) and d-mannitol (purple) and d-mannitol particles
and the air identified through thresholding.
Figure 4-14. Examples of a) watershed applied to particles for individual analysis and b) resulting theta
histogram
Figure 4-15. 3D rendering of a tablet divided into 72 cells for individual volume thresholding 88
Figure 5-1 Molecular structures of a) mefenamic acid and b) d-mannitol, highlighting main functional
groups
Figure 5-2. 3D packing within a unit cell of a) mefenamic acid and b) d-mannitol93

Figure 5-3. Molecular packing of mefenamic acid viewed along the a) a-axis, b) b-axis and c) c-axis
94
Figure 5-4. Molecular packing of d-mannitol viewed along the b- and c-axes
Figure 5-5. Hydrogen bond types in the d-mannitol lattice
Figure 5-6. Numbering of atoms in the mefenamic acid molecular structure96
Figure 5-7. Numbering of atoms in the mefenamic acid molecular structure
Figure 5-8. Schematic of calculating the intermolecular interactions based on the atom-atom method ¹⁹⁵
Figure 5-9. a) Lattice energy of mefenamic acid as a function of increasing limiting radius of the sphere
of calculation, and b) the percentage of added contribution to the lattice energy with increasing limiting
radius
Figure 5-10. a) Lattice energy of d-mannitol as a function of increasing limiting radius of the sphere of
calculation, and b) percentage of added contribution to the lattice energy with increasing limiting radius
Figure 5-11. Percentage contribution of functional groups to the lattice energy in a) mefenamic acid and
b) d-mannitol
Figure 5-12. (A-E) Six strongest pairwise intrinsic synthons calculated from the bulk structure of
mefenamic acid
Figure 5-13. (A-F) Six strongest pairwise intrinsic synthons calculated from the bulk structure of d-
mannitol
Figure 5-14. Predicted attachment energy morphology of mefenamic and the surface chemistry of each
face
Figure 5-15. Morphology of mefenamic crystals and the solvent structures of a) tetrahydrofuran ¹³⁴ , b)
ethanol ¹³⁷ , c) ethyl acetate ¹³⁸ and d) toluene ¹³⁸
Figure 5-16. Predicted attachment energy morphology of d-mannitol and the surface chemistry of each
face
Figure 5-17. Recrystallised β -d-mannitol from a) water ²¹⁴ , b) and c) antisolvent precipitation in acetone
215

Figure 5-18. The cohesive/adhesive energies on each facet of a) mefenamic acid and b) d-mannitol, and		
their respective surface weighted interactions, averaged over the whole crystal		
Figure 5-19. The cohesion and adhesion energies of mefenamic acid are broken down into dispersive		
and polar energies, at each facet and the total surface weighted mean		
Figure 5-20. The cohesion and adhesion energies of d-mannitol are broken down into dispersive and		
polar energies, at each facet and the total surface weighted mean		
Figure 5-21. Mefenamic acid packing of the potential slip planes of a) {100} and b) {001} viewed along		
the b-axis		
Figure 5-22. Intermolecular packing of mefenamic acid viewed along the a-axis, where h-bonding along		
the [010] direction can be seen		
Figure 5-23. Packing of d-mannitol's most likely slip-planes a) {002} and {011} viewed along the a-		
axis127		
Figure 5-24. Intermolecular packing of d-mannitol viewed along the b-axis, where h-bonding along the		
[100] direction can be seen		
Figure 6-1. a) The Cambridge Crystal Database reference PXRD pattern of mefenamic acid overplayed		
on the obtained pattern from the commercial sample; b) The DSC curve of the mefenamic acid sample.		
Figure 6-2. a) The Cambridge Crystal Database reference PXRD pattern of d-mannitol overplayed on		
the obtained pattern from the commercial sample; b) The DSC curve of the d-mannitol sample 134		
Figure 6-3. TGA curves of a) mefenamic acid and b) d-mannitol		
Figure 6-4. a) The DVS isotherm and b) the kinetic curve of mefenamic acid		
Figure 6-5. a) The DVS isotherm and b) the kinetic curve of d-mannitol		
Figure 6-6. SEM images of d-mannitol at: a) 100x magnification, b) 300x magnification and mefenamic		
acid at: c) 100x magnification, d) 300x magnification		
Figure 6-7. The particle size distributions of a) mefenamic acid and b) d-mannitol		
Figure 6-8. Angle of repose measurement of d-mannitol		
Figure 6-9. Heckel plots of a) d-mannitol, highlighting three stages of compression and b) mefenamic		
acid not reaching stage 3 strain hardening		

Figure 6-10. a) The old compaction tooling and resulting mefenamic acid tablet, and b) optimised
punch-tip and resulting mefenamic acid tablet
Figure 6-11 a) Heckel plots and b) compressibility of d-mannitol and mefenamic acid and their
compositions
Figure 6-12. Compactibility of the five tablets: mefenamic acid, d-mannitol, 50-50, 65-35 and 75-25
blends
Figure 7-1. 2D reconstructed XCT slices of mefenamic acid and d-mannitol at 0, 10, 20 and 30 taps
Figure 7-2. 3-D reconstructed image of mefenamic acid powder bed cross-section at 30 taps
Figure 7-3. Variation in powder density of the bed height of a) mefenamic acid and b) d-mannitol. The
height is closer to the top of the bed as a function of the number of taps
Figure 7-4. Variation of particle orientation of a) mefenamic and b) d-mannitol particles as a function
of taps
Figure 7-5. 2D reconstructed XCT slices of a 50-50 mixture of mefenamic acid and d-mannitol at 0, 10,
20 and 30 taps
Figure 7-6. 2D reconstructed XCT slices of a 65-35 mixture of mefenamic acid and d-mannitol at 0, 10,
20 and 30 taps
Figure 7-7. 2D reconstructed XCT slices of a 75-25 mixture of mefenamic acid and d-mannitol at 0 and
30 taps
Figure 7-8. Variation in powder density of the bed height of powder mixtures, a) 50-50, b) 65-35 and
c)75-25 function of the number of taps
Figure 7-9. Variation of particle orientation of powder mixtures, a) 50-50, b) 65-35 and c)75-25 function
of the number of taps
Figure 7-10 a) 3-D reconstructed image of mefenamic acid tablet, b) 3-D pore-network and c) grayscale
histogram of the entire reconstructed XCT image of the mefenamic acid tablet164
Figure 7-11. Temperature map of the density distribution of the pore network of mefenamic acid 165
Figure 7-12. a) 3-D reconstructed image of d-mannitol tablet, b) 3-D pore-network and c) grayscale
histogram of the entire reconstructed XCT image of the d-mannitol tablet

Figure 7-13. a) Temperature map of d-mannitol pore network and b) 3D rendering of internal crack
Figure 7-14. Particle orientation of d-mannitol and mefenamic acid tablets
Figure 7-15. a) 3-D reconstructed image of the 50-50 tablet, b) 3-D pore-network and c) grayscale
histogram of the entire reconstructed XCT image of the 50-50 tablet
Figure 7-16. a) 3-D reconstructed image of the 65-35 tablet, b) 3-D pore-network and c) grayscale
histogram of the entire reconstructed XCT image of the 65-35 tablet
Figure 7-17. a) 3-D reconstructed image of the 75-25 tablet, b) 3-D pore-network and c) grayscale
histogram of the entire reconstructed XCT image of the 75-25 tablet
Figure 7-18. Temperature map of the a) 50-50, b) 65-35 and c) 75-25 tablet pore network
Figure 7-19. Variation of particle orientation of 50-50, 65-35 and 75-25 tablet mixtures
List of Tables
Table 1-1: The Four Classes of the Biopharmaceutical Classification System
Table 2-1: The 14 Bravais lattices across the 7 crystal systems, outlining the angles (α, β, γ) between
the axes and the length of the axes $(a, b, c)^{37}$ and examples of crystal shapes ³⁸
Table 2-2: Types of Crystal Defects
Table 3-1. The Four Classes of the Biopharmaceutical Classification System
Table 3-2. Types of Excipients ⁹⁶
Table 3-3. Criteria for appropriate route selection
Table 4-1. Raw material information
Table 5-1. List of molecular properties of mefenamic acid and d-mannitol
Table 5-2. Solid-State Properties of mefenamic acid and d-mannitol
Table 5-3. Fractional Coordinates and Atomic Charges of all 33 atoms of Mefenamic Acid96
Table 5-4. Fractional Coordinates and Atomic Charges of all 26 atoms of D-mannitol
Table 5-5. Relative contribution of dispersive and electrostatic energy of mefenamic acid and d-
mannitol contributing to their lattice energies

Table 5-6. Mefenamic acid energetics and percentage contribution of functional groups to lattice energy
Table 5-7. D-mannitol energetics and percentage contribution of functional groups to lattice energy
Table 5-8 Top 6 Intrinsic Synthons Contributing to the Lattice Energy, Ranked in Order of Total
Interacting Energy
Table 5-9. Top 6 Intrinsic Synthons Contributing to the Lattice Energy, Ranked in Order of Total
Interacting Energy
Table 5-10. Analysis of H-bond interactions involved in the synthons listed in Table 5-8 and Table 5-
9, where the geometric details of donor (D) and acceptor (A) contributions have been highlighted, and
their relative polarities. Single-bonded oxygen atoms have been denoted O- and double-bonded oxygen
atoms have been denoted O= for clarity
Table 5-11. The Morphologically Important Surfaces of Mefenamic acid and their: Interplanar spacing
(in Å); Attachment and slice energies (in kcal/mol); Percentage Surface Saturation (ξhkl); Percentage
Surface Area; Surface energies (in mJ/m2) and the Extrinsic Synthon Contribution to Attachment and
Slice Energies at each Morphologically Important Face
Table 5-12. The Morphologically Important Surfaces of D-mannitol and their: Interplanar spacing (in
Å); Attachment and slice energies (in kcal/mol); Percentage Surface Saturation (ξhkl); Percentage
Surface Area; Surface energies (in mJ/m2) and the Extrinsic Synthon Contribution to Attachment and
Slice Energies at each Morphologically Important Face
Table 5-13. The top 500 mean cohesive/adhesive interaction energies of mefenamic acid and d-mannitol
116
Table 5-14. The interaction energies at each facet of mefenamic acid, and the total surface weighted
interactions, averaged over the whole crystal
Table 5-15. The interaction energies at each facet of d-mannitol, and the total surface weighted
interactions, averaged over the whole crystal
Table 5-16. Values of attributes in the decision matrix, hydrogen breaking, interdigitation, rugosity and
surface energy 122

Table 5-17. Normalised values of each attribute in the decision matrix	!2
Table 5-18. Weighted normalised values and Euclidean distance from ideal best Si+ and ideal worst Si	i-
. The ideal value is the lowest value of each attribute	!3
Table 5-19. Final Slip-Plane Ranking of Mefenamic acid	23
Table 5-20. Analysis of the Key Potential Slip-Planes of Mefenamic acid detailing Surface Plan	ıe
Satisfaction, Rugosity, Surface Energy, Degree of Interdigitation and Hydrogen Bond Breaking 12	!4
Table 5-21. The Nature of the Three Strongest Intermolecular Interactions of Mefenamic acid, the	ir
Direction, and their Contribution towards Potential Slip Plane (hkl) Surfaces	25
Table 5-22. Values of attributes in the decision matrix, hydrogen breaking, interdigitation, rugosity an	ıd
surface energy	26
Table 5-23. Normalised values of each attribute in the decision matrix	26
Table 5-24. Weighted normalised values and Euclidean distance from ideal best Si+ and ideal worst Si	i-
. The ideal value is the lowest value of each attribute	26
Table 5-25. Final Slip-Plane Ranking of D-mannitol	26
Table 5-26. Analysis of the Key Potential Slip-Planes of D-mannitol detailing Surface Plan	ıe
Satisfaction, Rugosity, Surface Energy, Degree of Interdigitation and Hydrogen Bond Breaking 12	27
Table 5-27. The Nature of the Three Strongest Intermolecular Interactions of D-mannitol, the	ir
Direction, and their Contribution towards Potential Slip Plane (hkl) Surfaces	28
Table 6-1. Classification of hygroscopicity as defined by the European Pharmacopoeia ²²⁹	;7
Table 6-2. Particle size distribution of mefenamic acid and d-mannitol	Ю
Table 6-3. Scale of Flowability and Corresponding Carr's Index, Hausner Ratio and Angle of Repose ²	:33
14	1
Table 6-4. Measured bulk density, tapped density (g/cm3), Carr's Index, Hausner Ration of d-mannito	ol
and mefenamic acid and angle of repose of d-mannitol	1
Table 6-5. Heckel Parameters and tensile strength	١7
Table 7-1. Comparison of lab-measured bulk and tapped density versus XCT-measured bulk and tappe	ed
density and Carr's Index and Hausner results of mefenamic acid d-mannitol	:4

Table 7-2. Comparison of lab-measured bulk and tapped density versus XCT-measured bulk and tapped
density and Carr's Index, and Hausner results of 50-50 mixture and mefenamic acid and d-mannitol
individually within the 50-50 mixture
Table 7-3. Comparison of lab-measured bulk and tapped density versus XCT-measured bulk and tapped
density, and Carr's Index and Hausner results of 65-25and 75-25 powder mixtures
Table 7-4. Comparison of XCT-measured volume fraction vs. lab-measured compressibility of
mefenamic acid
Table 7-5. Comparison of XCT-measured volume fraction vs. lab-measured compressibility of d-
mannitol
Table 7-6. Mixing Indices of 50-50, 65-35 and 75-25 mefenamic acid:d-mannitol tablets
Table 7-7. Comparison of XCT-measured volume fraction vs. lab-measured compressibility of the 50-
50 tablet
Table 7-8. Comparison of XCT-measured volume fraction vs. lab-measured compressibility of the 65-
35 tablet
Table 7-9. Comparison of XCT-measured volume fraction vs. lab-measured compressibility of the 75-
25 toblat

Chapter One

Introduction

This chapter provides the foundational context for this research, outlining the research question, aims and objectives and overall thesis structure. Additionally, it includes the project management team supporting this project.

1 Introduction

1.1 Research Background

The pharmaceutical industry is a huge part of the life science sector, with a reported global market size of approximately \$1.5 to 1.6 trillion in 2023 and is projected to reach \$1.8-2 trillion by 2030¹⁻³. The industry consists of several large and small companies engaged in the research, development, manufacture, and distribution of drug therapies for the use of humans and animals. Through the advancement of modern medicine, formerly fatal illnesses have been eliminated, and life-threatening diseases are more manageable, enhancing our quality of life. Drug therapy is now an essential part of the healthcare and well-being of the global population.

Over 70% of dispensed medicines are in the form of tablets and are the most preferred solid dosage form⁴. They have the highest patient compliance as they are convenient to use, have an acceptable taste and are the cheapest dosage form. They are suitable for large-scale production, and the cost of manufacturing is relatively low. Tablets are the most chemically stable dosage form, provide the greatest dose accuracy and lowest content variability^{5,6}. They offer the advantage of masking bad odour and bitter taste through coating techniques. Other formulation benefits of tablets include creating tablets with sustained release, as well as the ability to formulate tablets containing more than one active pharmaceutical ingredient (API).

Even with the great advances achieved by scientists, the industry still faces several challenges within tablet manufacture, which they continue to seek ways to resolve. The chemical and physical properties of drug compounds impact the efficiency of various unit process operations and the quality of the final drug product⁷. Drug powders must be able to remain chemically and physically stable during processing. Their processability is impacted by their flow and mechanical properties, governed by their surface chemistry, morphology and particle size^{8,9}. Crystalline drug compounds tend to exhibit morphologies of high aspect ratios, often needle-like, due to their anisotropic nature. It is well known that needle-like morphologies are problematic to process¹⁰. They are tough to filter, have poor flow properties, causing difficulty in transfer between equipment, and cause ununiform powder blends. They

have weak mechanical properties, which contribute to poor compressibility and compaction properties. Drug research and development are largely focused on the performance of the final product and its effect on the patient. The Biopharmaceutics Classification System (BCS) provides a system of ranking drugs based on their solubility and intestinal permeability, and in *vitro* dissolution properties¹¹. Though this is a vital step in pre-formulation, it is limited in that it does not account for any other attributes. Thus, research efforts over the past decade have focused on gaining a deeper understanding of crystal anisotropy and how physicochemical properties influence the various processes involved in pharmaceutical manufacture and how these processes impact the drug properties.

Table 1-1: The Four Classes of the Biopharmaceutical Classification System

	High Solubility	Low Solubility
High Permeability	CLASS I	CLASS II
Low Permeability	CLASS III	CLASS IV

The Material Science Tetrahedron (MST) has been suggested as a tool to aid in the development and research of pharmaceutical products. It outlines the relationship between structure, properties, process, and performance of drugs¹². Once there is an understanding of how material structure (chemical, crystal, granule, tablet structure and composition) affects its properties (surface, mechanical, flow and compaction, electrostatic and sticking properties) and performance (stability, content uniformity, manufacturability and dissolution); the desired performance can be achieved by altering processing steps such as chemical synthesis, crystallisation, milling, granulation and compaction parameters.

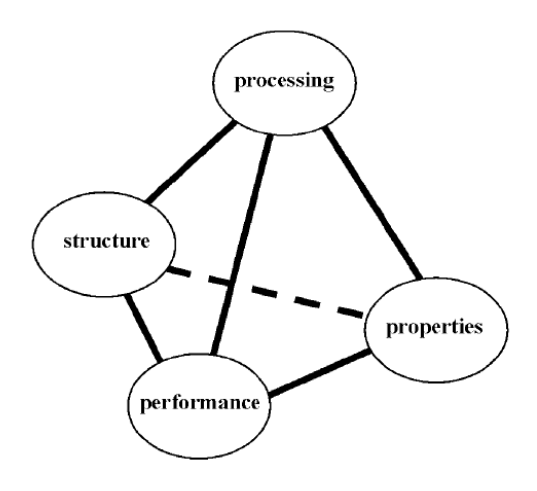


Figure 1-1. The Material Science Tetrahedron¹²

The desire to predict API properties has led to an intensive use of molecular modelling tools, which have aided in understanding crystal habit and how they differ depending on solvent medium^{13–17}. The BCS, MST, MCS and molecular modelling combined all form part of the move that pharmaceutical research and development has made from quality by testing (QbT) into quality by design (QbD)¹⁸. The old QbT approach was a form of "trial and error method" where the quality and performance of a product were only assured when testing was completed. The understanding of material behaviours and critical processing parameters is limited in this approach. Hence, the QbD approach is used as a way of improving the time and cost-efficiency of pharmaceutical manufacturing, as well as ensuring the production of safe and efficacious medicines.

After crystallisation and filtering of the API, milling and blending with excipients, the three main routes of manufacture for solid doses are wet granulation, dry granulation, and direct compression. Direct compression is the desired route of manufacture. It has the fewest unit operations and a reduced number of raw materials, making it overall the most cost-effective choice¹⁹. However, very few drug compounds possess properties suitable for direct compression. Content uniformity and production of a robust tablet are difficult to achieve with direct compression. Thus, developing formulations for direct compression becomes complex. Wet granulation, therefore, remains the most popular route partly due to its very well-known process but mainly for its ability to enhance the properties of powders with poor bulk

properties, followed by dry granulation. For successful compaction, particles with good flow, consolidation and tabletability properties are necessary, even more so for direct compression formulations. Poor particle properties can lead to various problems during compaction, the most common one being sticking.

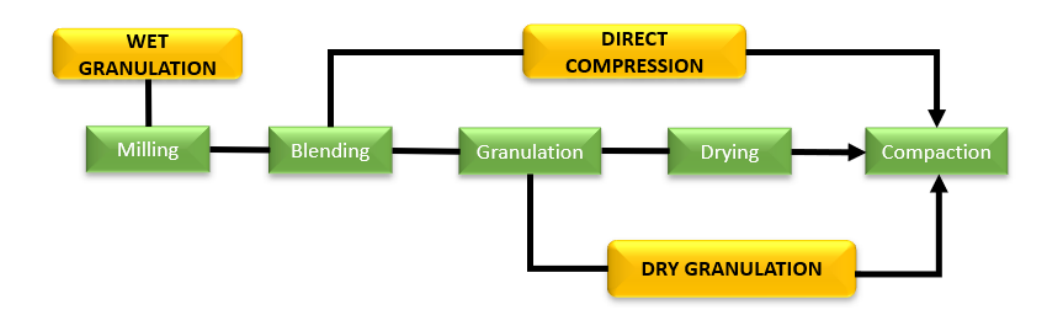


Figure 1-2. Unit operations for the three main pharmaceutical processing routes

Sticking is often referred to as punch sticking²⁰. It occurs after successive compactions and is therefore only discovered in the late stage of the development cycle. The sticking problem heavily reduces production efficiency. When identified, production must be stopped, and the equipment needs to be cleaned. Sticking is especially severe for debossed tablets, causing surface defects²¹. For mild sticking, surfaces may not be defective but tend to look dull instead of the typical attractive shiny appearance²². Sticking also affects content weight uniformity, affecting the final dosage of the drug in a tablet. The consequences of sticking ultimately cause an increased cost of production and delays in getting new medicines to market²³. Currently, punch sticking is managed on a case-by-case basis, where solutions are specific to the product in question. Punch sticking is a complex multi-factorial issue with little understood on how the physicochemical properties of a drug substance affect sticking.



Figure 1-3. Pharmaceutical powder mass adhered to the upper punch 24

Processing issues occurring down various unit operations, including punch-sticking at the final stage of production, drive the need for a thorough understanding of how drug product properties, individually and in formulation, influence processing at different scales of production. This type of optimisation will enhance tablet manufacturing, produce higher quality drugs and boost patient compliance.

1.2 Research Aims and Objectives

By investigating the relationship between molecular, solid-state and bulk-powder properties and downstream tablet processability, this research aims to provide a mechanistic understanding of how the interplay between the physicochemical properties and the mechanical behaviour influences compaction, as articulated through the following research question:

How do the surface and bulk properties of API's and excipients, as well as their relative formulation compositions, influence the processability of pharmaceutical materials?

This will be explored through the following core project objectives:

- Selection of model compounds with varied sticking propensities for investigation of their crystal and bulk powder properties.
- 2. Use of molecular modelling tools to investigate the molecular, solid-state, surface, and particle properties of selected compounds.
- 3. Identify what structural properties that drive the cohesion-adhesion mechanisms involved.

 Characterise flow and compressibility and determine to what extent API-excipient interactions affect compaction.

Through molecular modelling, the solid-state and surface properties of the model compounds will be investigated. Their bulk powder behaviour will be characterised, tablets will be created, and their compactibility will be assessed.

1.3 Selection of Model System

The compounds selected for study are mefenamic acid (MA) and d-mannitol (D-M). Mefenamic acid is a nonsteroidal anti-inflammatory drug (NSAID), used to treat short-term mild and moderate pain such as menstrual cramps and migraines ²⁵. Its molecular structure comprises two benzene rings connected by an amine bridge. One benzene ring is attached to a carboxylic acid group, and the other is attached to two methyl groups. The crystallisation of the drug compound typically yields needle-like crystals, causing a series of downstream processing issues, punch sticking being one of them. The "sticky" nature of MA powders is well documented in literature; however, there are limited publications on how its molecular nature governs its punch sticking nature^{26,27}.

The formulation of MA tablets requires a high drug loading due to the drug being a BCS class II drug, with poor water solubility but high gastrointestinal permeability ²⁸. Therefore, excipients are used to aid in the dissolution of the tablet.

In a mefenamic acid tablet formulation, d-mannitol is often used as a diluent excipient and is the second-largest component in the formulation²⁹. It is used as a bulking agent, improving the flow and compaction properties of the formulation as well as increasing its water solubility. The compound is a sugar alcohol comprising a six-carbon backbone with six hydroxyl groups, making it very water-soluble but impermeable to the gastrointestinal tract. DM powders have also been shown to have some cohesive behaviour³⁰.

Figure 1-4. The molecular structure of mefenamic acid and d-mannitol

Therefore, investigating these two components individually and as a binary mixture is of interest because:

- 1. Both compounds exhibit punch-sticking of varying degrees
- 2. They differ in chemistry and crystal properties
- 3. They have shown varied bulk powder properties
- 4. Both materials are of industrial relevance

1.4 Project Management

This PhD project is funded through the EPSRC Centre for Doctoral Training in Complex Particulate Products and Processes at the University of Leeds and is in collaboration with Pfizer, UK Ltd.

The research has been carried out at the School of Chemical and Process Engineering under the supervision of Professor Kevin J. Roberts, secondary supervisor Dr Ali Hassanpour. In addition to supervising the whole project, Prof. Kevin Roberts oversaw the molecular modelling procedures. Further aid and guidance was provided by research fellow Hien Nguyen, senior research fellow Cai Yun Ma and Dr Siti Ibrahim. Dr Hassanpour oversaw the powder experiments. The project was managed through weekly meetings with both supervisors.

After a successful application, beam time was granted through the Henry Royce Institute for Advanced Materials PhD student access scheme, just before the 2020 global pandemic. X-Ray Computed Tomography (XCT) work was carried out in collaboration with the Henry Royce Institute at the Henry Moseley X-ray Imaging Facility at the University of Manchester. Research associate Dr Parmesh Gajjar

and experimental officer Daniel Sykes provided guidance and supervision during the beam time and assisted with initial analysis. The global pandemic resulted in limitations on lab work; thus, subsequent samples could not be prepared. XCT access was gained again in July 2022 once restrictions were lifted and final samples could be scanned. This beam-time was supported by senior experimental officer Dr Tristan Lowe.

The initial project was aimed at investing in punch-sticking in collaboration with Pfizer, with placement on-site, performing punch-sticking experiments. Again, due to the pandemic and restrictions on outside visitors for a substantial amount of time, the aim of the project had to change. Nonetheless, the opportunity presented itself in June 2023 for an almost 4-week placement observing the punch-sticking of my model compounds. This was supervised by senior principal scientist Dr Lisa Taylor and formulation scientist Jennifer Dolman.

1.5 Thesis Structure

This report consists of six chapters summarised below and in a flow diagram, Figure 1-5.

Chapter 1: This chapter provides context and background to the purpose of the present PhD project. An introduction to the research background is presented, followed by the aims and objectives and the project management.

Chapter 2: This chapter outlines the fundamental crystal science underpinning the solid-state properties of organic crystals as well as the prediction of bulk and surface interactions for production-quality drugs.

Chapter 3: The unit operations involved in the journey of an active pharmaceutical ingredient to the final drug product are outlined. Literature detailing issues encountered during compaction is reviewed, and the knowledge gap which the project seeks to fill is identified.

Chapter 4: The materials used are described in this chapter, and the methods for carrying out the various experimental and computational techniques are explained.

Chapter 5: This chapter presents a deep investigation of the molecular, solid-state and surface properties of the model compounds, mefenamic acid and d-mannitol. By use of molecular modelling techniques, morphology, surface interaction, and mechanical properties have been predicted.

Chapter 6: The experimental results of the two compounds are presented in this chapter. From confirmation of solid-state and thermal properties, to flow and compaction properties.

Chapter 7: In this chapter, results from X-ray computed tomography analysis are presented. Results are discussed in connection with the results obtained in chapters 5 and 6.

Chapter 8: Findings are concluded, and future work is suggested.

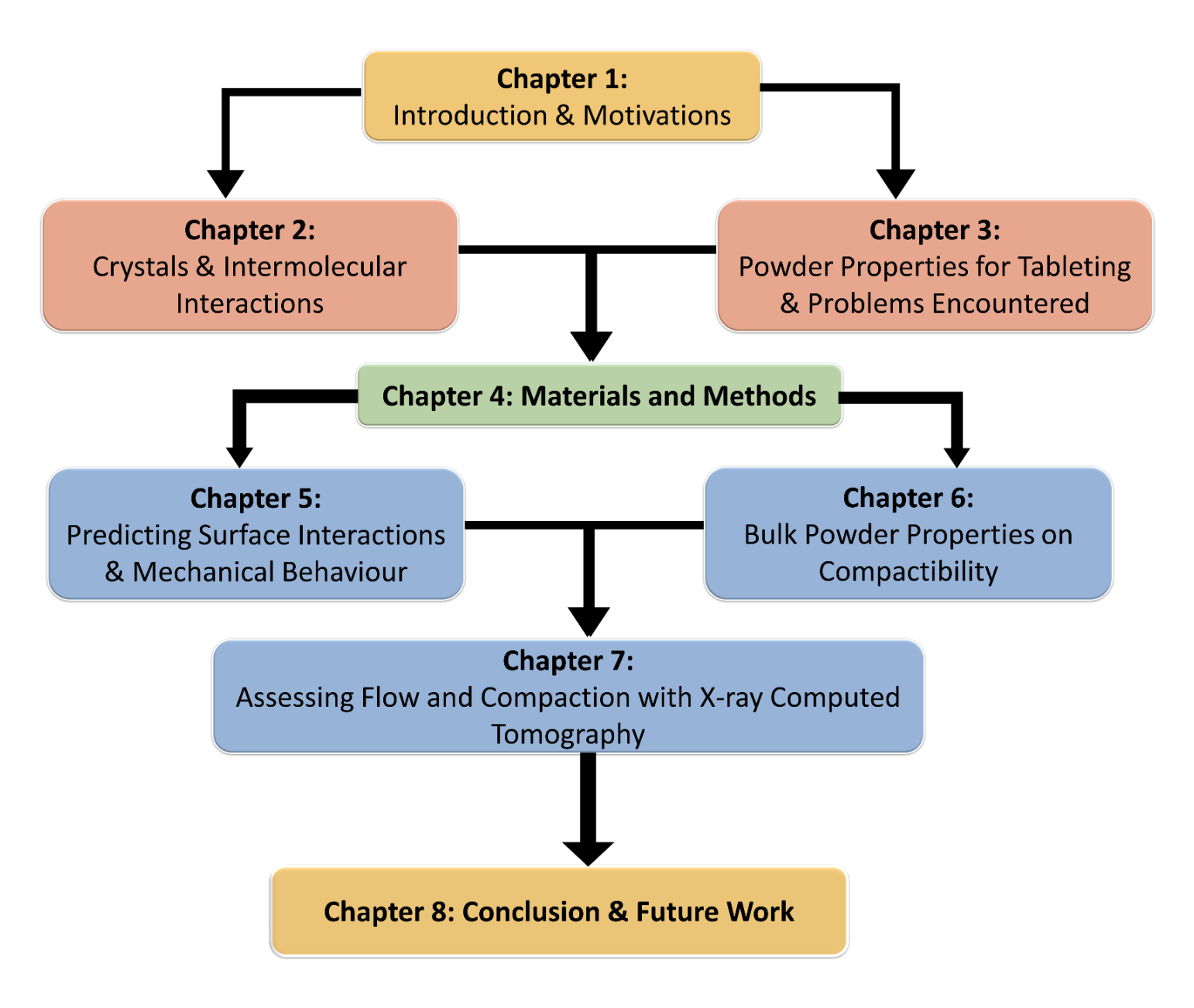


Figure 1-5. Outline of thesis structure

CHAPTER TWO

Crystal Science of Pharmaceutical Materials

This chapter explores the core science of organic crystals in solid-dosage form manufacturing. The bulk and surface interactions forming the solid-state properties are described, and the importance of predicting these for a quality drug product is highlighted.

2 Crystal Science of Pharmaceutical Materials

2.1 Basic Crystallography

The three main states of matter, gases, liquids and solids are differentiated by their intermolecular distances and mobility. Molecules in the gaseous state are the most mobile, with large intermolecular distances allowing for free and rapid movement of atoms within the occupied space. The intermolecular distances between molecules in the liquid state are shorter, however, large enough for considerable mobility to occur. Molecules are described as "sliding past each other"³¹. Gases and liquids are considered disordered systems as they have no regular arrangement. Solids, on the other hand, consist of molecules tightly packed in a regular arrangement. Their mobility is limited to vibrations, and their intermolecular distances are at a minimum. Thus, the molecules do not move outside of their arranged position unless disturbed by an external force.

There is a thermodynamic relationship during conversion between different states of matter, referred to as phase transitions. The transition involves a shift between phases that occurs across the equilibrium boundaries that separate these distinct states. This ordering and disordering of the molecular system is driven by temperature and pressure and alters the physicochemical properties of the substance.

At ambient conditions, active pharmaceutical ingredients (APIs) and excipients are solids, existing as either crystalline or amorphous forms.

The primary method of preparing an active pharmaceutical compound for processing is through crystallisation. It is a vital purification and separation method of separating a dissolved compound in a solvent, defining the purity, shape, and size of the crystals. The performance of drugs in the solid state is dependent on the properties of their crystals. Crystals are the building blocks of crystalline materials and are defined by properties such as lattices, unit cells and crystal systems and are thermodynamically stable. Amorphous solids, however, exist in a disordered state, thus thermodynamically unstable.

2.1.1 Lattices, Unit Cells, and Crystal Systems

Crystals are perfectly ordered three-dimensional solids with molecules (or atoms and ions) packed in a structured and symmetric pattern, repeated throughout the entire solid. The symmetrical three-dimensional arrangement that defines a crystal is referred to as the crystal lattice. The crystal lattice arrangement can be depicted by a two-dimensional pattern, and the repeated segment is called a motif (Figure 2-1). Each point in the pattern represents an atom or a group of atoms referred to as lattice points. The environment around each lattice is identical. The smallest portion which defines the structure of the entire crystal lattice is called a unit cell and is described using the lengths of the cell edges (a, b, c) and the angles between them (α, β, γ) .

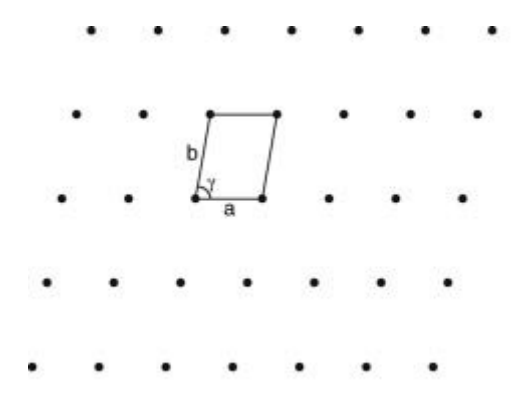


Figure 2-1. Two-dimensional depiction of a crystal lattice arrangement

There are three fundamental principles which underpin the science of crystallography³²:

- 1. *The Law of Constancy of Interfacial Angles:* The angles between specific crystal surfaces remain unchanging as they grow.
- 2. *The Law of Rational Indices:* This pertains to the systematic arrangement of crystal planes in space. These planes represent different crystal faces and are denoted by a three-coordinate-axis system. The point at which planes intersect axes can be described with whole integer numbers.

3. **Symmetry:** Plane symmetry is defined by imaginary planes that bisect the crystal into two identical parts. Through a fractional rotation around an axis of symmetry, crystal faces, edges, and corners replicate.

The three-coordinate-axis system mentioned above is called Miller indices and describes both direction and planes. When describing direction, the Miller indices are the coordinates of a vector starting from the origin of a unit cell to a particular point of the lattice, reduced to the smallest integer³³. The coordinate vectors are written in square brackets [hkl], and any negative coordinate is denoted by a horizontal bar above that coordinate. The direction related by symmetry is denoted by pointed brackets <hlk>. The Miller indices of planes are described as the reciprocals of the fractional intercepts of how the plane intercepts the crystallographic axes (x,y,z)³³. They are denoted in brackets, (hkl) and like directions, any negative coordinate is denoted by a bar above the corresponding integer. Curly brackets {hkl} are used to describe a set of planes related by symmetry known as forms.

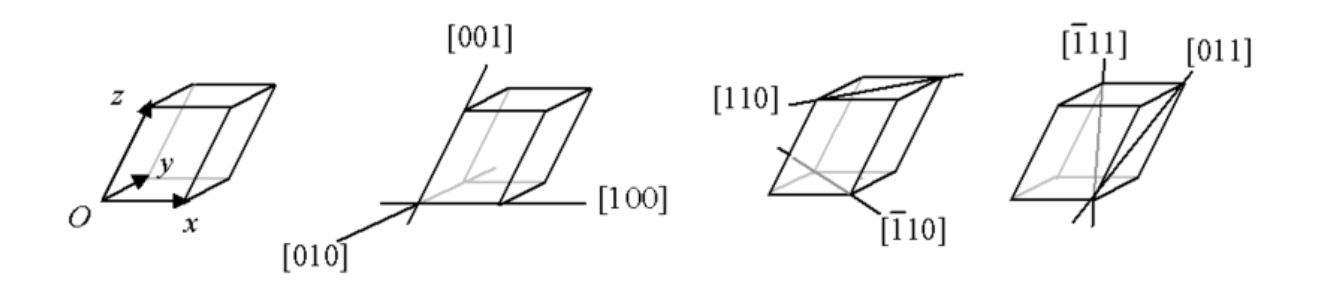


Figure 2-2. Example of crystallographic Miller indices for directions³⁴

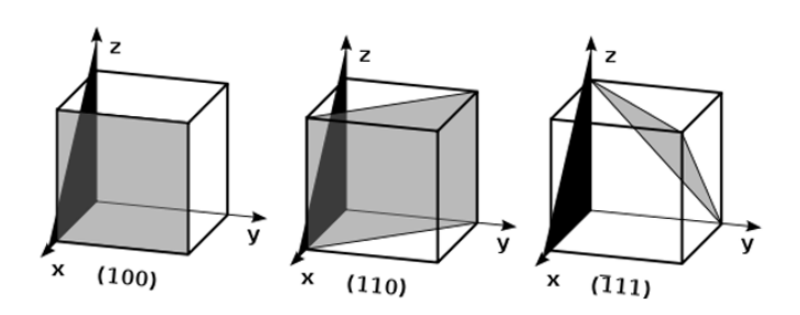


Figure 2-3. Example of crystallographic Miller indices for planes 35

The number of lattices which can be constructed is limited. This was proved by the prominent French crystallographer Auguste Bravais, who explained that in three-dimensional space, 14 possible lattice types can be arrangesd³⁶. Consequently, these specific lattice arrangements are referred to as the *Bravais* lattices. The Bravais lattices are categorised into four types: *primitive, base-centred, body-centred and face-centred.* They are described with respect to the 7 crystal systems. The 7 crystal systems classify crystals based on their symmetry and the relationship between their crystallographic axes. Each of these systems is characterised by distinct axial relationships and angles connecting the axes. The 7 systems are: *cubic, tetragonal, orthorhombic, monoclinic, triclinic, trigonal and hexagonal.* Table 2-1 illustrates the 14 Bravais lattices across the 7 crystal systems as well as examples of crystal shapes.

Table 2-1: The 14 Bravais lattices across the 7 crystal systems, outlining the angles (α, β, γ) between the axes and the length of the axes $(a, b, c)^{37}$ and examples of crystal shapes³⁸

	Bravais lattices			Cwratal	
Crystal systems	primitive	base-centered	body-	face-	Crystal shapes
			centered	centered	Shapes
Cubic $\alpha = \beta = \gamma = 90$ a = b = c	a				spinel
Tetragonal $\alpha = \beta = \gamma = 90$ $a=b \neq c$	c				rutile
Orthorhombic $\alpha = \beta = \gamma = 90$ $a \neq b \neq c$	a				sulfur
Monoclinic $\alpha = \beta = 90 \neq \gamma$ $a \neq b \neq c$	c a				gypsum

Triclinic $\alpha \neq \beta \neq \gamma \neq 90$ $\alpha \neq b \neq c$	c Bi a a		kyanite
Trigonal $\alpha = \beta = \gamma \neq 90$ a = b = c	a a a a		calcite
Hexagonal $\alpha = \beta = 90, \gamma = 120$ $a=b \neq c$	c a		quartz

2.2 Crystal Lattice Defects

Crystals are hardly ever perfect. As the raw materials interact with their local environment, there is a chance for disturbance to the lattice. Thus, it is common for defects to occur within the otherwise perfectly ordered crystal lattice. Crystal lattice defects are imperfections in the periodic arrangement of atoms or ions within a crystal structure. These defects can significantly influence the chemical, physical and mechanical properties of materials. Understanding the types, origins, and effects of lattice defects is crucial for materials scientists and engineers to tailor material properties for specific applications. There are various kinds of crystal defects, such as point defects, linear defects, planar and volume defects³⁹. These are summarised below in Table 2-2.

Table 2-2: Types of Crystal Defects

Types of crystal defects				
0-dimensional – Point	1-dimensional – Line	2-dimensional – Area/plane	3-dimensional –	
defect	defect	defect	Volume defect	
Vacancies: vacant	Edge dislocation: slip	Stacking faults: addition or	Voids and	
lattice site	caused by the addition	omission of a lattice	inclusions	
Interstitials/impurities:	of a half-plane	sequence		
extra atoms/ions or	Screw dislocation: slip	Grain boundaries: interface		
addition of foreign	caused by shear	between grains of		
particles		mismatched orientation		
Substitutional:				
replacement of				
atoms/ions				

2.2.1 Point, Plane and Volume Defects

Point defects are irregularities in the crystal lattice that deviate from their expected lattice positions. These defects include missing atoms/ions referred to as vacancies; extra atoms/ions called interstitials; these can also be impurities of foreign particles; and substitutional defects, which are the replacement of atoms/ions with another. The combination of vacancies and interstitials together in ionic crystals is called Frenkel defects, whereas Schottky defects refer to vacancies only⁴⁰. All these point defects affect the crystallisation process, thus altering the purity and psychochemical properties of the final crystal.

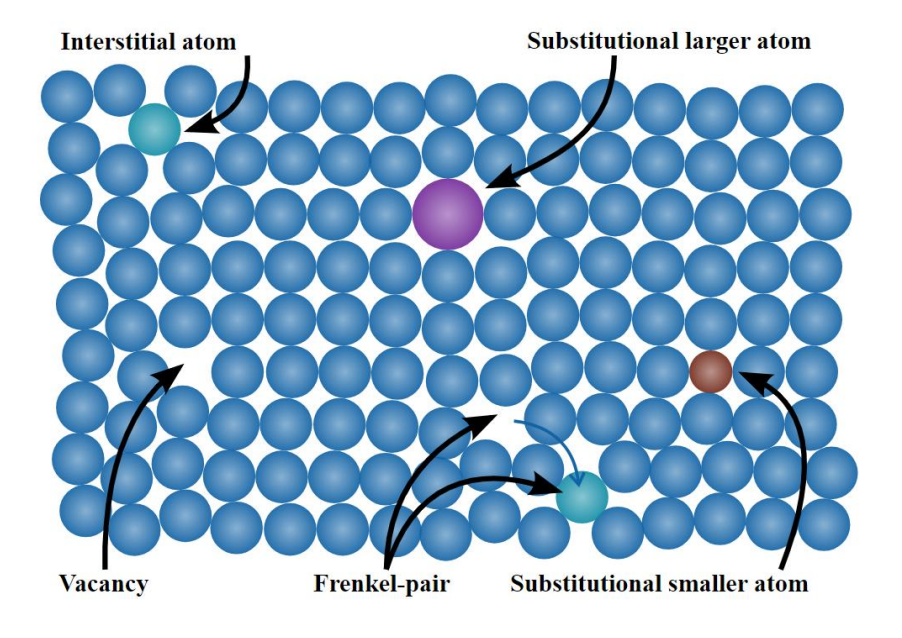


Figure 2-4 Point defects in crystal structures⁴¹

Planar defects are 2-dimensional imperfections that alter the lattice pattern, most commonly stacking faults⁴². This is the addition or omission of a lattice sequence, causing extrinsic and intrinsic stacking faults, respectively. Stacking faults can occur during crystal growth, evolve from other defects or be part of another defect, such as dislocations. Twinning faults can be induced when the stacking fault inverts on itself, creating a mirror image. They can be distinguished by the formation of boundaries between twin crystals with a varied lattice orientation. The occurrence of homogenous shear in an area of the lattice results in twin boundaries, causing a new lattice orientation in the crystal.

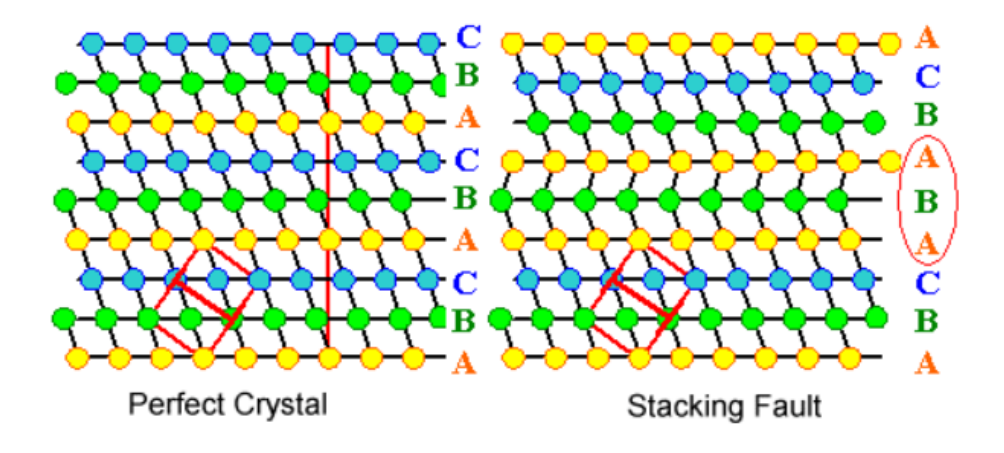


Figure 2-5. Perfect and faulted stacking sequence for a face-centred cubic crystal⁴³

Another 2-dimensional defect is grain boundaries. The process of crystallisation tends to yield crystals of irregular shapes referred to as grains. Each grain may have a different lattice orientation and patterns. The interface between grains is known as a grain boundary and separates the regions that have different orientations. Figure 2-6 displays the use of raft bubbles to distinguish the various defective grains compared to the perfect grain. Each grain can contain any of the previously mentioned defects.

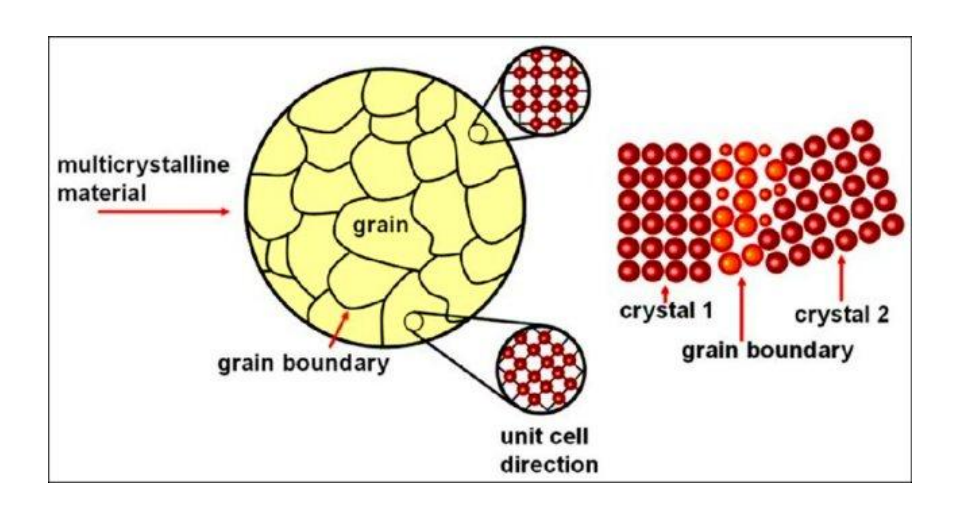


Figure 2-6 Grains and grain boundaries in a polycrystal. 40

Volume defects are 3-dimensional defects also referred to as bulk defects, i.e defects within the bulk of the crystal⁴⁴. These include voids, precipitates, and inclusions. Voids or pores can occur from an accumulation of vacancies or trapped gas during densification, whereas precipitates and inclusions are

the introduction of foreign particles into the crystal matrix⁴⁴. Precipitates tend to be smaller in size, and inclusions are impurities or larger precipitates.

2.2.2 Linear Defects

Linear defects are linear dislocations in the crystal lattice and occur when atoms along a particular crystallographic direction are displaced⁴⁵. This deviation of atoms from their original position causes the greatest crystal imperfection, impacting crystal growth and physicochemical properties⁴⁶. The significant effect on mechanical properties creates slip planes, allowing for plastic deformation of materials. It can either weaken or strengthen materials, affecting hardness, ductility and fracture behaviour. In organic crystals, this dislocation is defined by the Burgers vector, i.e the direction of the dislocation⁴⁷ and the slip plane, the plane in which the dislocation occurs⁴⁸. The dislocation energy is the required threshold for deformation and displacement to occur. It describes the weakening of materials beyond their theoretical strength. Equation 2-1 expresses the total energy of dislocation $(E_{disloc})^{47}$.

$$E_{disloc} = E_{core} + E_{line}$$
 Equation 2-1

Where (E_{core}) is the core energy and (E_{line}) is the line energy. The core energy describes a short-range non-crystallographic structural disorder surrounding the dislocation line, while the line energy is the long-range elastic deformation of the lattice caused by the dislocation core. The core energy is a difficult parameter to measure; however, it is often considered to be at least an order of magnitude smaller than the line energy⁴⁷. Thus, excluding this parameter introduces negligible errors when calculating the dislocation energy. Consequently, the dislocation energy for isotropic materials can be calculated by:

$$E_{line} = AK |\overline{b}|^2$$
 Equation 2-2

Where A is a constant, K is the elastic tensor and $|\bar{b}|$ is the Burgers vector magnitude. The equation reveals that the shortest Burgers vector corresponds to the lowest dislocation energy, where plastic deformation dominates⁴⁷.

The atom's path of dislocation within the distorted lattice is known as the Burgers circuit. In a perfect crystal lattice, the Burgers circuit is closed; however, following the same path in an imperfect crystal,

the circuit becomes incomplete, thus left open⁴⁵. The vector required to complete and close the circuit is the Burgers vector, and in molecular systems, it is defined as the shortest length in a 3D lattice translation. The Burgers vector is not affected by crystal morphology but rather dependent on the crystal system. Form I of the drug mefenamic acid has a primitive triclinic the Burgers vector is <010> as it is the shortest inter-molecular distance in the crystal lattice.

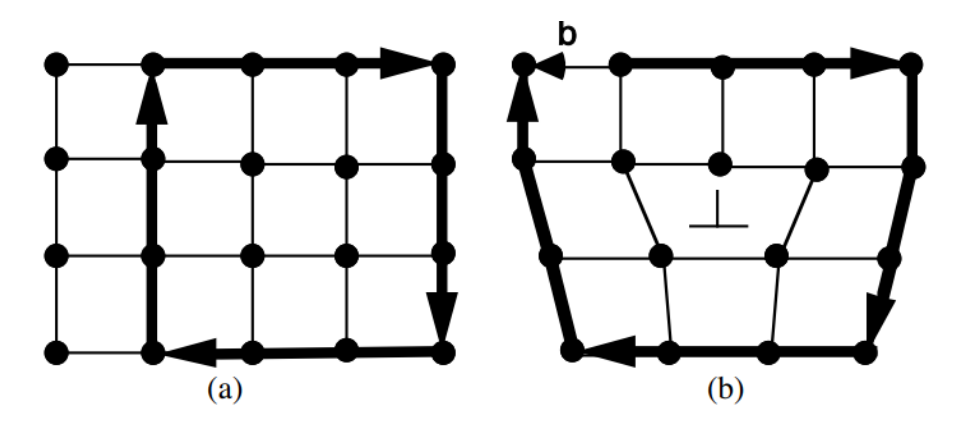


Figure 2-7. Example of (a) a closed Burgers circuit in a {100} plane of a cubic crystal and (b) an open, failed circuit needing vector b to close it⁴⁴

For plastic deformation to occur, an active slip system must be present. This is when the Burgers vector [uvw] lies within the slip plane (hkl), expressed in the Weiss zone law equation⁴⁵:

$$hu + kv + lw = 0$$
 Equation 2-3

As mentioned above, the slip plane is the face in which dislocation occurs, and it tends to be the densest plane. The dislocation, slip will start from a localised area and gradually extend outwards, resulting in a slip line that distinguishes itself from the slipped and unslipped regions⁴⁸.

The types of dislocations that can occur are categorised as edge and screw dislocations. An edge dislocation occurs when an extra half plane is inserted into the crystal structure. This causes displacement of atoms from their original lattice sites, resulting in distortion along the edges of the crystal. In an edge dislocation. The Burgers vector is perpendicular to the dislocation line and lies on the slip plane. Screw dislocations occur through shear stress, resulting in a spiral planar ramp in the crystal. In this event, the Burgers vector is parallel to the dislocation line and the slip plane. There is also the possibility of mixed dislocation, which is a combination of both the edge and screw dislocation.

In this case, the dislocation line and the Burgers vector are neither perpendicular nor parallel to each other.

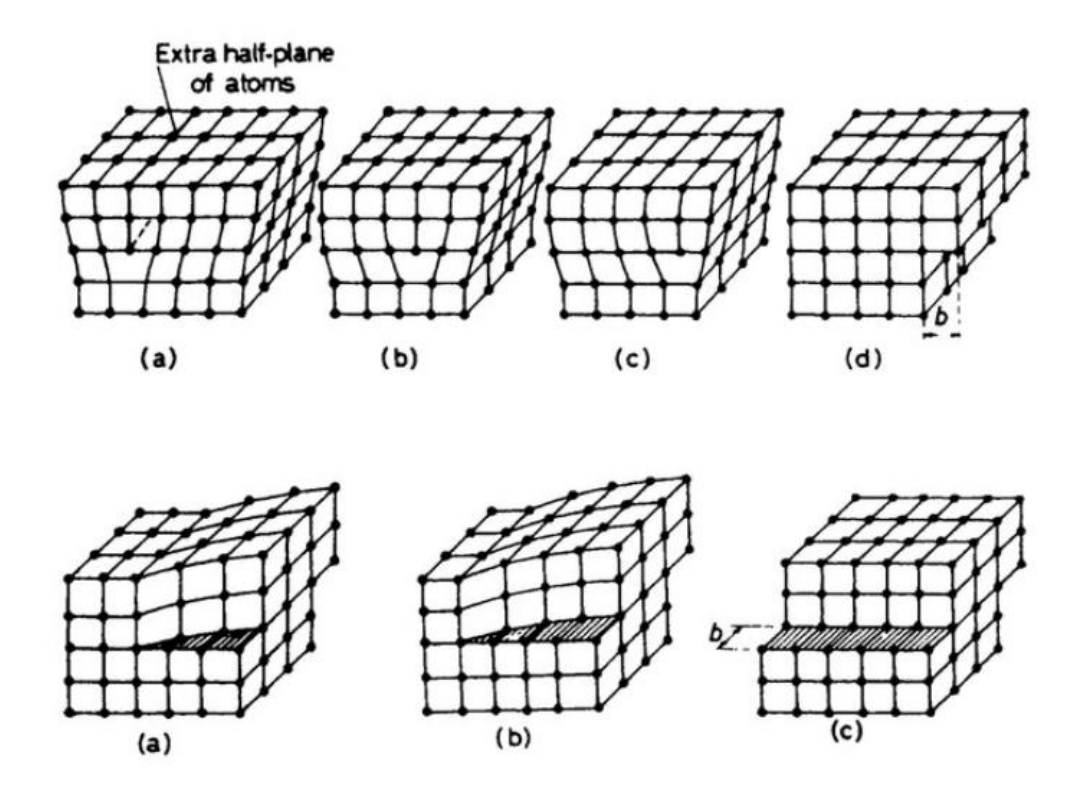


Figure 2-8. The movement of edge (top) and screw (bottom) dislocations during slip⁴⁹

2.3 Polymorphism

Solids can exist as crystals or be amorphous in nature. In contrast to crystals, amorphous solids do not exhibit long-range order. Some short-range order may be present; however, similar to the liquid state, they are often described as disordered. Amorphous solids often convert into their crystalline form due to being thermodynamically metastable. However, some have proven to maintain their amorphous structure. A typical example is silica (SiO₂), existing naturally as quartz, which is crystalline. Its amorphous form is what is known as glass. Through heating and rapid cooling, with the addition of impurities such as sodium, the ordered lattice structure is disturbed⁵⁰. This results in a clear, transparent material with a lower melting point. Though amorphous, its disordered structure is still thermodynamically stable due to the strength of the Si-O bonds.

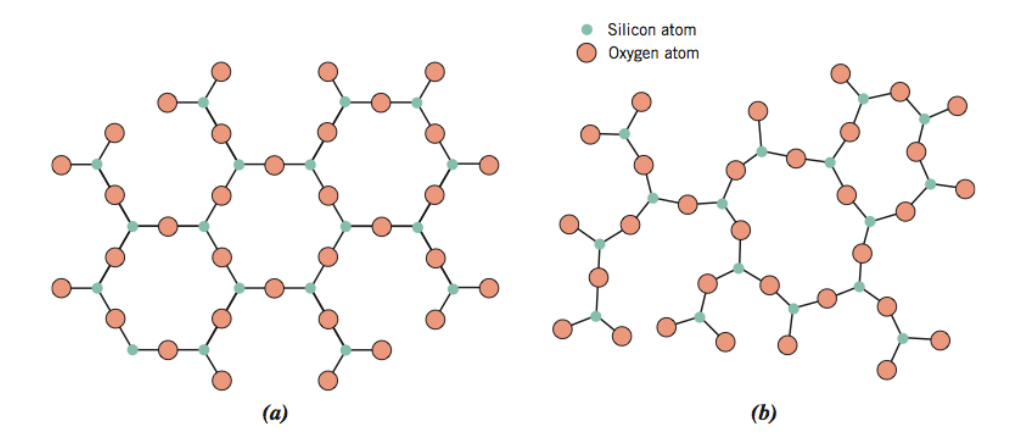


Figure 2-9. Structure of a) crystalline and b) amorphous (without impurities) silicon dioxide silica⁵⁰

In total, silica exists in 11 other crystalline forms and 2 non-crystalline forms⁵¹. Thus, quartz and glass are examples of polymorphs of the same substance. Polymorphism is the ability of a compound to exist in two or more crystal forms, known as polymorphs⁵². Polymorphs have identical chemical structures but different lattice structures within the unit cell, due to different molecular packing or molecular conformations.

Approximately 30% of pharmaceutical compounds are polymorphic⁵³. The structural difference within the crystals means that polymorphs of the same drug compound will have different properties and will behave differently during processing and in the body. Factors such as morphology (shape), solubility, dissolution, density, mechanical properties, and stability will vary between the polymorphs, affecting the quality of the final drug product⁵⁴. It is therefore very important to consistently produce the desired polymorph with the desired therapeutic effect. However, the presence of unknown polymorphs can't always be predicted, making it somewhat difficult to control the crystallisation process.

Andrew Bond provides a scheme for classifying pharmaceutical solids based on two principles: structural and chemical identity⁵⁵ (see Figure 2-11). The chemical identity (vertical axis) refers to the types of molecules present in the solid; they can either be single- or multi-component solids. Pure chemical compounds are solids denoted as "Single-component" substances, highlighting the presence

of polymorphs. "Multi-component" pharmaceutical solids contain more than one molecule type and can be subdivided into three categories: solvates/hydrates, co-crystals, and salts. Solvates contain solvent molecules stoichiometrically and non-stoichiometrically within their lattice structure. Hydrates are similar except that the solvent is water. The addition of non-volatile molecules in the lattice structure is called a co-crystal.

The structural identity (horizontal axis) classifies the solid into crystalline and amorphous. The scheme displays how the structural classification can be applied to the chemical nature of the solids. A given chemical composition may exist as both crystalline and amorphous. The amorphous forms of poorly soluble drugs tend to possess superior dispersion and dissolution performance, resulting in better bioavailability than their crystalline from⁵⁴. However, due to their nature of being less thermodynamically stable, they revert to their stable crystalline polymorph.

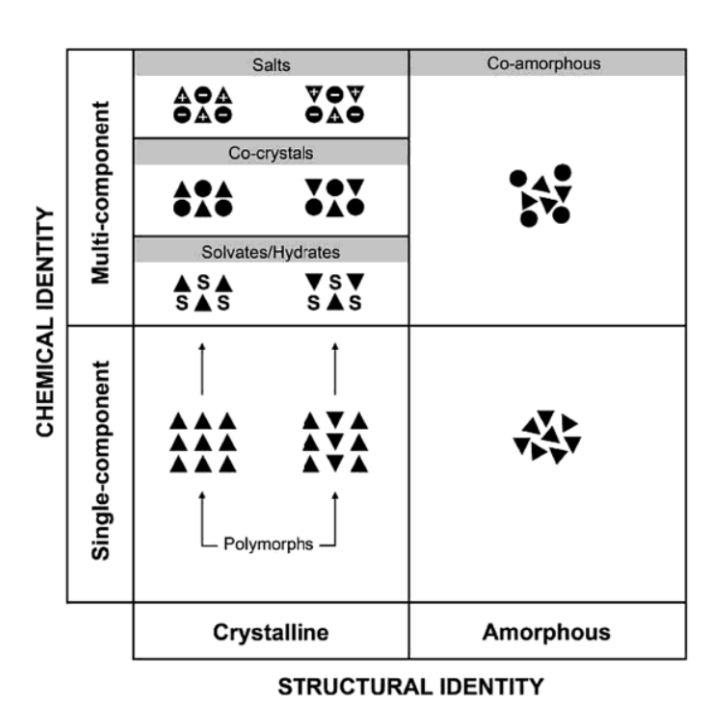


Figure 2-10. A systematic scheme for classification of pharmaceutical solids⁵⁵. Key: \triangle =API molecule, \bullet = co-crystal/salt, S = solvent molecule

The most stable form of a drug compound tends to be the desired polymorphic form, due to the reduced chance of converting into another form. However, sometimes the most stable form is not the form with the desired therapeutic effect. Such is the case for the HIV/AIDS drug ritonavir⁵⁶. When first launched in 1996, only one form had been discovered (Form I) and sold as a regular capsule. During the development of the drug, no stability issues had been identified, and the drug appeared fit for market. Two years later, batches of the drug were failing dissolution requirements, and it was found that this was due to the appearance of a more stable form, Form II. Form II compromised the therapeutic performance of the drug as it was less soluble and hence less efficacious. Batches of the drug were converted into the more stable Form II, causing the temporary withdrawal of the capsules from the market. The drug was later reformulated into a soft gel capsule, which needed to be kept refrigerated to avoid polymorphic conversion. The event highlights how important polymorphic screening is for the development of safe and efficacious medicines.

2.4 Intermolecular Interactions & Crystal Lattice Energetics

The molecules within a crystal lattice are bound together through intermolecular interactions. The structure and strength of the crystal depend on the type of intermolecular bonding present in the lattice ⁵⁷. It is important to differentiate between *intra*molecular interactions and *inter*molecular interactions. *Intra*molecular interactions are the types of bonds between atoms in a molecule, such as covalent, ionic, and metallic bonds. *Inter*molecular interactions are the forces between molecules. They dictate the packing pattern of the molecules during crystallisation. The types of interactions include van der Waals forces (vdW), hydrogen bonding (h-bond) and electrostatic forces.

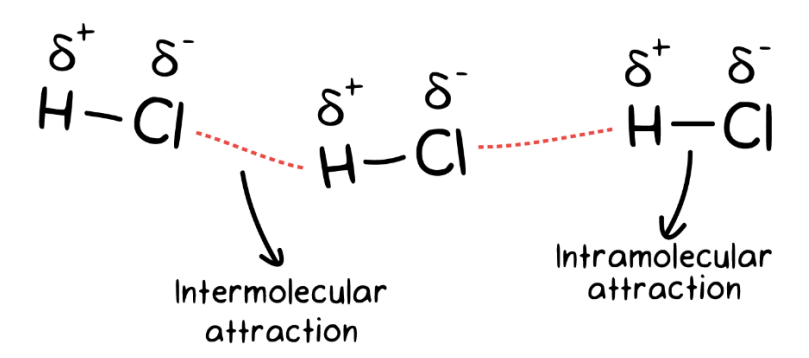


Figure 2-11. The difference between intermolecular interactions and intramolecular interactions

2.4.1 Interaction Types

• Electrostatic interactions: Also called *coulombic forces*, are the attractive and repulsive forces that occur between partially charged species and can be quantified by Coulomb's Law⁵⁸. Coulomb's Law is an experimental law that measures the force between two partially charged particles. It states that the absolute value of the electrostatic force between two point charges is directly proportional to the product of the magnitudes of the charges and inversely proportional to the squared distance between them⁵⁹. The negative and positively charged particles are attracted through this inverse-square law:

$$F = k \frac{q_1 q_2}{r^2}$$
 Equation 2-4

Where F is the electrostatic force, k is the Coulomb's constant, q_1 and q_2 are the magnitudes of charges, and r is the distance between the charges.

- Hydrogen Bonds: Relatively strong, directional, short-range electrostatic interactions between hydrogen covalently bonded to an electronegative atom (oxygen, nitrogen, or fluorine) and an electronegative atom with lone pair electrons, creating the bonding configuration: X-H···Y⁶⁰.
- <u>Van der Waals Forces:</u> These are weak, short-range attractive interactions between two nonpolar particles⁵⁹. The presence of electron distribution fluctuations in molecules induces temporary dipoles and the same in neighbouring molecules, giving rise to VdW interactions. It can further be separated into dipole-dipole, dipole-induced dipole, and London dispersion forces⁵⁹. Dipole-dipole interactions occur between molecules with permanent dipole moments (polar particles). Dipole-induced dipole interactions occur when a polar molecule approaches a nonpolar molecule, inducing a dipole by shifting its electron distribution, resulting in polarisation of the originally nonpolar molecule. The weakest form of VdW interactions is the London dispersion forces. The temporary fluctuations in electron distribution within molecules result in instantaneous dipoles. These then induce temporary dipoles in neighbouring molecules, creating this weak interaction.

2.4.2 Predicting Intermolecular Interactions

By use of atomistic force-fields, the intra- and intermolecular interactions within a crystal can be mathematically calculated, predicting certain physicochemical properties^{61,62}. Through this, the crystal lattice energy is calculated. The lattice energy is described as the energy contained within the crystal lattice of a compound. The value is given by the sum of all the molecular interactions between a central atom of a molecule and all the other surrounding molecules up to a distance where the energies become negligible, usually >18 Angstroms, assuming vacuum conditions and 0 Kelvin⁶³. This value is used to estimate the stability of the crystal and is given by Equation 2-5.

$$E_{cr} = \frac{1}{2} \sum_{k=1}^{N} \sum_{i=1}^{n} \sum_{j=1}^{n'} V_{kij}$$
 Equation 2-5

Where Vkij is the interaction energy between atom i in the central molecule and the atom j in the kth surrounding molecule. Atoms within a central molecule are denoted by 'n' and 'N', the surrounding molecules. A factor of ½ is added to account for the duplication of the interaction between two bodies. The accuracy of the force-field calculation can be verified by comparing it to the experimental enthalpy of sublimation:

$$E_{cr} = \Delta H_{sub} - 2RT$$
 Equation 2-6

where R is the gas constant and T is the temperature at which the sublimation enthalpy was measured.

The enthalpy of sublimation is the energy needed to transition one mole of a substance directly from solid to gas, at a given temperature and pressure⁶⁴.

Force fields often use the Lennard-Jones potential to describe the interactions between non-bonded atoms or molecules based on their distance of separation⁶⁵. It accounts for the difference between attractive and repulsive forces. The Van der Waal repulsive and attractive forces are described with an added coulombic term to describe the electrostatic interactions⁶⁶:

$$V_{ij} = -\frac{A}{r_{ij}^{12}} + \frac{B}{r_{ij}^{6}} + \frac{q_i q_j}{D r_{ij}}$$
 Equation 2-7

where A and B are constants to describe the atom-atom interaction, r is the distance between the atoms, q_i and q_j are the magnitudes of charges between each atom, and D is the dielectric constant.

2.5 Crystal Morphology & Modelling of Organic Crystals

The shape of crystals is often referred to as crystal morphology or crystal habit interchangeably. However, they do differ in their definitions. The habit is the final geometric appearance of a crystal, where qualitative terminology such as prismatic, lamellar, needle and plate-like is used as descriptors. Whereas the morphology of a crystal is the quantitative approach of describing the crystal shape using the Miller indices. It refers to the number and composition of the various faces that form the outer boundary planes of the crystalline material⁶⁷. Crystals can possess the same morphology but different habits. The facets of the crystals will be the same; however, the growth rate of these facets may differ, resulting in various habits (Figure 2-13, a). Crystal may also have the same habit but different morphologies. They exhibit similar dimensions within the principal space directions, yet they possess a different set of facets (Figure 2-13, b).

These variations occur due to the varied relative growth rates of each facet. Different particle formation methods and crystallisation conditions, such as solvent type, temperature and time, will influence the growth rate of the facets of a crystal, thus affecting the resulting morphology⁶².

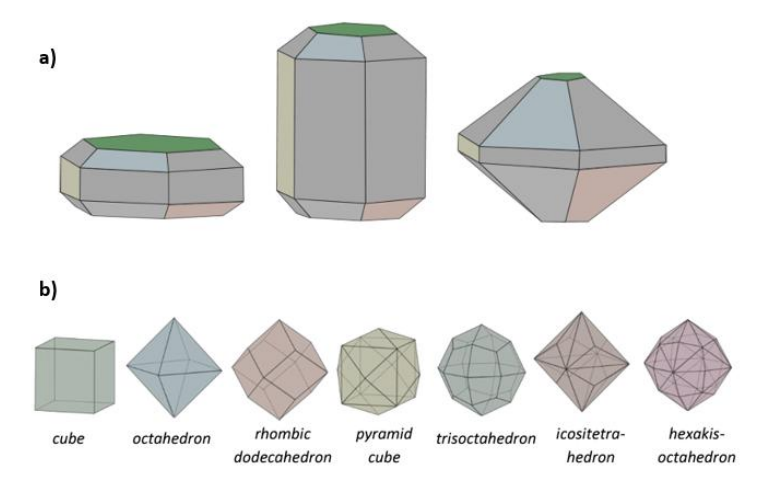


Figure 2-12. Examples of crystals of the a) same morphology but different habits and b) same habit (isometric habit) but different morphologies⁶⁷

The shape of crystals is a very important physical property in pharmaceutical manufacturing. It can affect various steps in downstream processing such as filtration, blending, die-filling, and tabletting, as well as the quality and biological performance of the subsequent drug product. Therefore, the ability to control and/or predict particle morphology of drug substances is valuable.

The ratio of the surface extrinsic synthons and the bulk intrinsic synthons is usually used for the prediction of crystal morphology. The Bravais, Friedel, Donnay and Harker (BFDH) model is used for the identification of the most morphologically important crystal faces^{36,68,69}. The model accounts for the lattice geometry and assumes that the growth rate of each crystal surface is inversely proportional to the interplanar spacing (d_{hkl}) and directly proportional to the attachment energy. Crystal surfaces with the largest interplanar spacing are identified as the most morphologically important.

The attachment energy is defined as the energy released as a new slice of width d_{hkl} is added to a growing crystal⁷⁰. It is calculated based on the strength of the extrinsic synthons and predicts a theoretical crystal morphology by taking into account the intermolecular interactions. Hence, the attachment energy model provides a more accurate morphology prediction than the BFDH model. Higher attachment energy values of a crystal surface correlate to a higher relative growth rate of that surface, indicating a surface of less morphological importance^{71,72}.

$$E_{cr} = E_{sl} + E_{att}$$
 Equation 2-8

where E_{cr} is lattice energy, E_{sl} is slice energy, and E_{att} is attachment energy.

Assuming that the relative growth rates of each surface are directly proportional to their attachment energies, an equilibrium crystal morphology can be calculated. This prediction only calculates vapour phase morphologies; hence, it does not consider the effects of growth in solvent media.

Habit98⁷³ is a molecular modelling tool that calculates the lattice energy of a crystal and predicts the crystal morphology by calculating the attachment energy described above. The morphology can be visualised and assessed in programmes such as Mercury⁷⁴ and Materials Studio⁷⁵. This tool can be coupled with a Systematic Grid-based Search (SystSearch)⁷⁶ method for the prediction of morphologies with respect to the crystals' surrounding environment, which has been used^{14,17,77–79}. The prediction is

made through the calculation of all the possible interactions between a chosen crystal face and a probe molecule. A specific slab of a crystal face is chosen for examination, a grid is built on top of it, and a probe is placed on the grid. The probe molecule is moved at each point of the grid in three translational movements, x, y, z and three rotational, θ , γ , δ . The interaction energy between the slab and probe is calculated at every rotational and translational position. An output file is created, sorting the interactions from strongest to weakest. The interactions are also divided into vdW, h-bond and electrostatic interactions.

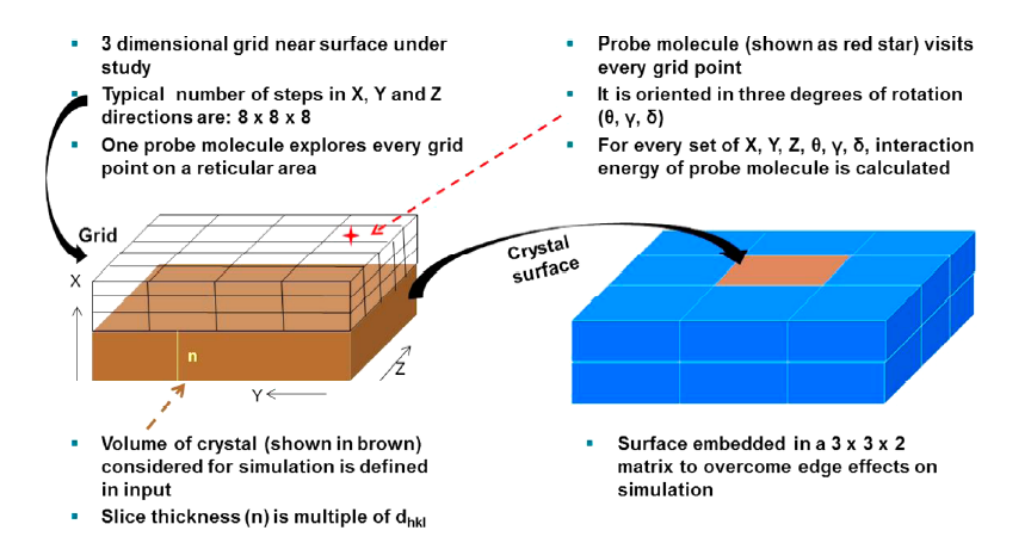


Figure 2-13. Schematic outline of the SystSearch prediction, illustrating the movement of the probe molecule on the grid over the slab¹⁷

Rosbottom et. al utilised the grid-based search method for the examination of solvent interactions with the {100}, {001} and {011} faces of RS-ibuprofen¹⁶. The molecular modelling technique identified the types of interactions present, calculated their strengths, which were related to the relative growth rates of each face. Results revealed that ethanol, ethyl acetate and acetonitrile form strong h-bond interactions to the {011} face due to the exposed –COOH synthons at that face, and weak van der Waals interactions to the {001} face. Ethanol, being a polar protic solvent, acts as both a hydrogen donor and acceptor, displaying the strongest interactions at the {011} face. Toluene was found to interact greater with the {001} face than the {011} face, where van der Waals interactions dominated.

The results were rationalised by comparing experimental growth rates of RS-ibuprofen in the same solvents ⁸⁰. It was suggested that polar protic solvents inhibit growth at the capping {011} face (called

capping face as it "caps" the crystal's growth along its primary axis), reflected by the slower growth rate at that face compared to non-polar solvents. This explains the observation of the larger defined {011} face from crystals grown in ethanol (Figure 2-14, a). Toluene is not able to form h-bond interactions and therefore interacts strongly with the side {001} face, showing a slower growth rate at that face and a faster growth rate at the {011} face. This explains the less defined shape of the {011} face and the overall needle-like morphology of crystals grown in toluene. The {100} face had the slowest growth rate in all solvents, hence the largest surface of the crystal, reflected in the experimental morphologies.

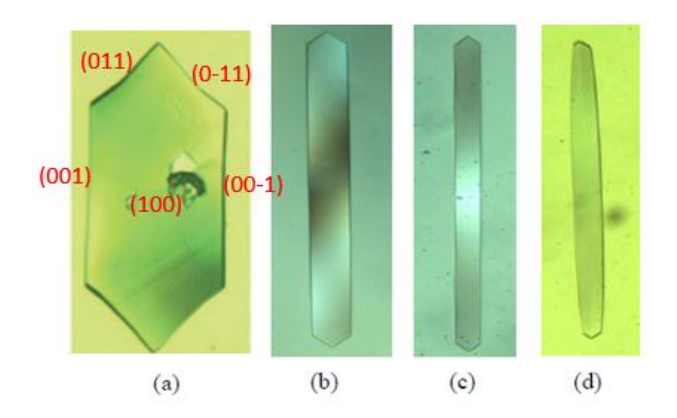


Figure 2-14. RS-ibuprofen crystals grown from a) ethanol, b) ethyl acetate, c) acetonitrile and d) toluene⁸⁰

The same methodology has also been used to examine APIs and excipients. The interactions between particles are primarily governed by two types of forces: cohesion and adhesion. Cohesion describes the intermolecular interactions between similar molecules or particles. In contrast, adhesion refers to the intermolecular interactions between different molecules. Ramachandran et al. used SystSearch to examine the cohesive/adhesive balance between APIs and excipients in inhalation formulations ¹⁷. The interactions between the APIs fluticasone propionate (FP), budesonide (Bud) and salbutamol base (SB) with the common drug excipient α-lactose monohydrate (LMH) were calculated. Results were compared to experimental results where the de-agglomeration of the powders where assessed using dry powder laser diffraction. The SystSearch calculated FP API-cohesivity to be the strongest, correlating with the de-agglomeration data, showing it required the highest de-agglomeration pressure. However, the prediction of LHM cohesion and adhesion to the other compounds did not directly correlate with

the experimental data. This was proposed to be due to the high electrostatic and h-bond surface of LMH not being accurately calculated. This highlights the possible limitation of such a simulation. The probe to surface interaction doesn't fully represent the surface-surface, particle-particle interactions found in real life. However, it does give a starting point on how to elucidate those interactions, aiding in preformulation screening of drug products.

A more recent study by Ma et al. used the SystSearch model to compare molecule-molecule, molecule-surface, and surface-surface cohesion/adhesion interactions between the inhalation drug terbutaline sulphate (TBS) and α -lactose monohydrate (LMH)⁸¹. The simulation results were compared to deagglomeration studies and X-ray computed tomography (XCT) analysis. Results revealed that the TBS cohesion was consistently the strongest interaction across all three scales. This was in good agreement with the experimental results. The study highlights the potential of the SystSearch to accurately predict cohesion/adhesion in inhalation powders. The surface-surface prediction is the most computationally intensive and demanding of the three simulation scales, thus potentially inefficient in the fast-paced, quick turnaround nature of the pharmaceutical industry. The results exhibiting a consistent trend across the three scales suggest that the less demanding probe-surface simulation is sufficient for prediction.

2.6 Conclusion

The crystal science outlined in this chapter provides the fundamental knowledge for understanding the solid-state and surface properties of organic crystals. Common crystal defects and the occurrence of polymorphic change have been described, both of which can impact the processability of drug substances. The intrinsic intermolecular interactions that hold the crystal lattice have been explained, as well as the calculation of force fields to predict them. The lattice energy provides a value for the stability of the crystal, which can be verified with the enthalpy of sublimation. The importance of crystal morphology has been discussed, and the potential of morphology prediction has been explored. Habit98 calculates intrinsic synthon prediction (lattice energy) and the ratio between intrinsic and extrinsic synthons (morphology). Whilst the SystSearch is useful for understanding particle-solvent and particle-

particle surface interactions. Although these methods have been used extensively to predict particleparticle interactions at various levels of drug manufacturing, there is still a lack of consistent correlation to experimental results. Nonetheless, they offer a good foundation for the direction in which formulation scientists should follow.

The properties described in this chapter provide the foundation for the powder bulk properties observed in downstream processing. This will be further explored in Chapter 3.

CHAPTER THREE

Drug Powder Properties Influencing Tabletability

This chapter details the processing steps involved in manufacturing the solid dosage drug form, from pre-formulation to compaction. The ideal powder properties are outlined, and problems encountered during manufacturing are explained. Assessment of these properties is provided.

3 Drug Powder Properties Influencing Tabletability

3.1 Pre-Formulation

Several factors need to be taken into consideration when manufacturing a drug tablet. It is here, at the pre-formulation stage, that the physicochemical properties of a drug molecule are studied and characterised to gain an understanding of its processability and its effects on biological performance⁸². The objectives of this critical stage of drug development are to i) establish physicochemical parameters of a new drug molecule, ii) determine the drug's kinetic rate profile and stability, iii) determine the API's compatibility with common excipients and iv) select the appropriate crystal form of the drug molecule ⁸³. This is achieved by examining the properties outlined in Figure 3-1.

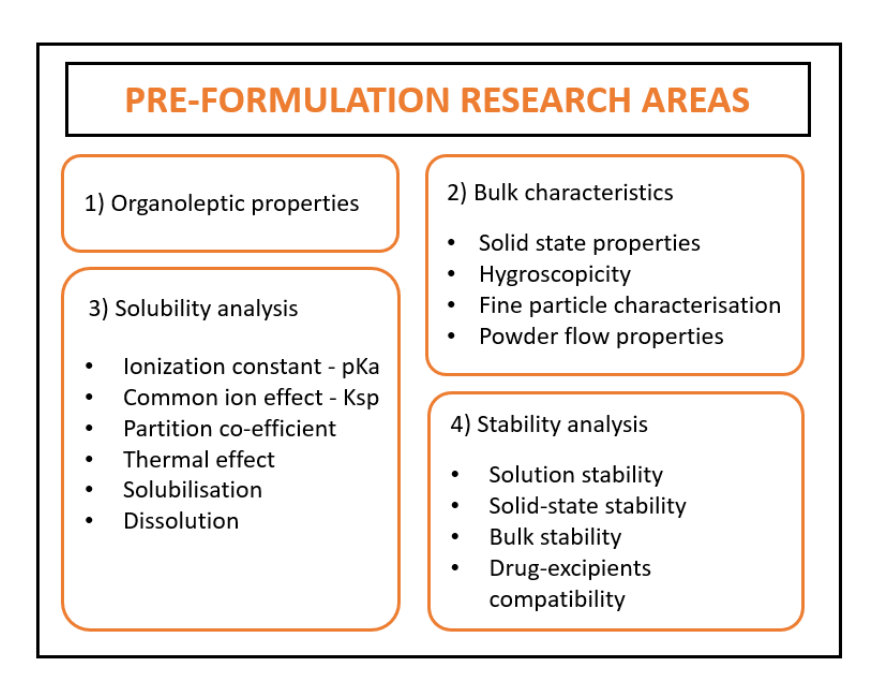


Figure 3-1. Pre-formulation research areas⁸³

3.2 Route of Administration

Drugs come in many forms and may be administered into the body through various routes. The routes of administration are enteral, topical and parenteral, and the choice depends on the nature of the drug;

the desired rate of onset of action, the duration of therapeutic effect and whether systemic or local therapy is needed⁸⁴.

Enteral administration is used when the desired effect is systemic. The drug passes via the gastrointestinal (GI) tract, and the route of administration includes oral, sublingual and rectal⁸⁵. Dosage forms include tablets, capsules, powders and solutions and suspensions.

Solid dosage forms need to possess both hydrophilic and lipophilic solubility as they need to dissolve in the aqueous medium of the GI tract yet pass through the lipid bilayer of the gut's membrane. The varying pH levels of the large and small intestine greatly affect the level of ionisation of weak acidic and weakly basic drugs, making them less soluble in those regions⁸⁶. Liquid formulations have the advantage of not needing to be dissolved, leading to faster absorption of the active ingredient.

Topical administration is used when the desired effect is local, i.e. the medicine must be applied directly to where the action is required⁸⁷. This can be done through direct application to the skin, through inhalation, the eyes and nose. The dosage forms of topical drugs tend to be ointments, creams, solutions, aerosols and gases and sprays.

Respiratory drugs such as aerosols and gases are inhaled straight to the lungs and quickly absorbed through the membranes of the airways. The large surface area of the lungs, their internal structure, as well as the thin air-blood barrier, cause this quick absorption, hence a fast onset of therapeutic effect. Respiratory therapy is mainly used for local action on conditions like asthma; however, it can be a useful route of administration for drugs of systemic therapy not suitable for oral administration.

The parenteral route of administration is used for systemic effect given by routes other than via the GI tract ⁸⁷. These drugs are administered through various injections such as intravenous, intramuscular, intra-arterial and subcutaneous or through implants. They are introduced directly to the bloodstream and are therefore absorbed quickly with an almost immediate onset of therapeutic action. This fast onset of therapeutic action makes them beneficial in an emergency, such as when a patient is unconscious. This route of administration serves as an alternative route of delivery for drugs which are not suitable

3.2.1 Drug Pathways

After a drug has been dissolved in the aqueous medium of the GI tract, it must pass through biological membranes into the bloodstream. These membranes are made up of phospholipid bilayers with a polar end consisting of a phosphoric acid group and a non-polar hydrocarbon chain. They are organised in such a way that the polar hydrophilic ends are in contact with the aqueous media both inside and outside the cell. Hence, the hydrocarbon chains serve as a way to separate various aqueous media in the body. To penetrate the phospholipid bilayers, drugs tend to bind to particular cellular constituents to produce their effect. These are large globular proteins embedded within the cell membrane, also referred to as drug targets. The main drug targets that drug molecules interact with are receptors, enzymes, ion channels and transporters. The drug molecules pass through the cell membranes by either transcellular or paracellular pathways⁸⁸.

The transcellular pathway includes passive and active diffusion⁸⁷. Passive diffusion is the movement of small lipid-soluble molecules across the phospholipid membrane. Molecules move across the membrane based on the concentration gradient, from a region of high concentration to an area of low concentration. Facilitated diffusion is a form of passive diffusion, which occurs when a drug molecule cannot move freely across the membrane. These molecules must be transported via transporter or carrier proteins. Active transport is the movement of molecules against the concentration gradient through the cell membrane via a transporter protein (usually an enzyme) and requires energy input.

The paracellular pathway involves the movement of molecules and ions via aqueous pores between cells. This route of transport is specifically for hydrophilic molecules, which cannot permeate through the lipid bilayer of the cell membrane through the transcellular pathway⁸⁷.

The majority of drug molecules are transported across the membrane via the transcellular pathway. The few which rely on the paracellular route tend to have much lower bioavailability.

3.2.2 Bioavailability

Bioavailability refers to the extent and rate at which the administered dose reaches the systemic circulation⁸⁴. It is dependent on the properties of a drug and the route by which the drug has been

administered. Intravenous drugs are injected directly into the bloodstream and are therefore by definition, 100% bioavailable. Drugs delivered orally are not as straightforward. After dissolution in the GI tract, the drug is transported across the lipid membranes and absorbed into the blood. This blood moves directly to the liver, where it is metabolised before it enters the systemic circulation. This means that only a small fraction of the API reaches the systemic circulation. Therefore, oral medications can never have a bioavailability of 100%; typical values range between 10-50% Another relevant factor affecting the concentration of the drug molecule in the bloodstream is the rate at which the API is metabolised and/or excreted from the body. Measuring the bioavailability of drugs is essential for determining the correct dosage of non-intravenous drugs and is done primarily through pharmacokinetic studies in pre-formulation

It is vital to ensure the drug concentration in the blood stays within the therapeutic range yet below the level of toxicity⁹⁰. As well as making sure that the drug is still effective for some time after it has been metabolised.

Another factor influencing the level of absorption of a drug is its formulation. The same drug but in a different formulation may act differently in the body due to its excipients and/or its manufacturing routes, which may either increase or decrease the rate of absorption, hence bioavailability.

3.2.3 Biopharmaceutical Classification System

The Biopharmaceutics Classification System (BCS) is a framework used for classifying drug compounds based on their intestinal permeability, aqueous solubility and dissolution¹¹. It is used to predict and correlate in vivo pharmacokinetics of immediate-release solid dosage forms to in vitro measurements. The BSC framework aids in pre-formulation studies for the selection of new drug candidates, choosing a suitable formulation approach and the criteria for in-vitro bioequivalence studies⁹¹.

Table 3-1. The Four Classes of the Biopharmaceutical Classification System

	High Solubility	Low Solubility
High Permeability	CLASS I	CLASS II
Low Permeability	CLASS III	CLASS IV

Drugs classified as Class I are highly soluble and show high permeability through the membranes of the GI tract. This class of drugs are expected to have good bioavailability and will therefore not be a problem for use in immediate-release dosage forms. The rate-limiting step for absorption of Class I drugs is drug dissolution.

Class II drugs are highly permeable but have low solubility. Slow dissolution is expected from low solubility. Even if dissolution were to be quick, the concentration gradient would be too low to push diffusion through the lipid membrane at an adequate rate. Hence, the rate-limiting step for Class II drugs is solubility. Ways to improve solubility include the selection of a salt possessing higher solubility, use metastable drug form, particle size reduction, etc.

Class III drugs are classified as highly soluble but have low intestinal permeability. To compensate for the low permeability, the drug must be released quickly to increase its time in contact with intestinal walls. Prodrugs and permeation enhancers are used to improve drug permeability through the intestinal lipid membrane. Prodrugs are derivatives of an API with different chemical properties, like hydrophilicity, affecting their intestinal permeability⁹². The prodrug is usually pharmaceutically inactive but must undergo rapid chemical conversion through metabolic processes to become the API. Permeation enhancers are compounds that transport poorly permeable drugs across the lipid membrane via the transcellular or paracellular route. Such compounds include fatty acids, glycerides, salicylates, and surfactants⁹³.

Finally, Class IV drugs have both low solubility and low permeability and are mostly unsuitable for oral administration.

3.3 Powder Properties for Downstream Processing

Once the API particles have been filtered and collected after crystallisation, there is a series of downstream processing steps which they must go through before becoming the final marketed tablet.

3.3.1 Particle Size Reduction

Particles formed from crystallisation are rarely the optimum size for further processing and need to be altered. Particles of small size and a narrow particle size distribution are a general desired property for all solid dosage forms. Reducing the size has the favoured benefits of a faster dissolution rate and API content uniformity throughout the tablet, enhancing the efficacy and bioavailability of the drug⁵⁴. Milling is the most common method used for particle size reduction. Specific milling equipment is selected based on the particle properties and the required size range. This process is also referred to as comminution. Comminution processes generate heat and exert a great amount of mechanical stress on the particles. These stresses can cause particles to deform to the point of altering their solid-state nature, turning them amorphous. The generated heat and the high level of mechanical stress can cause particles to undergo polymorphic transformations. This destroys the integrity of the drug product as its physicochemical properties change, altering its therapeutic effect. The generation of fines (very small particles) is common during comminution processes. The fines cause segregation due to the large particle size distribution in the powder blend, resulting in a non-uniform mixture. A non-uniform powder blend will impact the flow properties of the powder. Poor flowability will affect the consolidation behaviour of the powder blend, thus influencing its compressibility and ability to form a successful tablet.

3.3.2 Blending

Once the pre-formulation studies have been completed and the desired particle size has been attained, the API needs to be blended with excipients. Excipients are other materials added to the formulation to improve processability, to enhance and/or protect the stability of the drug molecule and to further enhance the bioavailability and overall quality of the drug^{94,95}. Common tablet excipients and their functions are presented in Table 3-2.

Table 3-2. Types of Excipients⁹⁶

Excipient Type	Function	Example
Binders	Holds the particles together, enhancing mechanical strength	Saccharides and their derivatives, e.g. sucrose and microcrystalline cellulose
Diluents	Bulking agent, enhancing flow and content uniformity	Sugar compounds e.g. sucrose, lactose d-mannitol
Glidants	Enhance powder flow, anti-caking agent	Silica gel, talc, magnesium carbonate
Lubricants	Similar to glidants and prevents sticking to tooling surfaces y reduction of friction	Stearic acid and its salts, e.g. magnesium stearate
Disintegrants	Aids in the dispersion of the tablet in the GI tract	Starch, cellulose derivatives
Coatings and films	Prevent tablet deterioration, taste- masking	hydroxypropyl methylcellulose
Colouring agents	Ease of identification and improve tablet aesthetics	Synthetic dyes and natural pigments e.g. titanium dioxide

Proper blending is very important to create an even distribution of all the different components and the API in the mixture. Segregation or demixing may occur during transport, processing or during the actual blending process itself. Components of the same nature may move and gather in the same area of the powder mass. This occurs due to the different particle properties of the various components in the mixture, such as size, shape and density⁹⁷.

De-mixing or poor content uniformity is often observed in directly compressed tablets, where particles of smaller particle size segregate from larger particles and denser particles segregate from lighter particles. The surface chemistry of the particles in the blend can also affect their degree of segregation and their cohesive and/or adhesive nature. Certain powders are difficult to handle due to their tendency to adhere strongly to equipment surfaces. This causes a loss in powder mass, resulting in an inconsistent blending process. Successful blending is also dependent on the blending time and speed. A short blend time will result in undermixing, whilst a long blend time will result in overmixing and degradation of the particles, creating very cohesive fine particles.

A blend of poor content uniformity will also impact its flow and compressibility. These are crucial to the subsequent unit operations in the manufacturing process, such as granulation and compaction. To ensure adequate mixing and optimal powder blends, the choice of mixer is important. Tumbling mixers such as higher shear mixers, V-blenders and double-cone blenders are commonly used. Highshear mixers are best for cohesive powders, as powerful mechanical forces are applied to break tough agglomerates in the mixture. Tumbling mixers work by rotating the vessel and are best for free-flowing powders.

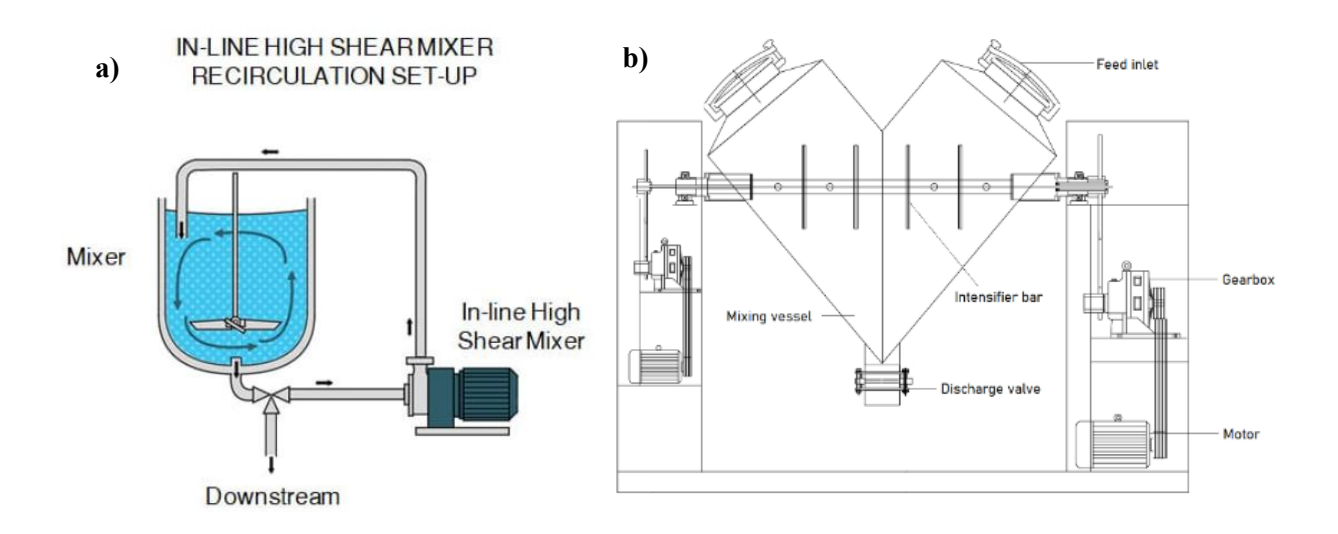


Figure 3-2. Schematics of a) a high-shear mixer and b) a v-blender 98

As part of the QbD approach, Ramen spectroscopy, near-infrared spectroscopy, and other process analytical methods (PAT) are routinely used for real-time monitoring of the blending process⁹⁹. Computational modelling and simulation tools such as Discrete Element Method (DEM) are employed for a deeper understanding of powder blending behaviour. This also offers a method of predicting blending behaviour, which can inform what adjustments need to be made in previous processing stages. This type of QbD approach has the potential to save time, resources and money, reducing experimental trial and error.

3.3.3 Tablet Manufacturing Routes

After the drug particles have been milled to an appropriate particle size range and blended with excipients, there is a choice of three different processing routes. The three main routes available for

tablets are wet granulation, dry granulation and direct compression, outlined in Figure 3-3. The choice of which route to take primarily depends on the physicochemical nature of the API and excipients.

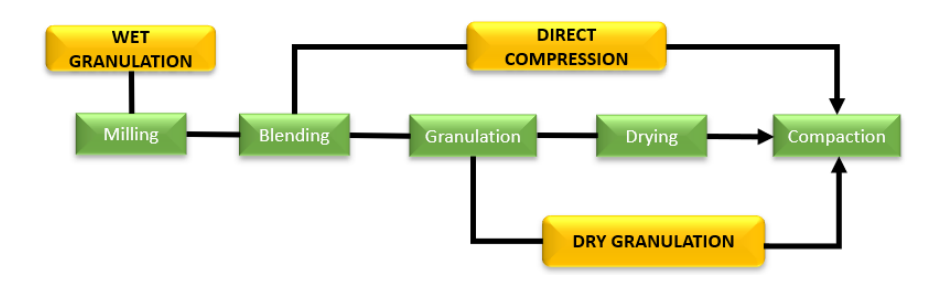


Figure 3-3. Schematic of the three main tablet manufacturing routes

Granulation is the process of adhering primary particles of the powder mix to each other, creating larger particles referred to as granules. Granulation prevents segregation of the different components, ensuring homogeneity, improves powder flow of the blend and prepares it for compaction.

3.3.3.1 Wet Granulation

Wet granulation is the process of forming granules through the addition of a liquid and agitation to a dry powder mixture ¹⁰⁰. The liquid needs to be a non-toxic and volatile solvent to ensure drying. Water is the preferred liquid as it is cost-effective, environmentally friendly and non-flammable. It can be used on its own; however, it is usually used with a binding agent, ensuring that the granules stay intact after drying. The powder mixture is aggregated to form granules in the presence of a solvent, binder and under the influence of an agitator. The resulting wet mass is passed through a screen to break up particles larger than desired. The granules are then dried and screened through milling to achieve the desired granule size. A lubricant is then blended with the granules, coating them so they do not stick to the tablet die surfaces.

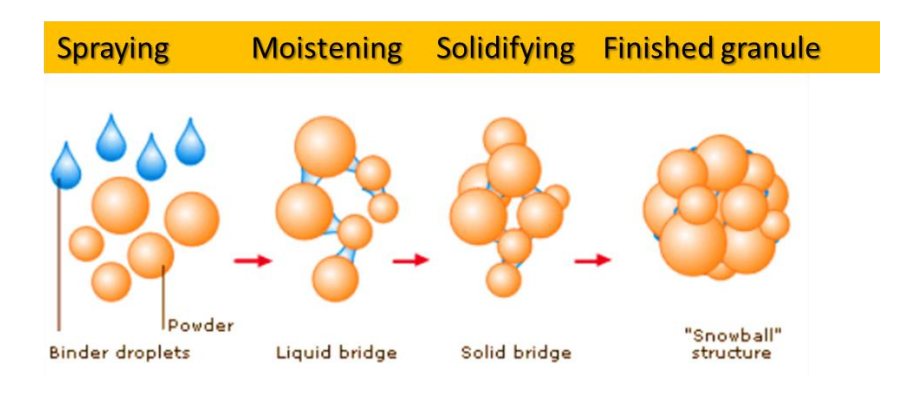


Figure 3-4. Stages of wet granulation (reconstructed)¹⁰¹

3.3.3.2 Dry Granulation

In the dry granulation process, granules are formed through aggregation under high pressure. This is done through two main methods, slugging and roller compaction. A dry binder is sometimes added to the mixture. The final granule size is achieved through sieving or milling, then coated with a lubricant. Dry granulation is best suited for moisture-sensitive materials with poor compaction properties after wet granulation 102.

3.3.3.3 Direct Compression

Direct compression is the route with the fewest unit operations and perhaps the cheapest. The powders are blended, then compacted into a tablet. It is used for APIs and excipients that already possess good compression and flow properties and don't require the formation of granules. This limits the use of direct compression, as very few materials have these properties without further processing. In formulations where the API is not the major component, it is easier to tailor the desired properties through careful excipient selection. This tends to be the diluent as it is typically the bigger portion of the formulation¹⁰³. To avoid segregation, components in the mixture tend to be of the same particle size range. Another method of avoiding segregation is through ordered mixing. This is when the powder blend contains big non-cohesive particles and small cohesive particles ¹⁰⁴. The smaller particles adhere to the bigger particles, creating a more uniform blend. This type of mixing is most suitable for formulations with low API concentrations¹⁰⁵.

3.3.4 Compaction

The final step for all three processing routes is compaction. Tablets are formed by use of a tablet press, which has three main components: a lower punch, a die and an upper punch. The die is filled with the powder blend through a hopper, compressed by the upper punch, forming a tablet, and then ejected by the lower punch Figure 3-5.

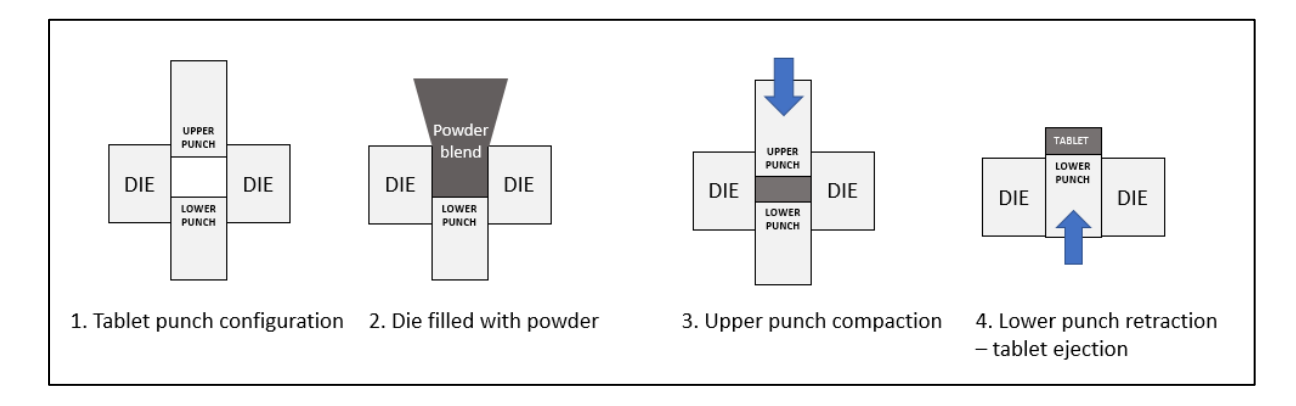


Figure 3-5. Schematic of steps in tablet compaction

3.3.4.1 Mechanisms of Compaction

For large-scale tablet production, manufacturers tend to use rotary tablet presses. They consist of a rotating turret, which is divided into the upper turret, which holds the upper punches, the lower turret, which holds the lower punches, and the die table, which holds the dies. Production capacity depends on the size of the turret and shape of the punches; typically, 250,000 to more than 1,700,000 tablets per hour can be produced¹⁰⁶.

Similar to single punch tablet presses, the dies are filled with powder through a feeder or hopper and the excess is scraped by a scraper. Unlike single tablet presses, compression is performed by both upper and lower punches, with the pre-determined force delivered through compression rolls. There are two compression rollers: pre-compression rollers, which are smaller in size and the main compression rollers, which are bigger. The pre-compression rollers exert a low pressure on the powder in the die, removing any trapped air between the granules before the main compression rollers exert the full force needed to compress the powder and create a tablet. The compressed tablets are removed by the scraper and pushed down a chute, where they are collected in a container.

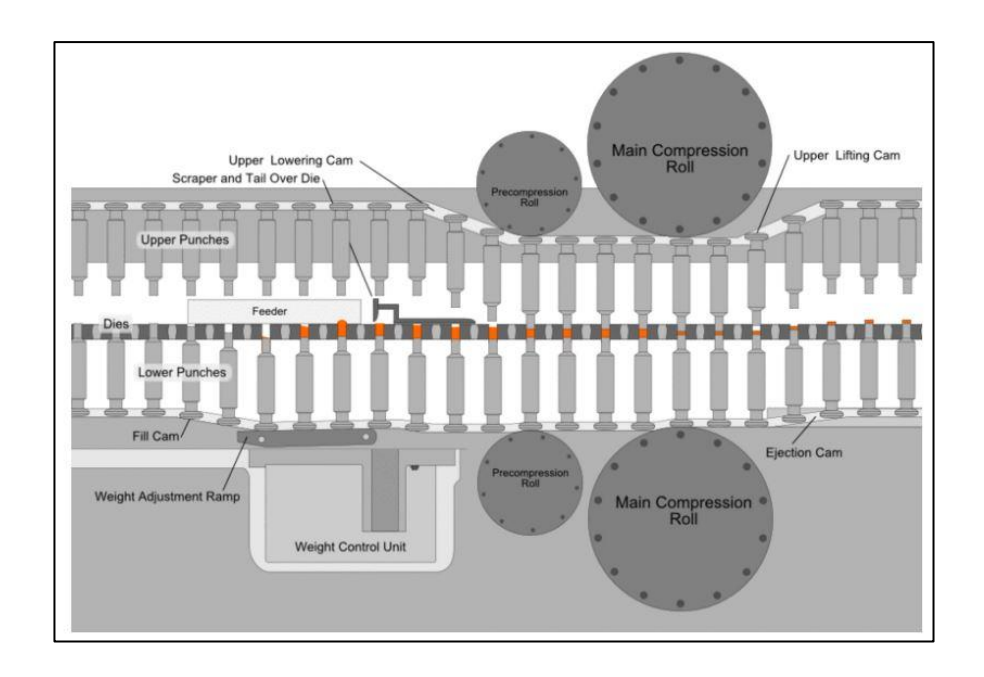


Figure 3-6. Schematic image of a rotary tablet press mechanism 107

Tablet compression involves the operation of two steel punches exerting stress on the powder blend within a steel die. Stress (σ) is the force being applied to the cross-sectional area of an object, in this case, the powder bed^{108,109}, and is calculated by Equation 3-1. The formed tablet takes on the size and shape of the die and punches. The powder undergoes several events in the die as compression occurs. As stress is being exerted on the powder, the particles undergo initial rearrangement. As the particles are being compressed, the air between the particles and pores is pushed out, and the particles move closer together, limiting their mobility.

$$\sigma = \frac{F}{A}$$
 Equation 3-1

where σ is stress, F is the force applied, and A is the cross-sectional area.

At a certain pressure, the movement of the particles becomes impossible. As the compression force continues to increase, deformation of the particles occurs. This deformation is referred to as strain (ε), a result of the applied stress, and can be either *elastic* or *plastic*¹⁰⁹. Strain is calculated by:

$$\varepsilon = \frac{\Delta l}{l}$$
 Equation 3-2

where ε = strain, Δl is the fractional change in length, and l is the original length.

The stress vs strain relationship is depicted in Figure 3-7. Elastic deformation occurs when the particles regain their original shape after the stress has been removed. It involves stretching of intermolecular interactions without breaking them. Microcrystalline cellulose (MCC), a common pharmaceutical excipient which is known to be very elastic and increases the viscosity of a formulation. The opposite is plastic deformation, which occurs when the particles do not completely recover after the release of the applied stress. This process involves the breaking of intermolecular interactions and the making of new ones. This is the ideal condition for the formation of a robust tablet. Plastic deformation is governed by active slip systems, described in Chapter 2. This type of deformation is observed in drug compounds such as lactose monohydrate, improving tablet compactibility 110 . The force which is required for plastic deformation to occur is known as the yield stress, P_y and occurs at the yield point. Deformation is a time-dependent process. If the compression speed is too quick, particles will experience weak bonding, resulting in a fragile tablet 109 .

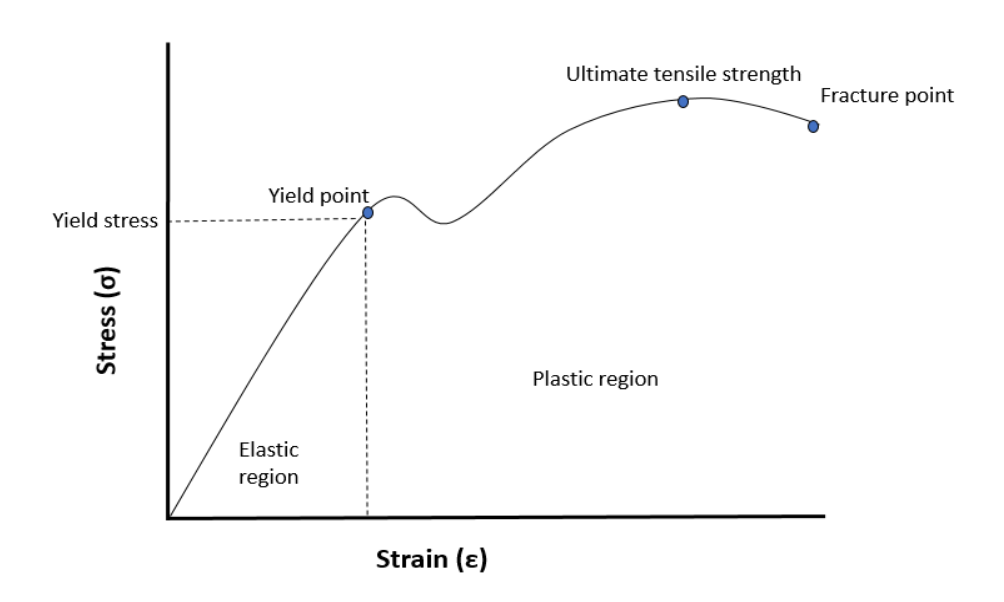


Figure 3-7. A typical stress vs. strain curve

The Young's modulus E is a mechanical property measuring the resistance of a material to elastic deformation. In other words, it is a measure of how stiff the material is and is given by stress (σ) over strain (ε):

 $E = \frac{\sigma}{\varepsilon}$ Equation 3-3

As compression occurs, different mechanisms of bonding are possible:

- Solid bridges may result from melting, crystallisation, sintering, binder hardening or a chemical reaction
- 2) Attraction between solid particles e.g. molecular and electrostatic forces as a result of increased particle-particle contact
- 3) Mechanical interlocking due to irregular particle shape and size distribution
- 4) Liquid film due to capillary forces and surface tension
- 5) Immobile liquid film as a result of viscous binders and absorbed liquids

As maximum pressure is reached, the bonded solid body is consolidated to a limiting density through plastic or elastic deformation inside the die. The successful formation of a robust tablet depends on its ability to withstand the stresses generated by elastic recovery during decompression and ejection. As the upper punch is retracted from the die cavity, the tablet is held in place by radial pressure, and elastic rebound occurs in the axial direction. If the decompression process is too fast, elastic recovery will be quick as well, causing the tablet to break.

The tablet is ejected as the lower punch rises and pushes it out of the die cavity, during which there is continued die-wall pressure and friction. Radial stress is still contained within the tablet, and after it is released from the die, the tablet radially expands 2-10% in volume¹¹¹. Radial die-wall forces and die-wall friction affect how easily the tablet is ejected. Unequal stress is exerted on the formed tablet during ejection. This can introduce stress planes in the compact, weakening its structural integrity and resulting in defects in the compact, especially if the compressed material is prone to brittle fracture.

Brittle fracture may occur if the compression stress exceeds the material's fracture strength of the powder blend¹¹². This leads to further densification of the tablet, as fragments fill the void spaces. Brittle deformation is the quick and sudden crack propagation of a material with little to no plastic deformation. This type of fracture tends to occur in materials with highly directional and strong bonds (e.g h-bonds) of low ductility. Cleavage fracture is a type of brittle fracture involving cleavage of a well-defined

crystallographic plane with the weakest bond strengths, resulting in a smooth, flat surface. This type of deformation is most common in crystalline organic materials, especially drug compounds^{113,114}. Compounds such as paracetamol, aspirin and sucrose are prone to cleavage fracture due to their crystalline structure and poor plasticity¹¹⁵.

The final tablet must be robust enough to withstand the stresses from elastic recovery during decompression and ejection, as well as the stresses induced by handling and packing without breaking or crumbling¹¹⁶. A good tensile strength is therefore required to assess material mechanical integrity. The most common method to assess tablet tensile stress is through diametric stress tests. This is done by applying a compressive force diametrically onto a flat cylindrical tablet until it fractures. The tensile strength is calculated by:

$$\sigma = \frac{2F}{\pi Dt}$$
 Equation 3-4

where σ is the tensile strength (MPa), F is the breaking force (N), D is the diameter of the tablet (mm), and t is the thickness of the tablet (mm).

The ideal tensile strength required for the standard drug tablet is 1.7 MPa¹¹⁷.

3.3.4.2 Issues During Compaction

It is not uncommon for tablet defects to occur during the tabletting process. Typical tablet defects include capping, lamination, picking and sticking.

Capping is the complete or partial fracture from the top or the bottom of the tablet from the rest of the tablet, whilst lamination is the fracture of two or more layers in the tablet, both due to entrapped air during compression¹¹⁸. Capping and lamination tend to occur at high tabletting speeds and under high compression forces. With an increase in tabletting speed, there is an increase in elastic versus plastic strain. It is thought that the stored elastic energy after unloading is what causes stress cracks leading to capping and/or lamination¹¹⁹.

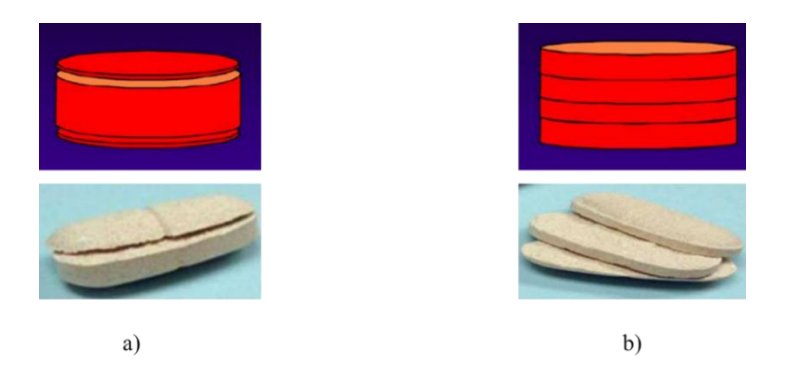


Figure 3-8. Tablet defects: a) Capping, b) Lamination 120

Picking and sticking are the most common tablet issues during tablet manufacturing. It happens when powder granules stick to the punch surfaces rather than locking together and forming a uniform, robust tablet¹²¹. Picking is a specific type of sticking where powder adheres to the logos or letters of embossed or debossed tablets. The main cause is said to be insufficient lubrication in the powder blend¹²². However, research has shown that the problem is more complex than that.

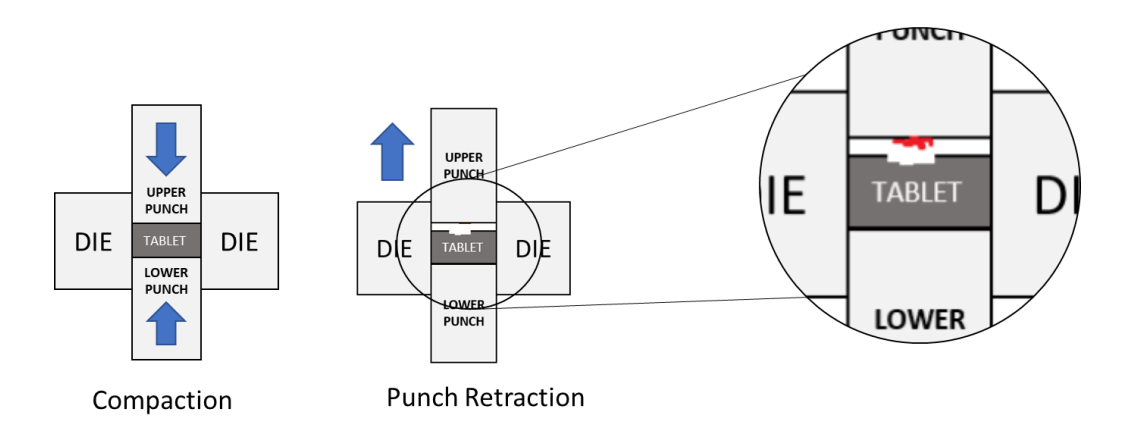


Figure 3-9. Schematic of punch-sticking highlighting the deformed tablet

The sticking phenomenon is a complex, multifactorial problem which has been studied from various angles. It has been correlated to the choice of manufacturing route, punch tooling properties, process conditions, environmental conditions, and electrostatics 108,121,123–129. However, studies reveal that powder properties have the greatest impact.

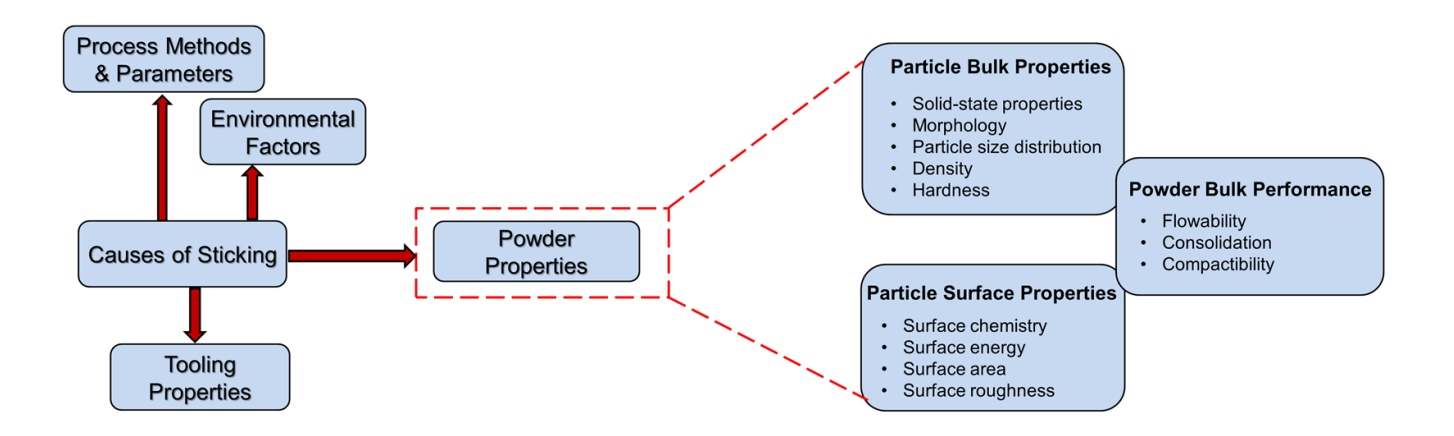


Figure 3-10. Causes of punch-sticking, highlighting powder properties

Powder properties such as flow and particle size distribution, crystal morphology, size, and surface energy, as well as the intrinsic chemical and molecular structure of an API, can all contribute to sticking. It is therefore important to understand the interplay of these properties as they impact how the powders will deform and eventually stick. Certain APIs and excipients stick more than others. Thus, understanding their material properties is key to addressing the sticking phenomenon.

Crystal morphologies and surface energies have been seen to affect sticking propensity. Studies have shown that needle-like crystals stick more than plate-like crystals ²⁶. This was attributed to high surface energies and the exposure of polar functional groups on the crystal surface. Crystals with higher surface energies and exposed polar groups have been observed to increase cohesion to the metal surface of the punch ¹³⁰.



Figure 3-11. Effect of morphology on the sticking tendency of needles and plates to tablet punches during compression²⁶

More research is focusing on the use of particle engineering methods as a solution for sticking. Optimising particle shape and reducing the exposure of high-energy surfaces may lead to materials with reduced sticking propensity¹³⁰.

Paul, S., et al used a statistical approach to identify what powder properties and compaction conditions will affect sticking behaviour the most³⁰. The sticking data of 24 chemically diverse compounds were obtained by quantifying the adhered powder mass using a removable upper punch, at two compaction pressures, 100 MPa and 200 MPa. Using partial least squares statistical analysis, it was found that the most significant factors attributed to punch sticking were surface area and tensile strength. Other factors shown to affect punch sticking, but to a lower extent, were ejection force, take-off force and die-wall pressure. Individual factors did not show a direct correlation to punch sticking, suggesting that the chemical diversity of the compounds outweighs the effects of these individual factors. However, it was found that the ratio of surface area and tensile strength positively correlates to sticking, at both 100 MPa and 200 MPa. The study further highlights how it is difficult to isolate the effects of one property from another.

A model was developed describing the sticking kinetics for a range of compounds based on the strength of cohesion and adhesion of API, excipients and punch surfaces²³. Using a similar methodology as Paul, S., et al³⁰, the adhered powder mass on the punch tip was chemically analysed by UV/vis spectroscopy after compaction. Results displayed that the mass adhered to the punch tip was that of the API powders alone. This led to deeper considerations of the interplay of the bonding strength present between the punch surface, API and excipient matrix. The model suggests that sticking occurs when API-punch adhesive forces (F1) are larger than the forces within the powder blend. Mild sticking (or filming) occurs when the API-excipient matrix adhesion forces (F3) are greater than the API-API cohesion forces (F2). Whereas severe sticking occurs when the F2≥F3. Filming was referred to as Type I sticking, and severe sticking was referred to as Type II sticking.

The model suggests that sticking can be modulated by controlling the F2 and F3 interplay.

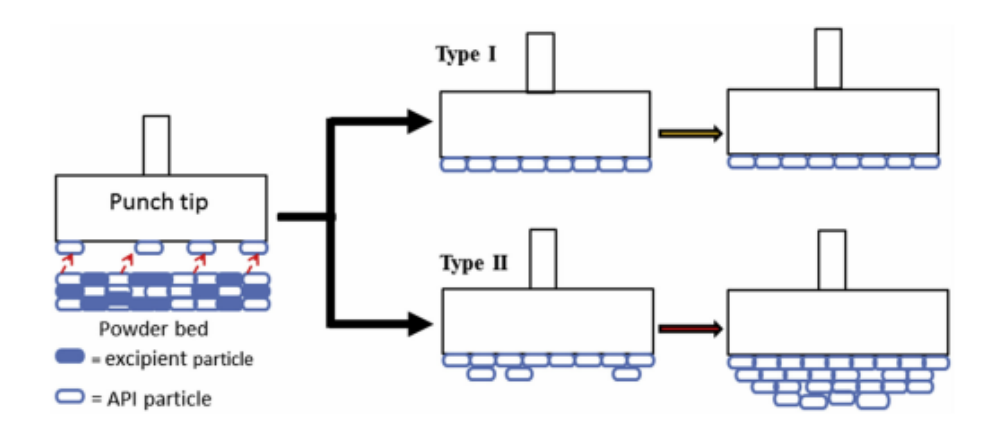


Figure 3-12. Schematic of the model describing Type I sticking (monolayer filming) and Type II severe $sticking^{23}$

Following this study, Paul & Sun investigated the influence of changing the API-excipients matrix (F2) on the sticking propensity of given APIs¹³¹. Four different direct compression formulations of 20% high-sticking compounds, celecoxib and ibuprofen were prepared using two grades of microcrystalline cellulose (MCC); PH102 and PH105(n) (MCC nano-coated with colloidal silica for better flow), hypromellose (K15M) and a 3:1 mixture of starch and PH102 (S3P1). The tensile strength of ibuprofen and celecoxib was measured by assessing their tabletability and compactibility individually, and later in their different formulations. Tablets were made on a compaction simulator, and sticking was measured gravimetrically using a removable punch tip. Celecoxib had higher tensile strength, indicating stronger API-API cohesive bonding (F2) than ibuprofen. It also exhibited greater sticking propensity, which, according to the model, is expected due to its superior API-API cohesiveness.

The different formulations displayed the same trend in tensile strength for both APIs: PH105(n) < PH102 < K15 M< S3P1. This nicely correlated with their exhibited sticking propensities: PH105(n) > PH102 > K15 M> S3P1. Higher F3 correlates with a lower degree of sticking. The results coincide nicely with the developed model²³ and verify the notion that to overcome sticking, the API-excipient matrix adhesion needs to be greater than the API-API cohesion. Choosing more plastic excipients which enhance tensile strength seems to be a key factor in reducing sticking. As they readily deform, they reduce the API-API contact at the punch surface, reducing the chance of API build-up.

Powder properties and how they may change as a result of powder handling, processing, and tabletting, govern sticking propensity. The potential of crystal engineering methods to be employed to reduce sticking is therefore evident. As the physicochemical properties are chosen first and foremost based on their therapeutic effect, it somewhat restricts how much researchers can manipulate APIs and formulations. Nevertheless, the anisotropic nature of crystals does give the opportunity to alter properties like crystal size, morphology, and exposed polar surfaces.

This potential has been recognised many times; however, it has not been very well investigated, often lacking in mechanistic explanations for the correlation to sticking. Currently, there is no specific methodology in place that can be utilised to select a particle engineering technique based on its impact on surface properties. A fundamental understanding of the interplay between structure, property, process, and performance is what the Material Science Tetrahedron¹³² suggests is the basis for addressing material-specific issues during tablet manufacturing.

3.3.5 Advantages and Disadvantages of the Tablet Manufacturing Routes

Wet granulation is the most used manufacturing process and can be used for many different types of materials. The main advantages of wet granulation are:

- It increases the size of the powders, creates an even particle size distribution, creating a uniform blend, reduces segregation, and improves the flow properties of the granules.
- The compressibility of the powder blend is improved as the process reduces its elasticity.
- High shear granulation causes a high level of densification of the powder blend, improving die filling of voluminous materials and reducing the potential of air entrapment during compaction.
- By using a hydrophilic binder, the wettability of hydrophobic materials is increased, improving their disintegration and dissolution profiles.

Even with these benefits, wet granulation still has its disadvantages. The large number of processing steps means it becomes an expensive process as a time-consuming process, requiring more manual labour, equipment, and space. There is a risk of losing material during the transfer from one unit

operation to the next, also increasing the possibility of cross-contamination¹³³. Another limitation of wet granulation is the potential for stability issues of moisture sensitive materials. Aqueous wet granulation may cause API's may undergo hydrolysis or polymorphic changes.

The dry granulation process is more cost-effective than wet granulation due to its fewer processing steps. It offers the same flow, compressibility, and content uniformity benefits as wet granulation. Stability risks are avoided as no liquid is used in this process and is, therefore, a viable option for heat and moisture sensitive materials¹³³. The formation of granules in the dry granulation process involves the use of a roller compactor. This means that the powder is compacted before tabletting, possibly reducing their compactibility^{134–139}. This is a great disadvantage as these granules may not consolidate enough to produce a strong, robust tablet¹⁰². Hence, it is important that the materials chosen for dry granulation already have good compactibility features. Since it is a dry process, a lot of dust is produced, which can contaminate other drugs, but also cause health risks for the operators.

Direct compression can only be used when the components of the formulation already possess the desired flow and compaction properties. The key benefit of direct compression is its cost-effectiveness. The reduced unit operations mean the use of less equipment, hence use of less space, reduced power consumption, less labour and faster production time; all of which reduces the overall cost of tablet production¹⁹.

Similarly, to dry granulation, the process does not involve the use of any solvent, making it suitable for heat and moisture-sensitive materials, eliminating potential stability issues. Tablets made from direct compression tend to have faster dissolution rates as they disintegrate into primary particles rather than granules, resulting in a quicker release of the API.

Not many materials are suitable for direct compression. Suitable materials tend to be patented speciality products produced from various particle formation techniques, such as spray drying or co-crystallisation¹⁴⁰. These excipients are therefore more expensive than the raw materials. The physical properties of the powder blend are mainly governed by the diluent, as it is usually the component of highest concentration in the mixture. Drugs of low potency need to be at a high dose in the blend to exert their therapeutic effect. This means that unless the API already has good flow and compressibility

properties, direct compression is not suitable. Also, such medicines will result in rather large tablets, which are difficult to swallow, likely reducing patient compliance. Hence, direct compression is best suited for high-potency, low-dose APIs. Weight variability and lack of content uniformity can be a big issue in direct compression, affecting the safety and efficacy of the medicine. The different densities of the API and excipients, as well as static charge when mixing the dry powders, cause segregation in the powder blend.

3.3.6 Importance of Powder Flow and Compressibility

The production of a safe, efficacious, and robust tablet is dependent on the nature and properties of the powder components and bulk powder behaviour; specifically, content uniformity in the tablet and its mechanical strength. Proper content uniformity in the tablet is based on two main factors: weight variations in the tablet and API distribution.

The powder blend is added to the die cavity by volumetric filling. The bulk density and volume of the powder correspond to a specific weight and are monitored via a weight control unit. Low variations in weight between produced tablets are an indication of good content uniformity¹⁴¹. High variations in weight indicate poor filling of the die, which in turn indicates poor flow properties of the powder blend. Poor powder flow is often due to the individual particle properties of the components in the mixture, such as size, shape, surface roughness and true density. The increased surface area of smaller particles increases the presence of cohesive forces, leading to aggregated powders displaying poor flow¹⁴². Particles of irregular shape and rough surfaces also readily adhere to each other, causing a powder blend with poor flow properties. As filling occurs volumetrically, particles with low density will also display poor flow. Ideal particles, which display good flow properties, are larger, smooth, spherically shaped particles with higher density.

Process settings may be another reason for weight variations in the tablet, due to inconsistent filling of the die¹⁴³. Adjusting processing settings, such as feeder speed, is a way of optimising the die filling process.

Poor API distribution in the overall tablet is another cause of bad content uniformity. The primary

reason for poor API distribution is segregation. Segregation readily occurs in powder blends of varied sizes, shapes, and densities. This is the main reason for the granulation processes. Thus, segregation is more likely to happen in the direct compression processing route.

Common methods of assessing powder flowability include measuring the Carr Index, Hausner ratio and the angle of repose¹⁴⁴.

The Carr Index (CI) (Equation 3-4) and Hausner ratio (HR) (Equation 3-5) are both measured through assessing the ratio between the free settling powder bulk density and tapped density. These methods are often used in pharmaceutical research and indicate how well the powders flow.

$$CI = \frac{\rho_T - \rho_B}{\rho_T} \times 100$$
 Equation 3-5

$$H_r = \frac{\rho_T}{\rho_B}$$
 Equation 3-6

where, ρ_T is the tapped density and ρ_B is the bulk density.

The angle of repose (AOR) is another commonly used technique for the measurement of flowability¹⁴⁴. As bulk powder is poured over a flat surface, a cone-shaped heap is formed. The AOR is the internal angle between the heap and the horizontal base. An angle of below 35° is considered good flow and is given by Equation 3-7¹⁴⁵.

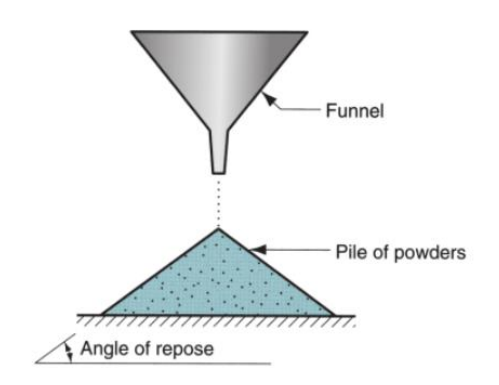


Figure 3-13. Illustration of angle of repose experiment 116

$$\theta = tan^{-1} \left(\frac{2h}{d}\right)$$
 Equation 3-7

Alyami et al. studied how excipient particle size, blending methods and processing parameters influence content uniformity and homogeneity of low-dose ergocalciferol (Vitamin D2) formulations¹⁴². Three

common excipients, microcrystalline cellulose (MCC), starch, and pre-gelatinised starch, were examined using laser diffraction for particle size analysis and angle of repose for flow analysis. Scanning electron microscopy (SEM) and interferometry were used to examine surface topology. The effect of different blending techniques on the formulations was also assessed. Geometric blending: the incremental addition of the excipient to the API, manual ordered blending: where the excipient is added all at once and a novel dry powder hybrid mixer was created at Aston University. UV spectrophotometry was used to examine the content uniformity of the blends.

Results revealed that the shape and size of excipients directly correlated to their flowability. MCC exhibited the best flow due to its granular particle shape and larger size than starch. Starch displayed poor flow because of its smaller particle size, and pre-gelatinised starch displayed average flow properties. MCC displayed higher surface roughness and provided better lodging of the fine API particles, which contributed to better content uniformity. When evaluating the blending techniques, researchers found that when blending for longer durations, geometric blending delivered a more homogenous blend at lower dilutions. Manual blending did not produce a homogeneous blend even at long blending times. The novel dry powder hybrid mixer was successful in producing homogeneous blends at low dilutions regardless of particle shape or size.

The study illustrates the difficulties in drug formulations, especially in the formulation of low-dose drugs. Content uniformity is greatly affected by particle properties of both the excipient and API, in addition to the appropriate selection of blending techniques and parameters. Thus, optimising excipient selection by understanding these properties is crucial to ensuring good content uniformity.

As previously mentioned, for a robust tablet to be produced, it must be able to withstand the stresses imparted upon it during compression, decompression, and ejection. Additionally, it must be able to stay intact during packaging, transportation, and dispensing. As the tensile strength is dependent on both the compressibility of the powder blend and how cohesive the tablet is after compression, understanding the effect of both bonding area (particle contact) and bonding strength (particle cohesion strength) is crucial in optimising overall tabletability¹⁴⁶.

Tabletability is the ability of powders to form quality tablets of adequate strength and is defined by two

key components: compressibility and compactibility.

Compressibility is the measure of a powder's ability to decrease its volume under a compressive force is described as. Good compressibility is an essential quality for pharmaceutical powders to have for successful compaction to be achieved. Poor compressibility results in larger voids and weak spots, resulting in poor content uniformity and poor tablet strength. However, good compressibility doesn't always guarantee a successful tablet. It is possible for a highly compressive powder to lack good compactibility.

Compactibility is the measure of a powder's ability to maintain cohesion after compression. As particles are compressed, porosity is reduced and the bonding area and strength increase. Strong tensile strength indicates good interparticulate bonding, such as h-bonding, vdW and/or mechanical locking.

When two tablets have the same porosity but differ in tensile strength, the one with higher tensile strength has stronger interparticulate bonding. In cases where two tablets are compacted with the same compaction pressure but one is denser, it indicates a larger bonding area between particles, allowing for more efficient and potentially better tensile strength¹⁴⁷.

The desired properties are for the powders to deform plastically as well as undergo a level of brittle fracture, increasing both particle bonding area and bonding strength. Powders which undergo elastic deformation will yield in a failed compression process, hence a failed tablet.

For the reasons discussed above, the flowability and compressibility are primary factors to consider when selecting a manufacturing route. Powders of great flow and compressibility are suitable for direct compression. Powders with good flow but poor compressibility are best suitable for dry granulation, and powders with both poor flow and compressibility are best suited for wet granulation.

Table 3-3. Criteria for appropriate route selection

		Compressibility	
y.	HIGH	HIGH	LOW
Flowability		Direct compression	Wet granulation
Flow	LOW	Dry granulation	wet granulation

The Heckel equation is a commonly used method to evaluate the compressibility of powders. It assumes that powder compression follows the first order of kinetics, where the interparticulate porosity is the reactant and the densification of the powder is the product¹⁴⁸. The Heckel equation is given by:

$$ln = \frac{1}{1-D} = kP + A$$
 Equation 3-8

where D is the relative density (ratio of bulk density to true density $\left(\frac{\rho_{bulk}}{\rho_{true}}\right)P$ is pressure applied, A is related to die filling and particle rearrangement, and the inverse of k gives the yield stress P_y of a material, at which it plastically deforms. A low P_y indicates better compression properties, i.e faster onset of plastic deformation. The equation is often rewritten as:

$$ln\left(\frac{1}{E}\right) = kP + A$$
 Equation 3-9

where E is the porosity (1-D). A smaller E value indicates better compression of the powder.

Another method of analysing the compressibility of powders is through the Kawakita and Lüdde equation (Equation 3-9), which characterises the relationship between pressure and he degree of volume reduction 115. Where C is the degree of volume reduction, Vo is the initial volume of the powder bed, Vp is the powder volume after compression, a linear plot of P/C and P allows for the evaluation of constants a and b. Constant a is related to the initial bed porosity, and b is the material's resistance to force. The inverse, 1/b, represents the yield stress.

$$C = \frac{V_o - V_p}{V_o} = \frac{abP}{bP}$$
 Equation 3-10

can be rearranged to:

$$\frac{P}{C} = \frac{P}{a} + \frac{1}{ab}$$
 Equation 3-11

3.4 X-ray Computed Tomography (XCT)

Lab flow and compaction analysis can be combined with the non-destructive imaging technique X-ray computed tomography (XCT) analysis for an even deeper insight into particle behaviour¹⁴⁹. It is an application that has been extensively employed within the medical field^{150,151} and has, in more recent

years, been used to study pharmaceutical powder properties and tablet compression^{152–154}. The general principles are depicted in Figure 3-14 and involve the illumination of a sample with x-rays from an x-ray source and a detector capturing the transmitted x-rays¹⁵⁵. The sample is rotated 360° degrees providing several radiographs resulting in several projections. Using a mathematical algorithm, these projections are computationally reconstructed, providing a 3-D representation of the sample¹⁵⁶. The virtual volume allows for the visualisation and study of internal morphological and structural features of powders and tablets.

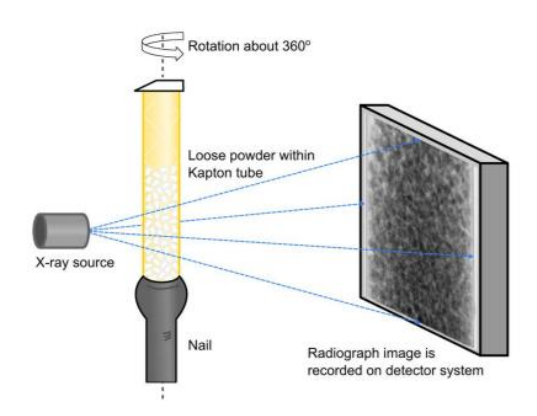


Figure 3-14. X-ray computed tomography set-up 3D inhale¹⁵⁴

3.5 Predicting Mechanical Behaviour

Various computational methods have been used to predict the mechanical behaviour of drug compounds. Bryant et al aimed to computationally predict material tabletability through topology-based descriptors¹⁵⁷. Using the Cambridge Structural Database (CSD) Python API, a geometric analysis protocol was used to identify likely slip planes. The program searches the crystal structure for the least obstructed Miller planes for ease of slipping. Slip is more likely to occur in less corrugated planes as these tend to present low obstruction under stress. However, some systems have highly corrugated planes but low interpenetration with the bottom layer and some planes are less corrugated with high interpenetration, reducing the possibility of slippage (see Figure 3-15). Therefore, planes are categorised by level of interdigitation (-) or separation (+), as the programme searches for the flattest plane, their d-spacing and whether orthogonal planes are present.

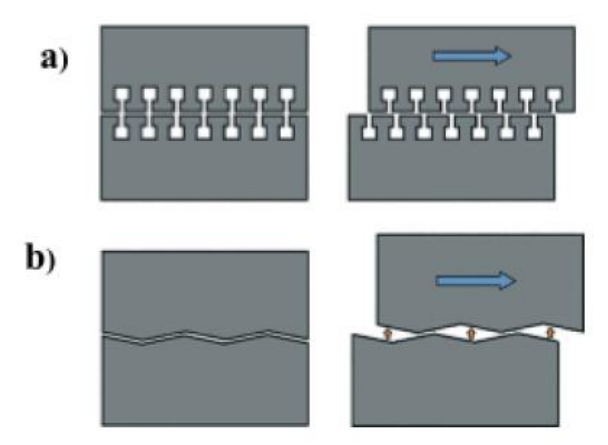


Figure 3-15. Diagram illustrating two different types of interfaces during slip, a) a highly corrugated plane with no interpenetration of layers, thus no obstruction to slip, and b) interpenetrated layers of a less corrugated plane, obstructing slip¹⁵⁷.

In combination with finding the least obstructed plane, the program also automatically detects the h-bond dimensionality of each plane. Planes bridged by strong h-bonding are less likely to slip, affecting the mechanical behaviour. The researchers used the CSD Python API tool to investigate eleven pharmaceutical systems and compared them to their polymorphs and some co-crystals. The polymorphs were ranked in order of predicted tabletability and correlated to experimental data from the literature. In the case of paracetamol, for example, the superior tabletability of Form II was successfully predicted. The analysis successfully predicted the trend of the other polymorphs. The prediction of co-crystals did not always predict the right tabletability, as these systems are a bit more complex. However, researchers suggest that adding the geometric analysis in addition to energetic considerations, more accurate results may be produced. Researchers also identify that a possible shortcoming of the program is that the direction of the slip is not considered. There are instances where a highly interdigitated plane can undergo slip in a specific direction (Figure 3-16).

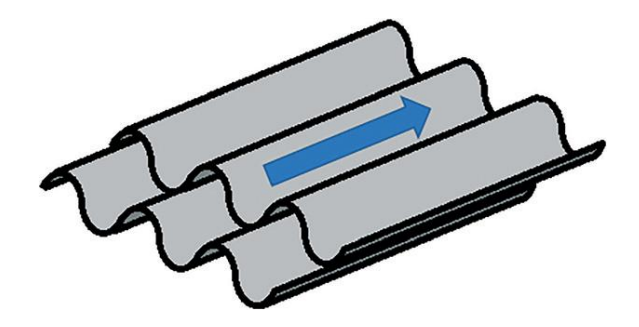


Figure 3-16. Illustration of a highly corrugated system displaying potential slip in a specific direction 157.

Nonetheless, the study demonstrated that topology-based descriptors are critical for the geometric analysis of tabletability and show strong correlation to experimental data. Although alone they may not fully define mechanical properties, they greatly aid in the understanding of mechanical behaviour. Combining these with the energetic data of each system will aid in a more comprehensive prediction of materials.

Through research by Olusamni et al., the attributes which influence the mechanical behaviour of organic crystals and ideal slip plane qualities were outlined¹⁵⁸. They stated that the highly anisotropic nature of organic crystals yields complex morphologies of low symmetry. These low-symmetry systems limit the available slip planes, thus restricting the material's ability to undergo plastic deformation. The deformation behaviour is also influenced by the strength and nature of intermolecular interactions involved. Studying the nature of the slip planes can aid in understanding the deformation and fracture behaviour, i.e brittle and semi-brittle fracture or cleavage of the material. The most likely slip planes will have the following characteristics:

- ❖ Low interplanar rugosity
- ❖ Low interplanar locking/interdigitation
- Low surface energy
- No/low breaking of strong intermolecular interactions (i.e h-bonds)

Using the above characteristics, likely slip planes were quantitatively identified, and the ideal Burger's vector direction was evaluated by taking the shortest unit cell parameter. The study successfully predicted slip systems of aspirin, correlating well with quasi-static indentation results of the material.

Ibrahim et. al. expanded on this type of mechanical prediction by combining the quantitative model with qualitative analysis¹⁵⁹. A predictive framework for the understanding of the deformation behaviour of organic crystals was created in an effort to produce quick yet comprehensive and efficient prediction tools (Figure 3-17).

The workflow starts with the selection of the crystal structure, then the determination of the most likely slip planes, statistically ranking them from most to least likely planes. The most probable Burger's vector is evaluated, and the Burgers magnitude is calculated. The slip plane and deformation vector analysis is combined to evaluate whether the material is ductile or brittle. If the Burger's vector [uvw] lies within the most likely slip plane (hkl), (forming an active slip plane hu + kv + lw = 0), it indicates that the material undergoes plastic deformation. Otherwise, the direction of the strongest intermolecular interactions is assessed. If the strongest interaction is found to lie within the direction of the slip plane, it suggests cleavage fracture; if not, it indicates rough fracture. The study successfully predicted the mechanical behaviour of pentaerythritol and pentaerythritol tetranitrate.

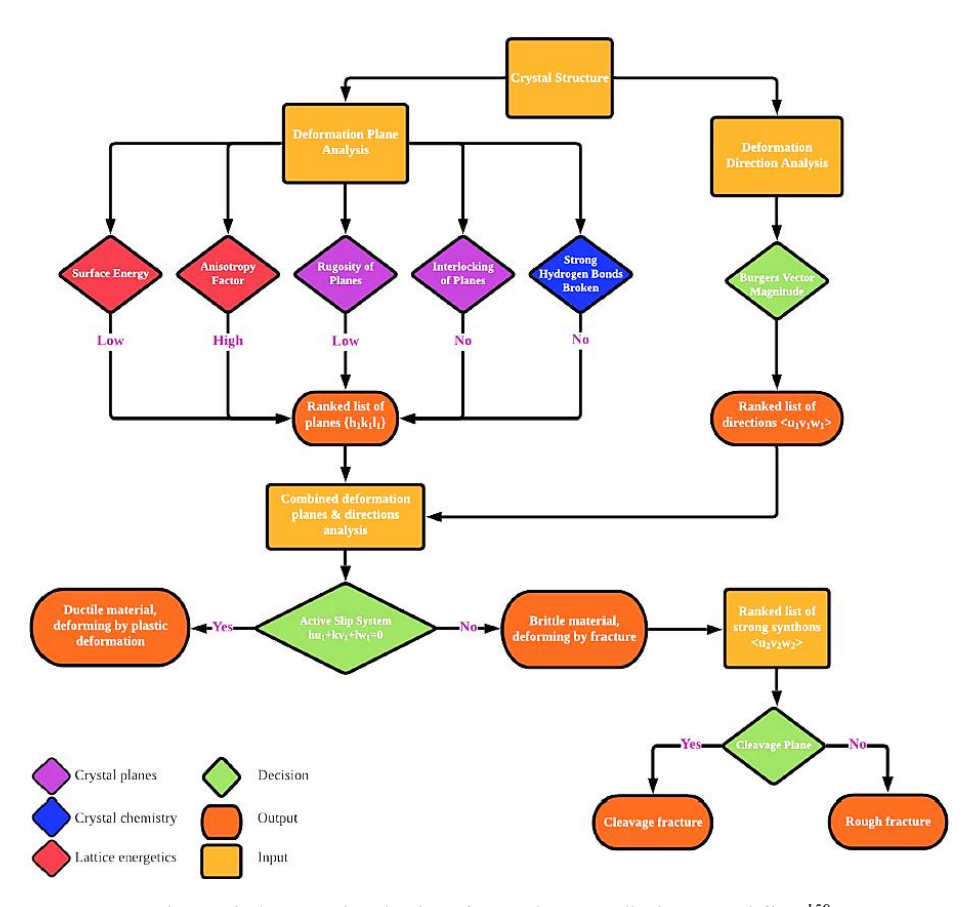


Figure 3-17. Mechanical Deformation Prediction Workflow¹⁵⁹

The provided prediction workflow offers a rational method of characterising mechanical deformation, improving the drug product design process. However, the application of any predictive models or workflows needs to apply to a wide range of organic crystalline compounds to be truly robust.

3.6 Model System – Mefenamic acid and D-mannitol

The selected model systems, mefenamic acid and d-mannitol, were introduced in Chapter 1, and a summary of the reasons for selection was stated. Here we go a bit deeper into their background, properties, and industrial relevance.

3.6.1 Mefenamic acid (MA)

Mefenamic acid is an odourless off-white powder that is part of the fenamate subgroup of nonsteroidal anti-inflammatory drugs (NSAIDs). These are NSAIDs comprising the fenamic acid as their core structure (Figure 3-18, a). Mefenamic consists of two additional methyl groups on the second benzene ring, bridged by the amine group. In addition to mefenamic acid, the other fenamate NSAIDs include tolfenamic acid, meclofenamic acid and flufenamic acid (Figure 3-18, c-d).

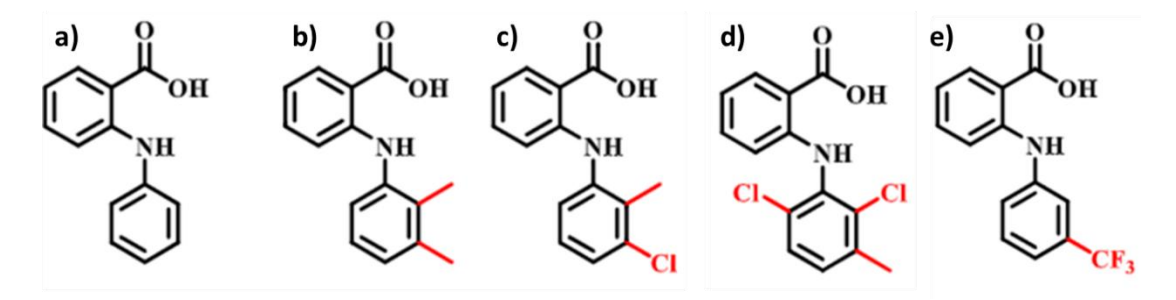


Figure 3-18. Fenamate chemical structures: a) parent structure-fenamic acid, b) mefenamic acid, c) tolfenamic acid, d) meclofenamic acid, e) flufenamic

The evidence of the analgesic, anti-inflammatory and antipyretic nature of the fenamate compounds has been documented as early as the 1950s by Dr Claude Winder, who later led the development of mefenamic acid in 1961¹⁶⁰. Dr Winder first introduced the drug to the market and patented it in 1962/1963 under the then-pharma company Parke, Davis and Company, now Parke-Davis - a subsidiary of Pfizer.

The drug is now used globally to treat various pains and inflammation. Even with its wide use, the chemical and physical nature of the drug causes several processing challenges in the pharmaceutical industry. Unit operations from crystallisation to final compaction of the tablet are impacted, affecting the quality and performance of the final drug product.

Classified as a BCS class II drug, it has very poor aqueous solubility but high gastrointestinal permeability. Thus, high drug loading in MA tablets is needed in the formulation to increase bioavailability, and the addition of excipients aids solubility and dissolution.

MA naturally crystallises in thin needle-like and irregular morphologies and has a wide, irregular particle size distribution, resulting in poor filtration and flowability. The particles are prone to static accumulation, causing difficulties in handling and blending. The poor flow further affects die-filling during, resulting in poor content uniformity. It is therefore essential to use diluents and glidants to improve the flowability. MA particles also cause various issues during compaction due to poor compressibility. The particles cannot undergo direct compression as they possess low interparticle bonding under stress¹⁴⁷. Therefore, when manufacturing MA tablets, the particles must go through wet granulation and addition of excipients for successful tabletting. Hence, MA tablets are not suitable for direct compression. The poor compressibility can also lead to capping or lamination if compression forces are too high, and the compaction speed is too fast. Consequently, excipients with better plastic deformation are added to the formulation, and careful optimisation of compaction parameters is needed. Punch-sticking is another major manufacturing issue during tabletting of MA. The static nature of MA causes a tendency for it to stick to all compaction tooling, such as punches and dies. A detailed review of the impacts of sticking is found in section 3.3.4.2. The production inefficiencies cost the industry about \$20,000 an hour, whilst wasted materials and batch rejections can contribute to annual losses of millions of dollars 161,162. The use of lubricants such as magnesium stearate can be added to reduce the sticking propensity. The amount of lubricant added to the formulation should be carefully evaluated, as too much can adversely affect dissolution and bioavailability. Even with the addition of lubricant, once a layer of MA has been formed, and the API-cohesion is stronger than the API-excipient-adhesion, the MA powder mass can quickly accumulate. Thus, a greater understanding of material physicochemical properties is needed in addition to an accurate API-excipient formulation balance.

3.6.2 D-mannitol (D-M)

D-mannitol is a white odourless alcohol and sugar compound, used in drug formulations as both an API and an excipient. It is a highly water-soluble compound due to its multiple hydroxyl groups (-OH), ready to interact with water, forming h-bonds. Its molecular shape is also relatively small and linear, allowing for easy interaction between the -OH groups and water.

Figure 3-19. Molecular structure of d-mannitol

Its pharmaceutical use started in the mid-20th century and quickly became popular for treating kidney failure, cerebral edema and glaucoma due to its osmotic diuretic properties ¹⁶³. It functions by pulling excess fluid from tissues into the bloodstream, to be safely excreted, reducing pressure and fluid build-up in affected tissues. Over the years, d-mannitol quickly emerged as a vital excipient in drug formulations, tablets, inhalation drugs and freeze-dried injectables ¹⁶⁴. It is often used as a diluent and bulking agent. Its non-hygroscopic nature means it doesn't easily absorb moisture. Therefore, adding it to a formulation will improve the stability of moisture sensitive drugs. It's added to drugs of poor aqueous solubility to improve dissolution and drug release. Its overall good flow and compressibility will also improve the flow and compressibility of drug powders, making it a good candidate for direct compression formulations. The compound is inert and non-reactive, meaning it does not interact with most APIs. For the properties listed and its low toxicity to the body, it makes it a preferable and valuable ingredient in many formulations. For these reasons, d-mannitol is often used in mefenamic acid tablet formulations²⁹.

The selection of mefenamic acid and d-mannitol as model compounds for study is highly valuable due to their industrial relevance and diverse physicochemical and mechanical properties. Investigation of their solid-state, surface and bulk properties - individually and in combination - will provide critical insight into their interactions and effects on flow and compaction performance.

3.7 Conclusion

This chapter explored the unit operations involved in tablet manufacturing and the issues that can be encountered during any of the processing steps. Capping, lamination, and punch-sticking are all very common tablet defects affecting overall production efficiency and drug quality. The factors influencing successful tabletting have been narrowed down to flowability and compressibility, and the importance of these properties has been explained. These powder properties are governed by the physicochemical and mechanical properties of the API and excipients. Hence, control of these properties is imperative for the production of robust, safe and efficacious solid-dosage forms. Computational methods of predicting deformation behaviour of organic compounds are available, and the importance of including both geometric and energetic information in a model for more accurate predictions has been highlighted. The physicochemical properties of individual materials have been extensively studied; thus, they are

The physicochemical properties of individual materials have been extensively studied; thus, they are easier to understand. However, issues arise when studying multi-component systems. The interactions between API and excipient surface properties are complex, as the interparticle cohesion-adhesion involved can be difficult to determine. The surface effects in bulk powder properties are challenging to decouple. This results in further struggle in decoupling the influence of collective bulk powder properties like flow and compressibility on manufacturing processes.

Determining the API-excipient ratios, especially for modern formulations with low-dose excipients, is poorly characterised. Quality by testing (QbT) is still the most reliable method for industry, leading to wasted resources and production delays. Thus, utilising tools which optimise the manufacturing process is highly favoured. There are currently no robust predictive frameworks for formulation optimisation based on its effects on processability. The understanding of how formulation composition affects deformation and bonding during compaction is limited. This PhD project hopes to fill this gap by

providing a mechanistic understanding of how the interplay between the physicochemical properties and the mechanical behaviour of formulations influences flow and compaction.

CHAPTER FOUR

Materials and Methods

This chapter describes the materials used and the various instrumentation of experimental methods, as well as the molecular modelling techniques used in this study. The experiments range from standard material characterisations to bulk powder assessments.

4 Materials and Methods

4.1 Materials

All powders used in this project were of as-received raw materials from suppliers.

4.1.1 Chemical Powders

Table 4-1. Raw material information

Compound	% Purity	Source
Mefenamic acid	≥ 99	Sigma Aldrich
D-mannitol	≥ 98	Sigma Aldrich
Magnesium Stearate	≥ 98	Sigma Aldrich

4.1.2 Molecular Structure

The mefenamic acid compound consists of a carboxylic acid group at the end of a phenyl ring, two methyl groups on another phenyl ring and an amino group connecting the two rings (Figure 4-1, a). The compound crystallises in a triclinic crystal lattice with a space group of P $\overline{1}$. It consists of two molecules in its unit cell, defined by the unit cell parameters: $\mathbf{a} = 14.556 \, \text{Å}$, $\mathbf{b} = 6.811 \, \text{Å}$, $\mathbf{c} = 7.657 \, \text{Å}$, $\mathbf{\alpha} = 119.57^{\circ}$, $\mathbf{\beta} = 103.93^{\circ}$, $\mathbf{\gamma} = 91.30^{\circ}$, $\mathbf{Z} = 2$ and $\mathbf{Z}' = 1^{165}$ (Figure 4-1, b).

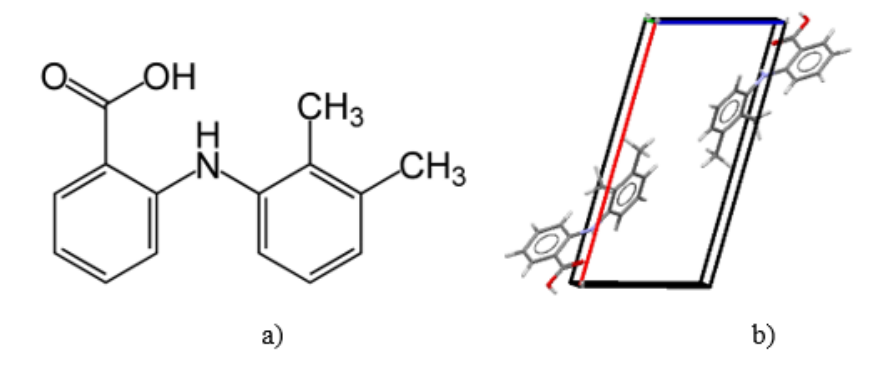


Figure 4-1. a) The 2D molecular structure of mefenamic acid depicting its atom types and b) its 3D packing within a unit cell

The d-mannitol compound comprises a six-carbon backbone with six hydroxyl groups (Figure 4-2 a). It is orthorhombic, crystallising in a space group of P2₁2₁2₁. It consists of four molecules in its unit cell, defined by the unit cell parameters: a = 5.5381 Å, b = 8.580 Å, c = 16.795 Å, $\alpha = 90^{\circ}$, $\beta = 90^{\circ}3$, $\gamma = 90^{\circ}$, Z = 4 and $Z' = 1^{166}$ ((Figure 4-2 b)).

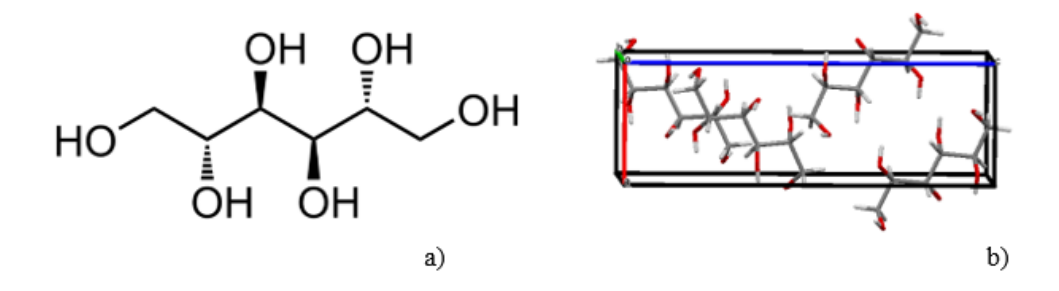


Figure 4-2. a) The 2D molecular structure of d-mannitol depicting its atom types and b) its 3D packing within a unit cell.

4.2 Molecular Modelling Methods

4.2.1 Lattice Energy and Habit Prediction

The molecular structure of mefenamic acid was downloaded from the CSD, reference code: XYANAC¹⁶⁵ and d-mannitol reference code: DMANTL09¹⁶⁶. The file includes crystallographic information, which was used to calculate partial atomic charges using the semi-empirical quantum mechanics program MOPAC¹⁶⁷, using the PM7 Hamiltonian. This is a parameterisation well-suited for organic molecules. It is important to note that these semi-empirical charges used may differ from those obtained from more computationally demanding methods such as Density Functional Theory (DFT) using the common calculation set-up B3LYP/6-31G; and ChelpG charge partitioning⁶⁵. Even though semi-empirical methods are very effective, charges derived from DFT tend to provide a more accurate description of electron distribution¹⁶⁸. Using a different set of partial charges would directly affect the electrostatic contribution to the lattice energy. However, as the electrostatic contribution to the overall lattice energies of both MA and DM is significantly smaller than the dispersive components, the main conclusion about crystal packing and stability is unlikely to change^{169,170}. Therefore, the chosen method is consistent with being able to effectively calculate and rank the intermolecular forces for these

compounds. This approach is also commonly used in pharmaceutical solid-state and crystal engineering studies¹⁷¹.

The Momany force field was chosen to calculate the lattice energy based on the compound's structure and bonds. The force field has a 6-12 dispersive potential and a 10-12 general hydrogen bond potential suitable for calculating lattice energies of hydrocarbons, carboxylic acids, and amines¹⁷², key functional groups found in MA. More general force fields, such as DREIDING¹⁷³ or those applied for biomolecular compounds such as CHARMM¹⁷⁴ and AMBER¹⁷⁵; however, the Momany force field was selected based on its focus and design for solid-state packing of small organic molecules. This made it a suitable choice for predicting lattice energies and intrinsic and extrinsic interactions in the present study. It provides a reliable balance of dispersive, electrostatic and h-bond interactions, all of which are essential for accurately modelling the bulk and surfaces of organic crystals¹⁷¹.

The lattice energy was compared to the experimental lattice energy calculated from the enthalpy of sublimation for comparison. All intermolecular force calculations were carried out using the computer program HABIT98¹⁷⁶.

The morphologically important faces were selected using the BFDH method, and the lattice energy was divided into attachment (Eatt) and slice (Esl) energies for each face given by Equation 4-1. The BFDH considers lattice geometry, stating that the face with the larger interplanar spacing, dhkl, is more morphologically important. The attachment energy was assumed to be directly proportional to the relative growth rate of each face (Equation 4-2), and the three-dimensional morphology was predicted by operating HABIT98 in the FULL mode and visualised in Mercury⁷⁴.

$$E_{cr} = E_{att} + E_{sl}$$
 Equation 4-1
$$R_{hkl} \propto E_{att}$$
 Equation 4-2

The synthons that contribute to the attachment energy of each face were identified, and analysis of the surface chemistry of each face aided in rationalising observed experimental solvent morphologies. The surface energy of each crystal face was calculated by:

$$\gamma = \frac{Zd_{hkl}|E_{att}|}{2N_A V}$$
 Equation 4-3

where Z is the number of molecules in the unit cell, d_{hkl} is the interplanar d-spacing, N_A is Avogadro's Constant and V is the cell volume. The surface anisotropy was also calculated, i.e the degree of unsaturated interactions at the various crystal faces given by:

$$\xi_{hkl} = \frac{E_{Sl}}{E_{Cr}}$$
 Equation 4-4

4.2.2 API-Excipient Interactions

The interactions between mefenamic acid and d-mannitol were modelled using the Systematic Grid-Based Search (SystSearch)⁷⁶. All the possible interactions between a probe molecule and a crystal surface, referred to as a slab. The program builds a grid on top of the slab, and the probe molecule is placed on it and moved at each point of the grid in three translational movements, x, y, z and three rotational, θ , γ , δ . The interaction energy between the slab and probe is calculated at every rotational and translational position. An output file is created, sorting the interactions from strongest to weakest. The interactions are also divided into vdW, h-bond and electrostatic interactions. Once the interactions have been calculated for all crystal surfaces, an average interaction energy between the whole crystal and the probe molecule is calculated.

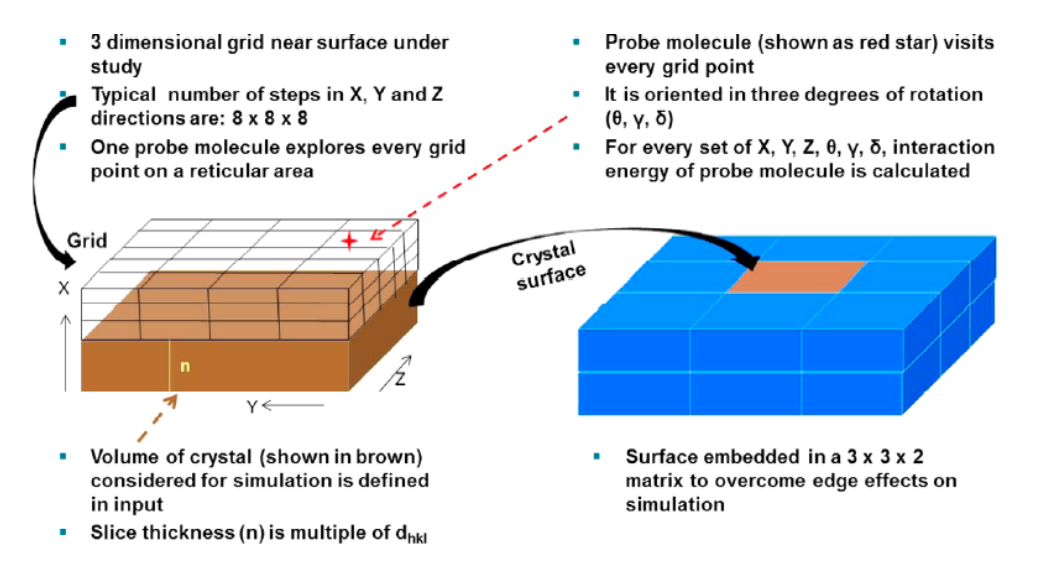


Figure 4-3. Schematic outline of the SystSearch prediction, illustrating the movement of the probe molecule on the grid over the slab¹⁷

4.2.3 Slip-Plane Identification

Potential slip-planes can be rapidly identified using the CSD-Particle tool embedded within the CCDC Mercury programme. All potential planes are scanned and a value of interdigitation (-), or separation (+) is calculated, referred to as slab separation, if the plane is bridged by h-bonding or not and the h-bond network dimensionality, d-spacing and the perpendicular planes to the selected plane. The CSD-Particle tool also allows for surface analysis of each face, obtaining information such as rugosity. The tool quantifies roughness on the molecular level by calculating the root-mean-square deviation of surface atoms relative to a best-fit plane across the crystal face.

Both packing features and solid-state energetics are used in the assessment of potential slip planes. The slip planes assessed in this project were the faces of morphological importance, as the energetics calculations of these have been completed using Habit98. It should be noted that out of these, the top-ranked plane may not be the material's actual active slip.

4.2.3.1 Statistical Analysis

As various attributes of both packing and energetics features define the ideal slip plane, the Multi-Attribute Decision Making (MADM) statistical analysis was used to select the most plausible slip plane. Two methods of MADM were used: the Analytical Hierarchy Process (AHP)¹⁷⁷ and the Technique for Order of Preference by Similarity to Ideal Solution (TOPSIS)¹⁷⁸. In the AHP, the attributes for analysis are chosen, in this case, the four most significant attributes defining a slip plane based on previous studies^{157,159,179}: h-bond breaking, interdigitation, rugosity and surface energy. Through pair-wise comparison of the attributes, weighting factors are assigned to one over the other, creating a decision matrix. The values of the decision matrix (d_{ij}) are then normalised (R_{ij}):

$$R_{ij} = \frac{a_{ij}}{\left\{\sum_{j=1}^{M} d_{ij}^{2}\right\}^{0.5}}$$
 Equation 4-5

The weighing factors are then multiplied by normalised values (R_{ij}) , giving a decision matrix with weighted normalised values (V_{ij}) . Next, TOPSIS is used to select the ideal slip plane. The ideal best, V^+

and ideal worst, V^{-} value of each attribute is determined. The Euclidean distance from the ideal best, S^{+} , positive separation and the ideal worst, S^{-} , negative separation are calculated:

$$S_i^+ = \left\{ \sum_{j=1}^N (V_{ij} - V_j^+)^2 \right\}^{0.5}$$
 Equation 4-6

$$S_i^- = \left\{ \sum_{j=1}^N (V_{ij} - V_j^-)^2 \right\}^{0.5}$$
 Equation 4-7

The shortest distance from the ideal best value is the optimum slip plane. The performance score P_i is calculated by:

$$P_i = \frac{S_i^-}{(S_i^+ + S_i^-)}$$
 Equation 4-8

4.3 Characterisation of Powders

4.3.1 Powder X-Ray Diffraction (PXRD)

The PXRD patterns of the compounds were obtained using the Bruker-AXS D8 Advance diffractometer. Powders were packed into sample holders and scanned at a range of $2.5 \le 2\theta \ge 50^{\circ}$, with a step size of 0.02 min^{-1} . The obtained PXRD patterns were compared to reference patterns provided by the Cambridge Structural Database (CSD) for verification of polymorphic form.

4.3.2 Thermal Analysis

4.3.2.1 Differential scanning calorimetry (DSC)

For further polymorph confirmation, the melting points and any possible phase transitions were examined using a differential scanning calorimetry (DSC) by Mettler Toledo. The instrument measures the heat flow differences between a sample and an empty reference crucible as a function of time and/or temperature. 15-21 mg of samples were weighed into 100µl aluminium crucibles covered with pin-holed lids, heated at 10°C min⁻¹ from 30°C to 300°C under nitrogen at 50ml min⁻¹. The STAR^e software was used to analyse the measurements by taking the onset temperature (T_{onset}) and the endset temperature (T_{endset}) and integrating the endothermic peaks.

4.3.2.2 Thermal gravimetric analysis (TGA)

A TGA instrument by Mettler Toledo was used to investigate the decomposition behaviour of the samples. Similar to the DSC, this was done to ensure the thermal stability and purity of the samples. The change in mass is measured as a function of temperature and time. Approximately 11 mg of sample was placed into an alumina crucible, hooked onto the microbalance and enclosed in the instrument oven. Measurements were recorded at 10°C min⁻¹ from 30-600°C under nitrogen at 50 ml min⁻¹.

4.3.2.3 Dynamic vapour sorption (DVS)

Water vapour sorption of the samples was measured using the DVS Resolution by Surface Measurement Systems (SMS) Ltd. DVS is similar to TGA as it measures the change in mass over time, but as a function of relative humidity (RH) rather than temperature. The sample is exposed to a specific RH until an equilibrium moisture content (EMC) has been reached. This is repeated at varying RH concentrations until a full sorption and/or desorption isotherm has been achieved. The temperature is kept constant throughout the measurement. 30-40 mg of sample was placed in a sample holder and hooked onto the microbalance inside the analysis chamber. The change in mass was measured as the percentage relative humidity (%RH) was changed stepwise from 0%RH to 90%RH, then back to 0%RH at 25°C. The data was plotted using the DVS Analysis Suite embedded within Microsoft Excel.

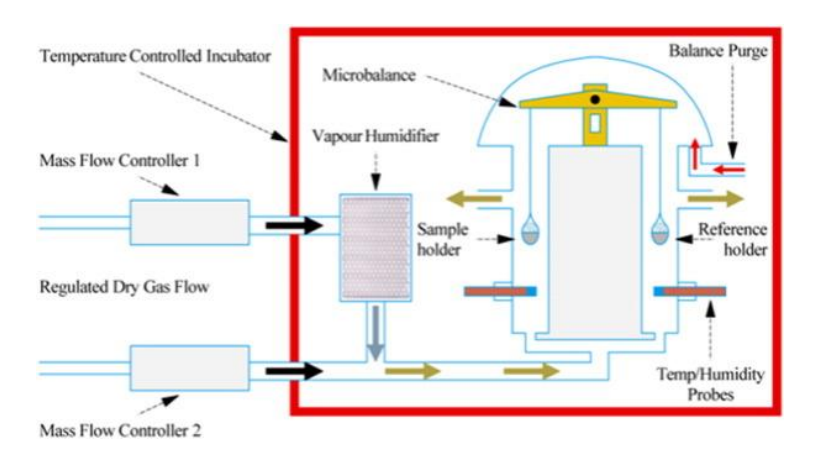


Figure 4-4. Schematic of DVS instrumental set-up¹⁸⁰

4.3.3 Morphological examination

The Hitachi High-Tech Tabletop Scanning Electron Microscope (SEM) TM3030Plus was used to examine the morphology of the powder particles. A thin layer of sample was placed on carbon stickers mounted on sample holders and placed in the analysis chamber. Images were captured at 100X and 300X magnifications under the MIX image signal mode. The MIX mode combines backscattered electron images with secondary electron images, allowing for the observation of both composition and the morphological roughness of the surfaces ¹⁸¹.

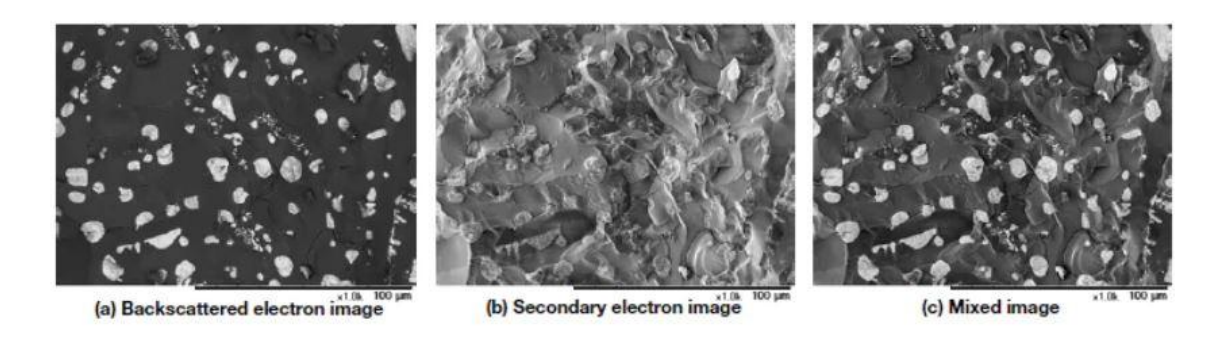


Figure 4-5. Example of differences between a) backscattered image, b) secondary electron image and c) mixed image 181

4.3.4 Particle Size Distribution

The Malvern Mastersizer 2000E dry disperser was used to measure the particle size distribution of the samples. The instrument uses laser diffraction to measure particle size and assumes that the particles are of spherical shape. By use of light intensity and angle changes, the instrument measures the angle at which the particles scatter light. The intensity pattern is dependent on the diameter of the particles. Smaller samples scatter light at smaller angles and larger samples scatter light at larger angles; thus, different-sized particles will give different intensity patterns. The diffraction pattern is therefore a combination of the scattered light from particles of varied sizes. Approximately 20 g of the sample was dispersed at 1.0 bar. The feeding rate was adjusted between 20-30% as needed for each sample.

4.3.5 Flowability

For evaluation of flow behaviour, the Carr's Compressibility Index and Hausner Ratio were determined by Equation 4-9 and Equation 4-10, respectively. This was done through measuring the bulk and tapped density of the powders. Humidity on testing days was between 35-45 % at 22 °C. A tared 100 ml cylinder was filled with the powder, and the initial weight and volume were recorded. The cylinder was then carefully transferred to a tap density apparatus (Copley Scientific Ltd., Nottingham). The apparatus was set to tap for 2 min, and the new volume was recorded. This was repeated until there was no longer a volume change. The bulk and tapped densities were calculated.

The Carr's Index is found by:

$$CI = \frac{\rho_T - \rho_B}{\rho_T} \times 100$$
 Equation 4-9

The Hausner ratio is found by:

$$H_r = \frac{\rho_T}{\rho_B}$$
 Equation 4-10

where, ρ_T is the tapped density and ρ_B is the bulk density.

As a secondary measure of flow behaviour, the angle of repose was determined. Approximately 30 g of material was poured through a funnel onto a base, forming a cone-like shape. An image of the final heap was captured, and the image processing program ImageJ was used to measure the angle of repose.



Figure 4-6. Angle of repose test on d-mannitol

4.3.6 Powder Compression

The Instron Mechanical Tester Figure 4-7, equipped with a 10 kN load cell, was used to create simple compacts and assess the compressibility of DM, MA and 3 compositions of MA to DM (50-50, 65-35 and 75-25). Using a 5 mm die, 0.030 ± 0.05 g of sample was compressed at varied compaction forces (1000 N- 5000 N) at varying piston speeds (0.05 mm/s – 0.5 mm/s), using tooling as displayed in Figure 4-8 a). The best tablets were created at a compaction force of 4000 N and a piston speed of 0.3 mm/s. Tool optimisation was required, creating a longer piston Figure 4-8 b), which could be used for better ejection. The Instron outputs force vs displacement data, which can be used to derive compression properties of the tested powders.



Figure 4-7. Intron Mechanical Tester

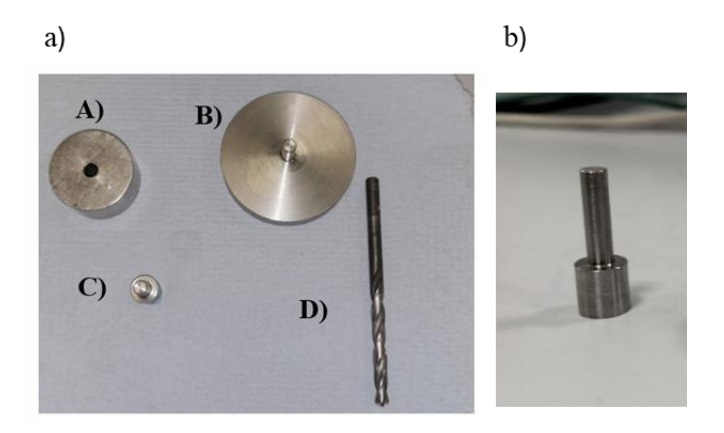


Figure 4-8. Tooling used for powder compression: a) A) 5 mm die, B) die base, C) piston ("punch") head and D) tool used to push out compacts from die, and b) optimised piston also used for better ejection

The Heckel equation was used to analyse compressibility and plasticity (Equation 4-11). The yield stress, P_y is calculated by the inverse of slope, k. A low P_y indicates better compression properties, i.e faster onset of plastic deformation.

$$ln\frac{1}{E} = kP + A$$
 Equation 4-11

Where E is the porosity (1-D, D is the relative density), P is the pressure applied (MPa), k is the slope (inverse of k gives the yield stress, P_y), and A is the intercept, related to die filling & particle rearrangement.

The strength of the tablets was evaluated through diametric stress tests. The Intron was fitted with a 100 N load cell, and tablets were aligned under a piston, and the breaking point was measured. The tensile strength is the force required to diametrically break the tablet and was calculated using Equation 4-12.

$$\sigma = \frac{2F}{\pi Dt}$$
 Equation 4-12

$$\sigma = \frac{2F}{\pi Dt}$$
 Equation 4-12

Where σ is the tensile strength (MPa), F is the breaking force, D is the diameter of the tablet (mm), and t is the tablet thickness or height (mm).



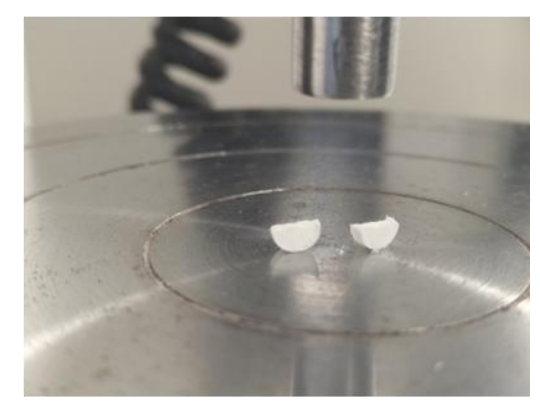


Figure 4-9. Tablet before and after diametric stress test

4.4 X-Ray Computed Tomography (XCT)

The general principles of the imaging technique, XCT, are depicted in Figure 4-10. It involves the illumination of a sample with X-rays from an X-ray source and a detector capturing the transmitted Xrays¹⁵⁵. The sample is rotated 360° degrees providing several radiographs resulting in several

projections. Using a mathematical algorithm, these projections are computationally reconstructed, providing a 3-D representation of the sample¹⁵⁶. The virtual volume allows for the visualisation and study of internal morphological and structural features of powders and tablets.

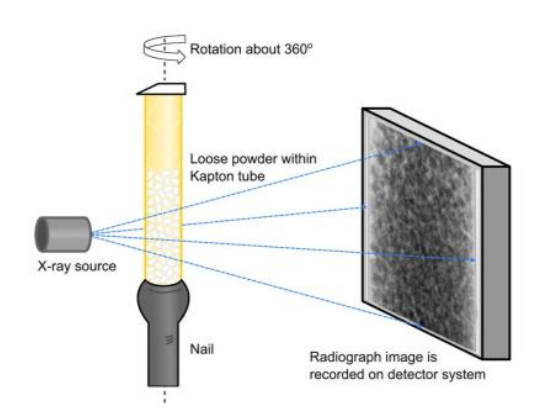


Figure 4-10. X-ray computed tomography set-up 3D inhale¹⁵⁴

The X-ray computed tomography facilities at the Henry Royce Institute in the University of Manchester were used to visualise the internal structure and consolidation of bulk powder and compacts of pure MA, DM and compositions of MA to DM 50-50, 65-35 and 75-25. The DM tablet was scanned before tooling optimisation.

4.4.1 Sample Preparation

Following a similar method reported by Turner et al¹⁸², the powder samples were poured into about half the height of a polyamide tube of 2-3 cm in height and 3 mm diameter, which was glued to a nail. The sample was then placed into a ZEISS Xradia Versa 3D-X-Ray System to be scanned. After scanning, the sample was removed from the X-ray and tapped ten times by hand, then scanned again. This was repeated, scanning the sample after 0, 10, 20 and 30 taps.

During the initial beam time granted in March 2020, the first powder samples scanned were of the pure MA and DM and the 50-50 powder mixture. These were scanned using the following parameters:

A voltage of 80 kV, a power of 7 W, using a 4x objective lens and source and detector distances of 11.5 mm and 13 mm, respectively, giving a pixel size of $3.17 \text{ }\mu\text{m}$. A 2x detector bin was used, collecting 1601 projections with a 1-second exposure time.

The rest of the powder mixtures, 65-35 and 75-25, were scanned during the second beam time granted in July 2022. The scan setting was adjusted to obtain better resolution than the first scans. A voltage of 80 kV, a power of 10 W, using a 4x objective lens and source and detector distances of 11.5 mm and 14.2 mm, respectively, giving a pixel size of $1.49 \text{ }\mu\text{m}$. A 2x detector bin was used, collecting 1999 projections with a 0.8-second exposure time.

During the first beam time, the DM tablet was also scanned. Sample preparation of the tablets involved mounting them to the end of a polyamide tube with epoxy glue, and the other end was glued to a nail. The compact was scanned at 80 kV and 7 W using 1x binning and the source and detector distances of 31.54 mm and 9.02 mm. A 4x objective lens was used, giving 1003 projections with 8 8-second exposure times, and a pixel size of 2.63 µm was obtained.

The 50-50, 65-35 and 75-25 tablets were scanned during the second beam time, with altered scanning settings. The tablets were scanned at 80 kV and 10 W using 1x binning and the source and detector distances of 13.5 mm and 10.2 mm. The objective lens used was 4x, giving 2006 projections with 1-second exposure time and a pixel size of 1.89 μm.

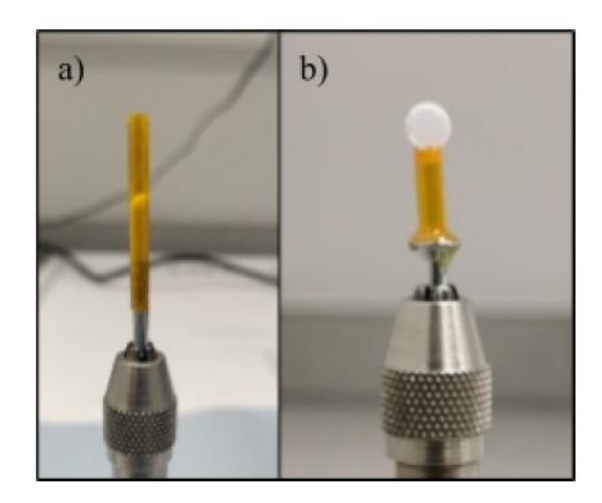


Figure 4-11. Sample preparations for the X-ray computed tomography experiments: a) free-flowing d-mannitol in a polyamide tube, b) 5 mm d-mannitol compact

4.4.2 Data Analysis

Reconstruction of the data was done by Zeiss Reconstruction software, forming three-dimensional volumes using the FDK algorithm, shown in Figure 4-12 a). The non-commercial version of software Dragonfly by Comet Technologies Canada Inc. 2021.1183 for Windows was used to analyse the 3-D volumes. The 3D virtual volume is a 3D grid divided into individual voxels. Each voxel has a greyscale value based on the atomic weight and density of the material inside it. Figure 4-12 b) displays a horizontal slice of MA at 20 taps, displaying different greyscale values: darker for air, as it gets lighter, and lighter for the tube and particles. A cylinder mask (height: 1.5 mm, diameter 1.24 mm) was created for the analysis region to ensure consistency in the analysis area of all scans and to avoid the glue and surface effects. Under the 'Image Processing' function in the software, a bilateral filter was applied to the selected analysis region. This filter smooths the data and is edge preserving, making thresholding more accurate (Figure 4-12, c). Thresholding allows for selecting voxels of the same greyscale, enabling separation of particles from the air (Figure 4-12, d), thus volume fractions can be calculated. It is difficult to distinguish mefenamic acid from d-mannitol in the powder blends as their greyscales are very similar, with mefenamic acid being slightly darker. Thus, regular thresholding is not sufficient to analyse the particle separately in the bulk powder. A phase retrieval filter (PPCF filter) developed by Zeiss was applied after the first beam time, allowing for clearer differentiation between the two powders. The algorithm makes the greyscales more distinguished, allowing for the identification of mefenamic acid and d-mannitol. The filter wasn't accessible after the second beam time.

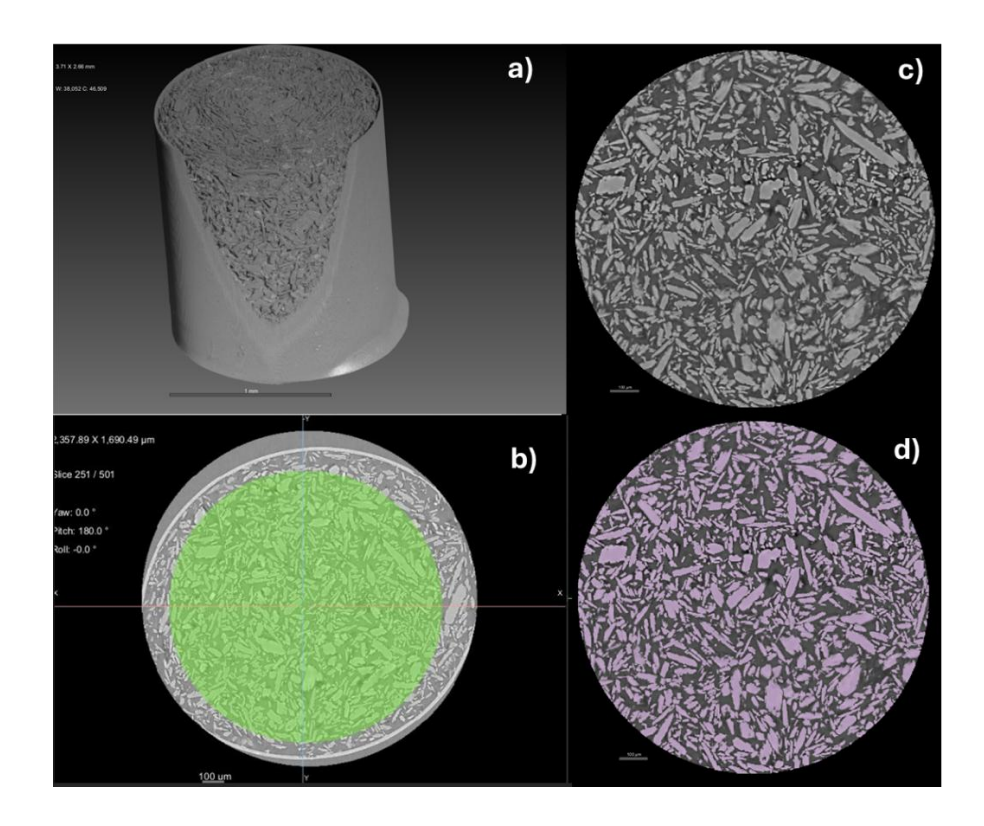


Figure 4-12. a) A 3D rendering of the mefenamic acid powder bed at 20 taps, revealing the powder in the tube, b) a horizontal slice through the powder bed with a cylinder analysis mask overlayed as the analysis region, c) the extracted analysis region with applied 'bilateral filtering' for better thresholding and d) the same slice with the particles identified through thresholding.

The volume fraction was calculated as the ratio of powder to the analysis mask, and the powder density was calculated by multiplying the volume fraction by the material density. The bulk and tapped density were determined by calculating the Carr's Index and Hausner ratio using Equation 4-9 and Equation 4-10, respectively. The consolidation behaviour of the powder bed at each tap was possible through horizontal slice analysis of the data. Density at different heights of the powder bed was measured, one voxel apart, plotting bed height against density.

Tablets were analysed similarly, selecting an analysis region by overlaying a box mask of dimensions: width: 1.01 mm, height: 0.43 mm and depth: 1.01 mm (Figure 4-13, a). Volume fractions were calculated by determining the solids and porosity in the tablets. The porosity was compared to the lab-measured porosity. Unlike in the bulk powder, the different densities of d-mannitol and mefenamic acid produce different greyscale when compacted. Therefore, the volume of mefenamic acid to d-mannitol was able to be determined through regular thresholding.

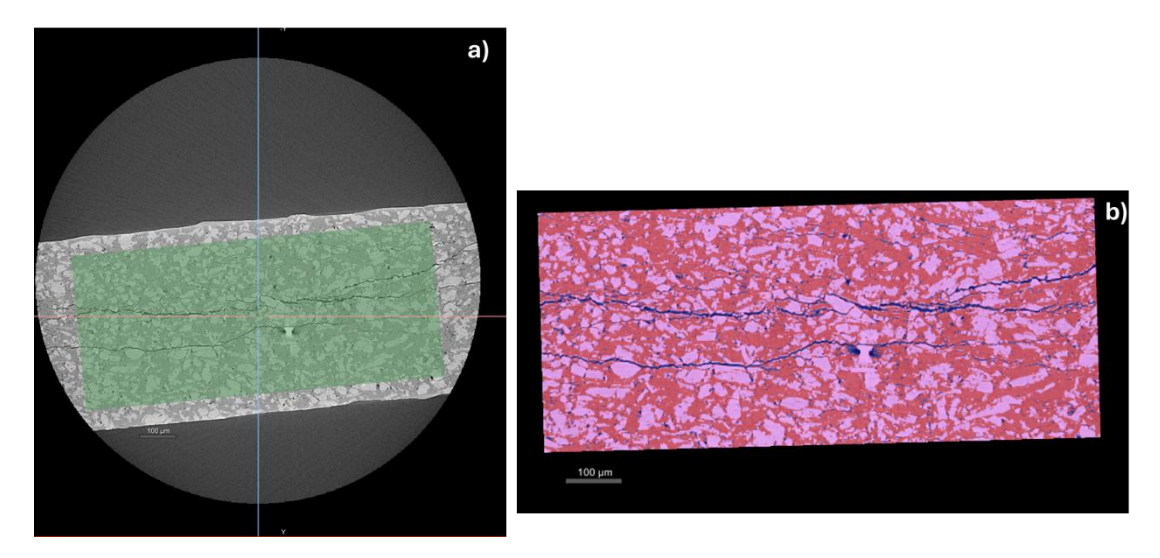


Figure 4-13. a) a horizontal slice through the 50-50 tablet with an analysis mask overlayed, b) the extracted analysis region with the mefenamic acid (red) and d-mannitol (purple) and d-mannitol particles and the air identified through thresholding.

4.4.2.1 Orientation analysis

The anisotropy of organic crystals and their intermolecular and interparticle interactions mean they tend to orient themselves in specific ways. In spherical coordinate systems, the theta (θ) angle represents the orientation of an object, measured between 180° to $180^{\circ 184}$. An object is defined as horizontal if it has a theta value of -90 and 90 degrees. This places the object in the xy-plane, which is perpendicular to the z-axis. A vertical object has the theta value of 180° , 0° and 180° parallel to the z-axis.

The 'Watershed' function in Dragonfly was used to separate the particles for individual analysis, including determining the theta orientation in the 'Objects Analysis' module (See Figure 4-14). In this study, the orientations are categorised into horizontal, vertical and angled based on the theta angle. Specifically:

- Horizontal orientations are defined as having theta angles in the ranges of -100 to -80° and 80° to 100°
- Vertical orientations are defined as having theta angles in the ranges of -180° to -170°, -10° to 10° and 170°-180°

Angled orientations are defined as having theta angles in the ranges of -55° to -35° and 35° to 55°

This classification allows for a systematic analysis of preferred particle orientation.

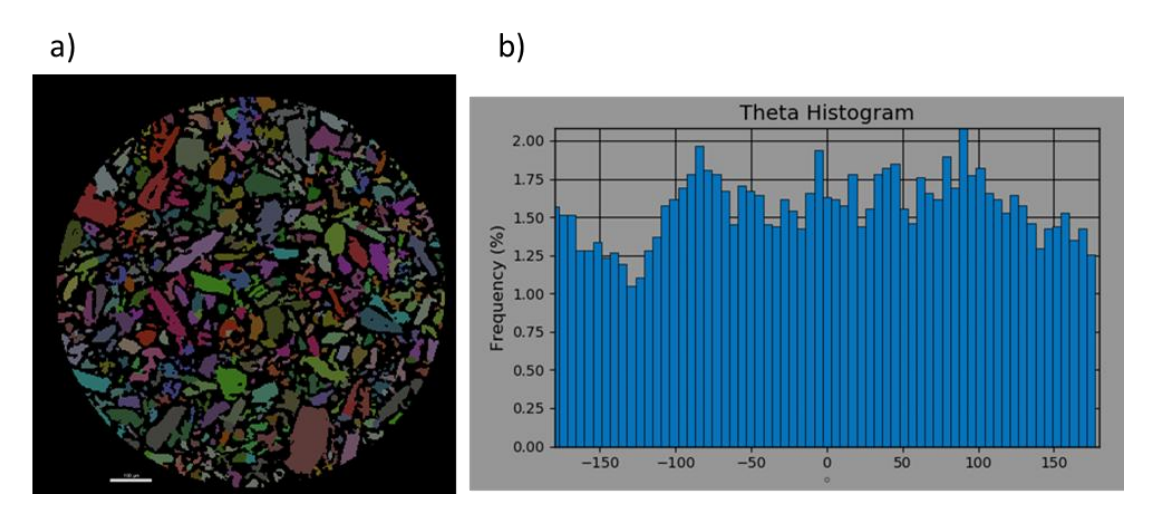


Figure 4-14. Examples of a) watershed applied to particles for individual analysis and b) resulting theta histogram

The resulting orientation of particles is plotted as a percentage frequency as a function of taps. The same analysis was performed for the 5 tablets.

It should be noted that the geometric probability of finding crystals of a certain theta angle in a random powder depends on sin (theta)¹⁸⁵. This means there is a natural bias towards finding horizontally oriented (theta near 90°) particles, instead of vertical (theta near 0° or 180°). The orientation preferences reported in this study are therefore considered to be deviations from this expected distribution¹⁸⁶.

4.4.2.2 Segmentation analysis

Segmentation analysis was carried out on the formulated tablets by calculating the mixing index. Each tablet was divided into 72 boxes (Figure 4-15), cells (*N*). The local composition of one component in each cell was determined by calculating the mass fraction from the volume fraction obtained by thresholding (Equation 4-13).

$$w_i = \frac{\emptyset_i \rho_i}{\emptyset_i \rho_i + \rho_m (1 - \emptyset_i)}$$
 Equation 4-13

Where w_i = mass fraction of component i, ϕ_i = volume fraction of component i, ρ_i = density of component i, ρ_m = density of matrix.

The Rose & Robinson Mixing Index¹⁸⁷ was calculated by Equation 4-14, by first calculating the standard deviation of the local composition and then the standard deviation of a completely random mixture. A mixing index, M, of 1 indicates a perfectly uniform mixture.

$$M = 1 - \frac{\sigma}{\sigma_0}$$

$$\sigma^2 = \sum_{i=1}^{N} \frac{(\varphi_{i-} \varphi_m)^2}{N-1}$$

$$Equation 4-15$$

$$\sigma_0^2 = \varphi_m (1 - \varphi_m)$$

$$Equation 4-16$$

Where σ^2 = the variance of the measured composition in the mixture, σ_0^2 = the variance of a completely random mixture, φ_i = composition in each cell, φ_m = mean composition, N = cell number.

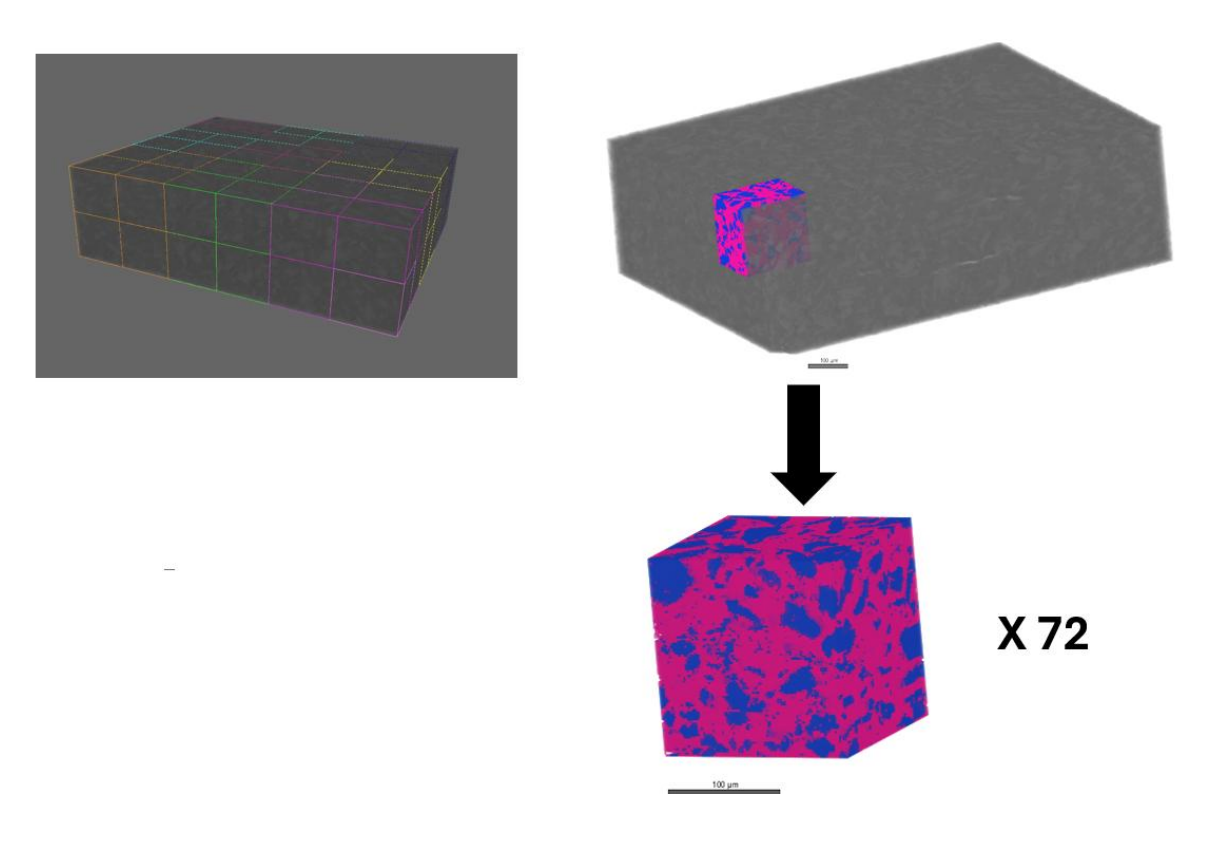


Figure 4-15. 3D rendering of a tablet divided into 72 cells for individual volume thresholding

4.5 Conclusion

This chapter has detailed the materials used and the experimental and computational methods. The experimental methods used to characterise solid-state, thermal behaviour, stability, morphology, and particle size distribution have been described. In addition, methods used to evaluate the mechanical properties, such as compression and consolidation, have also been outlined. The molecular modelling methods used for calculating the lattice energy, attachment energy, synthon analysis and API-excipient interactions have been detailed.

CHAPTER FIVE

Surface and Solid-State Study and Prediction of Molecular Interactions of Mefenamic Acid and D-mannitol using Molecular Modelling

This chapter presents the results from examining the surface, solid-state, and molecular interactions of mefenamic acid and d-mannitol using molecular modelling. The cohesive/adhesive interactions and mechanical behaviour are investigated, bridging theoretical prediction with experimental results in future research.

5 Surface and Solid-State Study and Prediction of Molecular Interactions of Mefenamic Acid and D-mannitol using Molecular Modelling

5.1 Introduction

Understanding pharmaceutical compounds on the molecular and solid-state level is essential in understanding their physicochemical bulk behaviour. Downstream processing issues during filtration, blending, die-filling and compaction are all affected by the solid-state and surface properties of the powders and their cohesive/adhesive nature. It is therefore advantageous to predict these properties by investigating them by use of molecular modelling tools.

In this chapter, the molecular, solid-state, and surface properties of mefenamic acid and d-mannitol are predicted. The vapour morphologies are predicted and compared to solvent morphologies. For an understanding of how these compounds behave in formulation, their cohesive and adhesive interactions have been predicted. Their mechanical behaviour has also been predicted through slip-plane analysis and Burger's vector identification. This chapter aims to illustrate the interconnection between these properties and how they link to experimental results in subsequent chapters.

5.2 Molecular Structure and Descriptors

The mefenamic acid compound consists of a carboxylic acid group at the end of a phenyl ring, two methyl groups on another phenyl ring and an amino group connecting the two rings (Figure 5-1, a). For the rest of this chapter, that carboxylic acid phenyl ring will be referred to as "Phenyl 1" and the alkylated phenyl ring will be referred to as "Phenyl 2". The d-mannitol compound comprises a six-carbon backbone with six hydroxyl groups (Figure 5-1, b). Table 1 provides a list of molecular properties of mefenamic acid and d-mannitol. The mefenamic acid compound consists of 33 atoms; thus, it has a heavier molecular weight than that of d-mannitol (241.29 g/mol and 182.17 g/mol, respectively), which consists of 26 atoms. With six hydroxyl groups, d-mannitol has six hydrogen bond donors and acceptors, whilst mefenamic acid has two hydrogen bond donors (amine and hydroxyl group) and three hydrogen bond acceptors (hydroxyl oxygen, carbonyl oxygen and nitrogen). The

nature of d-mannitol makes it unsurprising that it has a larger polar surface area than mefenamic, 121 Å and 49 Å, respectively. The six hydroxyl groups of d-mannitol make it very hydrophilic and lipophobic, as reflected in its low logP value of -4.67. On the other hand, mefenamic acid has a high logP value of 5.33, making it very lipophilic, thus very hydrophobic. It is therefore categorised as a Class II drug under the Biopharmaceutics Classification System (BCS)¹⁸⁸.

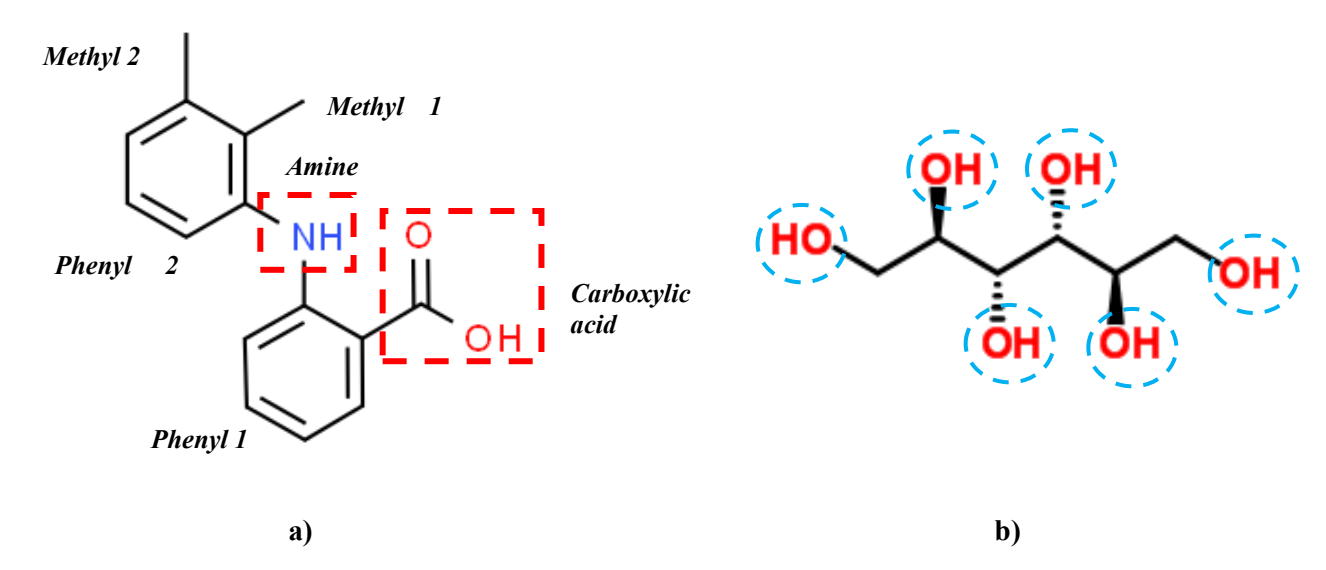


Figure 5-1 Molecular structures of a) mefenamic acid and b) d-mannitol, highlighting main functional groups

Table 5-1. List of molecular properties of mefenamic acid and d-mannitol

Molecular Properties	Mefenamic acid	D-mannitol
Number of atoms	33	26
Molecular weight (g/mol)	241.29	182.17
Hydrogen bond donors	2	6
Hydrogen bond acceptors	3	6
Number of rotatable bonds	3	5
LogP	5.33	-4.67
Polar surface area (Å ²)	49	121
Molecular volume (Å ³)	315.90	199.51

5.3 Solid-Sate Properties

Mefenamic acid crystallises in a triclinic crystal lattice with a space group of P $\bar{1}$. It consists of two molecules in its unit cell, defined by the unit cell parameters: $\bf a=14.556~ \rm \AA$, $\bf b=6.811~ \rm \AA$, $\bf c=7.657~ \rm \AA$, $\bf \alpha=119.57^{\circ}$, $\bf \beta=103.93^{\circ}$, $\bf \gamma=91.30^{\circ}$, $\bf Z=2$ and $\bf Z'=1^{165,189}$. D-mannitol crystallises in an orthorhombic crystal lattice with a space group of P $\bf 2_1~\bf 2_1$. It consists of four molecules in its unit cell, defined by

the unit cell parameters: a = 5.5381 Å, b = 8.580 Å, c = 16.795 Å, $\alpha = 90^{\circ}$, $\beta = 90^{\circ}$ 3, $\gamma = 90^{\circ}$, Z = 4 and $Z' = 1^{166}$. Table 2-1 provides a list of the solid-state properties of each compound.

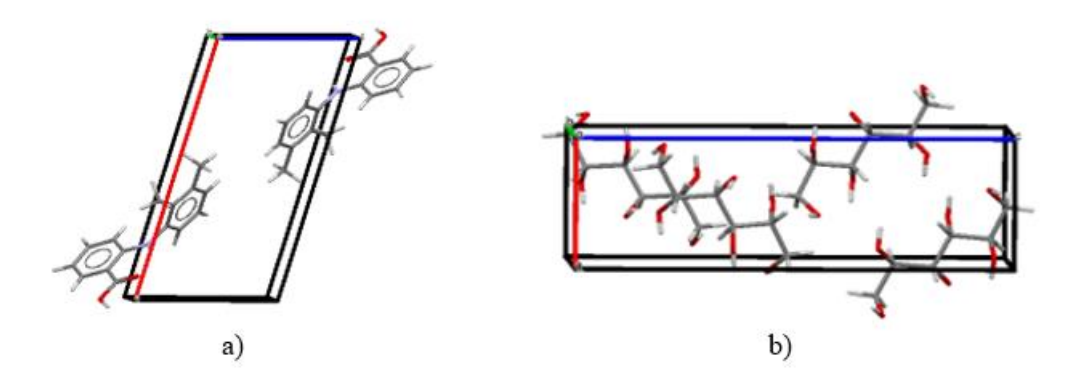


Figure 5-2. 3D packing within a unit cell of a) mefenamic acid and b) d-mannitol

The intermolecular packing of mefenamic acid is presented in Figure 5-3 viewed down the a, b and c-axes. The blue dashes represent hydrogen bonding, and the red potential hydrogen bonding. The molecular packing viewed down all axes displays the intramolecular interaction between the amine and carbonyl oxygen. The carbonyl oxygen accepts hydrogen from the amine, forming an imino bridge within the molecule. When viewed down the b-axis, it can be seen that the molecules orient themselves in a way which allows for the formation of symmetric carboxylic acid dimers through hydrogen bonding via $OH\cdots H$. These are connected by adjacent $C-H\cdots \pi$ interactions (represented by the black dashed line) through the ring of Phenyl 2 and aromatic C-H of Phenyl 1.

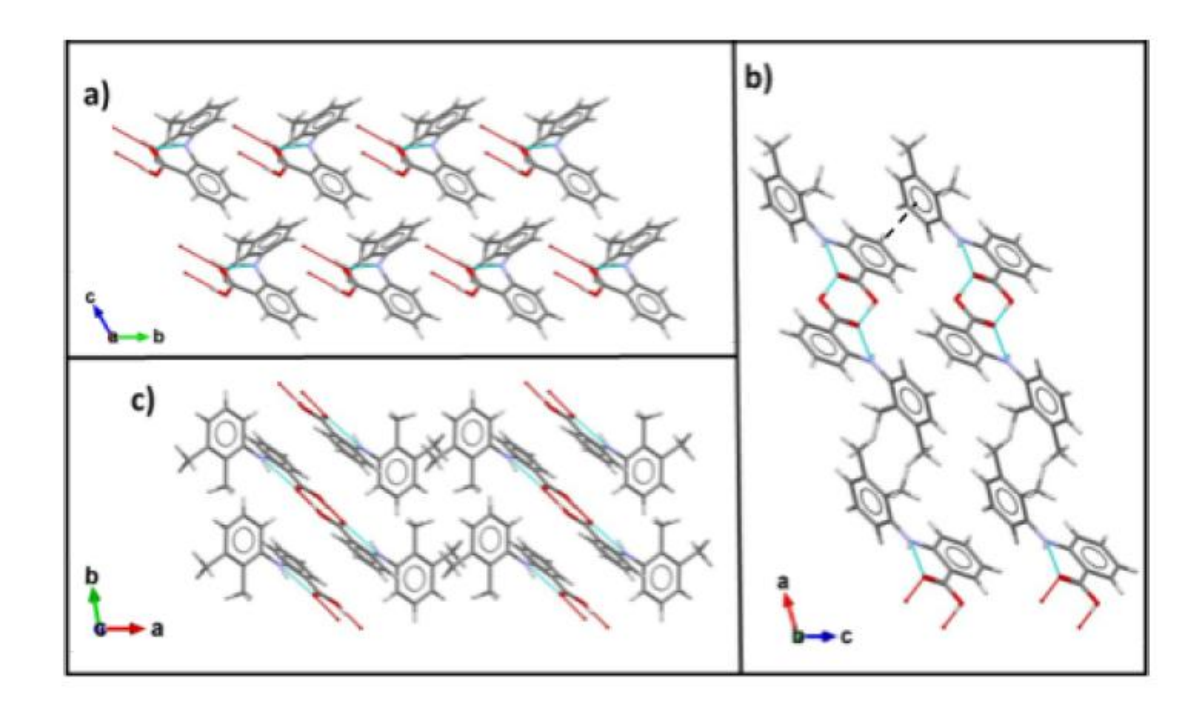


Figure 5-3. Molecular packing of mefenamic acid viewed along the a) a-axis, b) b-axis and c) c-axis

The packing of d-mannitol viewed down the b and c-axes is presented in Figure 5-4, where it can be seen that the hydroxyl groups of the d-mannitol form two different types of h-bond networks (note, the hanging/potential h-bonds have been omitted for visual clarity). One is between $O_3H_3\cdots O_4H_4\cdots O_5H_5\cdots O_6H_6$, forming an enclosed rectangle connecting four molecules, and the other is between $O_1H_1\cdots O_2H_2\cdots O_1H_1\cdots O_2H_2$ connecting three molecules and expands along the c-axis. These two h-bond network types are presented more clearly visualised in Figure 5-5.

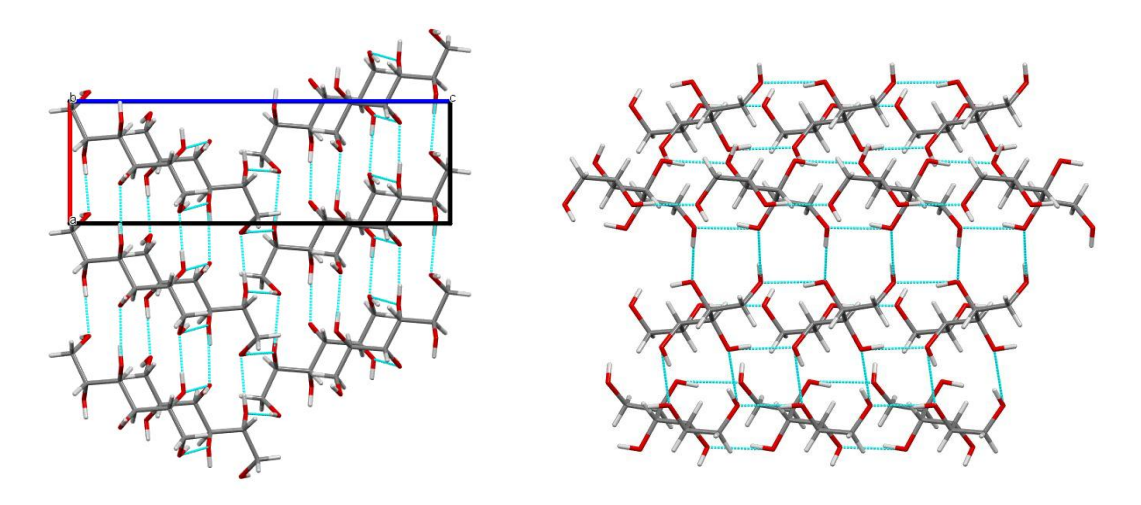


Figure 5-4. Molecular packing of d-mannitol viewed along the b- and c-axes

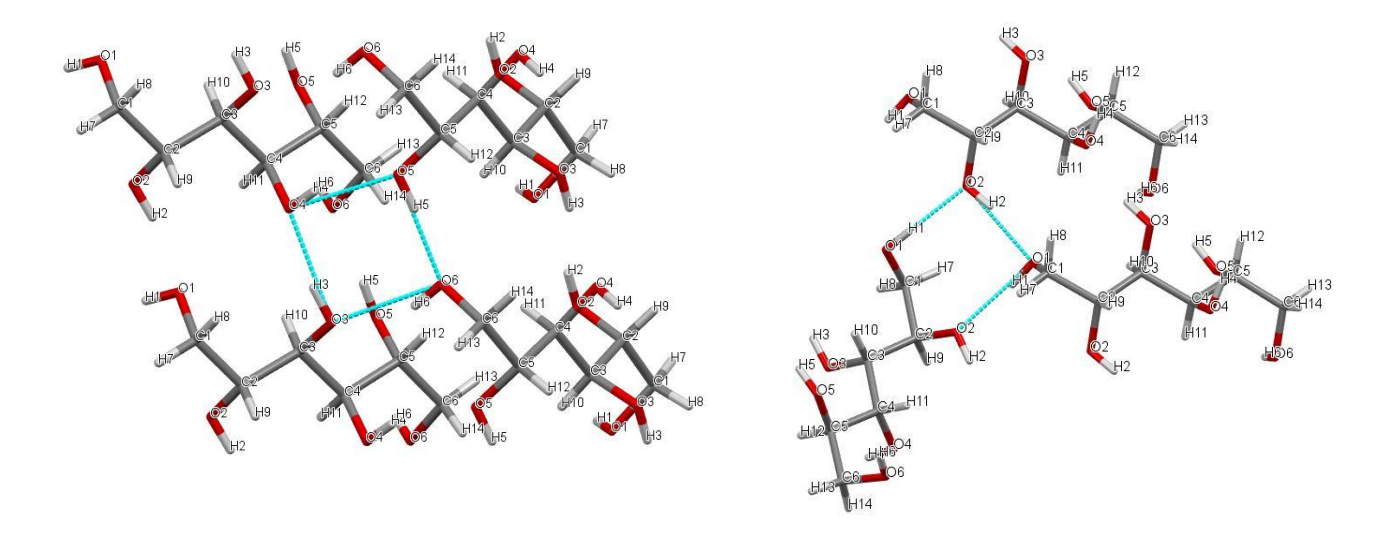


Figure 5-5. Hydrogen bond types in the d-mannitol lattice

Table 5-2 lists a summary of the solid-state properties of mefenamic acid and d-mannitol. Both compounds exist in various polymorphic forms. Mefenamic acid (MA) has three known forms, Form I, II and III, Form I being the stable one used in drug manufacture ^{139,190–193}. D-mannitol (D-M) can exist in four forms, α , β , δ and a hemihydrate form ^{194–196}. The β polymorph is the most stable form commonly used in pharmaceuticals.

The data show that mefenamic acid has a higher melting point than d-mannitol, indicating higher lattice energy. Interestingly, d-mannitol exhibits higher enthalpy and entropy of fusion, suggesting higher stability than d-mannitol. Although mefenamic acid has a higher melting point, more energy is needed to convert d-mannitol into a liquid, and this occurs at a lower temperature than for mefenamic acid. This higher enthalpy of fusion is due to the extensive hydrogen bond networks found in d-mannitol. It should be noted that the literature values for the enthalpy and entropy of fusion are not polymorph-specific. D-mannitol has a larger cell volume but a larger packing coefficient and consequently higher density than mefenamic acid, 1.51 g/cm³ and 1.26 g/cm³, respectively.

Table 5-2. Solid-State Properties of mefenamic acid and d-mannitol

Descriptor	Mefenamic acid	D-mannitol
Refcode	XYANAC ¹⁶⁵	DMANTL09 ¹⁶⁶
Polymorph	Form I	Beta
Melting point (°C)	230°C	166–168°C
Enthalpy of fusion (kJ/mol)	38.7 ¹⁹⁷	54.69^{198}
Entropy of fusion (J/mol·K)	74 ¹⁹⁹	127.8^{200}
Space group	P1	P 2 ₁ 2 ₁ 2 ₁
Crystal system	Triclinic	Orthorhombic
Z/Z'	2/1	4/1
Cell lengths (Å)	<i>a</i> : 14.56, <i>b</i> : 6.81, <i>c</i> : 7.66	<i>a</i> : 5.54, <i>b</i> : 8.58, <i>c</i> : 16.80
Cell angles (°)	α: 199.57, β: 103.93, γ: 97.30	α: 90, β: 90, γ: 90
Cell Volume (Å ³)	631.77	798.05
Packing coefficient	0.69	0.75
Density (g/cm ³)	1.26	1.51

5.3.1 Force-Field and Fractional Charges

All intermolecular interactions were calculated using the Momany force field. The atom coordinates of the crystal structure and their fractional charges of mefenamic acid and d-mannitol, calculated using the PM7 Hamiltonian in MOPAC, are listed in Table 5-3 and Table 5-4.

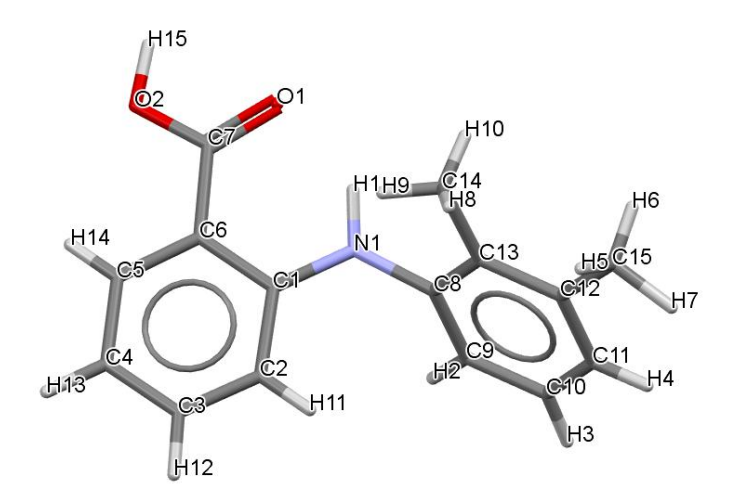


Figure 5-6. Numbering of atoms in the mefenamic acid molecular structure.

Table 5-3. Fractional Coordinates and Atomic Charges of all 33 atoms of Mefenamic Acid

Atom Number	Atom label	X coordinate	Y coordinate	Z coordinate	Charge
1	O1	0.0832	0.3466	-0.0189	-0.4077
2	O2	-0.0038	0.4298	0.2028	-0.2799

3	N1	0.2027	0.0547	-0.0457	-0.2746
4	C1	0.1756	0.0496	0.1108	0.1757
5	C2	0.2165	-0.0813	0.1964	-0.2129
6	С3	0.1888	-0.0846	0.3542	-0.037
7	C4	0.1195	0.0398	0.4341	-0.2022
8	C5	0.079	0.17	0.3542	-0.0038
9	С6	0.1055	0.1785	0.194	-0.2284
10	C7	0.0617	0.3227	0.1164	0.3667
11	С8	0.2702	-0.0648	-0.1452	0.0627
12	С9	0.253	-0.3021	-0.2606	-0.1267
13	C10	0.3161	-0.4169	-0.3677	-0.101
14	C11	0.3952	-0.2948	-0.3602	-0.1187
15	C12	0.4143	-0.0582	-0.2447	-0.0636
16	C13	0.3507	0.06	-0.1346	-0.0968
17	C14	0.3694	0.3162	-0.0062	-0.141
18	C15	0.5025	0.0701	-0.2372	-0.1518
19	H1	0.1826	0.1696	-0.0662	0.2504
20	H2	0.1968	-0.382	-0.2632	0.1297
21	НЗ	0.3061	-0.5772	-0.4388	0.1206
22	H4	0.4374	-0.3712	-0.4331	0.1142
23	Н5	0.5465	0.1725	-0.0916	0.0853
24	Н6	0.4844	0.1486	-0.3065	0.0798
25	Н7	0.5427	-0.0646	-0.3263	0.0727
26	Н8	0.4424	0.3692	0.0861	0.0764
27	Н9	0.3427	0.3568	0.1021	0.0686
28	H10	0.3507	0.3775	-0.0848	0.0892
29	H11	0.2627	-0.17	0.1396	0.1295

30	H12	0.2161	-0.1855	0.4005	0.1197
31	H13	0.1017	0.0384	0.5532	0.1314
32	H14	0.0307	0.2487	0.402	0.1253
33	H15	-0.0289	0.5183	0.1393	0.2482

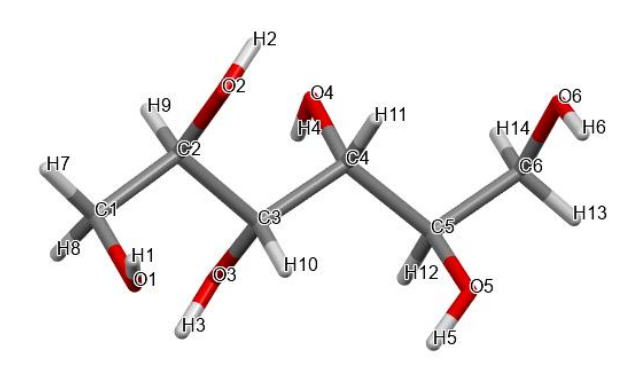


Figure 5-7. Numbering of atoms in the mefenamic acid molecular structure

Table 5-4. Fractional Coordinates and Atomic Charges of all 26 atoms of D-mannitol

Atom Number	Atom label	X coordinate	Y coordinate	Z coordinate	Charge
1	O1	1.076	0.61279	0.44986	-0.3399
2	H1	1.064	0.701	0.4691	0.2044
3	O2	0.55819	0.61711	0.46309	-0.3272
4	H2	0.411	0.598	0.4579	0.2021
5	О3	0.83302	0.27783	0.36445	-0.3419
6	Н3	0.987	0.294	0.3682	0.2034
7	O4	0.32682	0.28903	0.36741	-0.3085
8	H4	0.385	0.204	0.3547	0.1952
9	O5	0.6137	0.49857	0.2006	-0.341
10	Н5	0.766	0.491	0.2056	0.2038
11	O6	0.09906	0.49756	0.21181	-0.322

12	Н6	0.164	0.573	0.1902	0.1999
13	C1	0.9372	0.5011	0.49394	0.0166
14	H7	0.9166	0.5385	0.5493	0.072
14	Н8	1.0261	0.4011	0.4959	0.0932
16	C2	0.6897	0.47425	0.45681	-0.001
17	Н9	0.6032	0.3909	0.4871	0.095
18	С3	0.7118	0.42557	0.36894	-0.0151
19	H10	0.8089	0.5054	0.3397	0.098
20	C4	0.4667	0.40787	0.32857	0.0194
21	H11	0.3783	0.5088	0.3348	0.1286
22	C5	0.4879	0.37379	0.23879	-0.0172
23	H12	0.5793	0.2745	0.2308	0.0833
24	С6	0.2417	0.3607	0.19915	0.0271
25	H13	0.2636	0.3443	0.1413	0.0663
26	H14	0.1553	0.2691	0.2209	0.1055

As discussed in Chapter 2, the Lennard-Jones potential is used to describe the interaction energies between two molecules based on their distance. The Momany force field adds a 10-12 potential to account for hydrogen bonds to the 6-12 potential accounting for van der Waals interactions and the Coulombic term:

$$V_{ij} = -\frac{A}{r_{ij}^{6}} + \frac{B}{r_{ij}^{12}} + \frac{q_{i}q_{j}}{Dr_{ij}} + \frac{B}{r_{ij}^{12}} - \frac{A}{r_{ij}^{10}}$$
 Equation 5-1

where A and B describe atom-atom interaction, qi and qj are the fractional charges on atom i and j separated, r is the distance, and D is the dielectric constant.

Figure 5-8 provides a schematic of calculating the intermolecular interactions, where C is the central molecule, P is a molecule outside the slice, and S is a molecule within the slice²⁰¹.

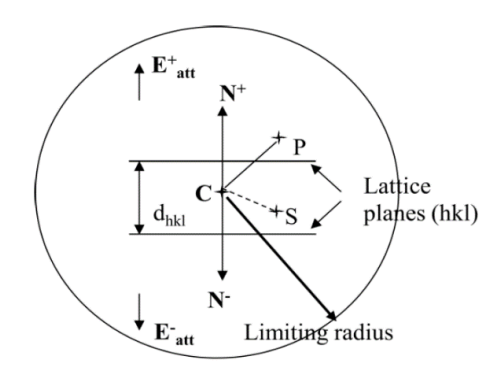


Figure 5-8. Schematic of calculating the intermolecular interactions based on the atom-atom method 201

5.3.2 Lattice Energies and their Convergence

The lattice energy convergence of mefenamic acid is displayed in Figure 5-9 a). The figure shows the compound fully converging at -33.16 kcal/mol, and the electrostatic energy converging at -2.55 kcal/mol. The calculated lattice energy was in good agreement with the experimental lattice energy from the heat of sublimation, -32.5 kcal/mol²⁰². This suggests the Momany forcefield accurately predicts the strength and nature of the intermolecular synthons within the crystal structure. Figure 5-9 b) displays the percentage of the lattice energy added with increasing radius in 3 coordination shells of energy of 61.04%, 13.14% and 1.03% at 0-10 Å, 10-16 Å and 16-26 Å, respectively. The graph shows that the lattice energy starts to converge in shell 2 at 16 Å. The reduction of percentage contribution with increasing limiting radius conveys the significance of nearest neighbouring synthons for the stabilisation of the crystal lattice. These become less important with increased distance.

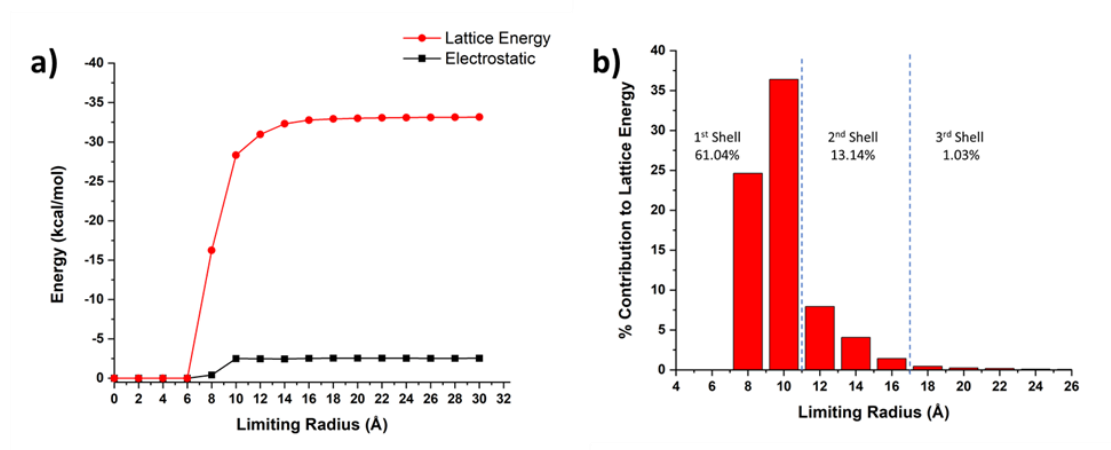


Figure 5-9. a) Lattice energy of mefenamic acid as a function of increasing limiting radius of the sphere of calculation, and b) the percentage of added contribution to the lattice energy with increasing limiting radius

The lattice energy of d-mannitol was calculated to be -31.68 kcal/mol, and its convergence is displayed in Figure 5-10 a). As stated earlier, the currently available enthalpy data for d-mannitol are not polymorph-specific and thus should be considered as approximate values. The reported enthalpy of sublimation for d-mannitol is 48.26 kcal/mol²⁰⁰. The calculated lattice energy is of relatively good agreement. The electrostatic energy converged at -3.85 kcal/mol. The percentage lattice energy contribution with increasing limiting radius, displayed in Figure 5-10 b, is divided into three coordination shells. The lattice energy starts to converge in Shell 2 at ca. 12 Å, thus d-mannitol converges at a shorter distance than mefenamic acid.

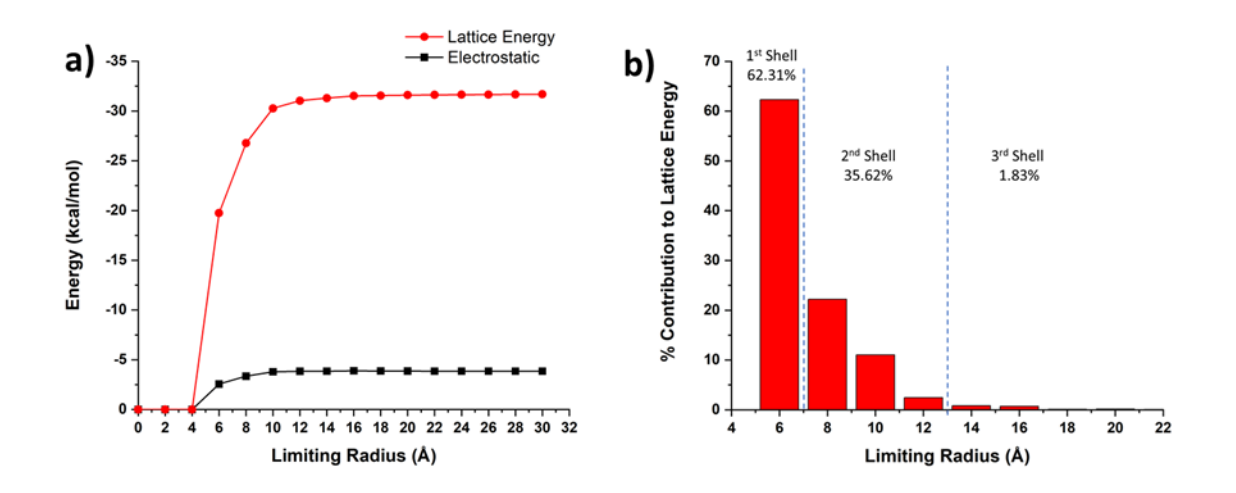


Figure 5-10. a) Lattice energy of d-mannitol as a function of increasing limiting radius of the sphere of calculation, and b) percentage of added contribution to the lattice energy with increasing limiting radius

Table 5-5 summarises the dispersive and electrostatic contributions of both compounds to their lattice energies. It can be seen that mefenamic acid has a slightly higher lattice energy than d-mannitol, as assumed by its higher melting point. Both compounds are dominated by dispersive interactions; however, d-mannitol possesses a greater electrostatic contribution to its lattice energy than mefenamic acid (12.5% and 7.70% respectively). This is expected due to its more polar nature.

Table 5-5. Relative contribution of dispersive and electrostatic energy of mefenamic acid and d-mannitol contributing to their lattice energies

Tomas	Mefenamic	D manuital	Percentage contribution	to lattice energy %
Туре	acid	D-mannitol	Mefenamic acid	D-mannitol
Dispersive energy (kcal/mol)	-30.61	-27.83	92.31	87.85
Electrostatic energy (kcal/mol)	-2.55	-3.85	7.70	12.15
Lattice Energy (kcal/mol)	-33.16	-31.68	100	100

5.3.3 Relative Contributions of the Molecular Fragments to the Lattice Energy

Table 5-6 and Table 5-7 list the contributions of the various functional groups of mefenamic acid and d-mannitol, respectively. In the mefenamic acid compound, the carboxylic acid group contributes to 35% of the lattice energy, reflecting the strong h-bond interaction. Together, the phenyl rings, Phenyl 1 and 2, contribute most to the overall lattice energy, 26.33% and 21.65% respectively, demonstrating the dominance of dispersive interactions in the lattice. Even so, the strong hydrogen bonding in the molecule suggests that it is directional in nature. Consequently, if a -COOH functional group is exposed on the crystal surface, i.e., part of an extrinsic synthon, it will affect the anisotropy of the crystal habit.

The fragment contributions of d-mannitol have been divided into the alkane backbone and the six hydroxyl groups. The data shows how the hydroxyl groups contribute the strongest to the lattice energy by both dispersive energy (-17.94 kcal/mol) and electrostatic energy (-2.94 kcal/mol), contributing 65.86% to the total lattice energy.

Table 5-6. Mefenamic acid energetics and percentage contribution of functional groups to lattice energy

Functional Group	Dispersive energy	Electrostatic energy	Total energy (kcal/mol)	%
Carboxylic acid	-9.54	-2.07	-11.61	35.01
Amine	-1.17	0.14	-1.03	3.11
Phenyl 1	-8.57	-0.19	-8.73	26.33
Phenyl 2	-6.86	-0.31	-7.17	21.62
Methyl x2	-4.48	-0.12	-4.61	13.90

Table 5-7. D-mannitol energetics and percentage contribution of functional groups to lattice energy

Functional Group	Dispersive Energy	Electrostatic energy	Total Energy	%
Alkane backbone (C ₆ H ₈)	-9.9	-0.91	-10.81	34.12
Hydroxyl groups x6	-17.94	-2.94	-20.88	65.86

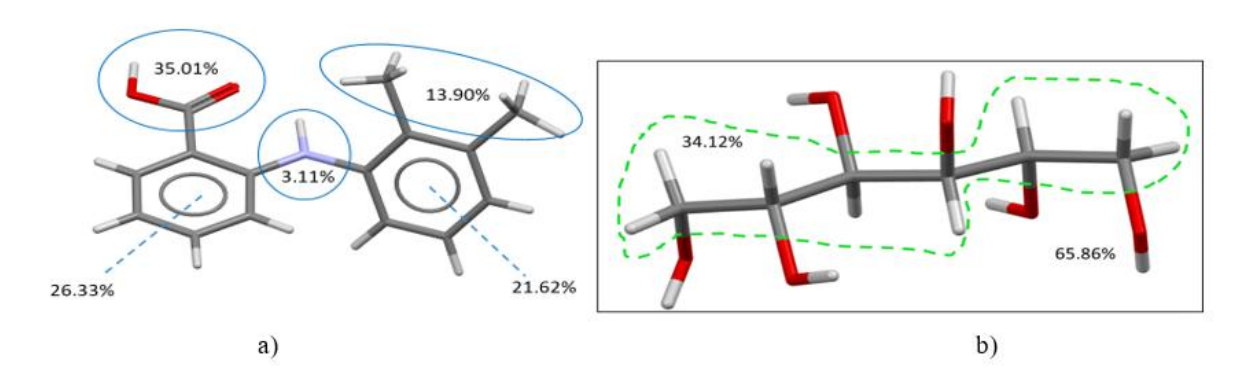


Figure 5-11. Percentage contribution of functional groups to the lattice energy in a) mefenamic acid and b) d-mannitol

5.3.4 Intrinsic Synthon Chemistry

5.3.4.1 Mefenamic acid

The top 6 strongest intrinsic synthons are imaged in Figure 5-12, and Table 5-8 shows their energetic values. The strongest calculated Synthon A is the OH···O h-bonding between two adjacent carboxylic acid groups and has a value of -7.94 kcal/mol. It is over 4 kcal greater than the next strongest Synthon B. This high difference in energy relates to the strong hydrogen bonding between the carboxylic acid dimers, also reflected in the high electrostatic energy of -2.00 kcal/mol (relative to the other synthons). This is unsurprising due to the polar nature of this functional group. This h-bonding is not seen in any of the other synthons, as there are no available polar hydrogens to bond to the carbonyl oxygen lone pairs. Synthons B and C are dominated by π - π stacking, whilst Synthons D, E and F are dominated by van der Waals interactions.

Table 5-8 Top 6 Intrinsic Synthons Contributing to the Lattice Energy, Ranked in Order of Total Interacting Energy

Synthon	Multiplicity	Distance	Dispersive	Electrostatic	Total energy	Dominating
Symmon	winiplicity	(Å)	energy	energy	(kcal/mol)	interaction
A	2	9.08	-5.94	-2.00	-7.94	h-bond
В	2	6.55	-4.04	0.15	-3.88	$\pi - \pi$
С	2	8.07	-3.13	-0.16	-3.29	$\pi - \pi$
D	4	6.81	-2.06	-0.04	-2.11	vdW
Е	4	7.66	-1.87	-0.20	-2.07	vdW
F	4	7.32	-1.97	0.66	-2.01	vdW

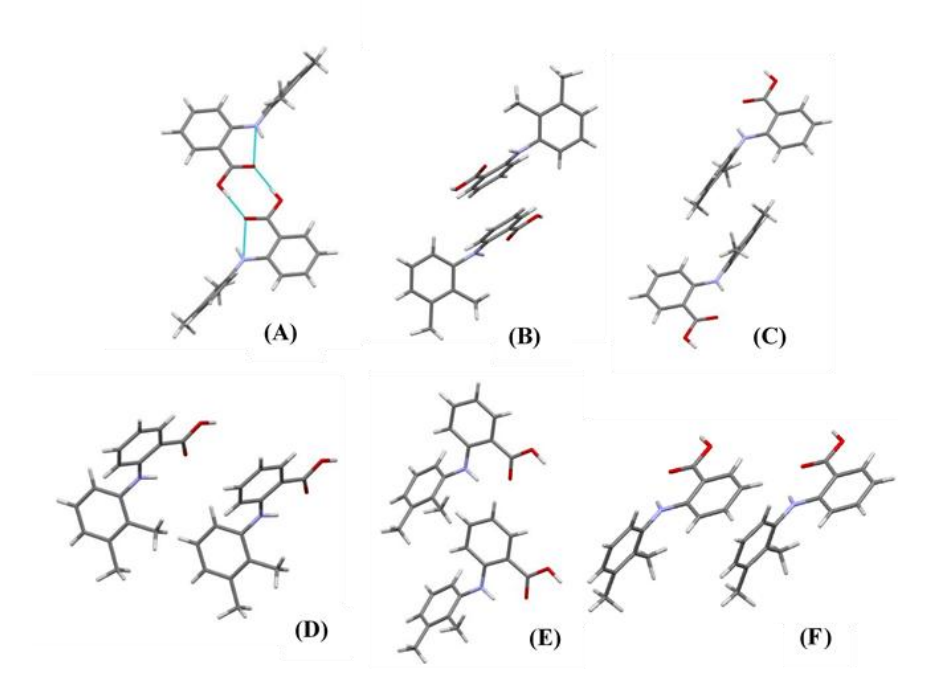


Figure 5-12. (A-E) Six strongest pairwise intrinsic synthons calculated from the bulk structure of mefenamic acid.

5.3.4.2 D-mannitol

The 6 strongest synthons are visualised in Figure 5-13 and listed in order of decreasing interaction energy in Table 5-9. Synthon A is the strongest synthon with three h-bond interactions between O₂-H₂···O₁, O₃-H₃···O₄ and O₅-H₅···O₆ with an interaction value of -5.82 kcal/mol. This is followed by Synthon B, dominated by two h-bonds between O₄-H₄···O₅ and O₆-H₆···O₃, which have an interaction value of -4.05 kcal/mol. Synthon C is also dominated by h-bonding between O₁-H₁···O₂ and has an interaction value of -1.88 kcal/mol. Synthons D, E and F are all dominated by van der Waals interactions, possessing interaction energies of -1.13, -0.66 and -0.57 kcal/mol, respectively.

Table 5-9. Top 6 Intrinsic Synthons Contributing to the Lattice Energy, Ranked in Order of Total Interacting Energy

Synthon	Multiplicity	Distance	Dispersive	Electrostatic	Total energy	Dominating
Symmon	Multiplicity	(Å)	energy	energy	(kcal/mol)	interaction
A	8	5.54	-4.99	-0.83	-5.82	h-bond
В	8	5.44	-3.6	-0.45	-4.05	h-bond
С	8	7.86	-1.59	-0.29	-1.88	h-bond
D	8	6.79	-1.08	-0.04	-1.13	vdW
Е	8	8.64	-0.57	-0.09	-0.66	vdW
F	8	8.43	-0.49	-0.08	-0.57	vdW

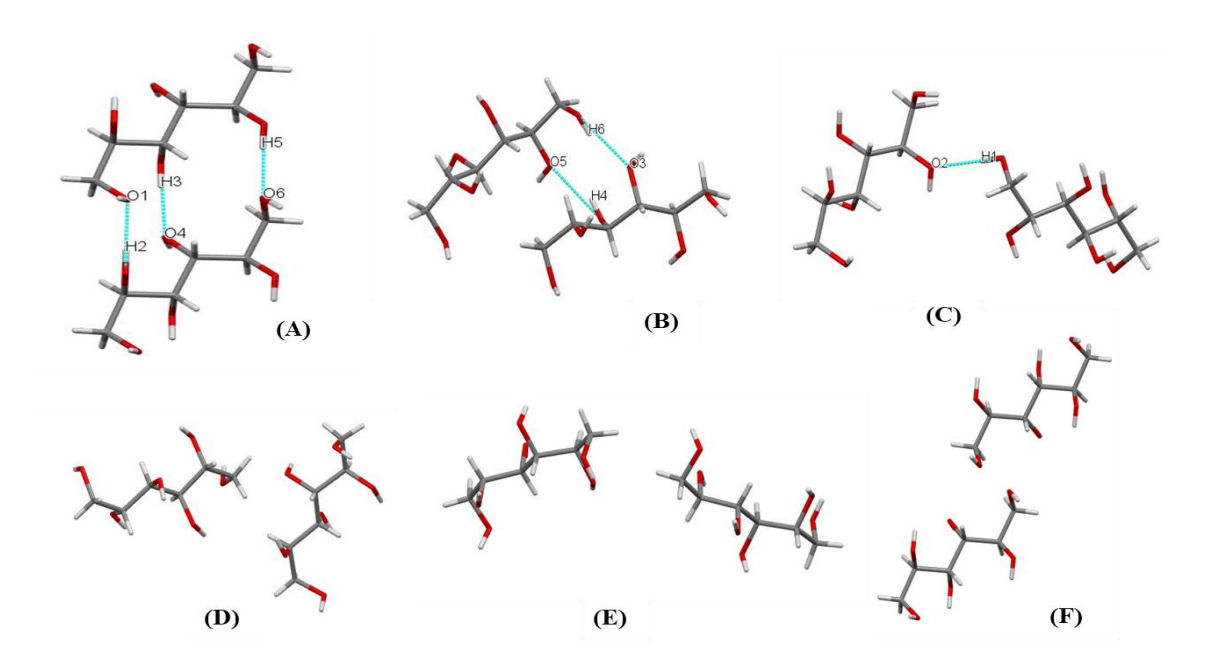


Figure 5-13. (A-F) Six strongest pairwise intrinsic synthons calculated from the bulk structure of d-mannitol

5.3.4.3 Hydrogen bond analysis

A more detailed analysis of the hydrogen bonds involved in each synthon (Table 5-10) reveals that the h-bonds in synthon A of MA are shorter, compared to all the h-bonding synthons of DM (1.685 Å and 1.848-1.992 Å, respectively). This indicates closer packing and stronger h-bonding in MA than in DM. This is further supported by the interaction strength of the synthons and the higher lattice energy of MA.

Table 5-10. Analysis of H-bond interactions involved in the synthons listed in Table 5-8 and Table 5-9, where the geometric details of donor (D) and acceptor (A) contributions have been highlighted, and their relative polarities. Single-bonded oxygen atoms have been denoted O- for clarity.

Compound	Synthons	H-bond Multiplicity	D-H···A	q _D	q _A	Qdiff	H···A/Å	D···A/Å	D-H····A/°
Mefenamic		2	O-H···O=	0.2482	-0.4077	0.6559	1.685	2.655	174.12
acid	Α	2	O-H···O=	0.2482	-0.4077	0.6559	1.685	2.655	174.12
			O_2 - H_2 ··· O_1	0.2021	-0.3399	0.5420	1.864	2.680	164.66
	A	3	O_3 - H_3 ··· O_4	0.2034	-0.3085	0.5119	1.882	2.737	5 174.12 5 174.12 0 164.66 7 168.52 5 173.40 1 154.65 0 154.57
D-mannitol			O_5 - H_5 ··· O_6	0.2038	-0.3220	0.5258	1.848	2.695	173.40
D-manintoi	В	2	O_4 - H_4 ··· O_5	0.1952	-0.3410	0.5362	1.992	2.761	168.52 173.40 154.65
_	Б	2	O_6 - H_6 ··· O_3	0.1999	-0.3419	0.5418	1.983	2.750	154.57
	С	1	O_1 - H_1 ··· O_2	0.2044	-0.3272	0.5316	1.932	2.742	166.51

5.4 Surface Properties

5.4.1 Crystal Morphology and Surface Chemistry of Mefenamic Acid

The attachment energy of the morphologically important faces is listed in Table 5-11. The resulting morphology is displayed in Figure 5-14. The prediction revealed that the morphologically important faces are {100}, {001} side face, and three capping faces {11-1}, {01-1} and {010}. These are in good agreement with previously reported faces of mefenamic acid²⁶, the largest and most dominant face is {100}. This is expected as it has the lowest attachment energy (-6.30 kcal/mol) and therefore the slowest growing face. The attachment energies of the three capping faces are larger, {01-1} and {010} being the largest (-19.98 kcal/mol and -20.20 kcal/mol, respectively), reflecting the fast growth rate of that face. The high attachment energies of the capping faces indicate that growth is favoured at these faces. This is further conveyed in the surface saturation and surface energies. The {01-1} and {010} faces have the lowest percentage of satisfied interactions (14.64% and 14.38%) and highest surface energies (135.57 mJ/mol and 129.7 mJ/mol), further confirming the fast growth rate at the capping faces.

Out of the top 6 synthons, only one contributes to the attachment energy at the $\{100\}$ face, synthon C, where π - π stacking of the "Phenyl 2" group is the dominating interaction, leaving the two methyl groups exposed at the surface. Two synthons, E and F, contribute to the $\{001\}$ face, where vdW interactions dominate. Synthon E leaves the ring and the hydroxyl group of "Phenyl 1" exposed, and synthon F leaves the ring and the methyl groups of "Phenyl 2" exposed. Synthons B, D and E contribute to the attachment energy at the $\{11\text{-}1\}$ face. The strongest interaction at this face is the π - π stacking of the "Phenyl 1", leaving the -COOH exposed at the surface, making it available for hydrogen bonding at this face. The amine group and the ring and methyl groups of "Phenyl 2" are also exposed at this surface. A, D and F all contribute to the $\{01\text{-}1\}$ and $\{010\}$ faces, indicating that hydrogen bonding is the most dominating interaction at these faces. This is visualised in the surface chemistry of the faces in Figure 5-14, where the -COOH groups are exposed. The $\{01\text{-}1\}$ has a fourth synthon, E, contributing to its attachment energy. The high attachment and surface energy, as well as the low surface saturation at this face, are reflected in its higher number of contributing extrinsic synthons.

Table 5-11. The Morphologically Important Surfaces of Mefenamic acid and their: Interplanar spacing (in Å); Attachment and slice energies (in kcal/mol); Percentage Surface Saturation (ζhkl); Percentage Surface Area; Surface energies (in mJ/m2) and the Extrinsic Synthon Contribution to Attachment and Slice Energies at each Morphologically Important Face

Crystal		%		E _{att}	$\mathbf{E_{sl}}$	%	Dispersive Surface	Electrostatic	Total Surface	Surface Attachm			Synthon Contribution to tent and Slice Energies		
Face	$\mathbf{d}_{\mathbf{hkl}}$	Surface Area	Multiplicity	(kcal/mol)	(kcal/mol)	Anisotropy Factor, ξ _{hkl}	Energy, γ (mJ/m²)	Surface Energy, γ (mJ/m²)	Energy, γ (mJ/m ²)	A	В	C	D	E	F
{100}	13.93	27.06	2	-6.30	-26.86	81.00	93.38	3.11	96.51	(E_{sl})	(E_{sl})	(Eatt)	(E_{sl})	(E_{sl})	(E_{sl})
{001}	6.37	11.74	2	-12.33	-20.83	62.82	83.31	3.07	86.37	(E_{sl})	(E_{sl})	(E_{sl})	(E_{sl})	(E _{att})	(E _{att})
{11-1}	5.87	6.62	2	-16.92	-16.23	48.94	106.52	2.72	109.23	(E_{sl})	(E _{att})	(E_{sl})	(E _{att})	(E _{att})	(E_{sl})
{01-1}	6.17	0.63	2	-19.98	-13.18	39.75	118.92	16.62	135.57	(E _{att})	(E_{sl})	(E_{sl})	(E _{att})	(E _{att})	(E _{att})
{0 1 0}	5.84	3.94	2	-20.20	-12.95	39.05	115.62	14.14	129.73	(E _{att})	(E_{sl})	(E_{sl})	(E _{att})	(E_{sl})	(E _{att})
	Average (whole crystal) Surface Energy, γ (mJ/m²)			94.81	4.09	98.90									

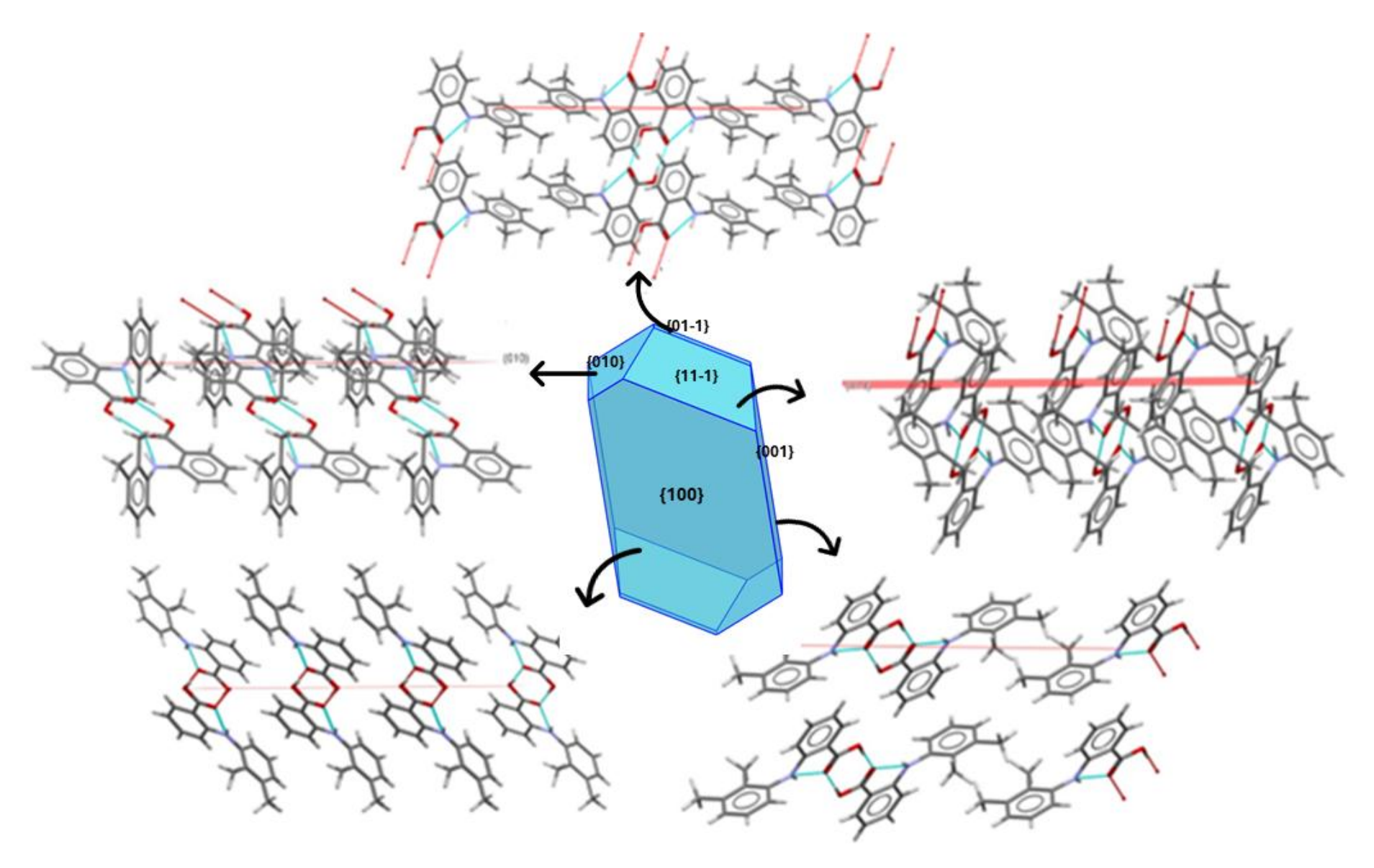


Figure 5-14. Predicted attachment energy morphology of mefenamic and the surface chemistry of each face

5.4.1.1 Mefenamic acid Solvent Interactions

The solvent effects on the crystal habit of mefenamic acid have previously been studied^{26,27,203–210}. Figure 5-15 displays morphologies of mefenamic acid crystallised from a) tetrahydrofuran (THF), b) ethanol (EtOH), c) ethyl acetate (EtOAc) and d) toluene. The solvent morphologies display a similar hexagonal prismatic shape to that predicted from the attachment energy model, but with varied aspect ratios. In all solvent morphologies, the {100} face remains the largest, verifying that it is indeed the slowest growing face, thus most morphologically important. The crystals grown from THF and EtOH exhibit more plate-like morphologies with a low aspect ratio compared to those of crystals grown from EtOAc and toluene, which yield more needle-like crystals. EtOH is a polar protic solvent; therefore, it can both donate and accept hydrogen. The {100} and {001} have no intrinsic synthons available for hydrogen bonding, so binding will occur at the polar capping faces, slowing their growth rate, and yielding more defined capping faces and crystals of low aspect ratios. THF is a moderately polar aprotic solvent, thus it can only accept hydrogens. The solvent will favour interaction at the capping faces, similarly to EtOH, inhibiting their growth. EtOH is expected to bind strongly to the capping faces than THF due to its more polar nature, producing crystals of a lower aspect ratio. Interestingly, the THF crystals display a morphology of a lower aspect ratio than that of the EtOH crystals. This may be due to THF binding to the 001 and 100 faces through dispersive interactions, slowing the growth rate at these faces as well as producing a more equant crystal, compared to EtOH. EtOH's interaction with the side face will be weaker, increasing its growth rate faster relative to that of THF crystals. However, it should be noted that the SEM images of THF and EtOH crystals are from different studies, hence the observed varied aspect ratios may be due to crystallisation parameters as well.

Crystals obtained from EtOAc display a more blade-to-needle-like morphology. Though EtOAc has two oxygens in its structure, they are weak hydrogen acceptors, with a weak dielectric constant of 6.02 and a strong dipole moment of 1.78²¹¹. Comparatively, EtOH and THF have dielectric constants and dipole moments of 7.52, 1.63 and 24.3, 1.69, respectively. The dielectric constant and the dipole moment are different measures of polarity, where the dielectric constant is the macroscopic polarizability of the solvent, and the dipole moment measures the polarity of the microscopic molecule.

Therefore, from the literature values, though the EtOAc molecule is slightly more polar than THF, its macroscopic solvent is less polar than THF, further explaining its preference to bind to the {001} face. Toluene is a nonpolar molecule, so it cannot form h-bonds; thus, it binds strongly to the {001} face, where vdW interaction dominates, reducing its growth rate, and yielding the observed long needle morphologies.

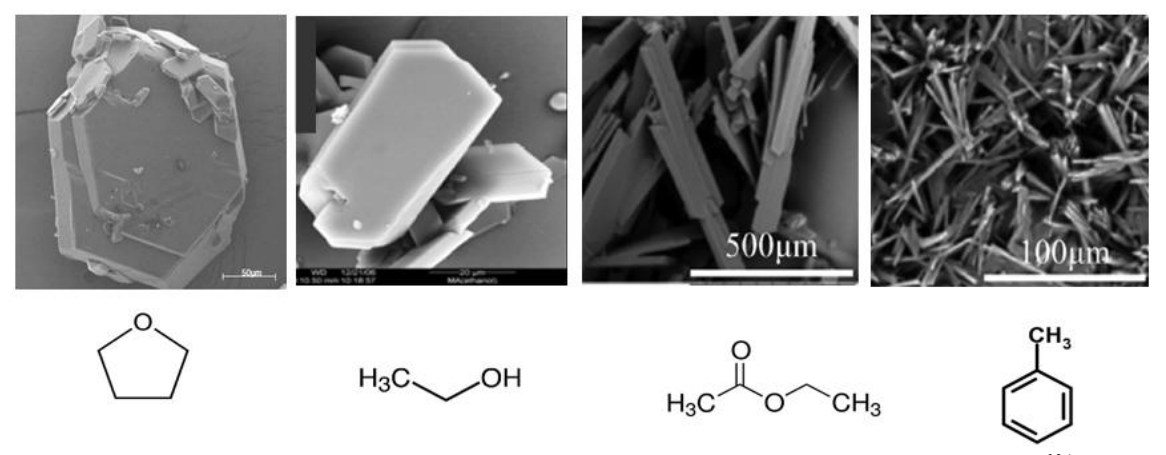


Figure 5-15. Morphology of mefenamic crystals and the solvent structures of a) tetrahydrofuran ¹³⁴, b) ethanol ¹³⁷, c) ethyl acetate ¹³⁸ and d) toluene ¹³⁸

5.4.2 Crystal Morphology and Surface Chemistry of D-mannitol

The computational prediction reveals a prismatic crystal morphology of d-mannitol with four morphologically important surfaces, {002}, {011}, {101} and {110}, visualised in Figure 5-16. The {002} is the largest surface with a percentage surface area of 14.92% and possesses two facets. This is followed by {011}, {101} and {110}, which all have four facets and percentage surface areas of 11.94%, 5.55% and 0.05% respectively. Table 5-12 lists these surfaces and their: interplanar spacing (in Å); attachment and slice energies (in kcal/mol); percentage surface saturation (ξhkl); percentage surface area; surface energies (in mj/m2), and the extrinsic synthon contribution to attachment and slice energies at each facet. Upon examination of the anisotropy factors, it can be seen that the two largest surfaces, {002} and {011}, have the highest degree of saturation, 71.21% and 67.39% respectively. The high-level saturated interactions suggest that growth at these faces will be slow due to unavailable bonding potentials. This is further reflected in their lower attachment energy values, -9.12 kcal/mol and 10.33 kcal/mol, thus the high morphological importance. The capping faces, {101} and {110}, have

lower percentage saturation of 39.68% and 28.82% respectively. The relatively saturated surfaces allow for higher bonding potentials, thus faster solute growth rates reflected in their higher attachment energies, 19.11 kcal/mol and 22.55 kcal/mol.

The synthon contribution at each surface further validates the above observation. The slowest growing face {002} is dominated by all eight C, D and E synthon interactions, whilst synthons A, B and F all contribute to the slice energy. Synthon C is dominated by a h-bond interaction. The interaction is highlighted in the dashed green box in Figure 5-16. However, the overall interactions at this surface are dominated by vdW interactions. The figure also clearly displays the slice energy contribution of synthon A.

Four B, C, D, E and F synthons contribute to the attachment energy on the {011} surface, whilst the remaining four and eight of the A synthons contribute to its slice energy. The B synthon is dominated by two h-bonds highlighted in the orange dashed box. The C synthon is again highlighted in green.

The attachment energy of the larger capping face, {101}, is attributed to contributions by all eight A and F synthons and four C, D and E synthons. As noted in Table 5-9, synthon A has the highest interaction energy of -5.82 kcal/mol and is dominated by three h-bond interactions. These are highlighted in the blue dashed box. The h-bond of the C synthon is also highlighted in green.

Similar to the {101} face, all eight A and F synthons contribute to the attachment energy of the smaller capping face, {110}. Four B, C, and D synthons also contribute to its attachment energy. Synthon B is the second strongest interaction, -4.05 kcal/mol, dominated by two h-bond interactions highlighted in orange. This face is the only face with all three h-bond dominating interactions contributing to its attachment energy, thus it is the least morphologically important surface, and as previously mentioned, most unsaturated. This is further conveyed in its low surface energy of 182.58 mJ/m2 compared to that of the {002} face, which has a surface energy of 133.39 mJ/m2.

Table 5-12. The Morphologically Important Surfaces of D-mannitol and their: Interplanar spacing (in Å); Attachment and slice energies (in kcal/mol); Percentage Surface Saturation (ξhkl); Percentage Surface Area; Surface energies (in mJ/m2) and the Extrinsic Synthon Contribution to Attachment and Slice Energies at each Morphologically Important Face

											xtrinsic Attachn	·			
Crystal Face	d _{hkl}	% Surface Area	Multiplicity	E _{att} (kcal/mol)	E _{sl} (kcal/mol)	% Anisotropy Factor, ξ _{hkl}	Dispersive Surface Energy, γ (mJ/m ²)	Electrostatic Surface Energy, γ (mJ/m²)	Total Surface Energy, γ (mJ/m²)	A	В	C	D	E	F
{002}	8.40	14.92	2	-9.12	-22.56	71.21	119.13	14.22	133.39	(E_{sl})	(E_{sl})	(E _{att})	(E _{att})	(E _{att})	(E_{sl})
{011}	7.64	11.94	4	-10.33	-21.35	67.39	122.73	14.68	137.42	(E _{sl})	(E _{sl})/ (E _{att})	(E _{sl})/ (E _{att})	$(E_{sl})/$ (E_{att})	$(E_{sl})/$ (E_{att})	$(E_{sl})/$ (E_{att})
{101}	5.26	5.55	4	-19.11	-12.57	39.68	152.19	22.80	175.02	(E _{att})	(E _{sl})	$\frac{(\mathbf{E}_{att})}{(\mathbf{E}_{sl})}$	$(E_{sl})/$ (E_{att})	$(E_{sl})/$ (E_{att})	(E _{att})
{110}	4.65	0.05	4	-22.55	-9.13	28.82	159.72	22.84	182.58	(E _{att})	$\frac{(\mathbf{E}_{att})}{(\mathbf{E}_{sl})}$	$\frac{(\mathbf{E}_{att})}{(\mathbf{E}_{sl})}$	$\frac{(\mathbf{E}_{att})}{(\mathbf{E}_{sl})}$	(E _{sl})	(E _{att})
	Average (whole crystal) Surface Energy, γ (mJ/m²)						128.27	16.36	144.63						

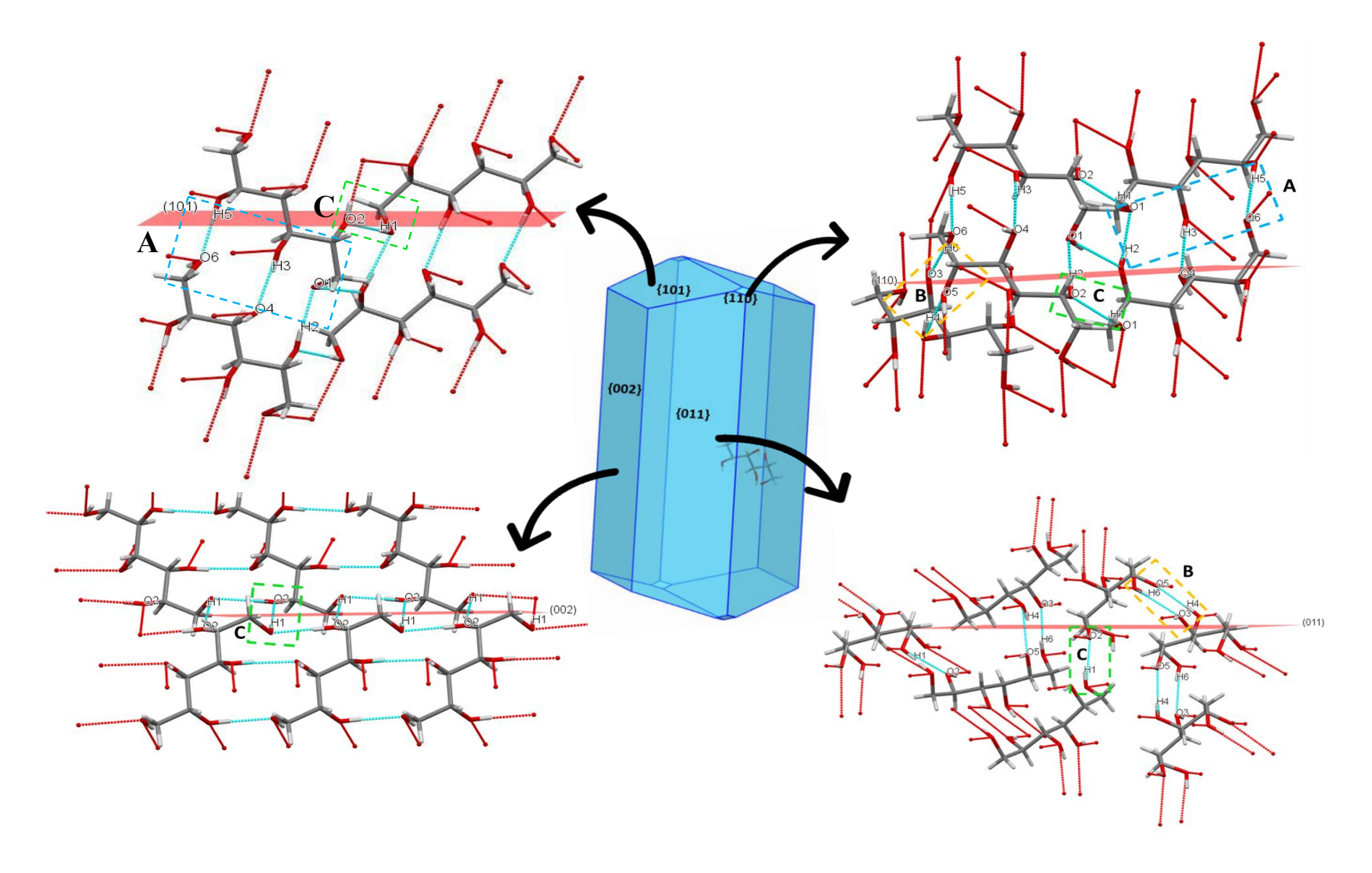


Figure 5-16. Predicted attachment energy morphology of d-mannitol and the surface chemistry of each face

5.4.2.1 D-mannitol Solvent Morphologies

The d-mannitol crystal is highly soluble in water, sparingly soluble in alcohol and essentially insoluble in other organic solvents. D-mannitol is known to have three different polymorphs, α , β and δ form²¹². The β form is the most thermodynamically stable form and the form mostly sold in the market and used in pharmaceutical drug products. The different forms have varied cell parameters; thus, they will crystallise differently. The α and β have the same orthorhombic space group P212121 and vary mainly in their h-bond network connectivity. The β form has stronger intermolecular interactions than the other forms, particularly the h-bond interactions²¹³. The δ form has the monoclinic space group P21, and a lower melting point of 155 °C than that of 166 °C of the α and β forms²¹⁴. This is described by the h-bond network only being one-dimensional, whereas three-, two- and one-dimensional h-bond networks are found in the α and β forms, resulting in weak h-bonds in δ -d-mannitol. The weaker bonds in this form are also related to its weaker stability and better solubility.

These differences highlight the importance of controlling the crystallisation process. Kaialy et al. found that the β form recrystallised in various ethanol/water ratios yields mixtures of d-mannitol polymorphs²¹⁵. Recrystallisation in 100 % ethanol yielded the α form, 95:5 (ethanol: water) yielded a mixture of the α and δ forms, 90:10 and 85:15 yielded mixtures of all three polymorphs. The most consistent way to obtain pure β form is through antisolvent precipitation. Crystallising in aqueous solutions can be difficult due to mannitol's high solubility in water; thus, it can take a very long time to precipitate out, and sometimes no crystals are yielded at all. It is a very time-sensitive method, as this method can yield crystals of all the polymorphs. Figure 5-17 provides SEM images of β -d-mannitol obtained from a) highly saturated aqueous solution²¹⁶, b) and c) an aqueous solution using acetone as the antisolvent²¹⁷. Both methods yielded rod-like morphologies matching the Habit98 prediction. Crystals from the aqueous solution display a more columnar habit and longer crystals. This is likely reflected by both the growth time during crystallisation and the high solubility in water. The highly polar surface of d-mannitol will bind strongly to the water molecules. Binding at the larger side faces slows the growth rate, producing longer rods than those found in acetone as an anti-solvent. As d-mannitol is not very soluble in acetone, crystals formed quickly.

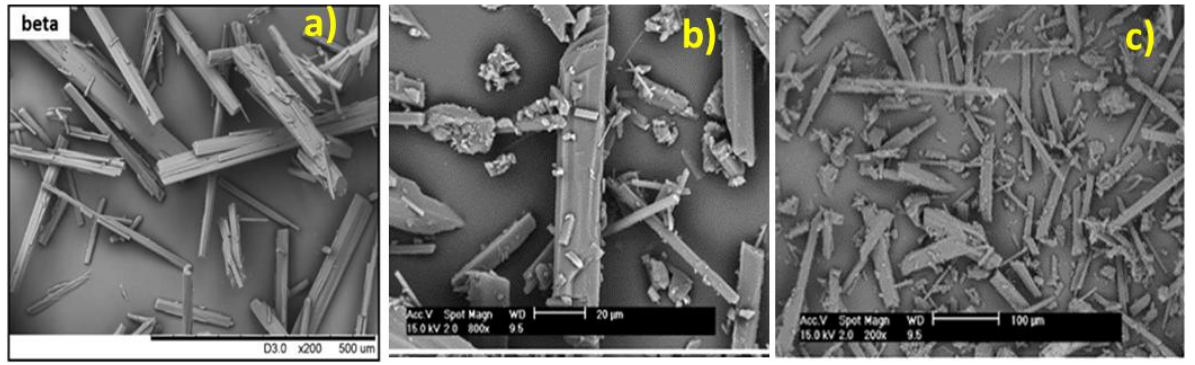


Figure 5-17. Recrystallised β-d-mannitol from a) water ²¹⁶, b) and c) antisolvent precipitation in acetone ²¹⁷

As mentioned in Chapter 4, the chosen PM6 Hamiltonian simplifies the calculations, leading to some quantitative differences compared to more computationally demanding methods like DFT. Its main advantage is efficiency, enabling quick habit predictions whilst providing a consistent and practical framework for meeting the aims of this project. Although the systems studied here show good agreement with the sublimation data found in literature and accurate habit predictions, it remains valuable to compare these results against DFT calculations. There is currently no DFT-derived lattice energies reported for MA and DM; however, Shishkina et al. used DFT to examine the relative stability of the three polymorphs of MA²¹⁸. In agreement with the semi-empirical results in this study, they reported that the h-bond in the carboxylic acid dimer was the strongest interaction in MA; however, they did not explicitly report the absolute lattice energies.

Other researchers have compared DFT with semi-empirical approaches ^{169,170}. For example, Řezáč and Hobza examined a custom dataset of 66 non-covalent complexes using both approaches ¹⁶⁹. They found that for neutral organic compounds, dominated by dispersive interactions, semi-empirical methods give results very close to DFT, with only minor differences. Thus, DFT is strongly preferred when accuracy is critical, such as in transition metal chemistry, reaction mechanism studies and electronic properties predictions. Whereas semi-empirical approaches are ideal for large-scale screening and initial geometry optimisations. The ideal workflow would include a hybrid approach using semi-empirical methods for initial screening and then refined by DFT.

5.5 API-Excipient Interactions – Prediction of cohesive/adhesive Interactions

The SystSearch simulation calculates over 10000s of interactions at each face; however, it is the minimum interaction values which are of most interest. These are the strongest interactions, thus the most stable and preferred, contributing most to the cohesive/adhesive behaviour of the compounds. In analysing slab/molecule interactions, only the top 1 minimum interactions at each facet are often examined ^{17,219–221}. However, by doing so, it is possible to miss the effect of other strong interactions. The distribution of the top 500 interactions has been examined. Table 5-13 displays the mean cohesive/adhesive interaction energies of mefenamic acid and d-mannitol. The lower subscript s and p are noted next to MA and DM, to indicate mefenamic acid/d-mannitol slab or probe, respectively.

In the top 1 and top 5 strongest interactions, the order of decreasing interaction energies is: DM_S - MA_P > MA_S - MA_P > DM_S - DM_P > MA_S - DM_P . Whereas from the top 10 to top 500 interactions, the order of decreasing interaction energies is: MA_S - MA_P > DM_S - DM_P > DM_S - DM_P > MA_S - DM_P . Thus, the current analysis examines the mean top 50 cohesive and adhesive interactions. These were determined to be a fair midpoint reflecting the influence of both the highest and lowest interaction energies.

Table 5-13. The top 500 mean cohesive/adhesive interaction energies of mefenamic acid and d-mannitol

Interaction Ranking	MA _S -MA _P Mean Interaction Energies	MA _S -DM _P Mean Interaction Energies	DM _S -DM _P Mean Interaction Energies	DM _S -MA _P Mean Interaction Energies
Top 1	-11.03	-6.73	-8.21	-11.23
Top 5	-10.39	-6.33	-7.80	-10.51
Top 10	-10.07	-6.15	-7.63	-9.93
Top 50	-9.14	-5.55	-6.70	-8.74
Top 100	-8.68	-5.26	-6.32	-8.26
Top 500	-7.52	-4.63	-5.36	-7.10
Standard deviation	1.28	0.77	1.07	1.54

The cohesive/adhesive energies on each facet of mefenamic acid and d-mannitol, and their respective surface weighted interactions, averaged over the whole crystal, are displayed in Figure 5-18 a) and b), respectively. As mentioned above, the interaction energies decrease in the order MA_S-MA_P > DM_S-MA_P > DM_S-DM_P > MA_S-DM_P. MA_S-MA_P cohesion strongly dominates over MA_S-DM_P adhesion with interaction energies of -9.14 kcal/mol and -5.55 kcal/mol, respectively. The capping faces of the MA crystal exhibit the strongest binding energies. This is consistent with the Habit98 prediction, where they have the highest attachment and surface energies, lower surface saturation, thus more available for binding. In the SystSearch prediction, the strongest capping face {11-1}, when weighted with the overall surface area. The favoured MA_S-MA_P cohesion predicts potential segregation in a powder blend. Its strong interaction energy suggests it prefers to bind to itself above the other pairs.

In the d-mannitol system, the binding values at each face are more homogeneous than mefenamic acid, with lower standard deviation across the whole crystal. DM_S-DM_P cohesion is less favoured, -6.70 kcal/mol and DM_S-MA_P adhesion dominates, -8.74 kcal/mol. In DM_S-DM_P cohesion, the {002} is strongest, whilst the {011} dominates in DM_S-MA_P adhesion.

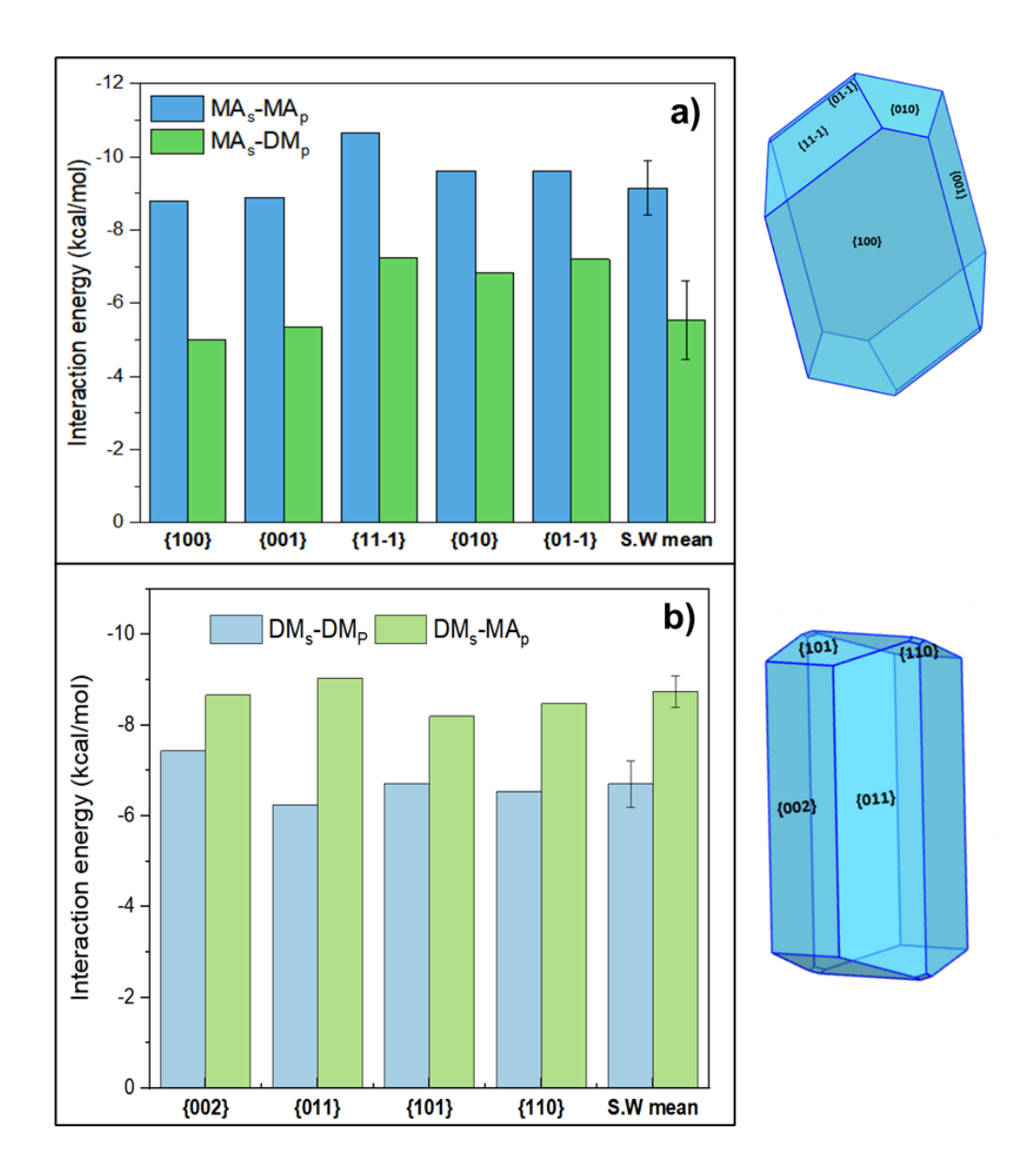


Figure 5-18. The cohesive/adhesive energies on each facet of a) mefenamic acid and b) d-mannitol, and their respective surface weighted interactions, averaged over the whole crystal

The nature of the two crystals results in different adhesion energies, depending on which one is the slab; DM_S-MA_P is 3.15 kcal/mol stronger than MA_S-DM_P. This is likely due to the d-mannitol's extensive h-bond network. As explained through the Habit98 prediction, d-mannitol has h-bonding potential on all its facets. It also has 14 facets in total, whilst mefenamic acid has 10, with only the capping faces available for h-bonding. Thus, mefenamic acid has a higher affinity to bind to the faces of d-mannitol, and d-mannitol has a lower affinity to bind to the faces of mefenamic acid, due to fewer h-bonding sites on the MA crystal. This suggests that in a formulation with more d-mannitol, good uniformity will be

present. However, in a formulation with excess mefenamic acid, a weak adhesive blend is observed, giving rise to potential segregation as mefenamic acid will naturally gravitate to itself.

Table 5-14 displays the interaction energies at each facet of mefenamic acid, as well as a breakdown of the interaction types contributing to them. The cohesion and adhesion energies are broken down into dispersive and polar energies in Figure 5-19 for a more detailed insight into which mechanisms they are driven by. The prediction reveals that the high cohesion of MA is dominated by strong vdW interactions, 93.53 %. The polar interactions contribute 6.47 % to the surface weighted mean interaction energy, where electrostatic interactions are 4.79 % and h-bond interactions are 1.68 %. Consistent with the Habit98 prediction, the capping faces have an increased polar interaction due to h-bond interactions from the -COO synthon.

The MA adhesion is also dominated by vdW interactions, 91.08 %, and polar interactions contribute 8.92 %. The contribution of h-bond and electrostatic interactions is more even in MA_S-DM_P than in MA_S-MA_P, 4.92 % and 4.00 % respectively. The contribution of polar and dispersive interactions on the capping faces is closer in value than what is seen in MA_S-MA_P. Although both systems are dominated by vdW interactions, these are decreased by -3.49 kcal/mol in MA_S-DM_P. The MA adhesion also has stronger h-bond interactions compared to the MA cohesion, reflecting the polar nature of the DM molecule.

Table 5-14. The interaction energies at each facet of mefenamic acid, and the total surface weighted interactions, averaged over the whole crystal

				MA _S -N	IA _P			MAs	-DM _P	
Face	Multiplicity	% Surface area	Intera	Interaction Energies, kcal/mol			Interaction Energies, kcal/mol			
			vdW	h-bond	elect.	total	vdW	h-bond	elect.	total
{100}	2	27.06	-8.43	0.00	-0.36	-8.80	-5.01	0.00	-0.01	-5.02
{001}	2	11.74	-8.55	0.00	-0.35	-8.90	-4.98	-0.02	-0.33	-5.34
{11-1}	2	6.62	-10.30	-0.01	-0.34	-10.65	-6.28	-0.58	-0.38	-7.24
{010}	2	3.94	-6.75	-1.62	-1.25	-9.62	-3.87	-2.03	-0.94	-6.83
{01-1}	2	0.63	-6.48	-1.79	-1.34	-9.60	-3.44	-2.50	-1.27	-7.21
Mean interaction energy weighted with										
the %	the % surface area of individual crystal		-8.55	-0.15	-0.44	-9.14	-5.06	-0.27	-0.22	-5.56
	surfaces									

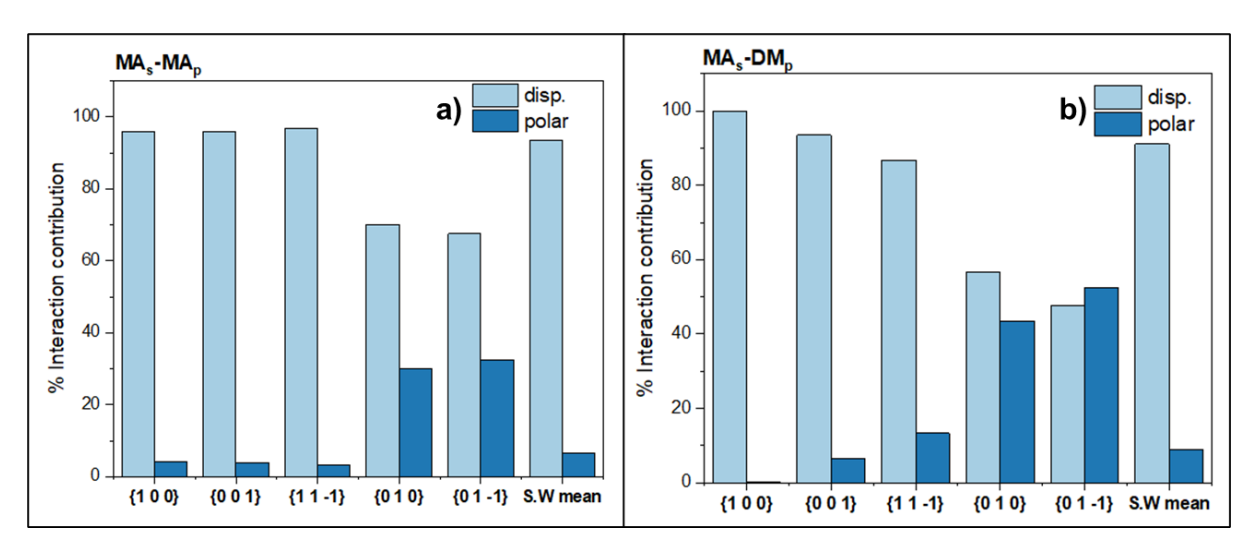


Figure 5-19. The cohesion and adhesion energies of mefenamic acid are broken down into dispersive and polar energies, at each facet and the total surface weighted mean

Table 5-15 displays the interaction energies at each facet of d-mannitol and a breakdown of the interaction types contributing to them. The cohesion and adhesion energies are broken down into dispersive and polar energies in Figure 5-20.

The DM cohesion prediction reveals vdW contributing 58.55 %, h-bond 27.38 % and electrostatic 14.07 %. Dispersive and polar interactions have close contributions on each face apart from the {011} face, 67.60 % and 32.40 % respectively. Polar interactions slightly dominate on the {101} capping face due to stronger h-bond interactions. The DM adhesion has a higher dispersive dominance of 75.29 % and polar contribution of 24.71 % of which 16.71 % is h-bond interactions and 8.01 % electrostatic interactions. The dispersive interactions dominate on all faces and decrease at the capping faces. The interaction energies on the {101} and {110} faces are 64.07 % and 65.85 % dispersive and 35.93 % and 34.15 % polar, respectively.

Table 5-15. The interaction energies at each facet of d-mannitol, and the total surface weighted interactions, averaged over the whole crystal

Face	Multiplicity	% Surface area	DM _S -DM _P Interaction Energies, kcal/mol				${ m DM_S ext{-}MA_P}$ Interaction Energies, kcal/mol			
			vdW	h-bond	elect.	total	vdW	h-bond	elect.	total
{002}	2	14.92	-4.02	-2.18	-1.23	-7.43	-7.22	-0.77	-0.68	-8.67
{011}	4	11.94	-4.22	-1.34	-0.68	-6.24	-6.79	-1.65	-0.59	-9.03
{101}	4	5.55	-3.17	-2.44	-1.11	-6.71	-5.25	-1.99	-0.96	-8.20
{110}	4	0.05	-3.63	-2.08	-0.82	-6.53	-5.58	-2.10	-0.79	-8.48
Mea	Mean interaction energy weighted with									
the ^c	the % surface area of individual crystal		-3.92	-1.83	-0.94	-6.70	-6.58	-1.46	-0.70	-8.74
	surfaces									

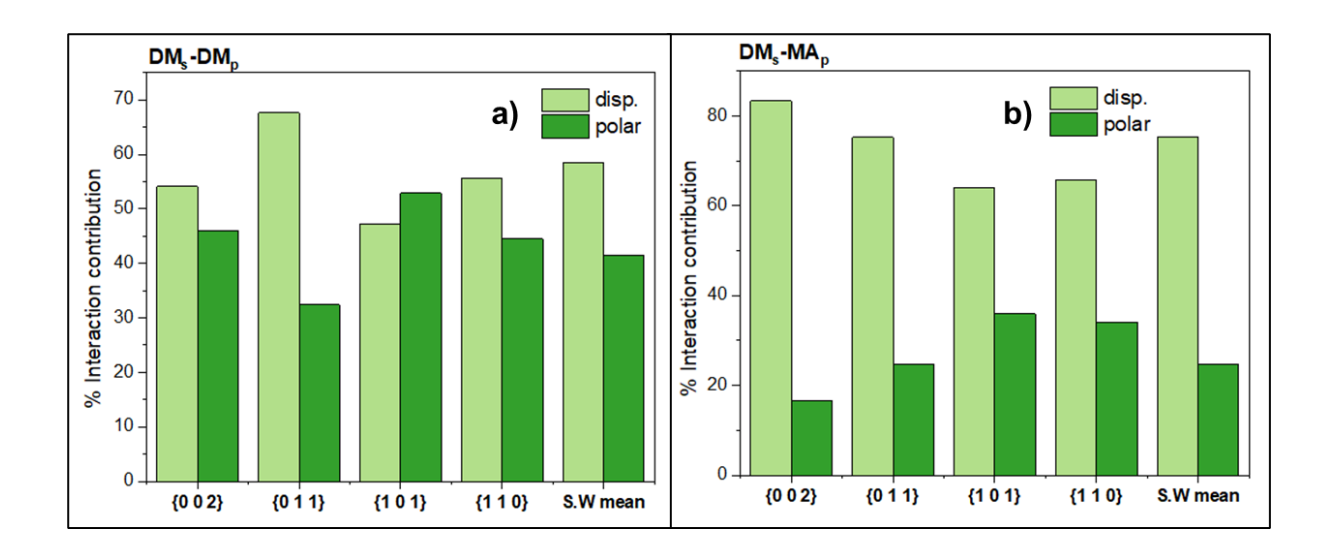


Figure 5-20. The cohesion and adhesion energies of d-mannitol are broken down into dispersive and polar energies, at each facet and the total surface weighted mean

The Systsearch predictions of all four systems reveal a trend of higher dispersive interactions driving the strength of cohesion and adhesion. DM's stronger and more evenly distributed adhesion interactions allow it to be a good excipient, providing more homogeneity in formulation. It can therefore be suggested that a good excipient should possess moderate cohesive interactions to avoid segregation, yet strong adhesive interactions for adequate binding to API's, promoting homogenous blends. The study highlights the importance of API-excipient compatibility and ratio, and the need for such investigations in the early stages of drug formulation.

5.6 Prediction of Mechanical Properties

The CDC-Particle application within the CCDC Mercury programme allows for quick identification of potential slip planes. It scans crystal structures for planes with the least obstruction for translational slipping. These planes are assigned a value of interdigitation (-), or separation (+) and analyse if the plane is bridged by an h-bond, thus creating broken h-bonds. Surface analysis on each plane gives a value for rugosity. The ideal slip plane is topologically flat, with no broken h-bonds, has low attachment and surface energy and a high anisotropy factor. Using the Multi-Attribute Decision Making (MADM), the plausible slip planes have been ranked in order of which satisfies the 'ideal' slip criteria the most. Calculations for AHP and TOPSIS were followed using the methods and equations described in Chapter 4.3.3. Weighting was assigned to each attribute based on the importance of one over the other for the ideal slip-plane characteristics. The attributes used in the decision matrix were h-bond breaking, interdigitation, rugosity and surface energy. The qualitative attribute of h-bond breaking was converted into numerical values, 0 for no and 1 for yes.

5.6.1 Mefenamic acid - Slip Plane Characterisation

The values of each attribute are listed in Table 5-16. These are normalised in Table 5-17 so that they can be assessed in the same dimension.

Table 5-16. Values of attributes in the decision matrix, hydrogen breaking, interdigitation, rugosity and surface energy

Attribute	h-bond breaking	Intendicitation (Å)	Dugasity (Å)	Symfo on Emanovy (ma I/ma²)
Face	n-bond breaking	interdigitation (A)	Rugosity (A)	Surface Energy (mJ/m ²)
{100}	0	1.30	1.74	96.51
{001}	0	0.68	1.33	86.37
{01-1}	1.00	1.06	1.37	135.57
{010}	1.00	0.90	1.33	129.73

Table 5-17. Normalised values of each attribute in the decision matrix

Attribute	h hand huaalsina	Intendicitation	Dugasity (Å)	Symfo on Emanay (m. 1/m.2)
Face	h-bond breaking	Interdigitation	Rugosity (A)	Surface Energy (mJ/m ²)
{100}	0.00	0.64	0.60	0.42
{001}	0.00	0.34	0.46	0.38
{01-1}	0.71	0.52	0.47	0.59
{010}	0.71	0.45	0.46	0.57

The weighted normalised values and positive and negative Euclidean distances are listed in Table 5-18. The optimum value is the shortest positive Euclidean distance.

Table 5-18. Weighted normalised values and Euclidean distance from ideal best Si+ and ideal worst Si-. The ideal value is the lowest value of each attribute.

Attribute	h hand huaalsina	Intendicitation	Dugasity (Å)	Symfo on Emanoy (m. I/m.2)	Si+	Si-
Face	h-bond breaking	Interdigitation	Rugosity (Å)	Surface Energy (mJ/m ²)	317	51-
{100}	0.000	0.180	0.102	0.030	0.089	0.340
{001}	0.000	0.094	0.078	0.027	0.000	0.351
{01-1}	0.339	0.147	0.080	0.042	0.344	0.040
{010}	0.339	0.125	0.078	0.040	0.341	0.060

The final ranking reveals the {001} being the most ideal slip-plane of mefenamic acid with 100 % followed by the {100} with 79.19 %. The capping faces {010} and {01-1} satisfy the ideal slip-plane the least, with 15.05 % and 10.35 % respectively.

Table 5-19. Final Slip-Plane Ranking of Mefenamic acid

Face	% Ideal	Rank
{001}	100.00	1
{100}	79.19	2
{010}	15.05	3
{01-1}	10.35	4

The potential slip planes are listed in Table 5-19 in the ranking order deduced by the MADM calculations. It should be noted that though the slip-plane search in Mercury predicted the morphologically important faces, they are not necessarily the materials' active slip planes. The interplanar spacing, attachment and slice energies and percentage surface satisfaction are also listed in the table. Out of the four planes listed, {010} and {01-1} involve the breaking of h-bond synthons and {001} and {100} do not. The {001} face ranked the highest, has the lowest rugosity (1.88 Å) and interdigitation (-0.68 Å) and surface energy (89.37 mJ/m²). The {100} face has the highest interplanar spacing (13.93), slice energy (-26.86 kcal/mol) and highest surface saturation (81 %); however, it is the most topologically rough surface with a rugosity of 1.33 Å and interdigitation of -1.30 Å, both highly weighted attributes in the MADM calculations. The {100} and {001} planes are depicted in Figure 5-

21, where the difference in rugosity and interdigitation of the {100} face is clearly seen. The rough topology of this face makes it less likely to slip.

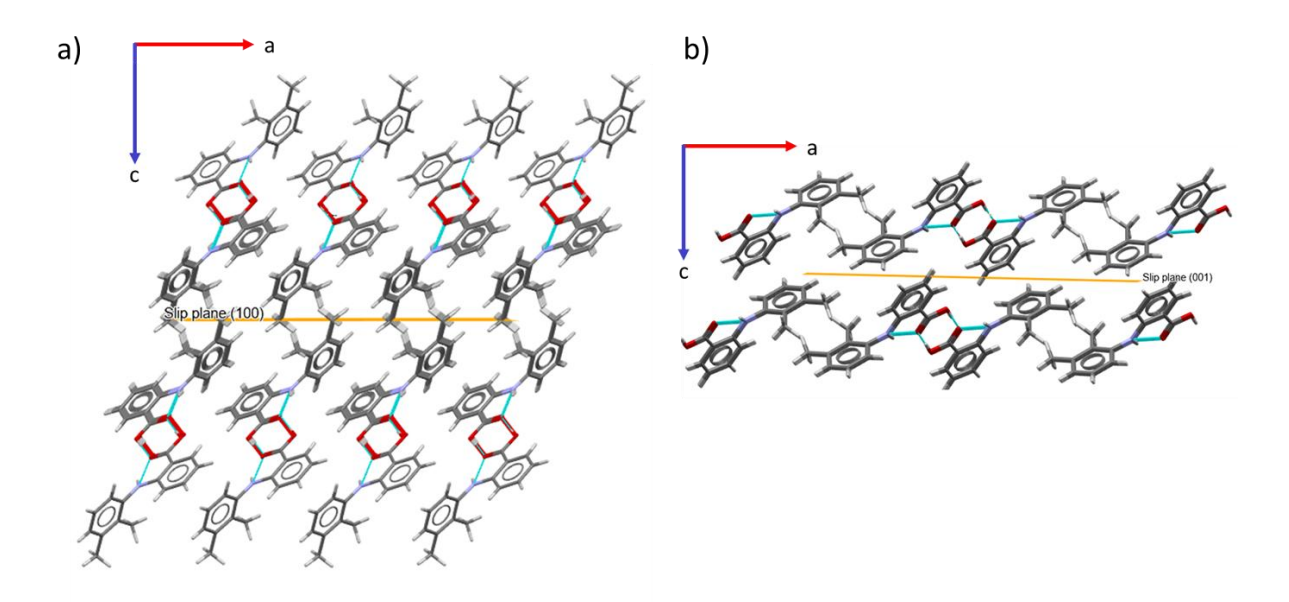


Figure 5-21. Mefenamic acid packing of the potential slip planes of a) {100} and b) {001} viewed along the b-axis

Both planes are corrugated, but {001} will be the least resistant to slip as there is little interdigitation at the interface. Whereas the slip in {100} is obstructed due to the clashing of the methyl groups. As for {010} and {01-1} faces, possessing h-bond breaking synthons, having the lowest slice energies, percentage satisfaction and highest surface energies, make them unideal candidates for slip.

Table 5-20. Analysis of the Key Potential Slip-Planes of Mefenamic acid detailing Surface Plane Satisfaction, Rugosity, Surface Energy, Degree of Interdigitation and Hydrogen Bond Breaking

Face	d_{hkl}	E _{att} (kcal/mol)	E _{sl} (kcal/mol)	% surface satisfaction	Rugosity (Å)	Surface Energy, γ (mJ/m ²)	Interdigitation (Å)	h-bond breaking	Rank
{001}	6.37	-12.33	-20.83	62.82	1.33	86.37	-0.68	no	1
{100}	13.93	-6.30	-26.86	81.00	1.74	96.51	-1.30	no	2
{010}	5.84	-20.20	-12.95	39.05	1.33	129.73	-0.90	yes	3
{01-1}	6.17	-19.98	-13.18	39.75	1.37	135.57	-1.06	yes	4

5.6.2 Mefenamic acid - Slip Direction and Slip System

The primitive triclinic nature of mefenamic acid means that the shortest Burgers vector in <010>, 6.811 Å, thus a geometrical magnitude (b^2) of 46.39 Å². This is the preferred direction of displacement and

will have the lowest dislocation energy. Longer Burgers vectors would require higher dislocation energies.

The strongest intermolecular interactions, their direction, and their contribution to either the slice or attachment energy are presented in Table 5-21. Synthon A contributes to the slice energy of both the {100} and {001} faces, giving them both strong h-bonded in-plane interactions, which is ideal for slip planes. This synthon is also in the same direction as the Burgers vector <010>, lying within the likely slip-plane {001}, satisfying the Weiss zone law for an active slip-system, indicating plastic deformation. However, the known poor powder properties and plasticity of mefenamic acid would suggest otherwise^{26,27,203,222}. Experimental results reported in Chapter 6 explore the mechanical properties of mefenamic acid further. This suggests that mefenamic acid is more likely to deform from either cleavage or rough fracture. As the strongest synthon, Synthon A, lies within the most likely slip plane, enabling cleavage-based fracture of mefenamic acid. Thus, the modelling predicts that mefenamic acid is brittle and deforms by cleavage fracture. The prediction coincides with what is known about mefenamic acid in industry and literature. The prediction coincides with the compound's known brittle nature and poor processing and compaction.

Table 5-21. The Nature of the Three Strongest Intermolecular Interactions of Mefenamic acid, their Direction, and their Contribution towards Potential Slip Plane (hkl) Surfaces

Synthon	Interaction Type	M	Distance (Å)	Synthon Strength (kcal/mol)	Synthon direction <uvw></uvw>	{100}	{001}	{01-1}	{010}
A	h-bond	2	9.08	-7.94	<010>	E_{sl}	E_{sl}	E_{att}	E_{att}
В	$\pi - \pi$	2	6.55	-3.88	<000>	E_{sl}	E_{sl}	E_{sl}	E_{sl}
С	$\pi - \pi$	2	8.07	-3.29	<100>	E_{att}	E_{sl}	E_{sl}	E_{sl}

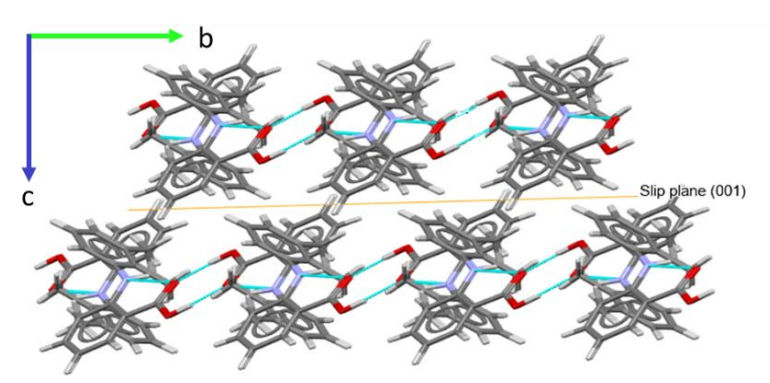


Figure 5-22. Intermolecular packing of mefenamic acid viewed along the a-axis, where h-bonding along the [010] direction can be seen

5.6.3 D-mannitol - Slip Plane Characterisation

The values of each attribute in the decision matrix for d-mannitol and its normalised values are listed in Table 5-22 and Table 5-23, respectively. The weighted normalised values and Euclidean distance are listed in Table 5-25.

Table 5-22. Values of attributes in the decision matrix, hydrogen breaking, interdigitation, rugosity and surface energy

Attribute	h-bond breaking	Interdigitation (Å)	Pugosity (Å)	Surface Energy (mJ/m ²)	
Face	ii-boild breaking	interdigitation (A)	Rugosity (A)	Surface Energy (mj/m ⁻)	
{002}	1.00	1.66	1.44	133.39	
{011}	1.00	2.45	1.31	137.42	
{101}	1.00	2.98	1.39	175.02	
{110}	1.00	3.03	1.48	182.58	

Table 5-23. Normalised values of each attribute in the decision matrix

Attribute	h hand huaalsina	Intendicitation	Duggaity (Å)	Symfo on Emanory (m. I/m.2)	
Face	h-bond breaking	Interdigitation	Rugosity (Å)	Surface Energy (mJ/m ²)	
{002}	0.500	0.321	0.512	0.420	
{011}	0.500	0.473	0.466	0.433	
{101}	0.500	0.575	0.494	0.552	
{110}	0.500	0.585	0.526	0.576	

Table 5-24. Weighted normalised values and Euclidean distance from ideal best Si+ and ideal worst Si-. The ideal value is the lowest value of each attribute

Attribute Face	h-bond breaking	Interdigitation	Rugosity (Å)	Surface Energy (mJ/m ²)	Si+	Si-
{002}	0.240	0.090	0.087	0.029	0.008	0.075
{011}	0.240	0.132	0.079	0.030	0.043	0.034
{101}	0.240	0.161	0.084	0.039	0.072	0.006
{110}	0.240	0.164	0.089	0.040	0.076	0.000

The potential slip-plane {002} satisfied the ideal slip-plane with 90.51 % and is therefore the most likely slip-plane of d-mannitol. It is followed by {011} with 44.66 % and {101} with 8.03 %. The {110} didn't satisfy the ideal slip-plane at all, with 0.00 %.

Table 5-25. Final Slip-Plane Ranking of D-mannitol

Face	% Ideal	Rank
{002}	90.51	1
{011}	44.66	2
{101}	8.03	3

{110}	0.00	4

Table 5-26 lists potential slip-planes of d-mannitol in the MADM ranked order. All faces of d-mannitol include h-bond breaking. D-mannitol has an extensive 3D h-bond network dimensionality, such that cleavage at any face will result in breaking of h-bonds. The top-ranked face {002} has the highest interplanar spacing, 8.40, the highest slice energy, -22.56 kcal/mol, the highest percentage surface satisfaction, 71.21 % and the lowest surface energy, 133.39 (mJ/m²). It is not the flattest face, having a rugosity value of 1.44 Å; however, it does have the lowest interdigitation value of -1.66 Å, meaning interlocking is less likely to occur at this plane. The smoothest surface is the {011} face, and it has a rugosity of 1.31 Å; however, it ranks below {002} in all the other properties.

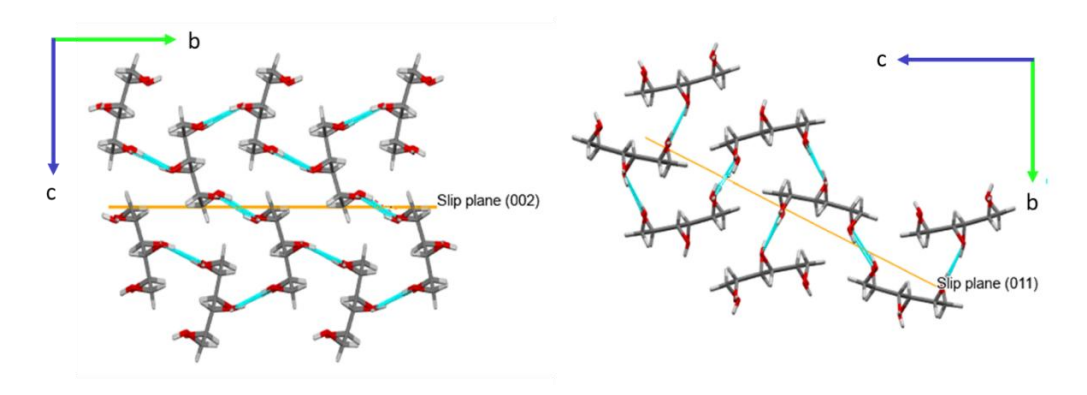


Figure 5-23. Packing of d-mannitol's most likely slip-planes a) {002} and {011} viewed along the a-axis

Table 5-26. Analysis of the Key Potential Slip-Planes of D-mannitol detailing Surface Plane Satisfaction, Rugosity, Surface Energy, Degree of Interdigitation and Hydrogen Bond Breaking

Face	d_{hkl}	E _{att} (kcal/mol)	E _{sl} (kcal/mol)	% surface satisfaction	Rugosity (Å)	Surface Energy, y (mJ/m2)	Interdigitation (Å)	h-bond breaking	Rank
{002}	8.40	-9.12	-22.56	71.21	1.44	133.39	-1.66	yes	1
{011}	7.64	-10.33	-21.35	67.39	1.31	137.42	-2.45	yes	2
{101}	5.26	-19.11	-12.57	39.68	1.39	175.02	-2.98	yes	3
{110}	4.65	-22.55	-9.13	28.82	1.48	182.58	-3.03	yes	4

5.6.4 D-mannitol - Slip Direction and Slip System

D-mannitol crystallises in the primitive orthorhombic crystal system; therefore, the shortest translational vector is <100>, 5.538 Å is the Burger vector, with a geometrical magnitude (b^2) of 30.67 Å². The Burgers vector does lie on the {002} slip plane, creating an active slip system, predicting plastic deformation. Examining the three strongest synthons of d-mannitol, the strongest synthon, Synthon A, lies on the slip-planes {002} and {011}, contributing to their slice energies. The next strongest synthon, Synthon B, also lies on {002} and {011}, contributing to their slice energies and the attachment energy of {011}. The direction of Synthon A, <100>, lying on the {002} slip-plane predicts potential cleavage fracture as well as the possibility of plastic deformation due to the active slip system.

Table 5-27. The Nature of the Three Strongest Intermolecular Interactions of D-mannitol, their Direction, and their Contribution towards Potential Slip Plane (hkl) Surfaces

Synthon	Interaction Type	M	Distance (Å)	Synthon Strength (kcal/mol)	Synthon direction <uvw></uvw>	{002}	{011}	{101}	{110}
A	h-bond	8	9.08	-5.82	<100>	E_{sl}	E_{sl}	E_{att}	E_{att}
В	h-bond	8	6.55	-4.05	<100>	E_{sl}	E_{sl} / E_{att}	E_{sl}	$E_{sl}/$ E_{att}
С	h-bond	8	8.07	-1.88	<011>	E_{att}	E_{sl} / E_{att}	E_{sl} / E_{att}	$E_{sl}/$ E_{att}

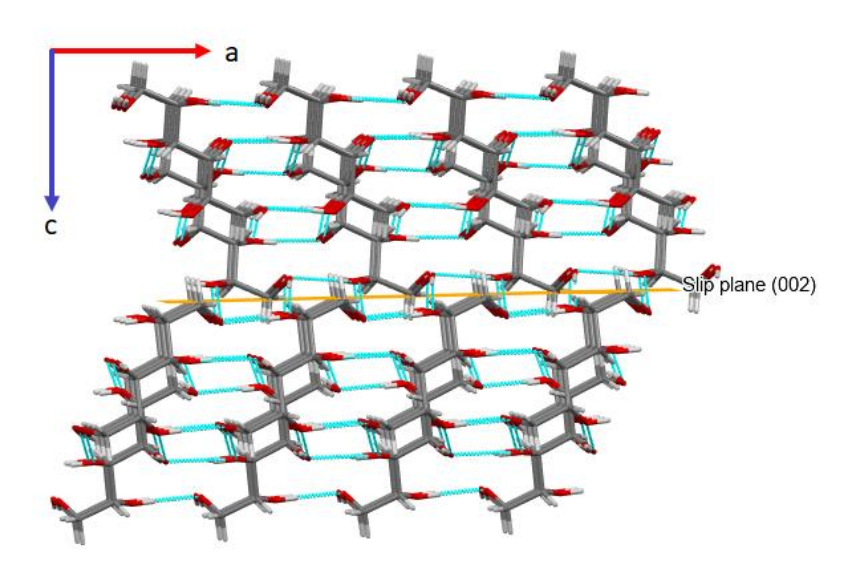


Figure 5-24. Intermolecular packing of d-mannitol viewed along the b-axis, where h-bonding along the [100] direction can be seen

Indeed, like most organic crystalline materials, DM is primarily classified as brittle and not dominated by plastic deformation¹⁶⁴. However, unlike MA, DM exhibits good processability and compactability as widely documented in pharmaceutical literature²²³. This suggests some plastic deformation does occur, driven by its intermolecular interactions.

Its extensive h-bond network enables some level of molecular rearrangement during stress, facilitating plastic deformation. As these molecules slightly shift themselves to fill voids, they create a denser structure, enhancing compression and compactability. The breaking and reforming of h-bonds allows for deformation without fracture, increasing cohesion between molecules and particles. This, in turn, allows DM to maintain its new compressed shape, enhancing its overall mechanical performance.

5.7 Conclusions

This chapter has explored the intricate molecular and solid-state interactions between mefenamic acid and d-mannitol. The comprehensive molecular modelling and analysis have allowed for accurate prediction of their lattice energies, morphologies, and surface interactions. The cohesive and adhesive interactions have been examined and broken down, and the compounds' mechanical deformation behaviour has been predicted.

The Momany force field successfully predicted the lattice energies of mefenamic acid and d-mannitol. Both lattices are dominated by dispersive interactions at varied percentages, with DM naturally possessing a larger electrostatic contribution. The strong h-bonding in the carboxylic acid functional group, coupled with its dispersive energy, contributes to 35 % of its lattice energy. In the DM compound, the six hydroxyl groups contributed 65.86 % of its lattice energy, the strongest in both electrostatic and dispersive energy relative to the rest of the compound. This initial breakdown analysis of the lattice energy of the compounds foreshadowed the importance of electrostatic interactions, specifically h-bonds, in the anisotropy of their crystal habit and surface interactions.

The top 6 intrinsic synthons of both MA and DM were investigated. It was found that indeed, within the MA compound, the carboxylic dimer was the strongest synthon with a total energy of -7.94 kcal/mol, and the h-bond was the dominating interaction. It is the only synthon that contains h-bonding in MA.

The strongest intrinsic synthon in DM contains three h-bonds (-5.82 kcal/mol), the second strongest two h-bonds (-4.05 kcal/mol) and the third strongest one-bond (-1.88 kcal/mol). The stronger h-bonding in the MA synthon was explained through a detailed analysis of the h-bonding synthons in both MA and DM. The analysis revealed that the h-bonds in MA were shorter than all the DM synthons, thus stronger.

Successful habit predictions of the MA and DM crystals were achieved through attachment energy calculations, revealing which synthons dominate at each facet. The synthon analysis of mefenamic acid explained its often need-like habit and suggested how it would interact with various solvents. The exposed carboxylic acid groups on the capping faces reveal that they will bind strongly in polar solvents through hydrogen bonding. This would slow down the growth rate at these faces, giving morphologies of lower aspect ratios. From the analysis, it can be explained why mefenamic acid causes many difficulties in processing, and it has a tendency to be very sticky. The crystallisation of DM is often performed using an antisolvent due to its high solubility in water, and can easily form very large rods not beneficial for processing. The results demonstrate how controlling the crystallisation process can change the aspect ratio of crystals, thus attaining desired crystal morphologies for quality drug products. The cohesive and adhesive interactions between MA and DM gave deep insight into their roles as API and excipient. MA was found to exhibit stronger cohesion forces when interacting with itself, whilst DM extensive h-bond network that drives its adhesive interactions. MA's dominance of vdW forces highlights its tendency to agglomerate, which can lead to segregation in formulations. Whereas DM's extensive h-bonding indicates potential for improved formulation homogeneity when used as an

The investigation of the mechanical properties of the two compounds was correlated to their known powder characteristics. Both compounds are characterised as brittle; however, DM's superior processability and compaction are attributed to the presence of some plastic deformation governed by its h-bond network and density. The importance of intermolecular interaction, crystal packing and slip-

excipient. The insights gained from this analysis provide an essential foundation for early-stage research

into API-excipient compatibility and the use of molecular modelling to achieve this.

availability in determining deformation is highlighted in the analysis. Such analyses are all valuable in providing an understanding of the processing and compaction behaviour of pharmaceutical ingredients.

The findings in this chapter emphasise the importance of the use of molecular modelling in pharmaceutical science. Researchers and formulators can anticipate and tailor the behaviour of drug substance ingredients for enhanced therapeutic efficacy.

CHAPTER SIX

Influence of Surface, Solid-State and Bulk Powder Properties on Compressibility

This chapter will present and discuss the results found from characterising the solid state, stability, and bulk powder properties, and how they impact compaction.

6 Influence of Surface, Solid-State and Bulk Powder Properties on Compactibility

6.1 Solid-State and Stability Characterisation

The powders used in this study were of as-received material from the manufacturers. Before any powder analysis, it is important to characterise the solid-state and stability of the powders, ensuring analysis is being conducted on the right polymorphs.

6.1.1 Determination of Solid-State

Mefenamic acid and d-mannitol both exist in different polymorphic forms. Mefenamic acid (MA) has three known forms, Form I, II and III, Form I being the stable one used in drug manufacture^{203–207}. D-mannitol (D-M) can exist in four forms, α , β , δ and a hemihydrate form^{166,224,225}. The β polymorph is the most stable form commonly used in pharmaceuticals.

Figure 6-1 a) and b) displays the PXRD and DSC data, respectively MA. Both results indicate that the used sample of MA is Form I. The PXRD analysis is in good agreement with the CSD reference pattern and results previously reported in literature ¹⁶⁵, showing characteristic peaks at 2θ values of 6.36°, 12.70°, 16.88°, 21.42° and 26.24°.

The DSC curve of mefenamic acid displays two endothermic peaks, one at 193.17 °C and another at 228.73 °C. The two peaks display the transition temperature from Form I to Form II and the melting of Form II, respectively^{207,226}. Studies have shown that the first endotherm of Form I can vary between 167-217 °C^{203–207}. This is usually attributed to the heating rate used in the DSC²⁰⁷. Panchagnula et al. studied the solid-state properties of commercial batches of MA from various manufacturers²⁰⁵. The DSC heating rate was kept constant, and variations of the first endotherm were still observed. Researchers reasoned that the difference was due to varied particle properties in the batches, such as particle size distribution and morphology.

The DSC curve reveals the enantiotropic behaviour of MA, thus the polymorphs can, through heating or cooling, reversibly transition from one form to the other.

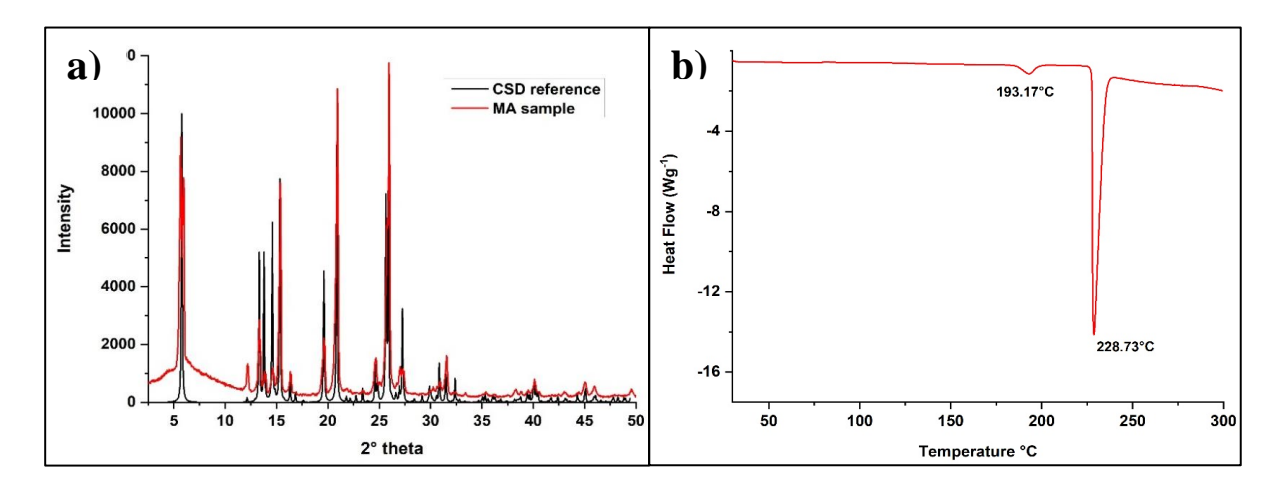


Figure 6-1. a) The Cambridge Crystal Database reference PXRD pattern of mefenamic acid overplayed on the obtained pattern from the commercial sample; b) The DSC curve of the mefenamic acid sample.

The PXRD pattern of DM in Figure 6-2 a) is well matched to the CSD reference pattern, displaying characteristic peaks at 2θ values of 9.99° , 14.02° , 18.33° , 23.01° and 29.02° , indicative of the β polymorph¹⁶⁶. The DSC curve (Figure 6-2 b) shows an endothermic peak at 164.40 °C, as reported in literature^{225,227}, further confirming that the sample is indeed β -DM.

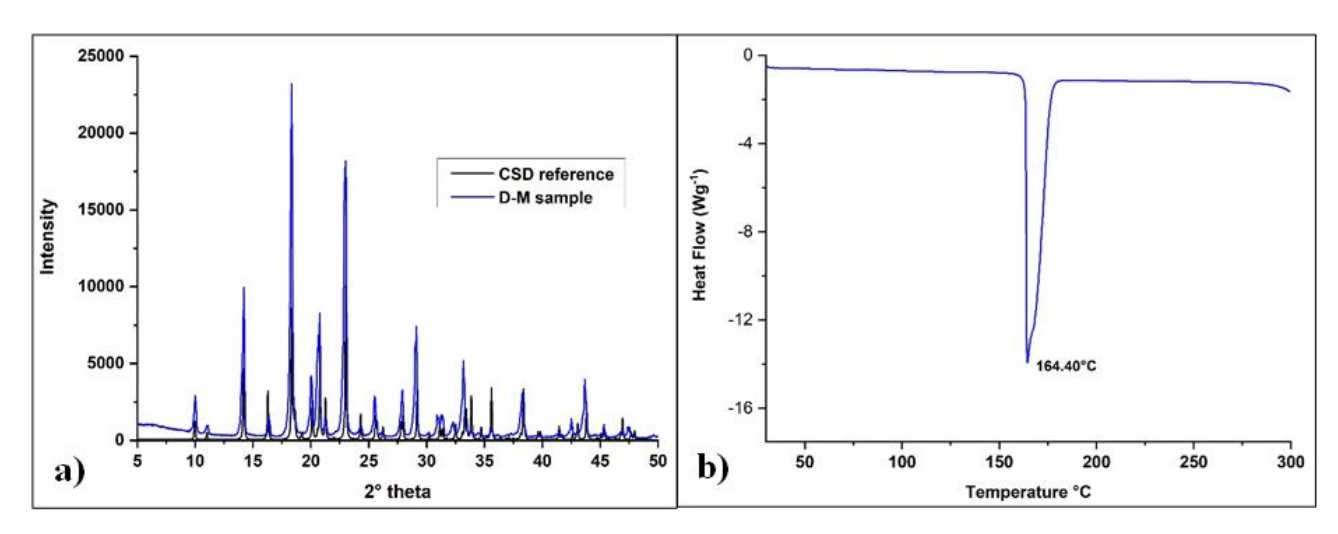


Figure 6-2. a) The Cambridge Crystal Database reference PXRD pattern of d-mannitol overplayed on the obtained pattern from the commercial sample; b) The DSC curve of the d-mannitol sample.

6.1.2 Material Stability

As previously mentioned in Chapter 3, the stability and processability of pharmaceutical compounds can be greatly affected by the environmental factors such as temperature and relative humidity. Generation of heat during processing steps like milling and high-speed compaction can threaten the integrity of the solid-state and the overall bulk powder properties²²⁸. Similarly, adsorption and absorption of moisture during processing can also change the solid-state form by the formation of hydrates²²⁹. This can also cause altered morphology and topography, making the powders more adhesive/cohesive, changing flow and compaction properties. Thus, measuring stability is an important step in pharmaceutical manufacture. TGA and DVS are common methods to study stability. TGA measures heat-induced changes by tracking the material's mass loss over temperature, whilst DVS measures humidity-induced changes by tracking the material's mass change over relative humidity (RH) at constant temperature.

The TGA results of MA acid and DM are shown in Figure 6-3 a) and b), respectively. Both materials display a one-step decomposition process, indicating that the samples are pure and not contaminated. Results show that mefenamic acid starts to decompose at 245 °C, and d-mannitol starts to decompose at 291 °C, both within the previously reported values^{227,230}.

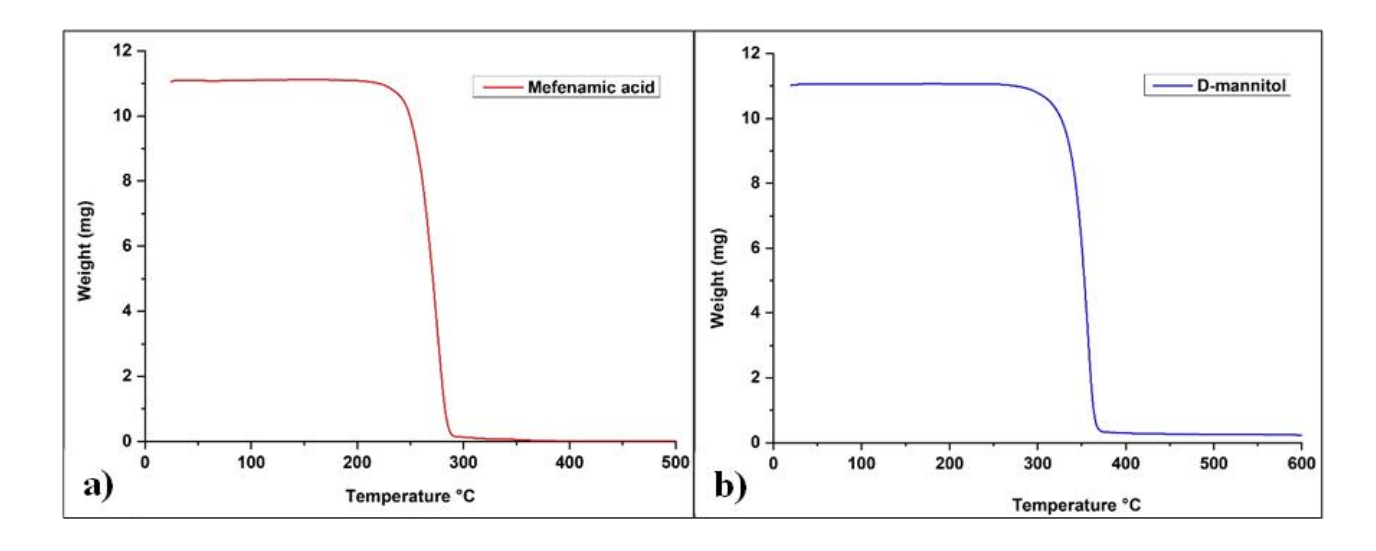


Figure 6-3. TGA curves of a) mefenamic acid and b) d-mannitol

Interaction with water vapour during storage can affect the chemical stability as well as particle properties, causing agglomeration and caking. Thus, determining the hygroscopicity of drug compounds is a vital step in the early development stage of medicines. Compounds that do not form stable hydrates from a water uptake of up to 2% at 25 °C/60% RH are generally expected not to disrupt the solid-state of the compound²³¹.

The DVS isotherm and kinetic curve of MA are displayed in Figure 6-4. The results display a steady increase in moisture uptake, then a faster increase between 80%RH and 90%RH. The isotherm shows that the majority of the water was evaporated by the end of the measurement, with just 0.0013 mg of water retained in the sample. The sample absorbed only 0.02% of water and only 5.39×10⁻⁷ moles of water at 90%RH.

Figure 6-5 displays the DVS isotherm and kinetic curve of DM. The results show a steady increase in the sorption of water until 70% then a faster increase between 80%RH and 90%RH. The isotherm is almost reversible as most of the water had evaporated by the end of the measurement, leaving only 0.0016 mg of water in the sample. The water uptake at 90%RH of d-mannitol was 0.044% with 1.03×10^{-6} moles of water in the sample.

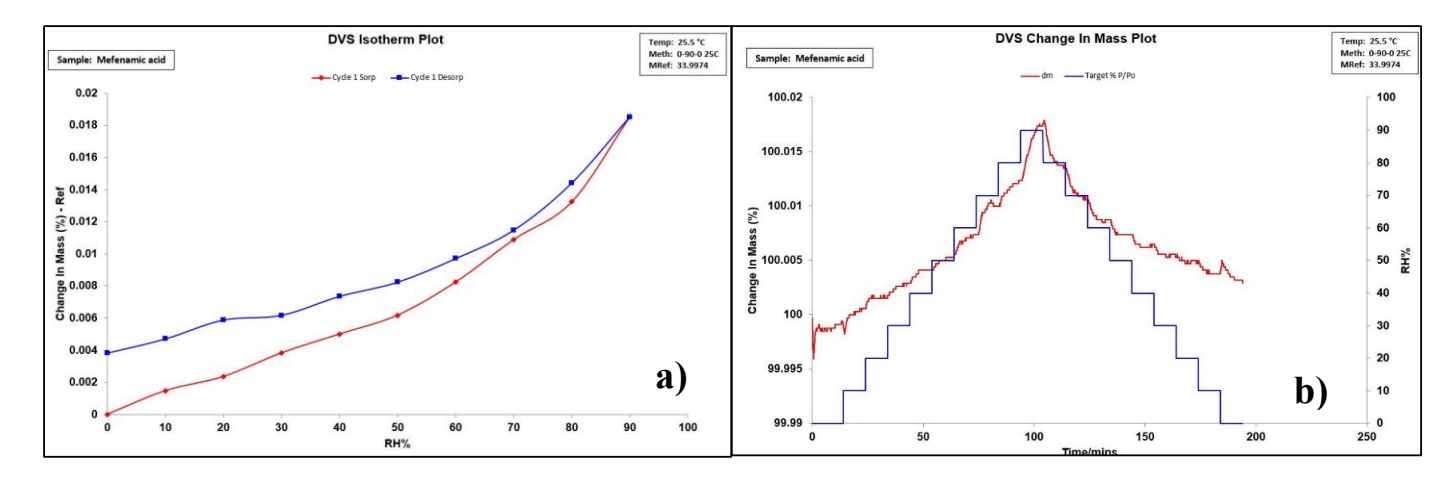


Figure 6-4. a) The DVS isotherm and b) the kinetic curve of mefenamic acid

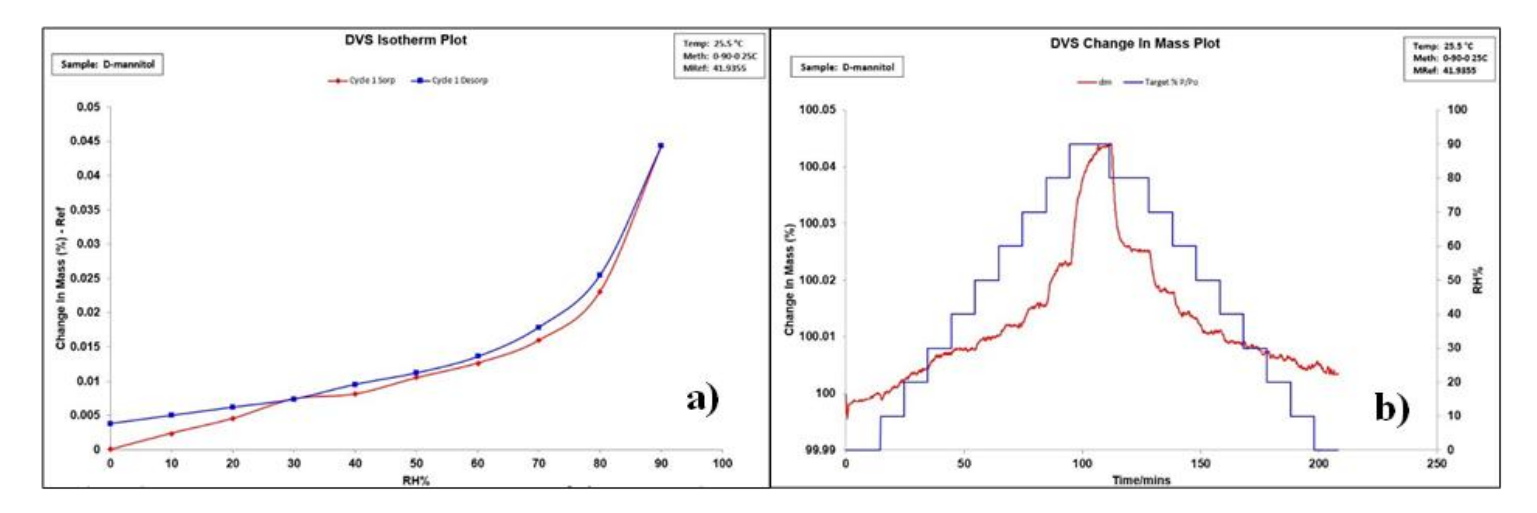


Figure 6-5. a) The DVS isotherm and b) the kinetic curve of d-mannitol

Both materials display very low percentage water uptake, though DM absorbed 0.024 % more water than MA. Thus, according to the European Pharmacopoeia (Table 6-1), both are classified as non-hygroscopic, being within the range of 0-0.12 % water absorption²³². The isotherms of both materials and their very small percentage moisture uptake reveal that they are both stable materials not greatly impacted by relative humidity. This suggests that for these compounds, relative humidity is not the primary cause of cohesion/adhesion during drug production.

Table 6-1. Classification of hygroscopicity as defined by the European Pharmacopoeia 232

Classification	% Water Uptake at 25°C/80%RH (w/w)
Non- hygroscopic	0-0.12
Slightly hygroscopic	0.2-2
Moderately hygroscopic	2.0-15.0
Very hygroscopic	>15.0

6.2 Influence of Particle Morphology, Size and Flow on Compaction

The results presented in this section discuss how particle morphology, size and flow properties impact compaction behaviour and how they affect each other in binary mixtures.

6.2.1 Morphology and Particle Size

Assessing the powder properties of pharmaceutical materials is a vital step in the drug manufacturing process. The morphology and particle size distribution of the bulk are properties that will impact their manufacturability and, consequently, the quality of the final drug product. As discussed in Chapter 3, even content uniformity of narrow particle size distribution is desirable. This will improve the flow of the powders, making them easier to handle in subsequent downstream processing steps. The flowability of the powders will affect their consolidation behaviour, thus influencing how well they compress and their ability to compact into strong tablets.

SEM images of both powders are provided in Figure 6-6. DM exhibits thick, irregular oblong particles compared to the MA particles. The surface of these particles is textured, and some seem to grow off each other, making the particles appear bulky, though actually columnar in nature. Thus, the 'bulky' particles are rather columnar aggregates or agglomerates. The size ranges from small particles of approximately 34 µm to the large, bulky particles of over 400 µm. In contrast, the MA crystals are thinner, smoother, and well-faceted hexagons of varied aspect ratios. They range from equant plates to more elongated, thick blades, almost needle-like, with an approximate size distribution of 12 to 220 µm. It can also be seen that some crystals are growing off each other or adhering on top of each other, mostly on the {100} face and some on the {002} side face. The thin plate-like nature of mefenamic acid suggests that the material is more brittle and will break more readily during processing and handling than DM^{203,222,233}. The morphologies of these particles suggest that MA may have poorer flow and compaction properties than those of DM²¹³.

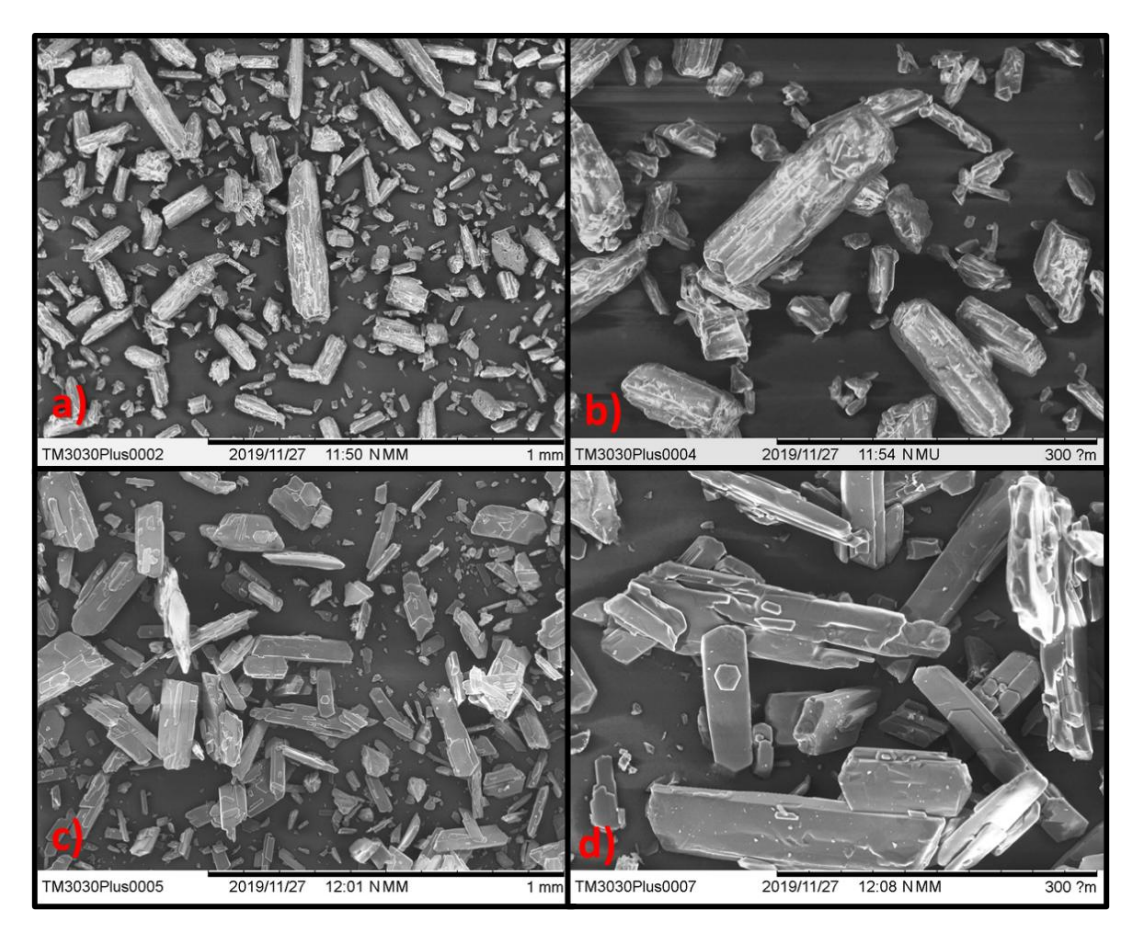


Figure 6-6. SEM images of d-mannitol at: a) 100x magnification, b) 300x magnification and mefenamic acid at: c) 100x magnification, d) 300x magnification

The particle size distribution was measured by the Mastersizer (dry dispersion), and the results are shown in Figure 6-7 a) and b) and Table 6-2. The MA powders had a size distribution between 4.4 μm and 61.4 μm with a d₅₀ of 19.9 μm and a span of 2.9. Whilst the DM had a size distribution between 9.1 μm to 152.4 μm and a d₅₀ of 52.1 μm, and a span of 2.8. These sizes are smaller than what is seen in the SEM images, primarily due to the different analysis dimensions. SEM provides 2-dimensional visual images of the particles, whilst the PSD, laser diffraction uses light scattering, assuming a spherical equivalent diameter²³⁴. Particles of higher aspect ratios can appear larger in SEM but have a smaller equivalent diameter in laser diffraction analysis. The varied sample dispersion methods are also a potential reason for the varied sizes. The powders are fed into the Mastersizer through a sieve, and the 1 bar pressure applied can break down any larger particles and agglomerates, resulting in the observed smaller size distribution²³⁵. Mefenamic acid has a slightly larger span and narrower size distribution than d-mannitol, indicating greater proportional variability of heterogeneous sizes. Whilst d-mannitol's

larger size distribution and lower span indicate that the larger particles a more uniformly distributed compared to the mefenamic acid particles.

Table 6-2. Particle size distribution of mefenamic acid and d-mannitol

Material	D (0.1)	D (0.5)	D (0.9)	Span
Mefenamic acid	4.4	19.9	61.4	2.9
D-mannitol	9.1	52.1	152.4	2.8

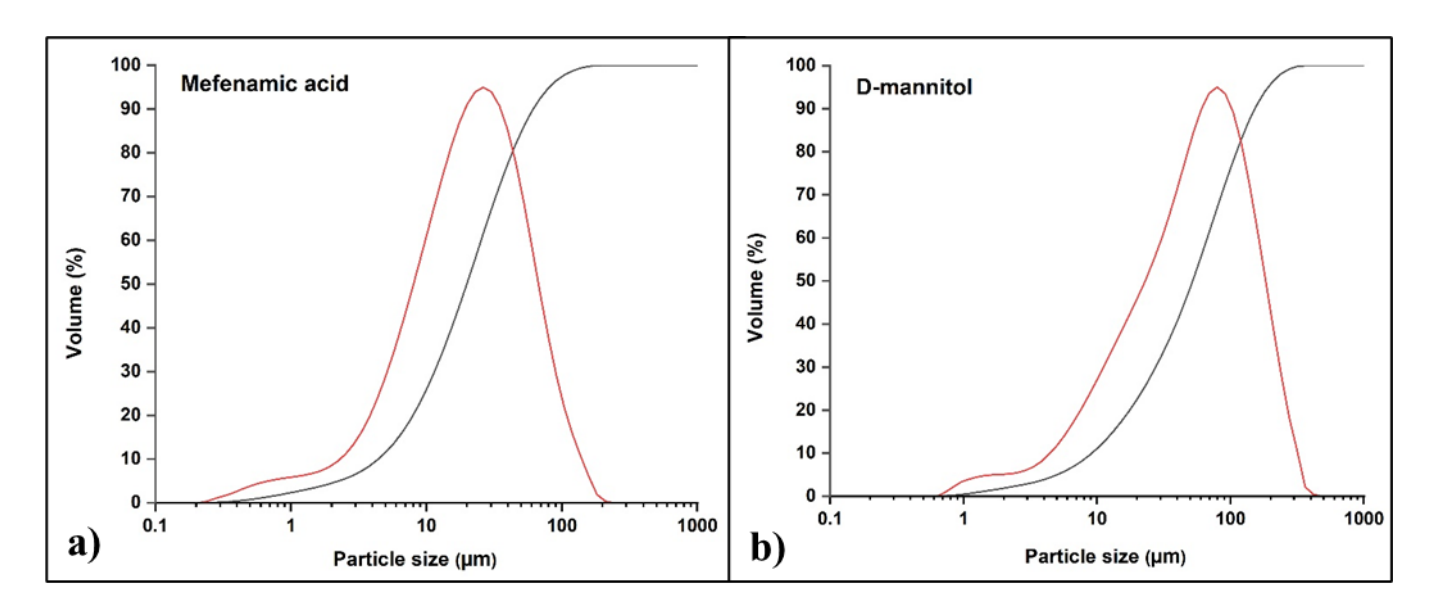


Figure 6-7. The particle size distributions of a) mefenamic acid and b) d-mannitol

6.2.2 Powder Flowability

Poor powder flow can negatively impact various stages of pharmaceutical manufacturing. It is one of the factors which cause demixing and segregation during blending. It also poses problems when transferring powders between various process equipment, reducing production efficiency. Poor flow can also cause poor die filling, affecting the content weight uniformity of the dosage form. Inadequate die filling may, in turn, result in trapped air during compaction, causing capping or lamination⁸⁷. Therefore, evaluating the flow properties of drug powders is important, so the most appropriate method of improvement can be applied. Although the granulation process generally improves the flow of powders, most powders still need the addition of a glidant and lubricant to improve their flow. The Carr's compressibility index (CI), Hausner ratio (HR) and the angle of repose (AOR) of the tested

powders were evaluated. Based on the obtained values, the flowability was characterised on a scale from *Excellent* to *Very, very poor* (Table 6-3) as per the European Pharmacopoeia²³⁶.

Table 6-3. Scale of Flowability and Corresponding Carr's Index, Hausner Ratio and Angle of Repose²³⁶

Flow	Carr's Index %	Hausner Ratio	Angle of Repose °
Excellent	0-10	1-1.11	25-30
Good	10-15	1.12-1.18	31-35
Fair	16-20	1.19-1.25	36-40
Passable	21-25	1.26-1.34	41-45
Poor	26-31	1.35-1.45	46-55
Very poor	32-37	1.46-1.59	56-65
Very, very poor	> 38	> 1.60	> 66

The flow properties of MA, DM and three binary mixtures of MA-DM, increasing the amount of MA: 50-50, 65-35 and 75-25, are averaged over 5 measurements each, and are displayed in Table 6-4.

Table 6-4. Measured bulk density, tapped density (g/cm3), Carr's Index, Hausner Ration of d-mannitol and mefenamic acid and angle of repose of d-mannitol

Material	Bulk density g/cm3	Tapped density g/cm	CI%	HR	Flow	AOR °	Flow
D-M	0.645 ± 0.017	0.729 ± 0.001	11.61	1.13	Good	39.20 ± 2.82	Fair
50-50	0.534 ± 0.010	0.689 ± 0.011	22.57	1.29	Passable	41.18 ± 3.42	Passable
65-35	0.476 ± 0.034	0.663 ± 0.010	24.81	1.33	Passable	45.03 ± 2.84	Passable
75-25	0.495 ± 0.007	0.632 ± 0.006	25.39	1.34	Passable	45.19 ± 1.80	Passable
MA	0.446 ± 0.032	0.612 ± 0.037	27.15	1.37	Poor	44.55 ± 1.45	Passable

As suspected from examination of their morphologies, DM has superior flow properties. The CI and HR of DM were 11.61 % and 1.13, respectively, indicating *Good* flow. The AOR results for DM did not result in the same classification as the CI and HR results, being 39.20°, classifying it as Fair. In fact, two of the 5 measurements were 41.13° and 42.09°, reflected in the standard deviation, giving those a classification of *Passable*. Figure 6-8 displays an image of one AOR experiment of DM. It can be seen that the DM powder contains large agglomerates that did not break during the experiment. During the experiment, it was observed that these agglomerates sometimes blocked the flow of the surrounding free powders down the funnel and/or rolled off the formed heap. It can be reasoned that the agglomerates increase the interparticle friction within the powder, giving a larger angle, thus poorer flow. DM's

irregular particle morphology and rough surface texture can cause interlocking between particles, resulting in the observed agglomerates. The superior flow observed under tapping would be due to the agglomerates breaking during the measurements. Consequently, this resulted in the better classification of the CI and HR than the AOR o results. It can then be argued that, naturally, the flow of DM is overall quite average, and it needs extended tapping/vibration to achieve *Good* flow classification. It has been previously recorded in literature that out of the polymorphs of DM, the β form has the poorest flow properties ^{157,217}.

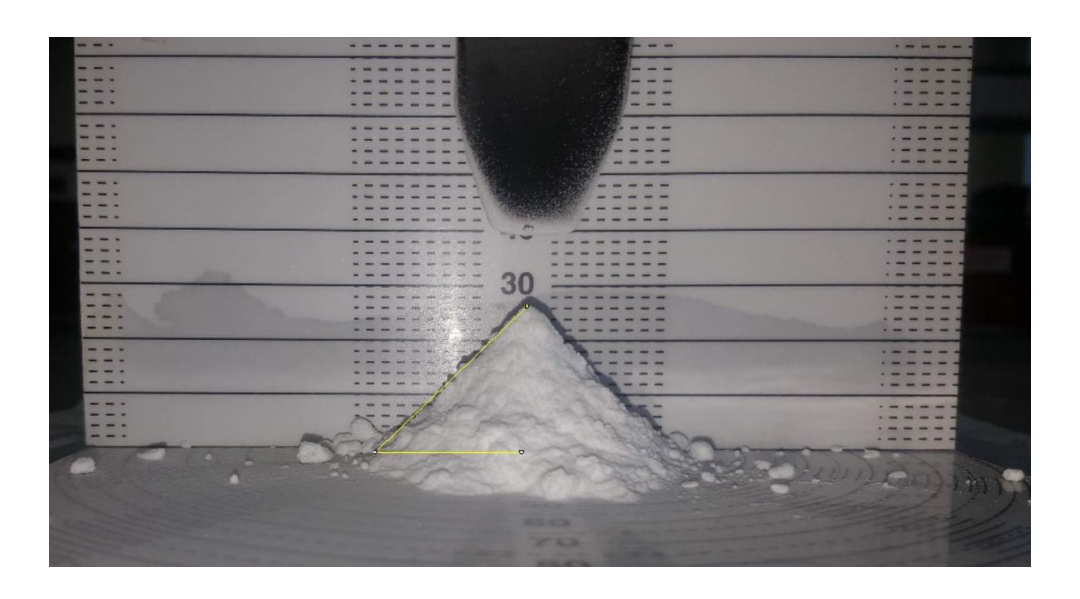


Figure 6-8. Angle of repose measurement of d-mannitol

The CI and HR values for the 50-50 mixture were 22.57 % and 1.29, respectively, representing *Passable* flow. The AOR was 41.18°, also classifying it as a *Passable* flow. The 65-35 and 75-25 blends performed very similarly, with a CI and HR of 24.81 %, 1.33 and 25.39 % 1.34, respectively. Naturally, they also had similar AOR values of 45.03° for the 65-35 blend and 45.19° for the 75-25 blend. Their performance gives them the flow classification of *Passable*. The MA powder performed the worst with a CI and HR of 27.15 % and 1.37. When performing the AOR measurements, the powder did not flow naturally with the vibration of the instruments. Therefore, it needed a gentle push by a spatula for the heap to be formed. The resulting AOR was 44.55°, and coupled with the CI and HR values, gives MA *Poor* flow. During both experiments, agglomerates of different sizes were observed. Unlike DM, these agglomerates did not break even after tapping. This suggests that MA creates quite strong agglomerates,

indicating high cohesive forces in the powder, thus poorer flowability. The powder flow measurements show how the increase of MA decreases the flow of the formulations.

6.2.3 Powder Compactibility

As outlined in Chapter 3, compressibility is the ability of powders to reduce volume under a compressive force, and compactibility is the ability of the tablet to maintain cohesion, an intact tablet, after compression. These two components describe the overall tabletability of powders.

5 mm tablets of each powder batch (DM, MA, 50-50, 65-35 and 75-25) were created by direct compression using the Instron mechanical tester. Literature values for direct compression of MA and DM suggested compaction pressures between 50-200 MPa^{21,52}. After compaction at various pressures, tablets were created at 204 MPa (~4000 N); however, some issues were still observed, which will be discussed below.

The three main mechanisms of compression outlined in Chapter 3 can be summarised as follows:

- 1. Initial rearrangement and volume reduction of the powder bed. (Weak agglomerates may undergo a level of deformation and/or fragmentation).
- At higher pressure, plastic deformation and fragmentation take place, filling any voids in the powder bed.
- 3. At maximum compaction pressure, porosity is reduced, nearly eliminated. The powder bed is no longer individual particles but one solid unit. Above this pressure, the solid unit behaves elastically. As pressure is being removed, elastic recovery occurs where the solid relaxes and slightly expands.

A typical Heckel plot shows all three mechanisms: an initial non-linear region related to rearrangement of particles, a linear region related to plasticity, followed by another non-linear region related to strain hardening.

Figure 6-9 Figure 6-9 displays the full Heckel plots of a) DM and b) MA. Upon observation, MA does not reach stage 3 of the compression process. Indicating that at 204 MPa, MA is unable to form a robust

compact and requires more pressure than DM to reach its yield point. Indeed, this resulted in MA tablets that broke upon ejection or split with a slight touch.

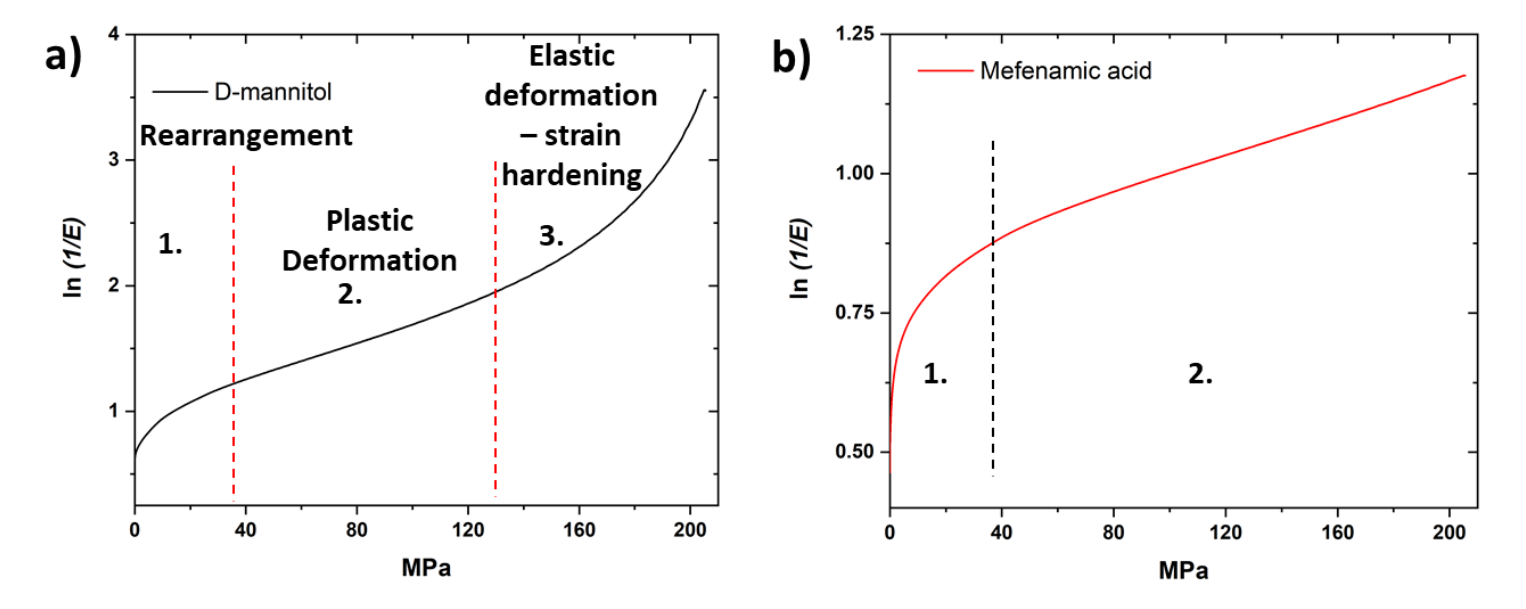


Figure 6-9. Heckel plots of a) d-mannitol, highlighting three stages of compression and b) mefenamic acid not reaching stage 3 strain hardening

The failed compact of MA was also attributed to the poor ejection method and the punch-tip design. Compactions of all the other powder blends resulted in compactions that also split upon ejection. Thus, for improvement of the compaction process, the die walls were lubricated with magnesium stearate and a new punch tip was created, long enough to push the tablet out. The old punch-tip had bevelled edges (Figure 6-10, a), which can be a cause of rapid elastic expansion during relaxation, resulting in capping of the tablet²³⁷. This was observed in the case of MA. Optimisation of the tooling was achieved by creating a flat surfaced punch-tip (Figure 6-10, b), long enough to be used for ejection, resulting in successful MA tablets and the other blends. More robust tablets of DM were also produced using the new tooling.

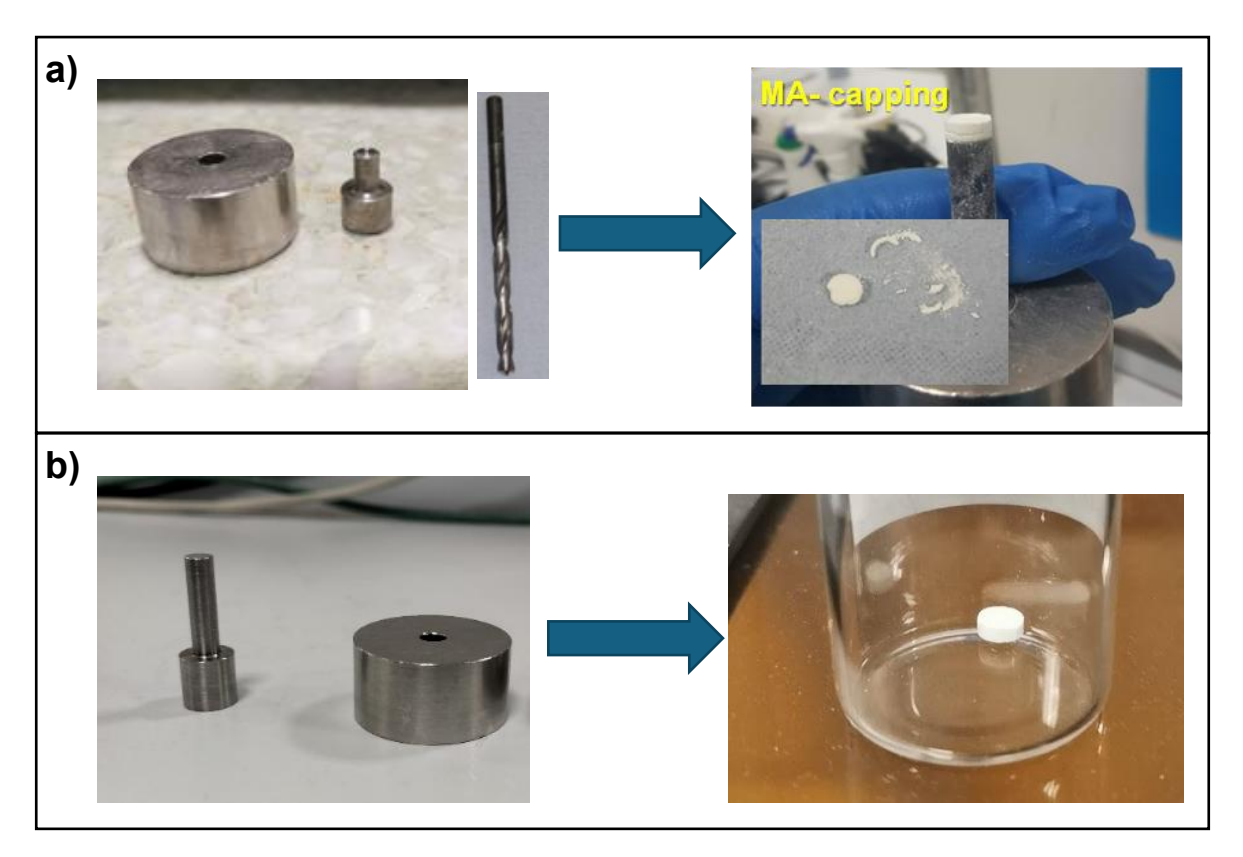


Figure 6-10. a) The old compaction tooling and resulting mefenamic acid tablet, and b) optimised punch-tip and resulting mefenamic acid tablet

The Heckel and porosity plots of all powder blends are presented in Figure 6-11 a) and b), respectively and the Heckel parameters are listed in Table 6-4. The Heckel constants are determined through linear regression using the least squares. Accurate selection of the linear region is very important; therefore, R^2 values above 0.95 must be selected for accurate analysis²³⁸. By taking the inverse of the slope, the yield stress P_{ν} is calculated.

The full Heckel plot reveals how only the DM and 50-50 tablets reached full strain hardening, reflecting their faster onset of plastic deformation. The P_y of DM is 65.79 MPa, and 50-50 95.24 MPa. The other samples followed increasing P_y , thus slower plastic deformations in the order 65-35 < 75-25 < MA, with the following values respectively: 147.06 MPa < 153.85 MPa < 370.37 MPa.

The results also show that DM displayed significantly better compressibility than all the other powders, 0.03, indicating a close bonding area between particles. The three powder blends displayed very similar

compression profiles in the increasing porosity order: 50-50: 0.05 < 65-35: 0.06 < 75-25: 0.08. The MA tablet displays the largest porosity, hence the poorest compressibility of 0.22.

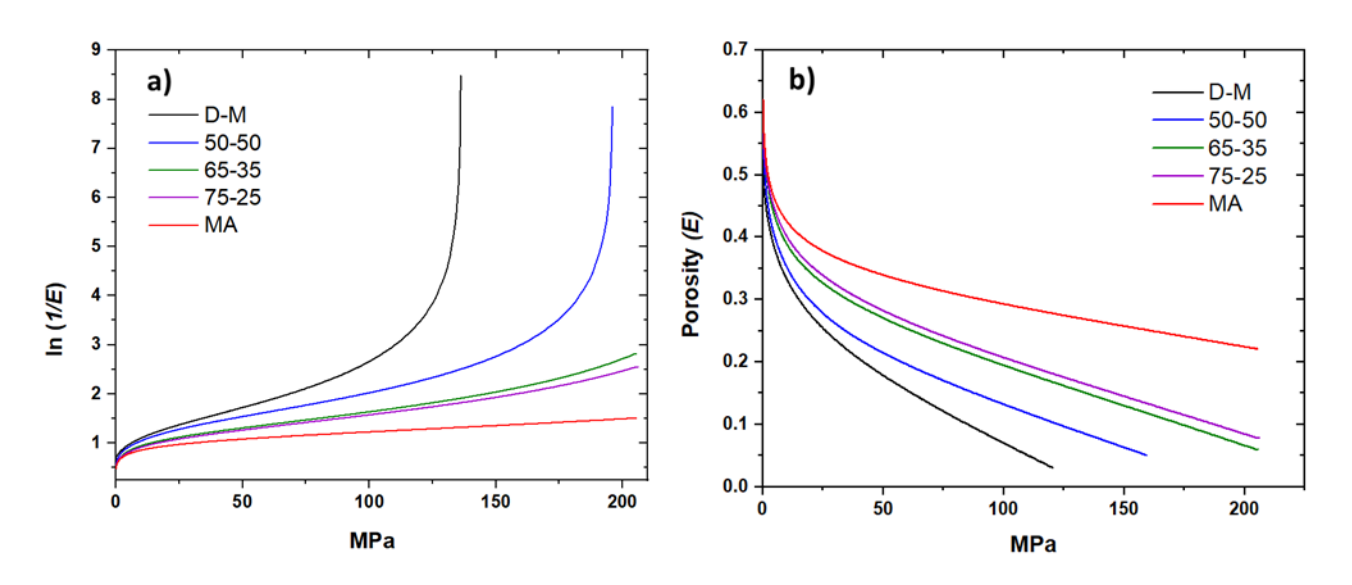


Figure 6-11 a) Heckel plots and b) compressibility of d-mannitol and mefenamic acid and their compositions

The strength of all the tablets was tested through diametric stress tests described in Chapter 4, and the values are presented in Table 6-4. In formulated tablets for sale, a tensile strength above 1.7 MPa is generally required.

As all the tablets were made with as-received materials and with no additional excipients, they were naturally weaker than the average marketed tablet. Consequently, very low pressure was required to break them. Nonetheless, a clear difference in their strength was still observed. Consistent with the compression results, DM had the highest tensile strength, 1.07 MPa. This was followed by the 50-50 blend at 0.54 MPa, 65-35 at 0.42 MPa, 75-25 at 0.23 MPa and MA at 0.08 MPa.

Table 6-5. Heckel Parameters and tensile strength

Sample	Н	- (MDa)			
Sample	$P_y(1/k)$	E	A	\mathbb{R}^2	σ _T (MPa)
DM	65.79	0.03	0.97	0.99	1.07
50-50	95.24	0.05	0.98	0.99	0.54
65-35	147.06	0.06	0.96	0.99	0.42
75-25	153.85	0.08	0.94	0.99	0.23
MA	370.37	0.22	0.96	0.99	0.08

As the porosity value E represents the void space in the tablet, the solids occupied in the tablet are the solid fraction. Plotting the tensile strength against the tablet's solid fraction gives a measure of the material's compactibility. Figure 6-12 displays an exponential relationship between the tensile strength and the tablet's solid fraction, following the increasing order of: MA (0.78) < 75-25 (0.92) < 65-35 (0.94) < 50-50 (0.95) < DM (0.97). The solid fractions/porosity of the 50-50, 65-35, 75-25 and DM tablets are very close; however, they differ significantly in their tensile strengths. This reveals that even with similar levels of porosity, their interparticulate bonding varies. The increase of MA in the formulation reduces the strength of interparticle bonding in the tablets, producing tablets of poor compactibility.

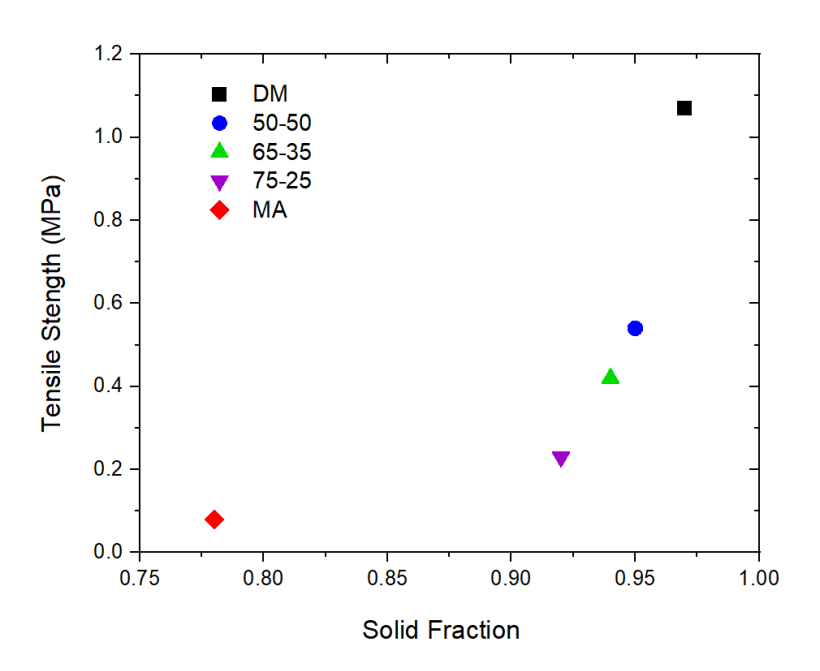


Figure 6-12. Compactibility of the five tablets: mefenanic acid, d-mannitol, 50-50, 65-35 and 75-25 blends

The ideal tablet solid fraction for most solid dosage forms is between 0.85-0.95; solid fractions above this are undesirable as they tend to take longer to dissolve²³⁹. Even though DM has the highest solid fraction and strongest tensile strength, such a tablet may not be desired for therapeutic use. Highlighting the importance of achieving the optimum API-excipient balance.

6.2.4 Summary of Bulk Powder Properties

Literature reports that a d50 range between 50-500 μm is desired, and morphologies of aspect ratio close to 1:1:1 is desired^{240,241}. Particles which are too small tend to be very static and sticky and are difficult to handle²⁴². The surface texture can also affect the bulk properties. Although generally smooth surfaces are preferred, too smooth surfaces may be difficult to blend, causing challenges in content uniformity as they remain primary particles²⁴⁰. MA possesses a smaller particle size (D₅₀: 19.9μm), increasing its surface area, causing high vdW forces and electrostatic charges, increasing its cohesive/adhesive nature, making it sticky and prone to agglomeration. Its platy morphology, coupled with its higher span, results in inconsistent packing and poor powder flow. This is reflected in its poor flowability (HR: 1.37, AOR: 44.55°). The variability in particle size and thin, platy, bladed morphology causes interlocking of the particles, which increases interparticulate friction, preventing free flow of the powder. The presence of strong agglomerates in the powder mass would further exacerbate this problem. This poor flow also results in poor die filling when making tablets. In this study, the die was filled manually, which was of some difficulty because of the MA's poor flow and cohesivity.

Crystals of platy morphology have weaker bonding due to their tendency to align and slide during compression, resulting in weaker tablets²⁴³. This increases the tendency for delamination and capping after decompression. Weaker particle bonding was observed for the platy MA powder, having a high porosity (E: 0.22) and low tensile strength (0.095 MPa), limiting effective packing and resulting in weak interparticulate bonding. Its high yield stress (357.14 MPa) reveals the brittle nature of the MA, displaying very poor plasticity. This poor deformation behaviour explains the resulting weak and porous tablet.

D-M's wider size distribution (9.1–152.4 μ m) and slightly smaller span (2.8) promote better packing, as smaller particles fill any voids. The thicker columnar morphology and more textured surface promote particle rearrangement and increase interparticle contacts. All these factors are reflected in D-M's superior flow properties (HR: 1.13, AOR: 39.20°), compressibility (E: 0.03) and better plasticity, lower yield stress (P_y : 65.79 MPa), thus displaying desired deformation behaviour. Its higher tensile strength (1.07 MPa) confirms strong interparticulate interactions. The results demonstrate DM's ability to effectively withstand mechanical stress.

When comparing the three mixtures, it is clear that including d-mannitol in the formulation significantly impacts flow, compressibility and mechanical behaviour. In the 50-50 mixture, the flowability is improved compared to pure MA. The introduction of the thicker columnar particles of DM has counteracted the adverse effect of the thin platy MA particles by reducing interparticle friction and improving powder consolidation. The flow is not as good as pure DM; however, it's significantly better than pure MA. The improvements are also observed in the compressibility and tensile strength. Compared to pure MA, porosity is significantly reduced (*E*: 0.05) and compressibility greatly improved (*Py*: 95.24 MPa), undergoing plastic deformation. The combination of plastically deforming DM and brittle/fragmenting MA enhances both the contact area and bonding strength compared to that of pure MA. This drastically increases the tensile strength from 0.095 MPa of pure MA to 0.535 MPa of the 50-50 mixture.

The increase of MA from 50 % to 65%, then 75 % reduces the favourable contribution of D-M, resulting in poorer flow, compressibility and tensile strength. The presence of more MA shifts the particle size distribution towards finer particles with increased surface area, thus increasing interparticle friction. This reduces the flow and compressibility of the 65-35 and 75-25 mixtures, with the 75-25 mixture starting to resemble that of pure MA. The increase in yield stress reveals a pronounced reduction in plastic deformation, confirming the dominant influence of the brittle MA particles. The mechanical strength drops significantly from 65-35 to 75-25, 0.424 MPa, 0.176 MPa, respectively.

Among the three tested MA-DM formulations, the 50-50 mixture strikes the optimum balance between flowability, compressibility and tensile strength, making it the most suitable option for tablet production.

6.3 Conclusions

In this chapter, we have explored the intricate molecular and solid-state interactions between mefenamic acid and d-mannitol through comprehensive molecular modelling and analysis. The investigation highlighted the significant role that hydrogen bonding and crystal lattice energies play in determining the adhesive and cohesive properties of these compounds. Mefenamic acid exhibited stronger intermolecular interactions, attributed to its structural features, particularly its carboxylic acid and phenyl groups, which contribute significantly to the overall lattice energy.

In contrast, d-mannitol, with its extensive hydroxyl groups, demonstrated a robust hydrogen bonding network that influences adhesive interactions across its crystal facets. This unique bonding potential enhances its uniformity and stability in formulations, making it a reliable excipient in pharmaceutical applications. The comparative analysis of these compounds provides valuable insights into their behaviour during downstream processing stages—such as filtration, blending, and compaction—where their solid-state properties directly affect performance.

Understanding these molecular interactions not only aids in predicting the physicochemical behaviour of mefenamic acid and d-mannitol but also serves as a crucial foundation for optimising their application in various formulations. The findings from this chapter underscore the importance of molecular modelling in pharmaceutical science, as it enables researchers and formulators to anticipate and tailor the behaviour of drug excipients for enhanced therapeutic efficacy and stability. Future studies should continue to explore these interactions further, potentially integrating experimental validation to reinforce the predictive models established here.

CHAPTER SEVEN

Investigating Powder and Tablet Properties using X-ray Computed Tomography

This chapter presents the results obtained from X-ray computed tomography analysis. The powders and tablets of pure mefenanic acid, d-mannitol and their three binary mixtures are examined, and their properties are characterised. A discussion on the interplay of molecular, flow and compaction properties is provided.

7 Investigating Powder and Tablet Properties using X-ray Computed Tomography

7.1 Introduction

The results of the X-ray computed tomography (XCT) methods described in Chapter 4 are now presented and discussed. The consolidation nature and internal microstructure of mefenamic acid (MA) and d-mannitol are evaluated individually and as binary mixtures. By use of XCT, the density and porosity levels of each material have been quantified both as bulk powder and compacted tablet. Identifying how these factors change with varying formulation compositions will aid in gaining a deeper understanding of their flow and consolidation behaviour. A final discussion at the end of this chapter brings all the findings of the work together, providing an understanding of the interplay between the physicochemical properties and the mechanical behaviour influencing compaction.

7.2 Powder Packing Analysis of Mefenamic acid and D-mannitol

Figure 7-1 displays the 2D reconstructed slices of d-mannitol and mefenamic acid powder beds at various consolidation stages, using the described tapping method (0, 10, 20 and 30 taps). Filling the polyimide tube with mefenamic acid was somewhat difficult due to its sticky and static nature. This can be seen in the powder bed slice at zero taps, where some particles are separated from the main powder bed and stick to the wall of the tube. As the powder consolidates, the particles orient themselves in a manner resulting in relatively big void spaces, preventing them from optimal packing. Interestingly, the formation of a denser cluster can be observed on the lower left of the powder bed. The agglomerated cluster increases in size between 10 taps and 20 taps. At 30 taps, the agglomerate appears denser than at 20 taps, revealing the tendency of MA to stick to itself and agglomerate. This is better visualised in Figure 7-2. On the initial filling of D-M, a large agglomerate is observed at the bottom of the tube. However, this appears not to withstand subsequent tapping, indicating that in the occurrence of DM agglomerates, they are easy to break apart. DM displays greater densification during the consolidation

process compared to that of MA, with smaller void spaces. These observations are further supported through quantitative analysis of the consolidation process.

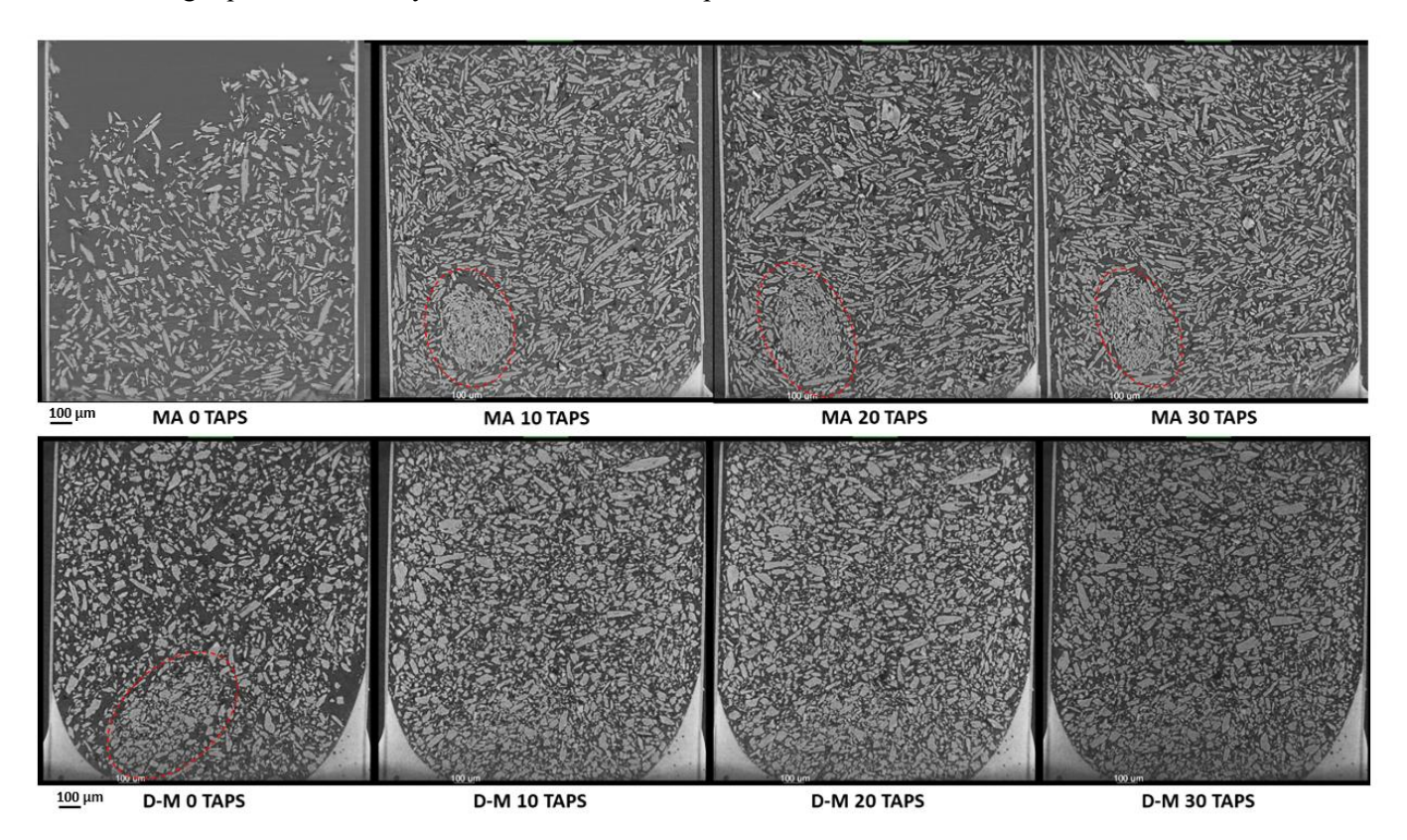


Figure 7-1. 2D reconstructed XCT slices of mefenamic acid and d-mannitol at 0, 10, 20 and 30 taps

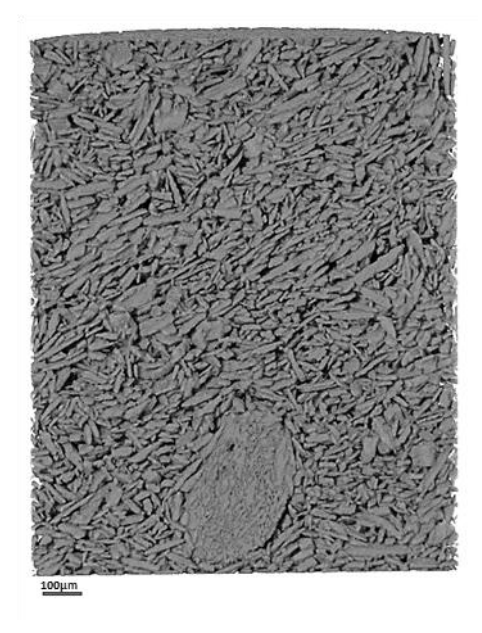


Figure 7-2. 3-D reconstructed image of mefenamic acid powder bed cross-section at 30 taps

Table 7-1 compares the bulk and tapped density values measured by the traditional lab "tapped density" method to those measured from the X-ray tomographic analysis. From those values, the Carr's index and Hausner ratio are measured to give the powders a classification of *flowability*.

The lab-measured bulk and tapped density of MA were 0.45 g/cm³ and 0.61 g/cm³, respectively, and 0.65 g/cm³ and 0.73 g/cm³ for DM. The values give a Carr's index and Hausner ratio of 27.15% and 1.37, respectively, for MA and 11.61% and 1.13 for D-M; classifying MA as having *poor flowability* and DM as *good flowability*.

The XCT measured bulk and tapped density of MA were 0.36 g/cm³ and 0.60 g/cm³, respectively, and 0.61 g/cm³ and 0.80 g/cm³ for DM. MA had a Carr's index and Hausner ratio of 40.16% and 1.67, respectively, classifying MA as having *very*, *very poor flowability*. DM had a Carr's index and Hausner ratio of 23.01% and 1.30, respectively, classifying DM as *passable flowability*.

The XCT flowability analysis is consistent with the lab analysis, though resulting in one step lower in the classification scale. This may be due to using a much smaller volume than what was used in the lab. However, the slight difference in results is most likely due to the powders not reaching their optimum densification.

Table 7-1. Comparison of lab-measured bulk and tapped density versus XCT-measured bulk and tapped density, and Carr's Index and Hausner results of mefenamic acid, d-mannitol

Sample	Lab-measured	XCT measured powder density (no. taps)				
Mefenamic acid	Bulk density (g/cm ³)	Tapped density (g/cm ³)	0	10	20	30
	0.45	0.61	0.36	0.57	0.58	0.60
	Flowability (CI/HR)	Poor (27.15%, 1.37)	Very, very poor (40.16%, 1.67)			
D-mannitol	Bulk density (g/cm ³)	Tapped density (g/cm ³)	0	10	20	30
	0.65	0.73	0.61	0.76	0.79	0.80
	Flowability (CI/HR)	Good (11.61%, 1.13)	Passable (23.01%, 1.30)			

7.2.1 Consolidation Pattern and Orientation Analysis of Mefenamic acid and D-mannitol

Exporting the XCT slice data allowed for the density variations of each sample to be assessed as a function of powder bed height. The data of MA in Figure 7-3 a) at 0 taps, reveals a low-density region at the top of the bed, which gets increasingly denser moving down the base of the bed. This reflects

what is visually observed in the 0 taps of MA in Figure 7-1. At 10 taps, the top of the powder bed has evened out due to particle arrangement from tapping and displays an even density distribution throughout the powder bed. The even powder density distribution continues between 10-30 taps, slightly increasing in density as the taps are increased.

The density variations of DM are observed in Figure 7-3 b). A high-density region at 0 taps is observed at the bottom of the powder bed between 0.4 mm to the bottom. This is consistent with the observed initial agglomerate in Figure 7-1. The powder bed undergoes significant densification between 0-10 taps as consolidation has started and particles are rearranged, reducing the wide density variation between the initial high-density region at the bottom and the bed above 0.4 mm. Gradual consolidation of the bed is observed from 10-30 taps. The top of the beds reveals an initial lower density, before evening out all the way down to 0.4 mm, where the initial high-density region was observed. This region is still slightly higher in density compared to the bed above. This is likely reflecting the segregation of larger particles settled at the bottom and smaller particles filling voids.

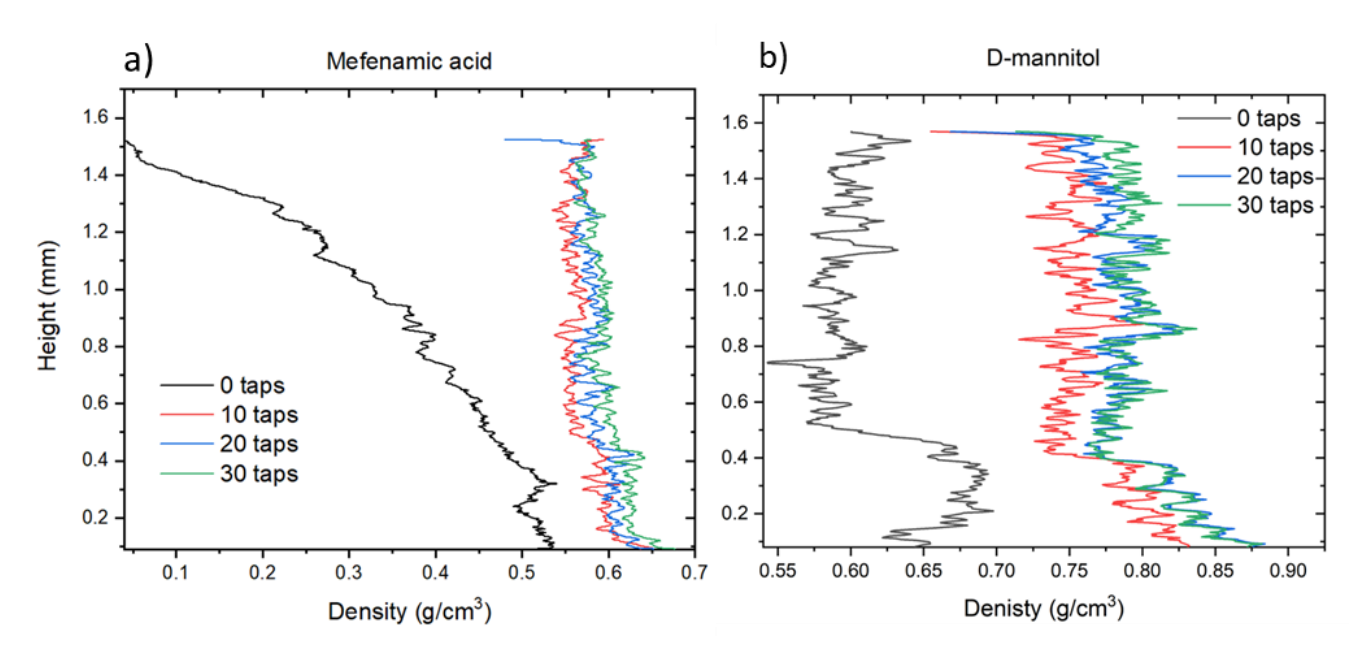


Figure 7-3. Variation in powder density of the bed height of a) mefenamic acid and b) d-mannitol. The height is closer to the top of the bed as a function of the number of taps.

The preferred orientation of MA and DM as a function of taps is displayed in Figure 7-4, a) and b) respectively. Results reveal that MA strongly tends to orient itself horizontally, then vertically. From 0 to 10 taps, the percentage of horizontal particles increases from 15.52 % to 18.10 %, vertical particles from 13.03 % to 14.48 % and angled particles drop from 11.79 % to 10.01%. This shift represents the initial rearrangement from tapping and the particles not yet reaching optimum densification. From 10 to 20 taps, it is seen that the horizontal particles go down from 18.10 % to 15.02 % then slightly increase and settle at 15.58 %. The vertical and angled particles settle at 12.80 % and 10.55 % respectively, at 30 taps. The orientation behaviour of DM appears very consistent throughout all taps. Horizontal orientation dominates, followed by angled, then vertical. The percentage of horizontal particles across taps ranges between 14.20 % and 14.50 %, the angled range between 13.02 % and 13.48 % and the vertical range between 11.76 % and 12.77 %. Although MA and DM both preferentially orient themselves horizontally, they differ in their trends. The MA orientation is not as even as DM. It exhibits a higher percentage of vertical and horizontal particles than DM and lower angled particles than DM. These variances reflect not only their morphological differences but also their varied surface interactions. The MA crystals are thin plates and blades and are dominated by vdW interactions. This type of crystal tends to prefer face-to-face, parallel stacking ²⁴³. Particles pack themselves in a manner to maximise contact area, ensuring more closely packed powders. The largest face of the MA particle is the {100}, which is dominated by $\pi - \pi$ stacking, followed by the side face {001}, which has even stronger $\pi - \pi$ interactions. Thus, it can be reasoned that the MA particles will try to achieve these contact areas, which is easier horizontally and vertically. Even so, the low density and higher interparticle friction due to the morphology work against achieving a close-packed powder. Vertical particle orientation has also been linked to poor flow²⁴⁴. They tend to interlock, increasing interparticle friction and cohesion. This corresponds with MA's flowability and visual images displaying the interlocking of particles.

The denser, bulkier DM of columnar morphology reaches optimum densification quicker than MA. This is reflected in its consistent orientation throughout the series of taps. The dominance of h-bonding in DM on all its facets leads to more evenly distributed preferred areas of contact. It also possesses more

facets than MA, further increasing contact areas for interparticle interaction. This can explain the difference in higher-angle orientation in DM. The orientation consistency throughout taps reveals that as densification increases, there is not much free movement of the particles, reflecting the denser, bulkier particles and h-bond dominance. {002} is the largest surface of the DM particle and has the strongest cohesive interactions; thus, stacking horizontally would be preferred.

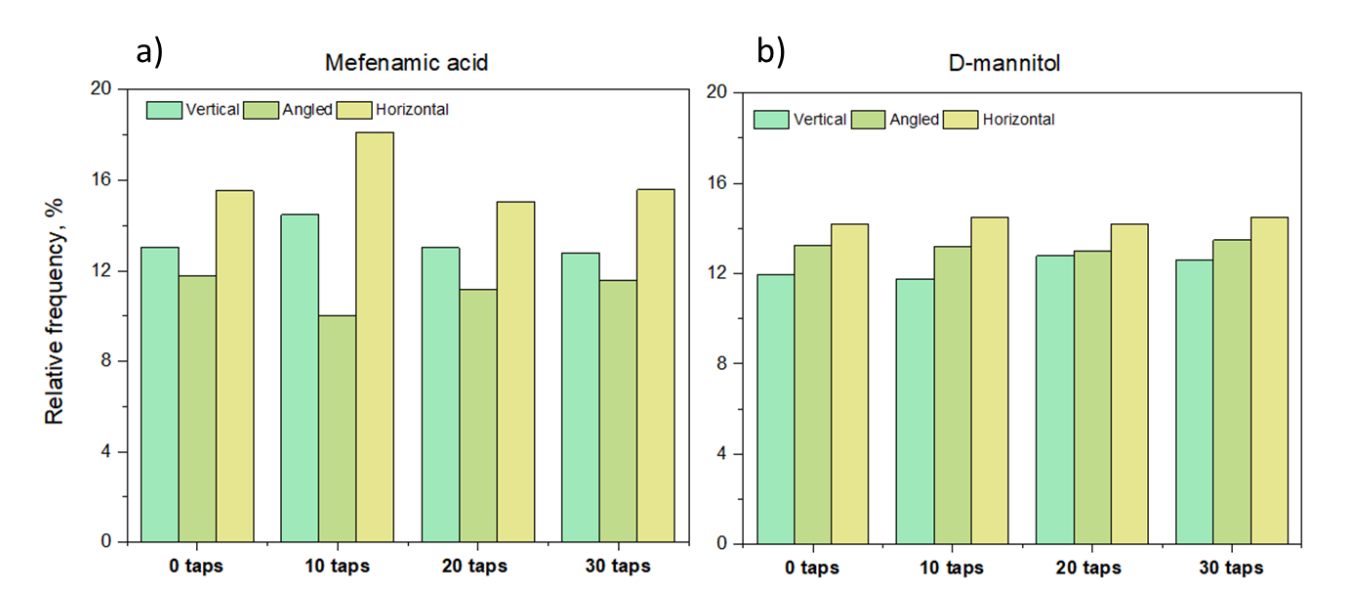


Figure 7-4. Variation of particle orientation of a) mefenamic and b) d-mannitol particles as a function of taps

7.3 Powder Packing Analysis of Mefenamic acid-D-mannitol mixtures

Using the same conditions and tapping method, a 50-50 mixture of DM and MA was also scanned to investigate how the packing and consolidation of the two powders behave in a binary mixture. A phase retrieval filter (PPCF filter) developed by Zeiss was applied, allowing for clearer differentiation between the two powders (Figure 7-5). The DM particles are lighter as it has a higher density, and the MA particles are darker.

Table 7-2 provides the lab and XCT tapping data for the 50-50 mixture. The lab-measured bulk and tapped densities were 0.53 g/cm³ and 0.69 g/cm³, respectively. The lab values give a Carr's index and Hausner ratio of 22.57% and 1.29, giving the 50-50 mixture a flowability classification of *passable*. The XCT measured bulk and tapped densities were 0.61 g/cm³ and 0.81 g/cm³, respectively and give a Carr's index and Hausner ratio of 25.32 % and 1.34, classifying it as *passable flowability*. Although

both lab and XCT flow were classified as passable, the XCT flow was on the lower end of the scale, hence displayed slightly poorer flow than the lab-measured flow.

The application of the PPCF filter allows for the segregation of the two powders, thus the flow of MA and DM could be assessed individually within the mixture. The measured bulk and tapped densities of MA were 0.50 g/cm³ and 0.63 g/cm³, respectively. The values give a Carr's index and Hausner ratio of 20.74% and 1.26, giving MA within the mixture *passable flow*. The DM bulk and tapped density results were 0.32 and 0.38, giving a Carr's index and Hausner ratio of 16.90% and 1.20, thus DM has *fair flowability*. DM maintains better flow than MA; within the 50-50 mixture, results show DM.

When compared with the previously measured individual sample XCT results, the flow of MA improved from very, very poor to passable. This indicates that the presence of DM improved the flow properties of MA. On its own, DM had passable flow and *fair* flow in the 50-50 mixture. This suggests that the 50-50 mixture has benefited the flow of both MA and DM.

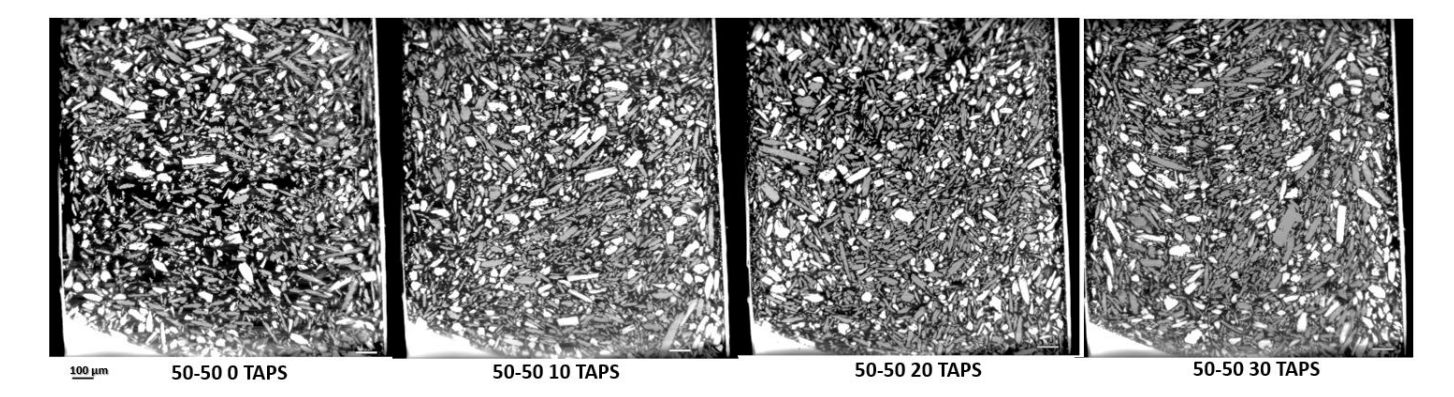


Figure 7-5. 2D reconstructed XCT slices of a 50-50 mixture of mefenamic acid and d-mannitol at 0, 10, 20 and 30 taps

Table 7-2. Comparison of lab-measured bulk and tapped density versus XCT-measured bulk and tapped density and Carr's Index, and Hausner results of 50-50 mixture and mefenamic acid and d-mannitol individually within the 50-50 mixture

Sample	Lab-measured powder density		XCT measured powder density (no. taps)			
50:50 mixture	Bulk density (g/cm ³)	Tapped density (g/cm ³)	0	10	20	30
	0.53	0.69	0.61	0.67	0.78	0.81
	Flowability (CI/HR)	Passable (22.57, 1.29)	Passable (25.32, 1.34)			
Mefenamic acid in the 50:50 mixture			0	10	20	30
Metenanne acid in the 50.50 mixture		0.50	0.57	0.60	0.63	
Flowability (CI/HR)			Passable (20.74, 1.26)			
D-mannitol in the 50:50 mixture $\frac{0}{0.3}$		0	10	20	30	
		0.32	0.33	0.35	0.38	
Flowability (CI/HR)		Fair (16.90, 1.20)				

The same flow analysis was performed on 65-35 and 75-25 mixtures (see Figure 7-6 and Figure 7-7), and the results are compared to the lab flow results. At the time of analysis, the PPCF filter was no longer available for use; thus, analysing the two compounds separately within the mixture was not possible, as with the 50-50. Nonetheless, the overall bulk and tapped densities were analysed and presented in Table 7-2

The lab-measured bulk and tapped densities of the 65-35 mixture were 0.48 g/cm³ and 0 0.63 g/cm³, respectively. The lab Carr's index and Hausner ratio of 24.81 % and 1.33, resulting in a *passable* flow. The XCT measured bulk and tapped densities were 0.58 g/cm³ and 0.74 g/cm³, respectively and give a Carr's index and Hausner ratio of 21.04 % and 1.24, matching the lab flow classification of *passable* flow.

The bulk and tapped densities of the 75-25 mixture measured in the lab were 0.50 g/cm³ and 0.66 g/cm³, respectively, resulting in *passable* flow. Through XCT analysis, the 75-25 bulk and tapped densities were 0.52 g/cm³ and 0.67 g/cm³, respectively. The Carr's index and Hausner ratio are 22.40 % and 1.29, thus the 75-25 mixture is consistent with the lab *passable* flow.

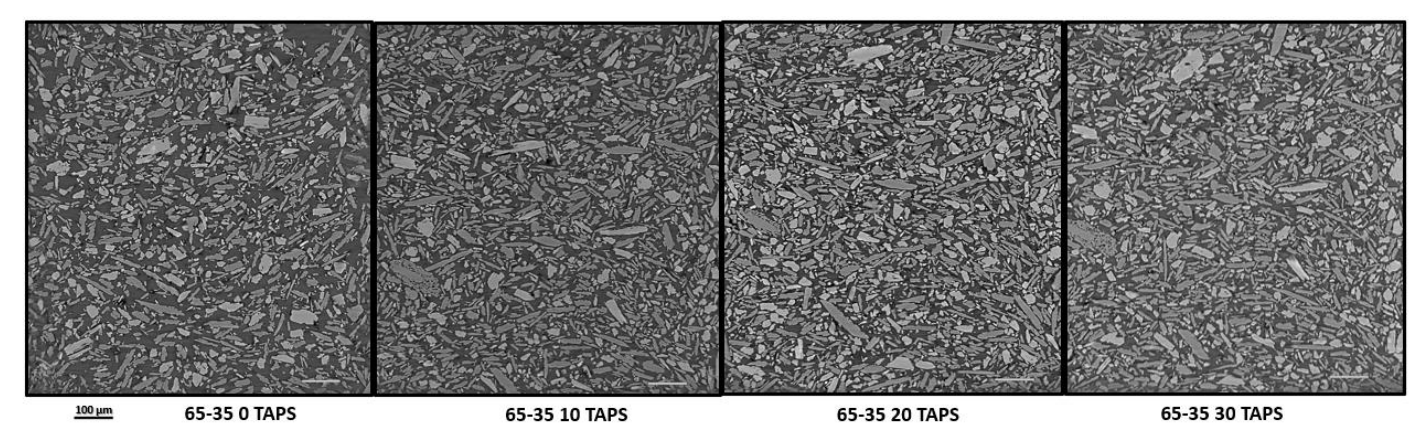


Figure 7-6. 2D reconstructed XCT slices of a 65-35 mixture of mefenamic acid and d-mannitol at 0, 10, 20 and 30 taps

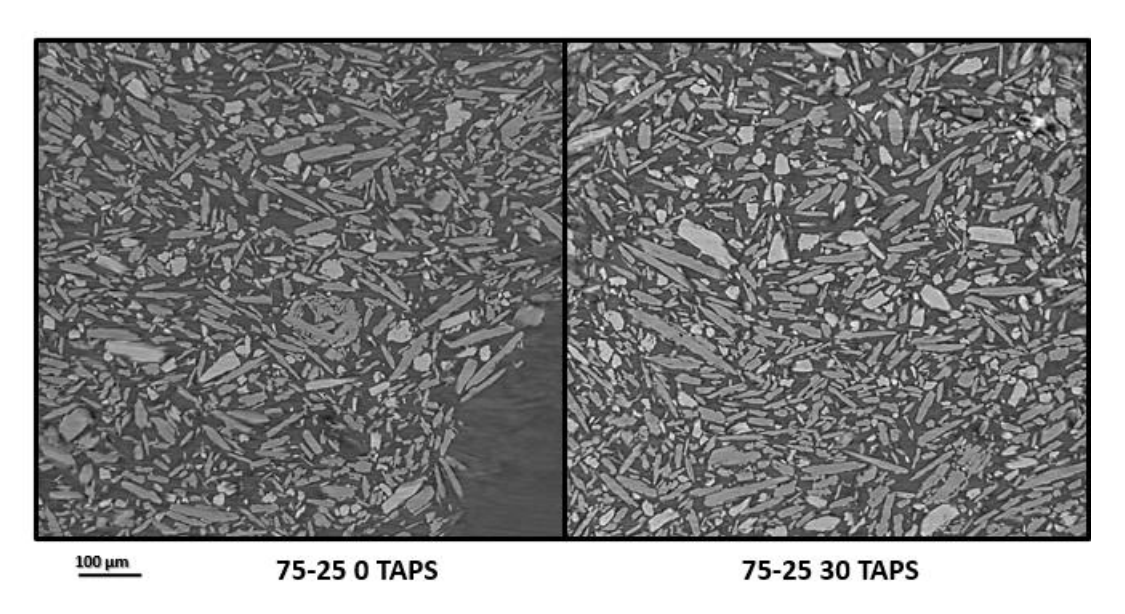


Figure 7-7. 2D reconstructed XCT slices of a 75-25 mixture of mefenamic acid and d-mannitol at 0 and 30 taps

Table 7-3. Comparison of lab-measured bulk and tapped density versus XCT-measured bulk and tapped density, and Carr's Index and Hausner results of 65-25 and 75-25 powder mixtures

Sample	Lab-measure	XCT measured powder density (no. taps)					
65:35 mixture	Bulk density (g/cm ³)	Tapped density (g/cm ³)	0	10	20	30	
	0.48	0.63	0.58	0.65	0.70	0.74	
	Flowability (CI/HR)	Passable (24.81, 1.33)	Passable (21.04, 1.27)				
75:25 mixture	Bulk density (g/cm ³)	Tapped density (g/cm ³)	0			30	
	0.50	0.66	0.52		0.67		
	Flowability (CI/HR)	Passable (25.39, 1.34)	Passable (22.40, 1.29)			9)	

7.3.1 Consolidation Pattern and Orientation Analysis of Mefenamic acid-D-mannitol mixtures

The density variations of the powder mixtures 50-50, 65-35 and 75-25 are presented in Figure 7-8 a), b) and c), respectively. At 0 taps, the 50-50 mixture displays a gradual increase in density from the top to the bottom of the powder bed. At 10 taps, the effects of initial particle rearrangement are observed. The very top of the powder bed is higher in density, then it starts to decrease from 0.9-0.8 mm. A low-density region is then observed between 0.8-0.2 mm, before the very bottom of the bed increases in density. The consolidation pattern at this stage suggests great segregation in the powder. At 20 taps, the powder bed has gained a more uniform consolidation pattern, steadily increasing toward the bottom of the bed. After final tapping at 30 taps, the powder has maintained a relatively uniform pattern, increasing toward the bottom.

The consolidation between 0 taps and 10 taps is less pronounced in the 65-35 blend than in the 50-50 blend, reflecting poorer consolidation. Nonetheless, the density gradient of the bed height is seen to be smoother, increasing in density specifically in the 0.45-0.67 mm region. This smoother gradient generally continues as consolidation increases. The very bottom of the powder beds at each stage of consolidation displays lower density compared to the rest of the bed. This is possibly due to some particle interlocking occurring at the bottom of the bed, contributing to the lower density in that region. At 0 taps, the powder bed of the 75-25 blend displays a higher density region from the top, down to approximately 0.4mm, where it drastically decreases towards the bottom of the bed. This may reflect difficulty in tube filling. As this blend contains the most MA, it is a more cohesive and static powder, resulting in more powder mass at the top of the tube. At 30 taps, the density gradient has improved

The analysis reveals the effect of increasing MA on the density gradient of the powder blend. The degree of initial consolidation (10 taps) is also correlated to how well the tube was filled in sample preparation. After 10 taps, more consistent consolidation trends are observed.

significantly, improving the density of the initially very low-density region.

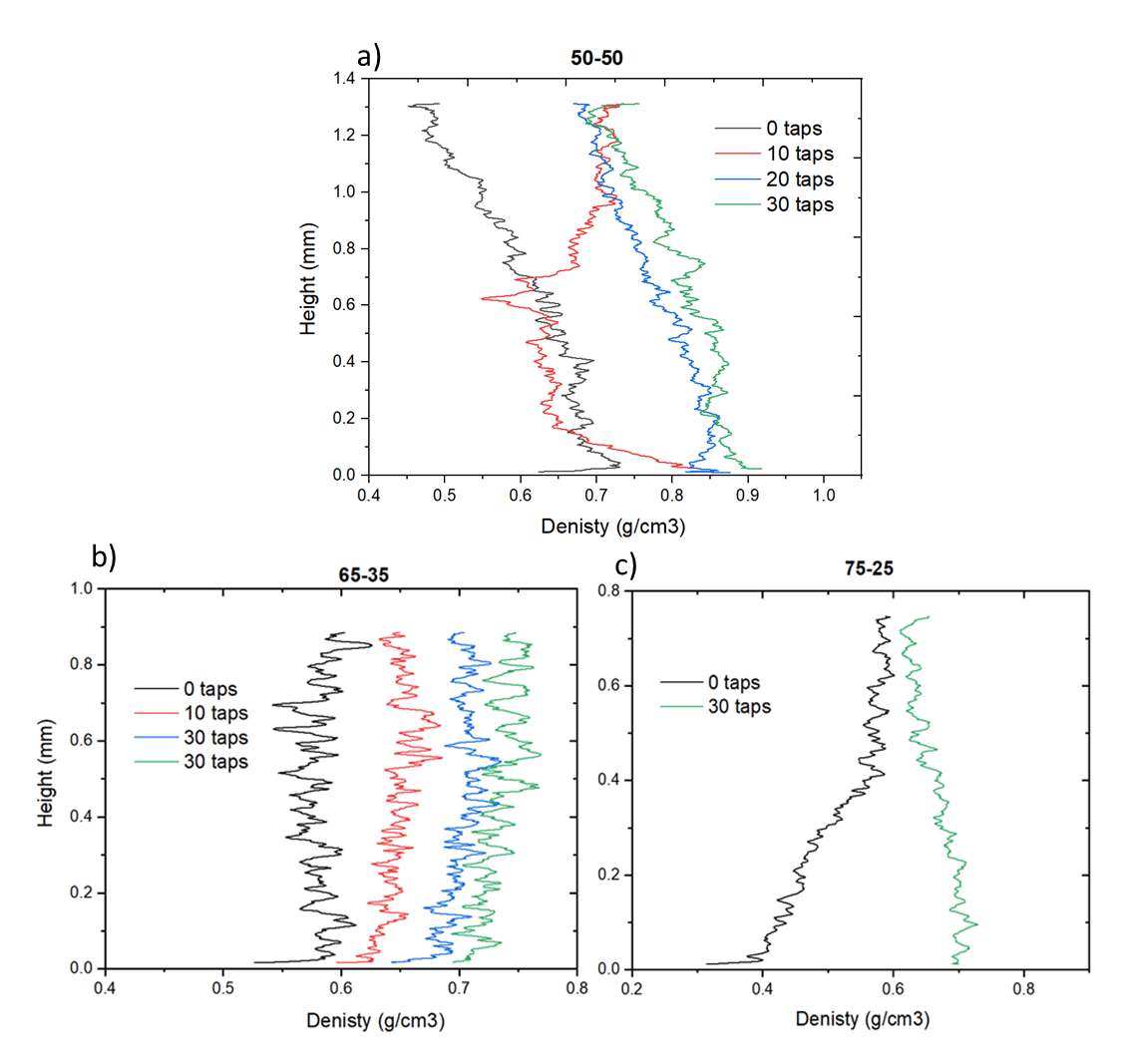


Figure 7-8. Variation in powder density of the bed height of powder mixtures, a) 50-50, b) 65-35 and c)75-25 function of the number of taps

The particle orientation of each powder blend is presented in Figure 7-9. The 50-50 and 65-35 powder blends largely prefer horizontal orientation. The initial state in all powders is likely randomly oriented, yet the 50-50 and 65-35 powders both start with a high percentage of 16.59 % and 17.18 % respectively. The 50-50 powder starts with a lower percentage of vertical powders of 14.20 %, compared to the 16.62 % in the 65-35 blend, and the percentage of angled particles is 10.85 % and 9.91 % respectively. As consolidation starts, the horizontal particles in the 50-50 blend slightly decrease to 16.43 % at 10 taps, then decrease further to 16.03 % at 20 taps and finally increase to 17.87 % at 30 taps. The horizontal particles in the 65-35 blend increase to 17.50 % at 10 taps, then 18.31 % at 20 taps. The horizontal particles slightly decrease to 18.17 % at 30 taps. At this stage, this blend has a higher percentage of vertical particles of 16.44 % than the 50-50 blend, which has 13.58 %. The increase in both vertical

and horizontal particles is likely due to particle interactions and packing dynamics. The larger amount of MA increases frictional cohesive forces, influencing some particles to remain vertical. The 65-35 blend may also create a less uniform packing structure than the 50-50 blend, potentially leading to a less dense powder. This coincides with the flow analysis above.

The 75-25 blend exhibits an even combination of vertical and horizontal particles at 17.28 % and 17.16 % respectively. At 30 taps, the number of horizontal particles decreases to 16.81 % and vertical particles increase to 18.32 %. This orientation reveals the inefficient powder packing of this blend caused by the larger amount of MA.

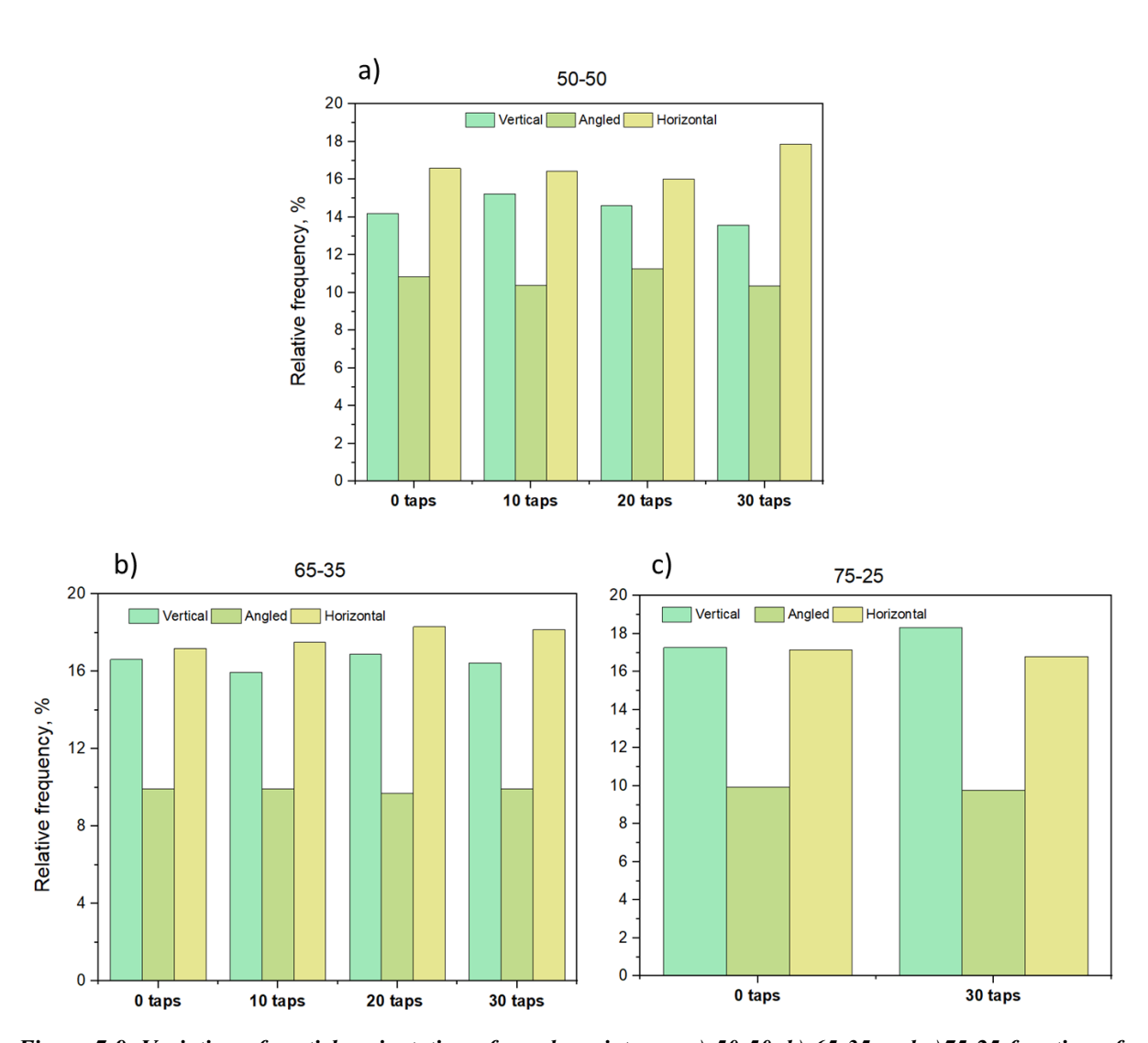


Figure 7-9. Variation of particle orientation of powder mixtures, a) 50-50, b) 65-35 and c)75-25 function of the number of taps

7.4 Tablet Analysis of Mefenamic acid and D-mannitol

Mefenamic acid, d-mannitol and mixtures of 50-50, 65-35, and 75-25 mefenamic acid to d-mannitol powders were compressed into 5 mm tablets at 4000 N \approx 204 MPa, for deeper analysis of their consolidation behaviour. This provides a better understanding of their different compaction properties and internal microstructure, and how the two compounds influence each other's properties. It should be noted that the XCT tablet analysis was conducted on a \approx 1 mm diameter region of each tablet.

7.4.1 Mefenamic acid tablet

Given MA's poor flowability properties, it is expected to exhibit poor compressibility properties, as the two are directly correlated. The MA tablet and its porosity network are displayed in Figure 7-10, a) and b) respectively. The 3D rendering of the pores in the tablet reveals a highly porous tablet with voids distributed throughout the entire compact. The tablet histogram provided in Figure 7-10 c) displays two density variations, and their quantified volume fractions are presented in Table 7-4. The data reveal that 79.06 % accounts for the MA particles, while 20.94 % accounts for the void space between the particles. This is in good correlation with the compressibility studies presented in Chapter 6, where the value for MA *E* is 0.22, corresponding to 22 % porosity.

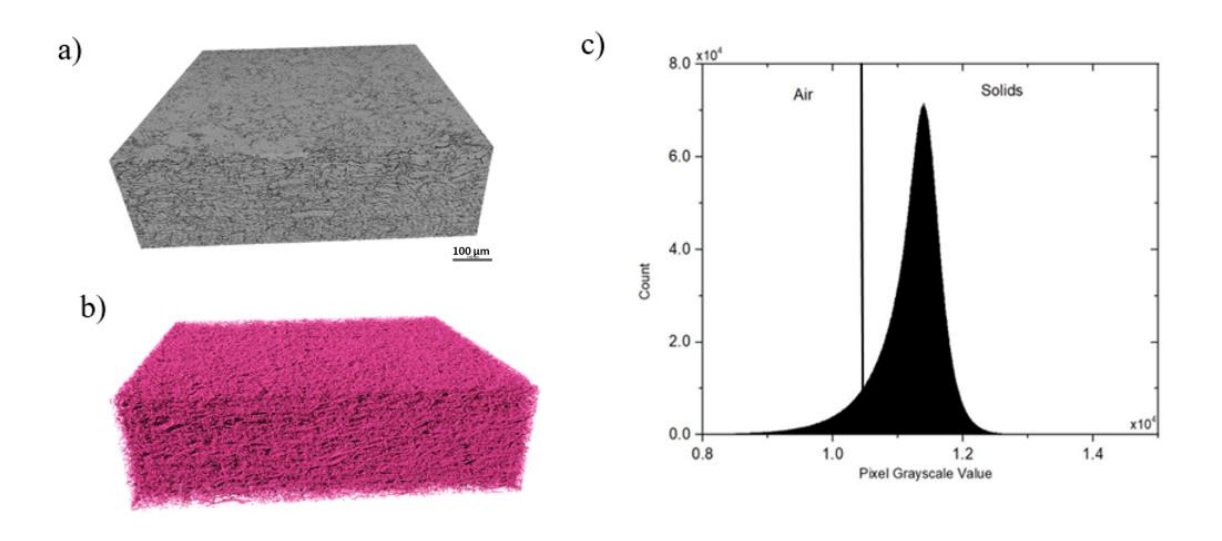


Figure 7-10 a) 3-D reconstructed image of mefenamic acid tablet, b) 3-D pore-network and c) grayscale histogram of the entire reconstructed XCT image of the mefenamic acid tablet

Table 7-4. Comparison of XCT-measured volume fraction vs. lab-measured compressibility of mefenamic acid

	Solids %	Pores %
XCT Volume fractions	79.06	20.94
Lab compressibility	78.00	22.00

The density distribution of the pore network of the MA tablet was further examined in the temperature map presented in Figure 7-11. The even distribution is more clearly visualised here, and a web-like pore network can be seen, with 'hotspots' of denser areas shown in red and low-density areas in blue. The XCT examination of the MA provides both qualitative and quantitative correlation to what is observed in the compaction studies in Chapter 6. This highly porous network confirms the poor tensile strength observed in MA.

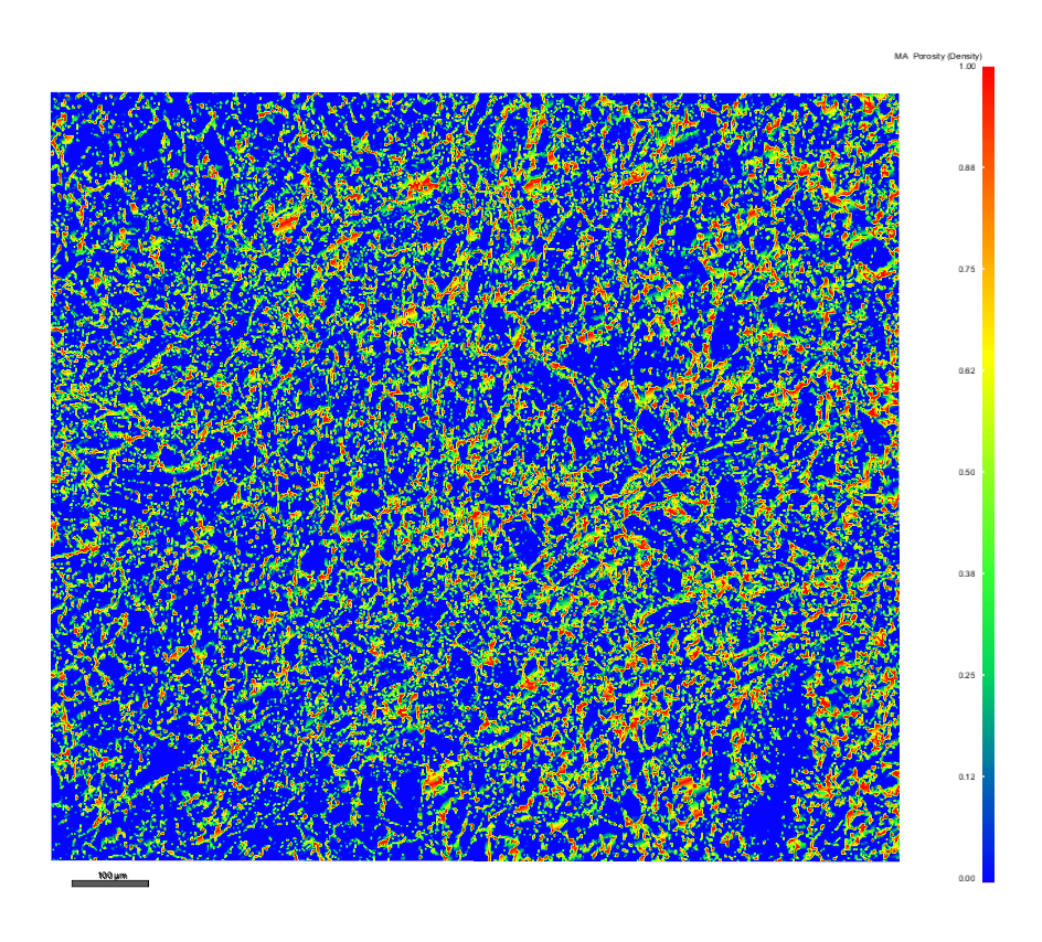


Figure 7-11. Temperature map of the density distribution of the pore network of mefenamic acid

7.4.2 D-mannitol

The DM tablet and its porosity are displayed in Figure 7-12, a) and b) respectively. The DM tablet scanned was produced before tool optimisation, as detailed in Chapter 6. The impact of poor tooling is evident in the 3D rendering of the pores, revealing a prominent crack running through the tablets.

The tablet histogram provided in Figure 7-12 c) displays two distinct density variations, which are presented in Table 7-5. Lab-measured compressibility was assessed for tablets produced after tool optimisation; as a result, they possess better compressibility properties than the XCT-scanned tablet. Nonetheless, XCT analysis confirms the superior compressibility of DM compared to MA.

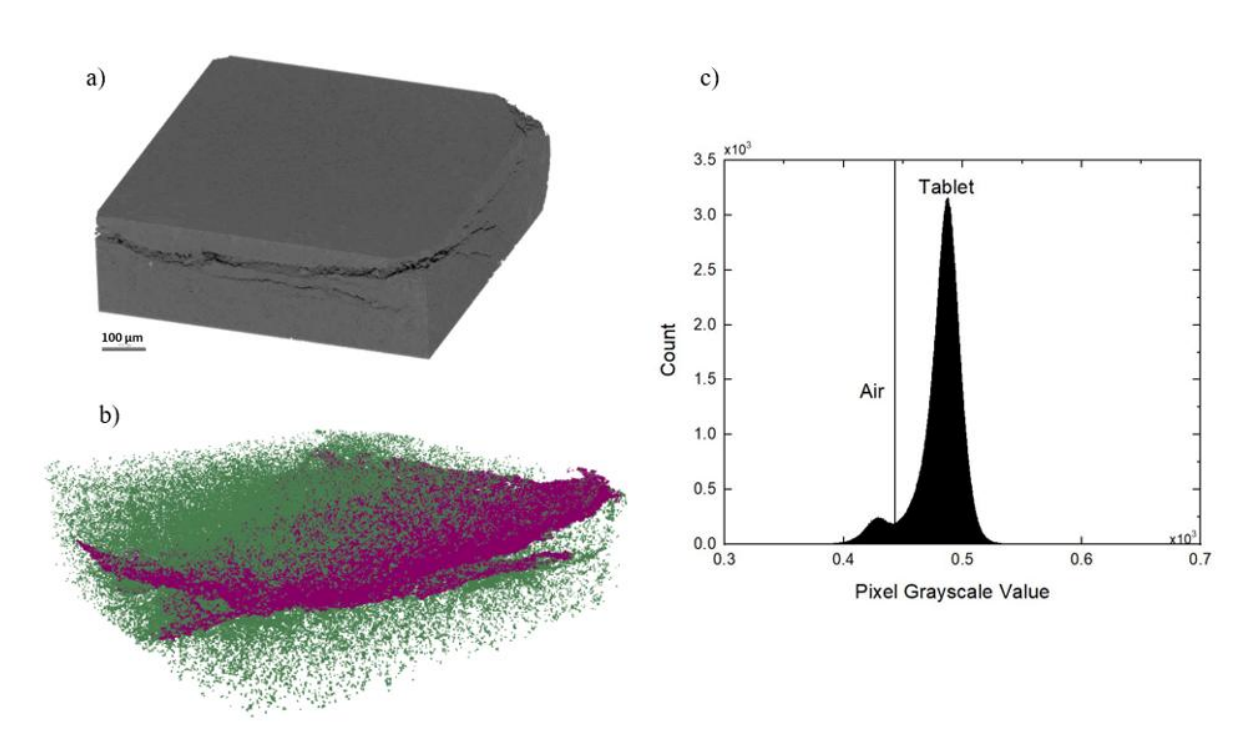


Figure 7-12. a) 3-D reconstructed image of d-mannitol tablet, b) 3-D pore-network and c) grayscale histogram of the entire reconstructed XCT image of the d-mannitol tablet

Table 7-5. Comparison of XCT-measured volume fraction vs. lab-measured compressibility of d-mannitol

	Solids %	Pores %
XCT Volume fractions	92.16	7.84 (crack: 5.52)
Lab compressibility	97	3

The temperature map of the DM porosity in Figure 7-13 a) illustrates blue areas of low pore density and red areas of high pore density. Most of the porosity in the tablet is attributed to the large crack, and Figure 7-13 b) displays a 3D rendering of this crack. This crack is likely a result of exacerbated diametrical expansion upon the ejection of a tablet. Poor tooling design can create areas of increased stress concentrations during both compression and ejection²⁴⁵. For tablets with poorer mechanical properties, this expansion can often lead to tablet capping or lamination, where the tablet breaks at the top layer or several layers.

In this case, the tablet remained intact upon ejection, indicating its relative strength. Without XCT analysis, this crack may go unnoticed, as the tablets still fall within the ideal solid fraction pharmaceutical range of 85 % to 95 %. Despite appearing structurally intact, the tablet may still fail other assessments, such as dissolution tests, depending on the required criteria. XCT analysis provides a deeper analysis into why tablets may perform well in certain aspects yet fail final quality testing, highlighting its benefit in pharmaceutical analysis²⁴⁶.

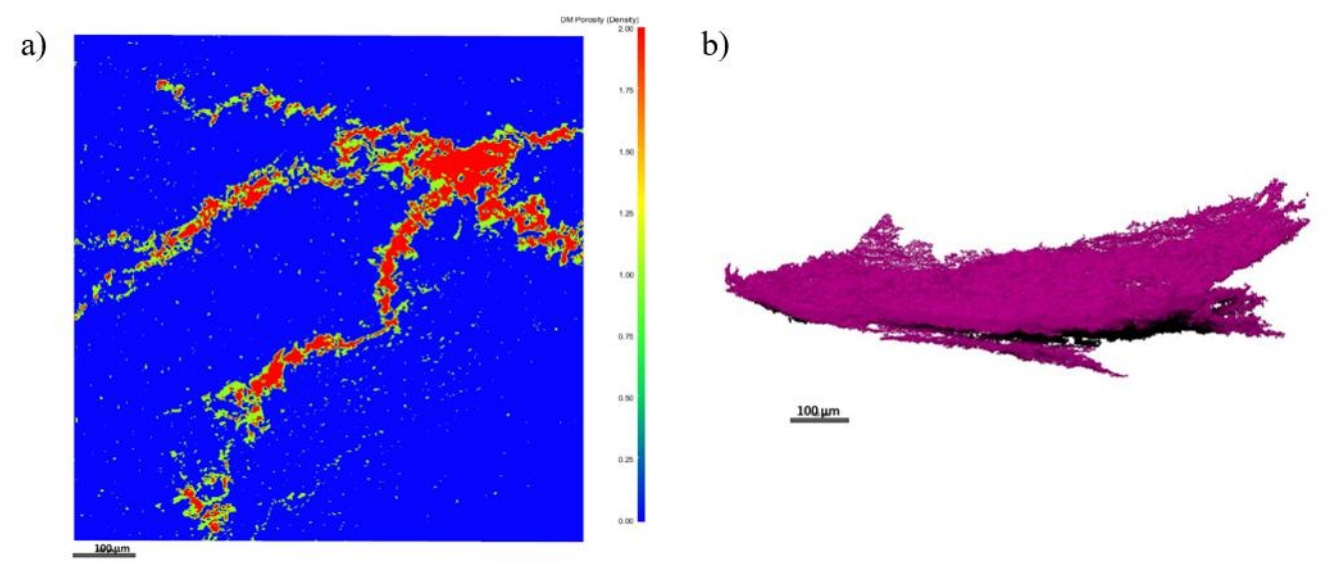


Figure 7-13, a) Temperature map of the d-mannitol pore network and b) 3D rendering of the internal crack

7.4.3 Orientation Analysis of Mefenamic acid and D-mannitol Tablet

The particle orientation of compacted DM and MA is presented in Figure 7-14. The results indicate an even distribution of vertical and horizontal particles in the DM tablet, accounting for 28.49 % and 28.75

% respectively. Angled particles account for 6.91 % of the particles. In contrast, MA exhibits a distinct orientation preference with vertical particles dominating with 21.90 %, followed by 15.77 % horizontal particles and 8.79 % angled particles.

As discussed in Chapter 5 and confirmed by literature, both DM and MA are primarily brittle compounds and deform by fragmentation. However, DM exhibit some plastic behaviour, as evident by its overall superior tabletability evaluated in Chapter 6. The reorientation of particles occurs due to applied stress, their morphology and interparticle interactions. Fragmentation further disrupts their initial orientation as particles are broken into smaller fragments. Additionally, plastic deformation also affects the orientation of particles as crystals align in response to the applied stress, often resulting in anisotropic particle arrangements²⁴⁷.

In the bulk powder state, DM particles predominantly adopt a horizontal orientation, followed by angled and then vertical. However, upon compression, the proportion of vertical particles is almost equal to horizontal particles. This shift results from compaction forces and reflects the higher plastic nature of DM compared to MA. The reorientation and subsequent interparticle bonding "locks in" the new arrangement, influencing mechanical strength. With DM's good compressibility, ideally, the horizontal particles are expected to be higher. Thus, the high number of vertical particles could be a combination of both its natural response to stress and the formation of the large crack, shifting particles to allow for stress relief.

MA particles, on the other hand, display a consistent preference in orientation in both bulk powder and compressed tablet. In the bulk state, horizontal particles dominate, whereas in the tablet, vertical orientation dominates. Assuming MA exhibits similar random orientation at the point of die filling as at 0 taps of the powder analysis, the compaction process has led to significant particle rearrangement. However, the clear preferences of one orientation above the other suggest a limited stress response and increased interparticle friction. This behaviour further explains MA's extensive pore network and lack of plastic deformation. It can also be suggested that both primary and fragmented particles maintain a preference for vertical orientation, displaying MA's resistance to stress. The shift from horizontal to vertical preference may also be a result of the fragmentation of primary particles. The results are

consistent with reported data on vertically aligned needle-shaped particles being prone to brittle fracture and poor mechanical strength²⁴⁴.

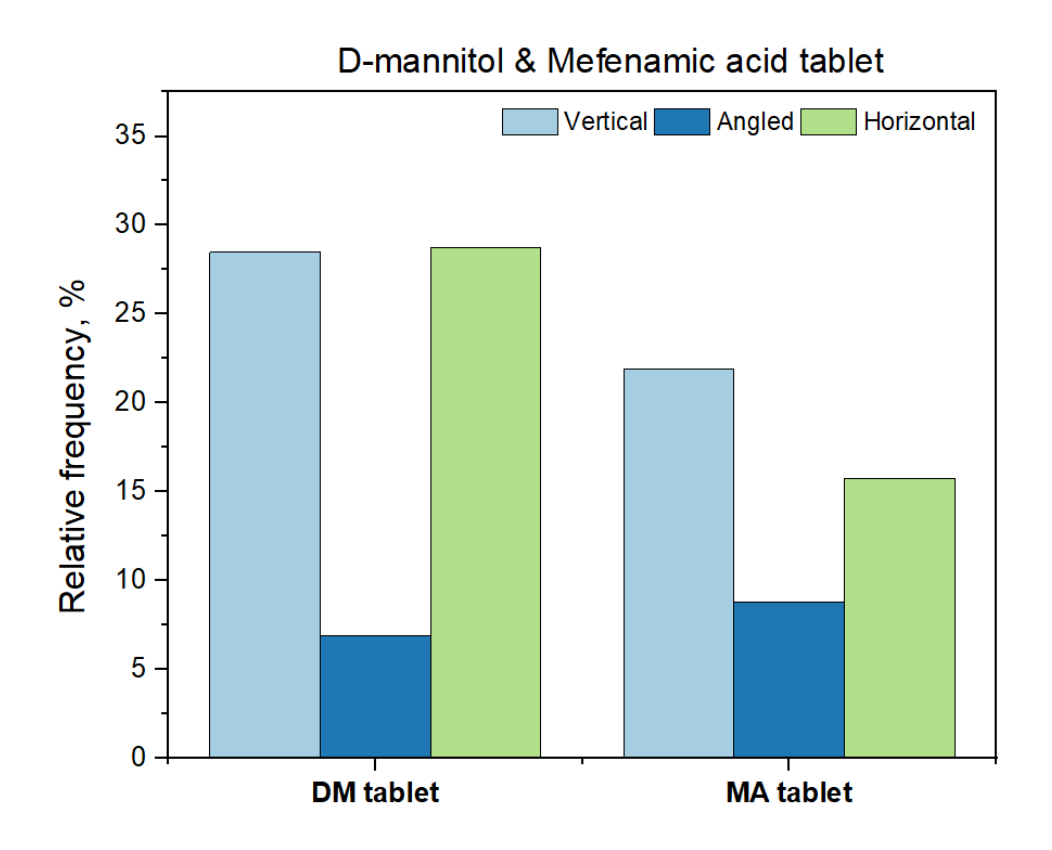


Figure 7-14. Particle orientation of d-mannitol and mefenamic acid tablets

7.5 Tablet Analysis of Mefenamic acid and D-mannitol binary mixtures

Following the method explained in Chapter 4, the mixing index of all formulated tablets was calculated to ensure tablet uniformity. The calculations reveal the 50-50 and 65-35 tablets have a mixing index of 0.91, indicating a well-mixed system. The 75-25 tablet also has a well-mixed system with a mixing index of 0.94, slightly more uniform than the other two tablets.

Table 7-6. Mixing Indices of 50-50, 65-35 and 75-25 mefenamic acid:d-mannitol tablets

Tablet	Mixing Index
50-50	0.91
65-35	0.91
75-25	0.94

7.5.1 50-50 tablet

The histogram analysis of the 50-50 tablet in Figure 7-15 c) reveals three distinct density variations, and the volume fractions are presented in Table 7-7. The MA particles are of lower density and account for 54.16 % of the tablet, while the denser DM particles account for 41.94 %. The remaining 3.9 % corresponds to the void spaces. The 3D porosity rendering in Figure 7-15 b) reveals the presence of laminar cracks are observed in, which account for 1.19 % of the void space.

It is often difficult to differentiate between two components in a mixture using XCT^{149,246}; however, due to the density variations between the two compounds and their different responses to stress, their volume fractions can still be well quantified. Indeed, the quantified volume fractions correlate well with the tablet compression analysis, where the value of E was 0.05, 5%.

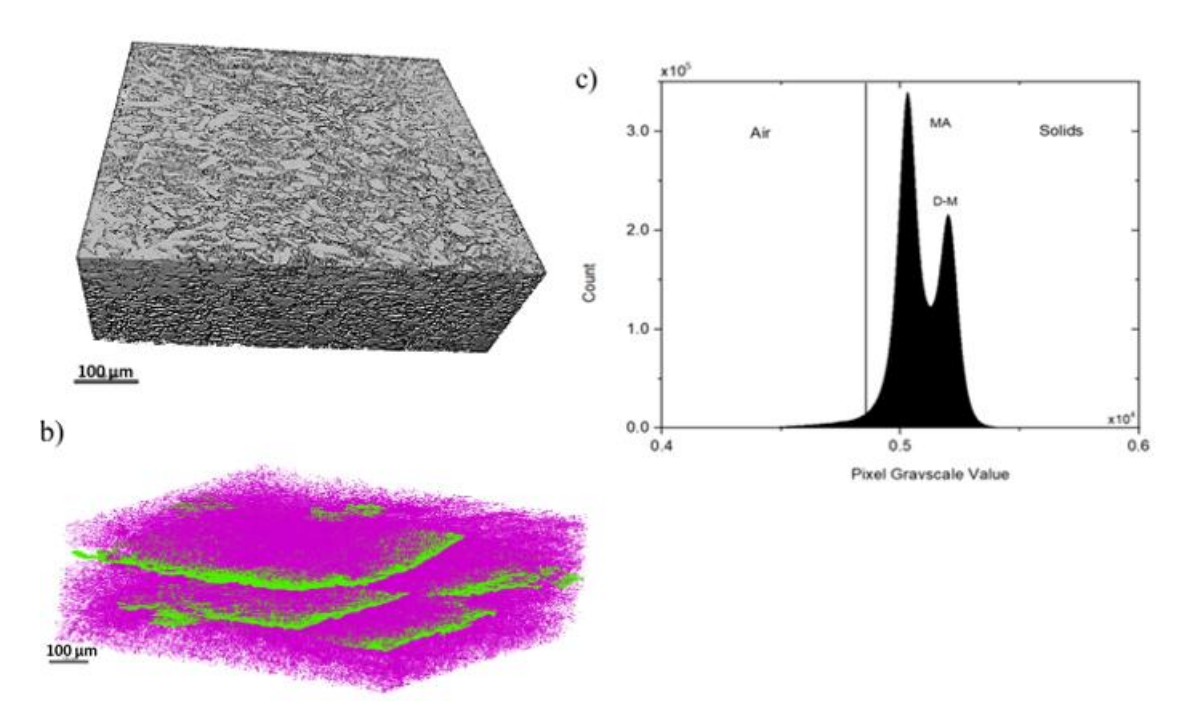


Figure 7-15. a) 3-D reconstructed image of the 50-50 tablet, b) 3-D pore-network and c) grayscale histogram of the entire reconstructed XCT image of the 50-50 tablet

Table 7-7. Comparison of XCT-measured volume fraction vs. lab-measured compressibility of the 50-50 tablet

	Solids, %	Porosity, %
XCT Volume fractions	96.1 (MA: 54.16, DM: 41.94)	3.9 (cracks: 1.19)
Lab compressibility	95	5

7.5.2 65-35 tablet

The 3D rendering of the 65-35 tablet and its porosity are presented in Figure 7-16, a) and b) and the tablet histogram in c). The three density variations observed in the histogram reveal that 67.24 % of the tablet accounts for the MA particles, 28.39 % the DM particles and 4.37 %. Compared to the 50-50 tablet, the MA and DM regions are not as distinct, thus there is a possibility of some overestimation of voxels labelled as MA and some underestimation of DM. Even so, the measured volume fractions are in relatively good alignment with the compression studies, where E was 0.06, 6 % (Table 7-8). The porosity in the tablet reveals regions of larger porosity, highlighted in green, accounting for 0.82 % of the void space.

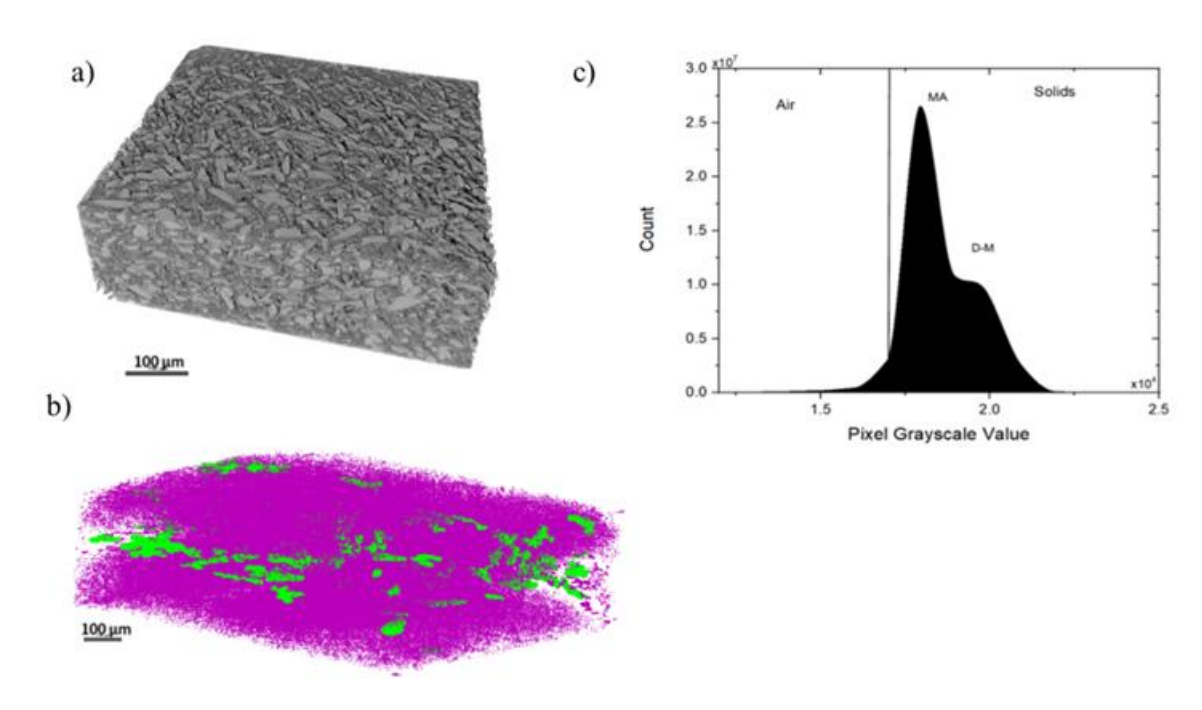


Figure 7-16. a) 3-D reconstructed image of the 65-35 tablet, b) 3-D pore-network and c) grayscale histogram of the entire reconstructed XCT image of the 65-35 tablet

Table 7-8. Comparison of XCT-measured volume fraction vs. lab-measured compressibility of the 65-35 tablet

	Solids, %	Porosity, %
XCT Volume fractions	95.63 (MA: 67.24, DM: 28.39)	4.37 (larger pores: 0.82)
Lab compressibility	94	6

7.5.3 75-25 Tablet

The 3D rendering of the 75-25 tablet and its porosity are visualised in Figure 7-17 a) and b), where, like the 50-50 tablet, laminar cracks are revealed (highlighted in green). The histogram of the 75-25 tablet (Figure 7-17 c) shows that density variations were MA accounts for 72.15 %, DM 22.10 % and 5.81 %. Over half of the void space is attributed to the cracks, being 3.18 %. The porosity measured by XCT is slightly lower than the lab-measured compressibility E of 8 %, nonetheless still consistent (Table 7-9).

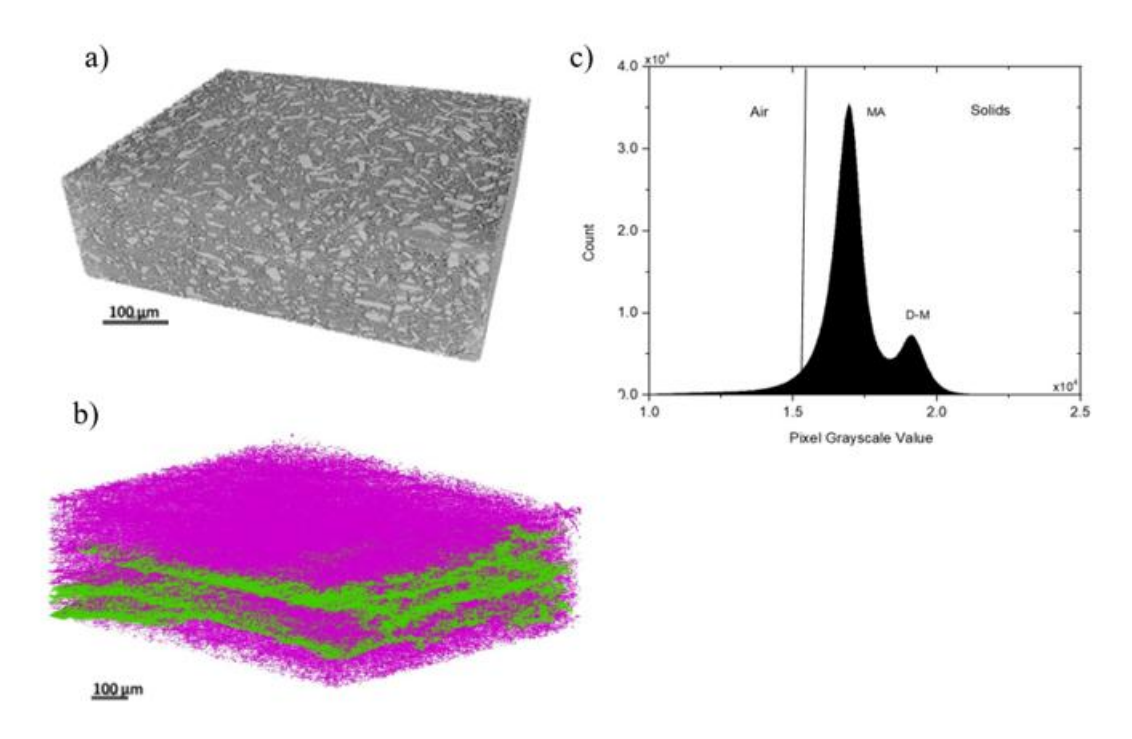


Figure 7-17. a) 3-D reconstructed image of the 75-25 tablet, b) 3-D pore-network and c) grayscale histogram of the entire reconstructed XCT image of the 75-25 tablet $_{100\,\mu m}$

Table 7-9. Comparison of XCT-measured volume fraction vs. lab-measured compressibility of the 75-25 tablet

	Solids, %	Porosity, %
XCT Volume fractions	94.19 (MA: 72.15, DM: 22.1)	5.81 (cracks: 3.18)
Lab compressibility	92	8

7.5.4 Comparison of Porosity

The temperature maps of the porosity density of the 50-50, 65-35 and 75-25 tablets are displayed in Figure 7-18 a), b), and c), respectively. The temperature maps reveal that the porosity density is not

evenly distributed throughout all the tablets. There are areas in red that correlate to the larger voids in the tablets. For tablets 50-50 and 75-25, these are the laminar cracks and 65-35 larger pockets of air.

The presence of laminar cracks in the 50-50 and 75-25 mixtures indicates structural weakness, likely due to poor interparticle bonding and diametrical expansion upon ejection. MAs' poor compressibility properties may hinder strong adhesion during tabletting. As the MA amount increases, there may be insufficient DM to facilitate effective fragmentation and bonding, leading to crack formation. In contrast, the presence of larger pores instead of cracks in 65-35 tablets indicates poor packing resulting in air entrapment during compaction. This uneven distribution of porosity in the tables indicates low tablet hardness. This correlates with the tensile strength measurements presented in Chapter 6. The tensile strength of 50-50 was 0.54 MPa, 65-35 was 0.42 MPa, and 75-25 was 0.18 MPa. All are below the acceptable tablet strength of solid dosage forms. The air pockets in the 65-35 tablet suggest structural vulnerability in the form of stress concentration points that could initiate mechanical failure upon pressure. Understanding these differences is crucial in tablet formulation optimisation to ensure quality tablets.

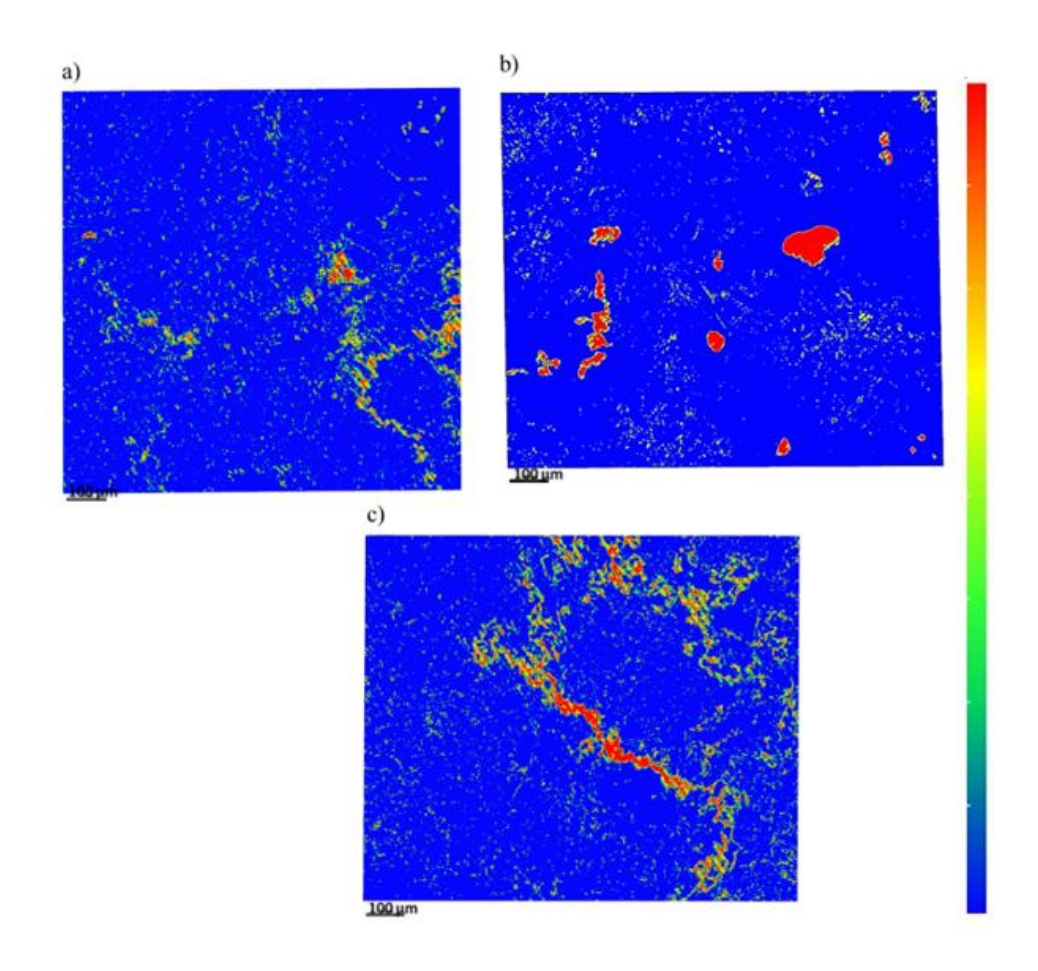


Figure 7-18. Temperature map of the a) 50-50, b) 65-35 and c) 75-25 tablet pore network

7.5.5 Orientation Analysis of Mefenamic acid-D-mannitol mixtures

The orientation analysis of the tablet mixtures is presented in The orientation analysis of the tablet mixtures is presented in Figure 7-19. The results show a fluctuation in the dominance of vertical particles as the proportion of MA is increased. The 50-50 tablet exhibits the highest percentage of vertical particles (33.73 %), which decreases in the 65-35 tablet (22.39 %) and before increases in the 65-35 tablet (27.71 %). Horizontal particles show an increase in the 65-35 tablet (29.67 %) compared to the 50-50 tablet (25.25 %) and then a decrease in the 75-25 tablet (19.30 %). Angled particles remain relatively consistent across all formulations, slightly increasing with increased MA: 50-50 (6.59 %), 65-35 (6.69 %) and 75-25 (7.41 %).

The addition of MA appears to shift particles to adopt a more vertical orientation, otherwise in the 65-35 tablet. The DM tablet showed a more balanced vertical to horizontal particle alignment than the pure MA tablet, which suggests that MA particles influence the vertical orientation.

The existence of laminar cracks in the 50-50 and 75-25 tablets and the absence of them in the 65-35 tablet may be the cause of the variation in particle orientation. The absence of these cracks in 65-35 indicates a more even stress distribution, and hence the particles can align themselves more horizontally without disruptions caused by cracking. In contrast, the existence of crack formation in the other tablets may lead to the particles realigning themselves either vertically or at an angle to permit stress relief. Hence, particles in 65-35 undergo a more stable particle rearrangement, favouring horizontal orientation.

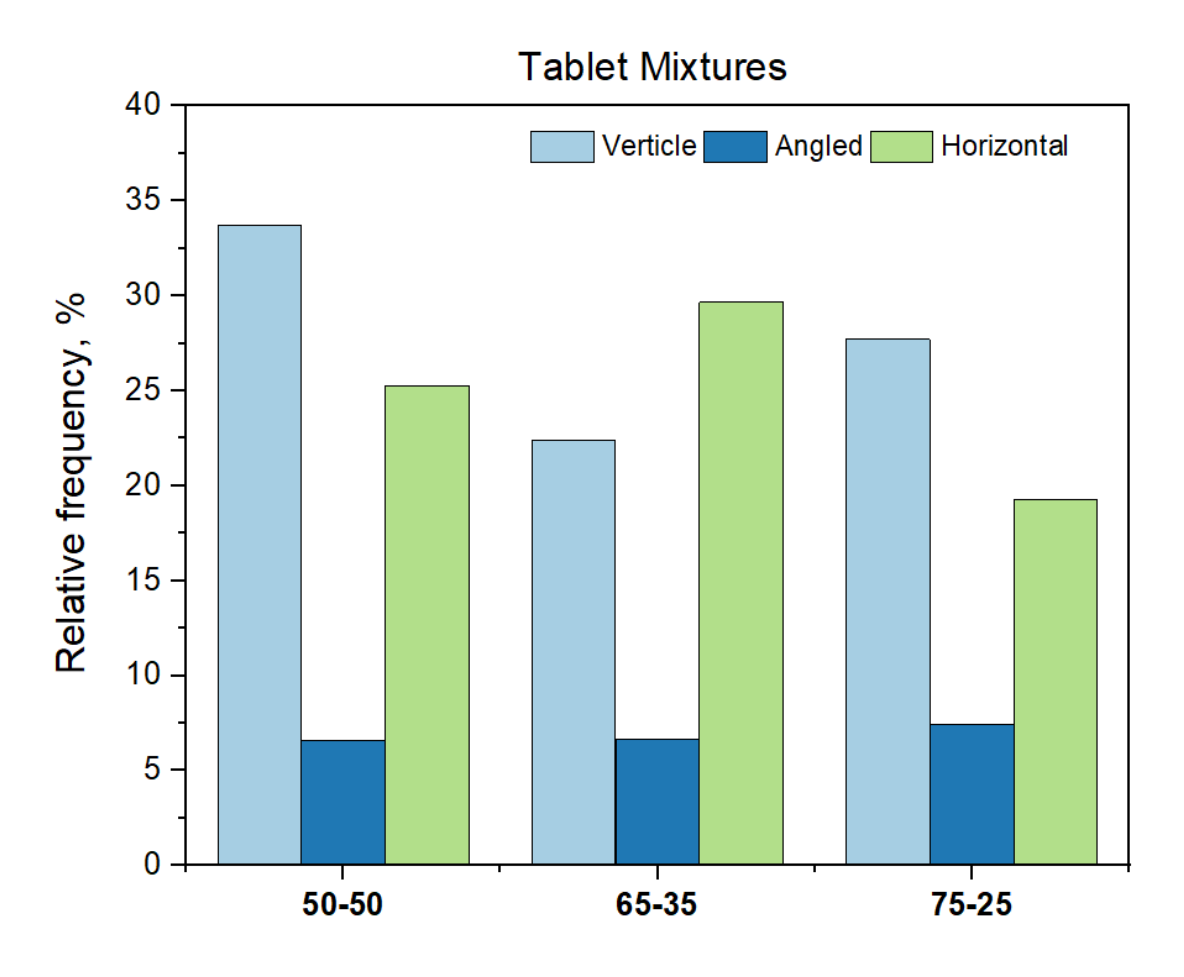


Figure 7-19. Variation of particle orientation of 50-50, 65-35 and 75-25 tablet mixtures

7.6 Discussion

The findings from this body of work demonstrate a clear relationship between molecular-scale interactions of mefenamic acid and d-mannitol and their bulk powder behaviour. The cohesive and adhesive interactions predicted in Chapter 5 directly correlate key processing properties, flow, compressibility and compactability.

7.6.1 Cohesive vs. Adhesive Interactions

The significance of good particle flow and compression has been highlighted throughout this work, and the various factors which influence it have been examined. Surface energy is one of these factors, and the cohesion and adhesion of pharmaceutical ingredients are highly dependent on it. Understanding how surface energy affects the cohesive and adhesive interactions is essential for the formulation optimisation of solid dosage forms.

Commonly, particles of higher surface energies possess stronger cohesive forces, resulting in particles of poor flow and agglomeration^{17,220,248}. This was the case observed when researchers studied the cohesive and adhesive strengths of various dry powder inhalation (DPI) drugs and excipient a-lactose monohydrate (LMH) using SystSearch¹⁷. LMH had the strongest cohesion interactions due to its high polarity, which was correlated to its high polar surface energy, measured by inverse gas chromatography (IGC). Ma et al. also used SystSearch to predict the cohesive and adhesive strengths of dry powder inhalation blends of the API terbutaline sulphate (TBS) and LMH. In this case, the TBS cohesion was higher than LMH, and this was correlated with TBS's higher surface energy compared to LMH.

However, in the case of the two model compounds, this is not the case. MA has a surface energy of 98.9 mJ/m² and DM 144.63 mJ/m², yet from the molecular modelling calculations, MA display stronger cohesive interaction energies. This is due to the nature and the strength of the intermolecular forces involved. The h-bonds in the carboxylic dimer synthon of MA are strong and directional (-7.94 kcal/mol, 1.69 Å), and the $\pi - \pi$ stacking further enhances cohesion between MA molecules. This results in strong cohesive forces (-9.14 kcal) and is driven by 93.53 % of dispersive interactions. The

result of this leads to the observed poor flowability and tendency to agglomerate (CI: 27.15, AOR: 44.55°).

On the contrary, the h-bonds in the strongest synthon of the DM particle are not as strong as in MA (-5.82 kcal/mol, 1.88 Å). Thus, its cohesion forces are weaker (-6.70 kcal/mol). They are driven by 58.55 % dispersive interactions and 41.45 % polar interactions. This more even balance of dispersive to polar interactions promotes a freer flowing powder verified by its measured good flowability (CI: 11.6, AOR: 29.20°).

The adhesive forces of DM are stronger than MA, -8.74 kcal/mol and -5.56 kcal/mol, respectively. Both are dominated by dispersive interactions to varying degrees, 91.03 % in MA and 75.29 % in DM. DM's extensive h-bond network and h-bonding potential on all its facets promote more evenly distributed interactions throughout the particle. This allows DM to be a good excipient for MA in formulation. It has low cohesion to itself and stronger cohesion to MA, promoting a homogeneous blend. This was confirmed in the 50-50 powder blend, having the best flow out of the three mixtures (CI: 22.57, AOR: 41.18°), improving the flow of pure MA. Increasing the MA ratio in the formulation resulted in poorer flow, reflecting the predicted poor adhesion of MA. As MA is increased, the cohesive interactions increase, overriding the favourable adhesive interactions DM provides. The result is a weak adhesive blend, increasing the potential for a segregated blend. The results are consistent with previous research suggesting that the addition of excipients with strong h-bonding potential improves powder blend uniformity and reduces segregation²⁴⁹. This is true for commonly used excipient microcrystalline cellulose, whose better flow and plasticity was attributed to high h-bonding potential. It was found to improve interparticulate bonding and improve blend composition^{249,250}.

7.6.2 Crystal Morphology and Powder Behaviour

The poor flow of MA is further explained by the predicted platy-bladed morphology via attachment energy. Literature has previously reported MA also growing in long needles in aprotic solvents^{26,209,210,233}. This thin, platy-bladed morphology tends to interlock and increase interparticle friction. XCT imaging provided visual evidence for this phenomenon and verified the lab-scale flow

measurements. The thin morphology also contributes to its brittle fracture under compression. MA exhibits poor compressibility (E: 0.22), exhibiting no plastic deformation (P_y: 370.37) and weak tablets (0.1 MPa). This is consistent with the predicted anisotropic nature of the MA crystal and its interactions. It was predicted to be brittle and deform by cleavage fracture, resulting in weak interparticle bonding and weak tablet strength. The porosity analysis of MA via XCT confirmed this prediction, aligning well with the lab compaction studies.

The columnar morphology of DM was well predicted by attachment energy calculations and facilitates better particle rearrangement, contributing to better packing and superior compressibility (E: 0.03). As predicted, its homogenous h-bond network allows for plastic deformation (P_y: 65.79 MPa) and leads to stronger interparticle bonding during compaction, resulting in better tablet strength (1.1 MPa).

The 50-50 tablet was the only tablet mixture that underwent plastic deformation (P_y: 95.24), highlighting the influence of DM's homogeneous h-bonding. DM reduced interparticle friction and enhanced bonding strength, further validating the molecular modelling predictions. However, the increased MA in the 65-35 and 75-25 tablet mixtures, the MA's brittle nature, dominated reducing plasticity, lowering bonding strength, resulting in weak tablets (0.42 MPa and 0.18MPa, respectively). The observed trend supports the notion that the choice of excipient must balance the properties of the API²⁵¹.

7.6.3 XCT Analysis and Microstructural Insights

The XCT analysis provided essential insights into the internal structure of the bulk powders and compacted tablets. The analysis allowed for factors influencing the mechanical properties and performance of solid dosage forms to be deduced. This enabled the molecular modelling, flow analysis and compaction results to be well validated. The modified tapping method for XCT by Turner et al.²⁵² proved to be sufficient to match lab-scale results. The slice analysis provided a good understanding of the consolidation patterns of the powder bed.

Significant differences in the bonding networks and porosity between pure MA, pure DM and their binary mixtures were identified in the XCT analysis. A highly porous structure with weak particle

bonding was exhibited in the tablets, entirely composed of MA. This aligns with its poor compressibility and brittle nature. MA's lack of effective plastic deformation resulted in weak interparticle adhesion. This contributes to low tablet strength and an increased likelihood of defects, including capping and lamination. These observations are supported by the compaction study findings, where increased propensity to mechanical failure and low tensile strength were found in MA-based tablets. The dominance of vertical orientation could be related to the observed poor compression and low tensile strength.

DM, on the other hand, displayed lower porosity, suggesting good interparticle interactions. More mechanically robust tablets were yielded due to DM's ability to undergo plastic deformation during compression, which produced stronger bonding and increased particle contact. The influence of poor tooling was also observed in DM by the large crack, highlighting how tooling can affect the quality of a tablet of good compressibility^{253,254}. The equal balance of vertical and horizontal particles was also correlated to DM's superior tabletting properties.

The effect of 50 % DM was observed and validated by lab-scale results in improving the flow of MA and compaction of MA. Whilst increasing the MA content increased porosity, and even larger cracks were observed in the 75-25 tablet. The microstructural observations were also correlated to their particle orientations. The 50-50 and 75-25 tablets dominated in vertical particles, and horizontal in the 65-35, which didn't have any cracks.

In pharmaceutical formulation development, these results highlight the importance of microstructural analysis. Porosity patterns of tablets directly influence their dissolution behaviour. Therefore, XCT analysis can explain why a seemingly good tablet is not achieving the desired dissolution performance. By so doing, the appropriate adjustments can be made, whether that is particle engineering-based, receipt compatibility or changing compaction parameters.

Incorporating XCT imaging with complementary analytical techniques provides a more comprehensive understanding of the interplay between molecular interactions, powder properties and tablet microstructure. Consequently, more informed decisions can be made in optimising formulation

composition and processing parameters. Minimising the reliance on approaches through trial-and-error and increasing the development of solid dosage forms that are of high quality.

CHAPTER EIGHT

Conclusions and Future Work

The chapter concludes the research, providing a review of the initial objectives, a summary of key findings and suggestions for future work.

8 Conclusions and Future Work

This PhD work sought to unravel the mechanisms underpinning the flow and compaction behaviour of pharmaceutical ingredients. The project focused on how their surface and bulk properties, and how the formulation compositions influence their processability. Using the model API, mefenamic acid (MA) and excipient d-mannitol (DM), a multi-scale approach was applied, combining molecular modelling, experimental and XCT techniques.

The success of the contribution of this work is evaluated by revisiting each of the initial objectives outlined in section 1.2. Suggestions for future work to expand the current research are also presented.

8.1 Revisiting Initial Aims and Objectives

Objective 1: Selection of model compounds with varied sticking propensities for investigation of their crystal and bulk powder properties.

Achieved:

- As sticking is a common industry problem in relation to cohesive APIs, a review of problematic
 APIs was conducted. MA was chosen as a deliberate investigation of its cohesive and adhesive
 interactions with excipients on the molecular scale were not found in literature.
- DM was chosen as a model excipient as it was reported to be less cohesive in sticking literature.
 It is a common excipient used in the pharmaceutical industry; therefore, a deeper analysis of both compounds is valuable and can support future research.
- Their crystal and bulk powder properties were investigated using methods outlined in objectives
 2-4

The findings of this work establish a clear link to the common punch-sticking issue. The modelling results predicted that MA has significantly stronger self-adhesion than DM. As discussed in the literature review, severe punch-sticking arises when API-API cohesion dominates – a condition which MA meets. Even though extensive sticking experiments were beyond the adapted scope of this project,

preliminary observations during the placement at Pfizer confirmed that MA exhibited substantial punchsticking, validating the modelling predictions.

Objective 2: Use of molecular modelling tools to investigate the molecular, solid-state, surface, and particle properties of selected compounds.

Achieved:

- Comparison of their molecular structure and descriptors provided the foundation in understanding their differences, particularly MAs' hydrophobic/lipophilic nature and DMs' hydrophilic/lipophobic nature.
- Momany forcefield provided accurate lattice energies calculations, and intrinsic synthons and their strengths were successfully identified.
- Attachment energy calculations provided good predictions of particle morphologies,
 calculations and extrinsic synthon at each face were identified. Surface energies were
 calculated, revealing that MA has lower surface energies but stronger extrinsic synthons.
- Prediction of mechanical properties predicted cleavage fracture of both particles, but potential for plastic deformation in DM.

Objective 3: Identify what structural properties drive the cohesion-adhesion mechanisms involved

Achieved:

- SystSearch analysis allowed for calculations of the cohesion and adhesion interactions. The nature of these calculations was successfully identified.
- MAs have stronger cohesion, driven by dispersive $\pi \pi$ and strong h-bond interactions. Its adhesion was significantly weaker, still driven by dispersive interactions.
- DM's cohesion was weaker than MA and is driven by an even balance of dispersive and polar interactions, with dispersive being slightly higher. Its adhesion to MA was strong, and dispersive interactions increased significantly.

Objective 4: Characterise flow and compressibility and determine to what extent API-excipient interactions affect compaction.

Achieved

- The smaller particle size and platy-bladed morphology of MA were linked to its poor flow and compressibility, resulting in weak tablets.
- DM is slightly larger and bulkier, and had better flow, underwent plastic deformation and produced strong tablets.
- The influence of DM was seen best in the 50-50 mixture, improving flow, compressibility and tablet strength. The 65-35 and 75-25 mixture declined in these properties, yet was still stronger than pure MA.
- XCT verified experimental observations and composition ratio effects on tablet quality. The
 orientation analysis gave insight into particle contact area, relating it to probable face contact
 and observed deformation.

The research has highlighted the importance of excipients with high h-bonding capabilities, which can reduce the effect of API cohesion driven by high dispersive interactions.

Overall, the objectives were met, and the findings of this work suggest that future development should focus on the development of predictive models, particularly the surface interactions of multi-component systems, to aid pre-screening and formulation development between APIs and excipients.

8.2 Suggestions for Future Work

As explained in section 1.4, time constraints and effects of the global pandemic meant that directions of the research had to be altered.

Ideally, larger batches of MA and DM would have been recrystallised, enough to perform the flow and compaction measurement as well as XCT analysis. This would have provided a clearer analysis of the effect of specific morphologies, and stress planes would have been more easily deduced experimentally. Alternatively, growing larger single crystals of both compounds would have allowed for nano-

indentation experiments and atomic force microscopy to validate cohesion and adhesion predictions. Inverse gas chromatography can also be used to validate cohesion and adhesion mechanisms.

To further understand the effect of the API-excipient ratio, intermediate ratios and ratios of larger DM quantity should be analysed similarly. Additionally, adding experimental analysis of the tablets' elastic recovery would further correlate with XCT observation, as the current compression-compaction analysis records in-die conditions.

The molecular modelling prediction of interaction energies could be developed further by analysing face-to-face interactions. This is, of course, more computationally challenging. However, it would provide an even more accurate view of real-life conditions. This can even inform particle engineering methods in tailoring the exposure of desired facets.

Due to the restricted time provided for beam-time access, repeat scans of the XCT samples were not possible. Ideally, repeating scans would provide greater robustness to the method used. Higher resolution scans take very long to scan; however, doing this will provide better 3D visualisation, making it easier to observe face-specific fragmentation and/or stress planes.

The presented study can move forward in various directions; nonetheless, it provides a good foundation for understanding the nature and behaviour of mefenamic acid and d-mannitol.

9 References

- (1) Statista. *Pharmaceutical market Statistics & Facts*. https://www.statista.com.
- (2) Research, G. V. Pharmaceutical Market Size, Share & Trends Analysis Report. https://www.grandviewresearch.com.
- (3) McKinsey & Company. *The Future of the Pharmaceutical Industry: Trends and Opportunities*; 2023.
- (4) Desai, P.; Vaerenbergh, G.; Holman, J.; Liew, C.; Heng, P. Continuous Manufacturing: The Future in Pharmaceutical Solid Dosage Form Manufacturing. *Pharm Bioprocess* **2015**, *3*, 357–360. https://doi.org/10.4155/pbp.15.19.
- (5) Desai, P.; Vaerenbergh, G.; Holman, J.; Liew, C.; Heng, P. Continuous Manufacturing: The Future in Pharmaceutical Solid Dosage Form Manufacturing. *Pharm Bioprocess* **2015**, *3*, 357–360. https://doi.org/10.4155/pbp.15.19.
- (6) Zhou, Q. T.; Li, T. Formulation and Manufacturing of Solid Dosage Forms. *Pharm Res* 2018, 36 (1), 16. https://doi.org/10.1007/s11095-018-2547-6.
- (7) Mullin, J. W. Crystallization (4th Ed.); 2001. https://doi.org/10.1016/B978-075064833-2/50005-X.
- (8) Rasenack, N.; Müller, B. W. Crystal Habit and Tableting Behavior. *Int J Pharm* **2002**. https://doi.org/10.1016/S0378-5173(02)00296-X.
- (9) Shi, L.; Sun, C. C. Overcoming Poor Tabletability of Pharmaceutical Crystals by Surface Modification. *Pharm Res* **2011**. https://doi.org/10.1007/s11095-011-0518-2.
- (10) Yu, Z. Q.; Chew, J. W.; Chow, P. S.; Tan, R. B. H. Recent Advances in Crystallization Control.
 Chemical Engineering Research and Design 2007. https://doi.org/10.1205/cherd06234.
- (11) Chavda, H. V.; Patel, C. N.; Anand, I. S. Biopharmaceutics Classification System. *Systematic Reviews in Pharmacy* **2010**, *I* (1), 62–69. https://doi.org/10.4103/0975-8453.59514.

- (12) Sun, C. C. Materials Science Tetrahedron A Useful Tool for Pharmaceutical Research and Development. *Journal of Pharmaceutical Sciences*. 2009. https://doi.org/10.1002/jps.21552.
- (13) Moldovan, A. A.; Rosbottom, I.; Ramachandran, V.; Pask, C. M.; Olomukhoro, O.; Roberts, K. J. Crystallographic Structure, Intermolecular Packing Energetics, Crystal Morphology and Surface Chemistry of Salmeterol Xinafoate (Form I). *J Pharm Sci* 2017. https://doi.org/10.1016/j.xphs.2016.11.016.
- (14) Hammond, R. B.; Hashim, R. S.; Ma, C.; Roberts, K. J. Grid-Based Molecular Modeling for Pharmaceutical Salt Screening: Case Example of 3,4,6,7,8,9-Hexahydro-2H-Pyrimido (1,2-a) Pyrimidinium Acetate. *J Pharm Sci* 2006. https://doi.org/10.1002/jps.20657.
- (15) Walker, E. M.; Roberts, K. J.; Maginn, S. J. A Molecular Dynamics Study of Solvent and Impurity Interaction on the Crystal Habit Surfaces of ∈-Caprolactam. *Langmuir* 1998. https://doi.org/10.1021/la970444h.
- (16) Rosbottom, I.; Pickering, J. H.; Etbon, B.; Hammond, R. B.; Roberts, K. J. Examination of Inequivalent Wetting on the Crystal Habit Surfaces of RS-Ibuprofen Using Grid-Based Molecular Modelling. *Physical Chemistry Chemical Physics* 2018, 20 (17), 11622–11633. https://doi.org/10.1039/c7cp08354h.
- (17) Ramachandran, V.; Murnane, D.; Hammond, R. B.; Pickering, J.; Roberts, K. J.; Soufian, M.; Forbes, B.; Jaffari, S.; Martin, G. P.; Collins, E.; Pencheva, K. Formulation Pre-Screening of Inhalation Powders Using Computational Atom-Atom Systematic Search Method. *Mol Pharm* 2015. https://doi.org/10.1021/mp500335w.
- (18) Rantanen, J.; Khinast, J. The Future of Pharmaceutical Manufacturing Sciences. *Journal of Pharmaceutical Sciences*. 2015. https://doi.org/10.1002/jps.24594.
- (19) McCormick, D. Evolutions in Direct Compression. *Pharmaceutical Technology*. 2005.
- (20) Paul, S.; Wang, K.; Taylor, L. J.; Murphy, B.; Krzyzaniak, J.; Dawson, N.; Mullarney, M. P.; Meenan, P.; Sun, C. C. Dependence of Punch Sticking on Compaction Pressure—Roles of

- Particle Deformability and Tablet Tensile Strength. *J Pharm Sci* **2017**, *106* (8), 2060–2067. https://doi.org/10.1016/j.xphs.2017.04.059.
- Waimer, F.; Krumme, M.; Danz, P.; Tenter, U.; Peter, P.; Schmidt, C.; Waimer, F.; Krumme, M.; Danz, P.; Tenter, U.; Peter, P.; Waimer, F.; Krumme, M.; Danz, P.; Tenter, U.; Schmidt, P.
 C. A Novel Method for the Detection of Sticking of Tablets A Novel Method for the Detection of Sticking of Tablets. 1999, 7450. https://doi.org/10.1081/PDT-100101371.
- (22) Simmons, D. M.; Gierer, D. S.; Simmons, D. M.; Gierer, D. S. A Material Sparing Test to Predict Punch Sticking during Formulation Development A Material Sparing Test to Predict Punch Sticking during Formulation Development. 2012, 9045. https://doi.org/10.3109/03639045.2011.637933.
- (23) Paul, S.; Taylor, L. J.; Murphy, B.; Krzyzaniak, J.; Dawson, N.; Mullarney, M. P.; Meenan, P.; Sun, C. C. Mechanism and Kinetics of Punch Sticking of Pharmaceuticals. *J Pharm Sci* 2017, 106 (1), 151–158. https://doi.org/10.1016/j.xphs.2016.07.015.
- (24) Boughton, P. Quality by design in biomanufacturing. https://www.scientistlive.com/content/quality-design-tableting.
- (25) Pringsheim, T.; Davenport, W. J.; Dodick, D. Acute Treatment and Prevention of Menstrually Related Migraine Headache. *Neurology* **2008**, *70* (17), 1555–1563. https://doi.org/10.1212/01.wnl.0000310638.54698.36.
- (26) Waknis, V.; Chu, E.; Schlam, R.; Sidorenko, A.; Badawy, S.; Yin, S.; Narang, A. S. Molecular Basis of Crystal Morphology-Dependent Adhesion Behavior of Mefenamic Acid During Tableting. 2014, 160–172. https://doi.org/10.1007/s11095-013-1149-6.
- (27) Shah, U. V; Olusanmi, D.; Narang, A. S.; Hussain, M. A.; Gamble, J. F.; Tobyn, M. J.; Heng, J. Y. Y. Effect of Crystal Habits on the Surface Energy and Cohesion of Crystalline Powders. *Int J Pharm* 2014, 472 (1–2), 140–147. https://doi.org/10.1016/j.ijpharm.2014.06.014.

- (28) Nurhikmah, W.; Sumirtapura, Y. C.; Pamudji, J. S. Dissolution Profile of Mefenamic Acid Solid Dosage Forms in Two Compendial and Biorelevant (FaSSIF) Media. *Sci Pharm* **2016**, *84* (1), 181–190. https://doi.org/10.3797/scipharm.ISP.2015.09.
- Yokoyama, R.; Kimura, G.; Schlepütz, C. M.; Huwyler, J.; Puchkov, M. Modeling of Disintegration and Dissolution Behavior of Mefenamic Acid Formulation Using Numeric Solution of Noyes-Whitney Equation with Cellular Automata on Microtomographic and Algorithmically Generated Surfaces. *Pharmaceutics* 2018, 10 (4). https://doi.org/10.3390/pharmaceutics10040259.
- (30) Paul, S.; Taylor, L. J.; Murphy, B.; Krzyzaniak, J. F.; Dawson, N.; Mullarney, M. P.; Meenan, P.; Sun, C. C. Powder Properties and Compaction Parameters That Influence Punch Sticking Propensity of Pharmaceuticals. *Int J Pharm* 2017, 521 (1–2), 374–383. https://doi.org/10.1016/j.ijpharm.2017.02.053.
- (31) Goodstein, D. L. States of Matter; Courier Corporation, 2014.
- (32) Miller, W. H. *A Treatise on Crystallography*; Printed at the Pitt Press, for J. & JJ Deighton, 1839.
- (33) Ashcroft, N. W.; Mermin, N. D. Solid State Physics. *Solid State Physics*. 1976. https://doi.org/10.1016/0038-1101(66)90069-4.
- (34) Chan, C. D. N. Exemple d'indices de Miller de Directions. 2005.
- (35) Chan, C. D. N. Exemple de Plans Cristallographiques et de Leurs Indices de Miller Pour Une Structure Cubique. 2010.
- (36) Bravais, A. Études cristallographiques; Gauthier-Villars: Paris, 1866.
- (37) Pastori, G.; Grosso, G. Geometrical Description of Crystals: Direct and Reciprocal Lattices. In *Solid State Physics*; Elsevier, 2014; p 71.
- (38) Perkins, D. Point Groups and Crystal Systems. In *Minerolgy*; University of North Dakota, 2023.

- (39) Föll, H. Defects in Crystals; 2019.
- (40) Jr, C.; D, W. Materials Science & Engineering: An Introduction. *Anti-Corrosion Methods and Materials* **2000**, *47*. https://doi.org/10.1108/acmm.2000.12847aae.001.
- (41) DaniFeri. Point Defects in Crystal Structures: Insterstitial and Substitutional Atom, Vacancy, Frenkel Defect. 2011. https://commons.wikimedia.org/wiki/File:Point defects in crystal structures.svg.
- (42) Knowles, K. M.; Kelly, A. A. *Crystallography and Crystal Defects*, 2nd Revise.; John Wiley and Sons Ltd: Hoboken, United States, 2012.
- (43) Perfect and Faulted Stacking Sequence for an Fcc Crystal. https://www.tf.uni-kiel.de/matwis/amat/iss/kap 5/illustr/stacking fault main.png.
- (44) Morris Jr, J. W. Defects in Crystals. *Materials Science*.
- (45) Hull, D.; Bacon, D. J. *Introduction to Dislocations Volume 37 of Materials Science and Technology*, 5th ed.; Materials science and technology; Elsevier Science, 2011.
- (46) Halfpenny, P. J.; Roberts, K. J.; Sherwood, J. N. Dislocations in Energetic Materials: I. the Crystal Growth and Perfection of Pentaerythritol Tetranitrate (PETN). *J Cryst Growth* 1984, 67
 (2), 202–212. https://doi.org/https://doi.org/10.1016/0022-0248(84)90179-9.
- (47) Anderson, P. M.; Hirth, J. P.; Lothe, J. *Theory of Dislocations*; Cambridge University Press, 2017.
- (48) Sir, Alan Howard, C. The Mechanical Properties of Matter; Wiley: New York, NY, 1964.
- (49) Couret, A.; Caillard, D. An in Situ Study of Prismatic Glide in Magnesium—I. The Rate Controlling Mechanism. *Acta metallurgica* **1985**, *33* (8), 1447–1454.
- (50) Callister, W. D.; Rethwisch, D. G. Fundamentals of Materials Science and Engineering: An Integrated Approach. *Wiley* **2015**, 964.

- (51) Heaney, P. J.; Prewitt, C. T.; Gibbs, G. V. Volume 29: Silica: Physical Behavior, Geochemistry, and Materials Applications.
- (52) J.-O., H.; U.J., G.; A., B. Polymorphism of Drug Substance. An Economic Challenge.

 Pharmazeutische Industrie 1997.
- (53) Polymorphs. In *Solid State Properties of Pharmaceutical Materials*; John Wiley & Sons, Ltd, 2017; pp 22–37. https://doi.org/10.1002/9781119264408.ch2.
- (54) Censi, R.; Martino, P. Di. Polymorph Impact on the Bioavailability and Stability of Poorly Soluble Drugs. **2015**, 18759–18776. https://doi.org/10.3390/molecules201018759.
- (55) Bond, A. *Pharmaceutical Crystallography: A Guide to Structure and Analysis*; Royal Society of Chemistry, 2019.
- (56) Bauer, J.; Spanton, S.; Henry, R.; Quick, J.; Dziki, W.; Porter, W.; Morris, J. Ritonavir: An Extraordinary Example of Conformational Polymorphism. *Pharm Res* **2001**, *18* (6), 859–866. https://doi.org/10.1023/A:1011052932607.
- (57) Dunitz, J. D.; Gavezzotti, A. Molecular Recognition in Organic Crystals: Directed Intermolecular Bonds or Nonlocalized Bonding? *Angewandte Chemie - International Edition*. 2005. https://doi.org/10.1002/anie.200460157.
- (58) Atkins, P. W.; De Paula, J.; Keeler, J. Atkins' Physical Chemistry; Oxford university press, 2023.
- (59) Housecroft, C. E.; Constable, E. C. Chemistry: An Introduction to Organic, Inorganic and Physical Chemistry; Pearson education, 2010.
- (60) Israelachvili, J. N. Intermolecular and Surface Forces; Academic press, 2011.
- (61) Hammond, R. B.; Pencheva, K.; Roberts, K. J. A Structural-Kinetic Approach to Model Face-Specific Solution/Crystal Surface Energy Associated with the Crystallization of Acetyl Salicylic Acid from Supersaturated Aqueous/Ethanol Solution. Cryst Growth Des 2006. https://doi.org/10.1021/cg0505618.

- (62) Price, S. L. Computational Prediction of Organic Crystal Structures and Polymorphism.
 International Reviews in Physical Chemistry. 2008.
 https://doi.org/10.1080/01442350802102387.
- (63) Clydesdale, G.; Roberts, K. J.; Walker, E. M. The Crystal Habit of Molecular Materials: A Structural Perspective. In *Molecular solid state syntheses, structure, reactions, applications.*Volume 2 Chapter 7 Theoretical aspects and computer modelling. Ed. A Gavezzotti.; 1997; pp 203–232.
- (64) Arai, Y. Chemistry of Powder Production; Springer Science & Business Media, 1996; Vol. 6.
- (65) Jensen, F. Introduction to Computational Chemistry; John wiley & sons, 2017.
- (66) Lennard-Jones Potential. In Encyclopedia of Microfluidics and Nanofluidics; Springer New York: New York, NY, 2015; pp 1625–1625. https://doi.org/10.1007/978-1-4614-5491-5 200139.
- (67) Hoffmann, F. The Fascination of Crystals and Symmetry, Unit 1.8. *Presentation* **2014**, 2–5.
- (68) Friedel, G. No Title. Bulletin de la Société Française de Minéralogie et de Cristallographie 1907, 30, 326.
- (69) Donnay, J. D. H.; Harker, D. A New Law of Crystal Morphology Extending the Law of Bravais. *Am. Mineral.* 1937, 22, 446.
- (70) Hartman, P.; Perdok, W. G. On the Relations between Structure and Morphology of Crystals. I. *Acta Crystallogr* **1955**, *8* (1), 49–52.
- (71) Docherty, R.; Clydesdale, G.; Roberts, K. J.; Bennema, P. Application of Bravais-Friedel-Donnay-Harker, Attachment Energy and Ising Models to Predicting and Understanding the Morphology of Molecular Crystals. *J Phys D Appl Phys* 1991. https://doi.org/10.1088/0022-3727/24/2/001.

- (72) Docherty, R.; Roberts, K. J. Modelling the Morphology of Molecular Crystals; Application to Anthracene, Biphenyl and β-Succinic Acid. *J Cryst Growth* **1988**. https://doi.org/10.1016/0022-0248(88)90272-2.
- (73) Clydesdale, G.; Roberts, K. J.; Docherty, R. HABIT95—a Program for Predicting the Morphology of Molecular Crystals as a Function of the Growth Environment. *J Cryst Growth* **1996**, *166* (1–4), 78–83.
- (74) Bruno, I. J.; Cole, J. C.; Edgington, P. R.; Kessler, M.; Macrae, C. F.; McCabe, P.; Pearson, J.; Taylor, R. New Software for Searching the Cambridge Structural Database and Visualizing Crystal Structures. *Acta Crystallogr B* **2002**. https://doi.org/10.1107/S0108768102003324.
- (75) BIOVIA, D. S. Materials Studio, 17.1. 0.48. Dassault Systèmes: San Diego, CA, USA 2017.
- (76) Hammond, R. B.; Ma, C.; Roberts, K. J.; Ghi, P. Y.; Harris, R. K. Application of Systematic Search Methods to Studies of the Structures of Urea—Dihydroxy Benzene Cocrystals. *J Phys Chem B* **2003**, *107* (42), 11820–11826.
- (77) Hammond, R. B.; Jeck, S.; Ma, C. Y.; Pencheva, K.; Roberts, K. J.; Auffret, T. An Examination of Binding Motifs Associated with Inter-Particle Interactions between Facetted Nano-Crystals of Acetylsalicylic Acid and Ascorbic Acid through the Application of Molecular Grid-Based Search Methods. *J Pharm Sci* **2009**. https://doi.org/10.1002/jps.21758.
- (78) Hammond, R. B.; Pencheva, K.; Roberts, K. J. Molecular Modeling of Crystal-Crystal Interactions between the α- and β-Polymorphic Forms of L-Glutamic Acid Using Grid-Based Methods. Cryst Growth Des 2007. https://doi.org/10.1021/cg0605234.
- (79) Hammond, R. B.; Pencheva, K.; Ramachandran, V.; Roberts, K. J. Application of Grid-Based Molecular Methods for Modeling Solvent-Dependent Crystal Growth Morphology: Aspirin Crystallized from Aqueous Ethanolic Solution. In Crystal Growth and Design; 2007. https://doi.org/10.1021/cg070310u.

- (80) Nguyen, T. T. H.; Hammond, R. B.; Roberts, K. J.; Marziano, I.; Nichols, G. Precision Measurement of the Growth Rate and Mechanism of Ibuprofen {001} and {011} as a Function of Crystallization Environment. CrystEngComm 2014, 16 (21), 4568–4586. https://doi.org/10.1039/c4ce00097h.
- (81) Ma, C. Y.; Nguyen, T. T. H.; Gajjar, P.; Styliari, I. D.; Hammond, R. B.; Withers, P. J.; Murnane, D.; Roberts, K. J. Predicting the Strength of Cohesive and Adhesive Interparticle Interactions for Dry Powder Inhalation Blends of Terbutaline Sulfate with α-Lactose Monohydrate. *Mol Pharm* 2023, 20 (10), 5019–5031. https://doi.org/10.1021/acs.molpharmaceut.3c00292.
- (82) desu, P.; Vaishnavi, G.; Divya, K.; Lakshmi, U.; Kumar, D. AN OVERVIEW ON PREFORMULATION STUDIES. **2019**, 1399–1407.
- (83) desu, P.; Vaishnavi, G.; Divya, K.; Lakshmi, U.; Kumar, D. AN OVERVIEW ON PREFORMULATION STUDIES. **2019**, 1399–1407.
- (84) Range, H, P.; Dale, M, M.; Ritter, J, M.; Flower, R, J.; Henderson, G. *Rang & Dale's Pharmacology*, 7th ed.; Elsevier Churchill Livingstone, 2012.
- (85) Range, H, P.; Dale, M, M.; Ritter, J, M.; Flower, R, J.; Henderson, G. *Rang & Dale's Pharmacology*, 7th ed.; Elsevier Churchill Livingstone, 2012.
- (86) Manallack, D. T.; Prankerd, R. J.; Yuriev, E.; Oprea, T. I.; Chalmers, D. K. The Significance of Acid/Base Properties in Drug Discovery. *Chem Soc Rev* 2013, 42 (2), 485–496. https://doi.org/10.1039/c2cs35348b.
- (87) Sinko, P. J. MARTIN'S PHYSICAL PHARMACY AND PHARMACEUTICAL SCIENCES -Physical Chemical and Biopharmaceutical Principles in the Pharmaceutical Sciences, Sixth.; Lippincott Williams & Wilkins: Baltimore, MD, 2011; Vol. 53. https://doi.org/10.1017/CBO9781107415324.004.
- (88) Rhoades, R. A.; Bell, D. R. *Medical Physiology: Principles for Clinical Medicine*, 4th ed.; Lippincott Williams & Wilkins, 2013.

- (89) Anderson, K. A.; Hillwalker, W. E. Bioavailability. *Encyclopedia of Ecology* 2008, 348–357. https://doi.org/10.1016/B978-008045405-4.00375-X.
- (90) Khadka, P.; Ro, J.; Kim, H.; Kim, I.; Kim, J. T.; Kim, H.; Cho, J. M.; Yun, G.; Lee, J. Pharmaceutical Particle Technologies: An Approach to Improve Drug Solubility, Dissolution and Bioavailability. *Asian J Pharm Sci* 2014, 9 (6), 304–316. https://doi.org/https://doi.org/10.1016/j.ajps.2014.05.005.
- (91) Chavda, H. V.; Patel, C. N.; Anand, I. S. Biopharmaceutics Classification System. *Systematic Reviews in Pharmacy* **2010**, *I* (1), 62–69. https://doi.org/10.4103/0975-8453.59514.
- (92) Rautio, J.; Meanwell, N. A.; Di, L.; Hageman, M. J. The Expanding Role of Prodrugs in Contemporary Drug Design and Development. *Nat Rev Drug Discov* 2018, 17 (8), 559–587. https://doi.org/10.1038/nrd.2018.46.
- (93) Maher, S.; Brayden, D. J.; Casettari, L.; Illum, L. Application of Permeation Enhancers in Oral Delivery of Macromolecules: An Update. *Pharmaceutics* 2019, 11 (1), 1–23. https://doi.org/10.3390/pharmaceutics11010041.
- (94) Sacher, S.; Khinast, J. G. An Overview of Pharmaceutical Manufacturing for Solid Dosage Forms. In *Methods in Pharmacology and Toxicology*; 2016. https://doi.org/10.1007/978-1-4939-2996-2 10.
- (95) Olusanmi, D.; Jayawickrama, D.; Bu, D.; McGeorge, G.; Sailes, H.; Kelleher, J.; Gamble, J. F.; Shah, U. V.; Tobyn, M. A Control Strategy for Bioavailability Enhancement by Size Reduction: Effect of Micronization Conditions on the Bulk, Surface and Blending Characteristics of an Active Pharmaceutical Ingredient. *Powder Technol* 2014, 258, 222–233. https://doi.org/10.1016/J.POWTEC.2014.03.032.
- (96) Haywood, A.; Glass, B. D. Pharmaceutical Excipients Where Do We Begin? Aust Prescr 2011. https://doi.org/10.18773/austprescr.2011.060.

- (97) Etzler, F. M.; Uddin, M. N. Powder Technology and Pharmaceutical Development: Particle Size and Powder Technology and Pharmaceutical Development: Particle Size and Particle Adhesion.
 2013, No. January. https://doi.org/10.14356/kona.2013014.
- (98) Directory, I. *High Shear Mixer*. https://www.iqsdirectory.com/articles/mixer/high-shear-mixer.html.
- (99) Berthiaux, H.; Marikh, K.; Gatumel, C. Continuous Mixing of Powder Mixtures with Pharmaceutical Process Constraints. Chemical Engineering and Processing: Process Intensification 2008, 47 (12), 2315–2322. https://doi.org/https://doi.org/10.1016/j.cep.2008.01.009.
- (100) Shanmugam, S. Granulation Techniques and Technologies: Recent Progresses. *Bioimpacts* **2015**, *5* (1), 55–63. https://doi.org/10.15171/bi.2015.04.
- (101) Excipients, P. Drug migration during drying of granules due to content non-uniformity in wet granulation. https://doi.org/3/04/2020.
- (102) Shanmugam, S. Granulation Techniques and Technologies: Recent Progresses. *Bioimpacts* **2015**, *5* (1), 55–63. https://doi.org/10.15171/bi.2015.04.
- (103) Thoorens, G.; Krier, F.; Leclercq, B.; Carlin, B.; Evrard, B. Microcrystalline Cellulose, a Direct Compression Binder in a Quality by Design Environment—A Review. *Int J Pharm* 2014, 473 (1), 64–72. https://doi.org/https://doi.org/10.1016/j.ijpharm.2014.06.055.
- (104) Crooks, M. J.; Ho, R. Ordered Mixing in Direct Compression of Tablets. *Powder Technol* **1976**, *14* (1), 161–167. https://doi.org/https://doi.org/10.1016/0032-5910(76)80018-6.
- (105) Crooks, M. J.; Ho, R. Ordered Mixing in Direct Compression of Tablets. *Powder Technol* **1976**, *14* (1), 161–167. https://doi.org/https://doi.org/10.1016/0032-5910(76)80018-6.
- (106) Sofer, G. Validation of Biotechnology Processes; 2003. https://doi.org/10.1201/9780203912119.ch7.

- (107) Dahl, J. Animation of a tablet press.

 https://commons.wikimedia.org/wiki/File:Tablet_press_animation.gif.
- (108) Hiestand, E. N.; Wells, J. E.; Peot, C. B.; Ochs, J. F. Physical Processes of Tableting. *J Pharm Sci* **1977**, *66* (4), 510–519. https://doi.org/10.1002/jps.2600660413.
- (109) Papantoniou, I.; Mantalaris, A.; Sonnaert, M.; Lambrechts, T.; Aerts, J.-M.; Geris, L.; Schrooten, J. Product and Process Design. *Tissue Eng* **2014**, 747–781. https://doi.org/10.1016/b978-0-12-420145-3.00021-3.
- (110) Patel, S.; Kaushal, A. M.; Bansal, A. K. Compression Physics in the Formulation Development of Tablets. *Crit Rev Ther Drug Carrier Syst* **2006**, *23* (1), 1–65. https://doi.org/10.1615/critrevtherdrugcarriersyst.v23.i1.10.
- (111) Sunil, J. *Pharmaceutical Dosage Forms: Tablets. Vol. 1.*; 1990; Vol. 79. https://doi.org/10.1002/jps.2600791123.
- (112) Podczeck, F. *Pharmaceutical Capsules and Tablets: Design and Evaluation*; Pharmaceutical Press: London, 2004.
- (113) Wu, C.Y. and Bentham, A. C. Tablet Fracture Mechanisms: An Overview. *J Pharm Sci* **2000**, 89 (6), 792–804.
- (114) Callister Jr, W. D.; Rethwisch, D. G. *Materials Science and Engineering: An Introduction*; John wiley & sons, 2020.
- (115) Kawakita, K.; Lüdde, K. H. Some Considerations on Powder Compression Equations. *Powder Technol* **1971**. https://doi.org/10.1016/0032-5910(71)80001-3.
- (116) Groover, M. P. Fundamentals of Modern Manufacturing. *J Chem Inf Model* **2013**. https://doi.org/10.1017/CBO9781107415324.004.
- (117) Sheinin, E. B. Pharmacopeial Methods and Tests. In *Specification of Drug Substances and Products*; Elsevier, 2020; pp 607–637.

- (118) Mazel, V.; Desbois, L.; Tchoreloff, P. Influence of the Unloading Conditions on Capping and Lamination: Study on a Compaction Simulator. *Int J Pharm* **2019**, *567*, 118468. https://doi.org/https://doi.org/10.1016/j.ijpharm.2019.118468.
- (119) Mazel, V.; Desbois, L.; Tchoreloff, P. Influence of the Unloading Conditions on Capping and Lamination: Study on a Compaction Simulator. *Int J Pharm* **2019**, *567*, 118468. https://doi.org/https://doi.org/10.1016/j.ijpharm.2019.118468.
- (120) Holland, I. OPTIMISE PRODUCTION Production Problems. https://tablettingscience.com/optimise-production/.
- (121) Tousey, M. D. Sticking and Picking: Some Causes and Rmedies. *Tablets & Capsules* **2003**, No. October.
- (122) Tousey, M. D. Sticking and Picking: Some Causes and Rmedies. *Tablets & Capsules* **2003**, No. October.
- (123) Roberts, M.; Ford, J. L.; MacLeod, G. S.; Fell, J. T.; Smith, G. W.; Rowe, P. H. Effects of Surface Roughness and Chrome Plating of Punch Tips on the Sticking Tendencies of Model Ibuprofen Formulations. *Journal of Pharmacy and Pharmacology* 2003, 55 (9), 1223–1228. https://doi.org/10.1211/0022357021684.
- (124) Sun, W. J.; Sun, C. C. Ribbon Thickness Influences Fine Generation during Dry Granulation.

 Int J Pharm 2017. https://doi.org/10.1016/j.ijpharm.2017.06.038.
- (125) Heng, J. Y. Y.; Thielmann, F.; Williams, D. R. The Effects of Milling on the Surface Properties of Form I Paracetamol Crystals. *Pharm Res* **2006**. https://doi.org/10.1007/s11095-006-9042-1.
- (126) El-Say, K. M.; Refaey, T. A.; Samy, A. M.; Badawy, A. A. Comparative Study among Different Techniques to Improve the Physical and Technical Properties Prevailing to Compression of Poorly Flowing and Highly Cohesive Drug. *Int. J Pharm Sci Rev Res* **2010**, *4* (1), 67–76.

- (127) Waimer, F.; Krumme, M.; Danz, P.; Tenter, U.; Schmidt, P. C. The Influence of Engravings on the Sticking of Tablets. Investigations with an Instrumented Upper Punch. *Pharm Dev Technol* 1999, 4 (3), 369–375. https://doi.org/10.1081/PDT-100101372.
- (128) Roberts, M.; Ford, J. L.; MacLeod, G. S.; Fell, J. T.; Smith, G. W.; Rowe, P. H.; Dyas, A. M. Effect of Punch Tip Geometry and Embossment on the Punch Tip Adherence of a Model Ibuprofen Formulation. *Journal of Pharmacy and Pharmacology* 2004, 56 (7), 947–950. https://doi.org/10.1211/0022357023736.
- (129) Abdel-hamid, S.; Betz, G.; Abdel-hamid, S.; Betz, G. A Novel Tool for the Prediction of Tablet Sticking during High Speed Compaction A Novel Tool for the Prediction of Tablet Sticking during High Speed Compaction. 2012, 7450 (May 2011). https://doi.org/10.3109/10837450.2011.580761.
- (130) Hooper, D.; Clarke, F. C.; Docherty, R.; Mitchell, J. C.; Snowden, M. J. E Ff Ects of Crystal Habit on the Sticking Propensity of Ibuprofen A Case Study. *Int J Pharm* 2017, 531 (1), 266–275. https://doi.org/10.1016/j.ijpharm.2017.08.091.
- (131) Paul, S.; Sun, C. C. Modulating Sticking Propensity of Pharmaceuticals Through Excipient Selection in a Direct Compression Tablet Formulation. **2018**, 1–10.
- (132) Sun, C. C. Materials Science Tetrahedron A Useful Tool for Pharmaceutical Research and Development. *J Pharm Sci* **2009**, *98* (5), 1671–1687. https://doi.org/10.1002/jps.21552.
- (133) Parikh, D. M. Handbook of Pharmaceutical Granulation Technology; 2005. https://doi.org/10.1201/9780849354953.
- (134) Waknis, V.; Chu, E.; Schlam, R.; Sidorenko, A.; Badawy, S.; Yin, S.; Narang, A. S. Molecular Basis of Crystal Morphology-Dependent Adhesion Behavior of Mefenamic Acid During Tableting. 2014, 160–172. https://doi.org/10.1007/s11095-013-1149-6.
- (135) Abdul Mudalip, S. K.; Adam, F.; Abu Bakar, M. R. Evaluation of the Intermolecular Interactions and Polymorphism of Mefenamic Acid Crystals in N,N-Dimethyl Formamide Solution: A

- Molecular Dynamics Simulation and Experimental Study. *Comptes Rendus Chimie* **2019**, *22* (11), 771–778. https://doi.org/https://doi.org/10.1016/j.crci.2019.08.005.
- (136) Abdul Mudalip, S. K.; Abu Bakar, M. R.; Jamal, P.; Adam, F.; Che Man, R.; Sulaiman, S. Z.; Mohd Arshad, Z. I.; Md Shaarani, S. Effects of Solvents on Polymorphism and Shape of Mefenamic Acid Crystals. *MATEC Web of Conferences* 2018, 150, 0–5. https://doi.org/10.1051/matecconf/201815002004.
- (137) Assafa, S. M.; Khanfar, M. S.; Obeidat, R.; Salem, M. S.; Arida, A. I. Effect of Different Organic Solvents on Crystal Habit of Mefenamic Acid. *Jordan Journal of Pharmaceutical Sciences* **2009**.
- (138) Shah, U. V; Olusanmi, D.; Narang, A. S.; Hussain, M. A.; Gamble, J. F.; Tobyn, M. J.; Heng, J. Y. Y. Effect of Crystal Habits on the Surface Energy and Cohesion of Crystalline Powders. *Int J Pharm* 2014, 472 (1–2), 140–147. https://doi.org/10.1016/j.ijpharm.2014.06.014.
- (139) Panchagnula, R.; Sundaramurthy, P.; Pillai, O.; Agrawal, S.; Raj, Y. A. Solid-State Characterization of Mefenamic Acid. *J Pharm Sci* **2004**, *93* (4), 1019–1029. https://doi.org/10.1002/jps.20008.
- (140) Lieberman, H. A.; Lachman, L.; Schwartz, J. B. *Pharmaceutical Dosage Forms: Tablets 2nd Edition*; 2017. https://doi.org/10.1017/CBO9781107415324.004.
- (141) Gad, S. C. Pharmaceutical Manufacturing Handbook: Production and Processes; 2007. https://doi.org/10.1002/9780470259818.
- (142) Alyami, H.; Dahmash, E.; Bowen, J.; Mohammed, A. R. An Investigation into the Effects of Excipient Particle Size, Blending Techniques & Processing Parameters on the Homogeneity & Content Uniformity of a Blend Containing Low-Dose Model Drug. *PLoS One* 2017. https://doi.org/10.1371/journal.pone.0178772.
- (143) Sunil, J. Pharmaceutical Dosage Forms: Tablets. Vol. 1. J Pharm Sci 1990, 79 (11), 1043. https://doi.org/10.1002/JPS.2600791123.

- (144) Emery, E.; Oliver, J.; Pugsley, T.; Sharma, J.; Zhou, J. Flowability of Moist Pharmaceutical Powders. *Powder Technol* **2009**, *189* (3), 409–415. https://doi.org/10.1016/j.powtec.2008.06.017.
- (145) Carr, R. L. Evaluating Flow Properties of Solids. Chem. Eng. 1965, 163–168.
- (146) Tye, C. K.; Sun, C.; Amidon, G. E. Evaluation of the Effects of Tableting Speed on the Relationships between Compaction Pressure, Tablet Tensile Strength, and Tablet Solid Fraction. *J Pharm Sci* 2005. https://doi.org/10.1002/jps.20262.
- (147) Aulton, M. E.; Taylor, K. Aulton's Pharmaceutics: The Design and Manufacture of Medicines; Elsevier Health Sciences, 2013.
- (148) Heckel, R. W. Density-Pressure Relationships in Powder Compaction. *Transactions of the Metallurgical Society of AIME* **1961**.
- (149) Hancock, B. C.; Mullarney, M. P. X-Ray Microtomography of Solid Dosage Forms. *Pharmaceutical Technology* **2005**, *29* (4), 92–100.
- (150) Maire, E.; Withers, P. J. Quantitative X-Ray Tomography.

 https://doi.org/10.1179/1743280413Y.0000000023 2014, 59 (1), 1–43.

 https://doi.org/10.1179/1743280413Y.0000000023.
- (151) Stock, S. R. X-Ray Microtomography of Materials. *International Materials Reviews* 1999, 44(4), 141–164. https://doi.org/10.1179/095066099101528261.
- (152) Hancock, B. C.; Mullarney, M. P. X-Ray Microtomography of Solid Dosage Forms. *Pharmaceutical Technology* **2005**, *29* (4), 92–100.
- (153) Turner, T. D.; Gajjar, P.; Fragkopoulos, I. S.; Carr, J.; Nguyen, T. T. H.; Hooper, D.; Clarke, F.; Dawson, N.; Withers, P. J.; Roberts, K. J. Measuring the Particle Packing of L-Glutamic Acid Crystals through X-Ray Computed Tomography for Understanding Powder Flow and Consolidation Behavior. *Cryst Growth Des* 2020, 20 (7), 4252–4263. https://doi.org/10.1021/acs.cgd.9b01515.

- (154) Gajjar, P.; Styliari, I. D.; Nguyen, T. T. H.; Carr, J.; Chen, X.; Elliott, J. A.; Hammond, R. B.; Burnett, T. L.; Roberts, K.; Withers, P. J.; Murnane, D. 3D Characterisation of Dry Powder Inhaler Formulations: Developing X-Ray Micro Computed Tomography Approaches. *European Journal of Pharmaceutics and Biopharmaceutics* 2020, 151 (April), 32–44. https://doi.org/10.1016/j.ejpb.2020.02.013.
- (155) Microtomography, T. X.; Flannery, B. P.; Deckman, H. W.; Roberge, W. G.; Amico, K. L. D. Three-Dimensional X-Ray.
- (156) Feldkamp, L. A.; Davis, L. C.; Kress, J. W. Practical Cone-Beam Algorithm. *Journal of the Optical Society of America A* **1984**, *I* (6), 612. https://doi.org/10.1364/JOSAA.1.000612.
- (157) Bryant, M. J.; Maloney, A. G. P.; Sykes, R. A. Predicting Mechanical Properties of Crystalline Materials through Topological Analysis. *CrystEngComm* 2018, 20 (19), 2698–2704. https://doi.org/10.1039/c8ce00454d.
- (158) Olusanmi, D.; Roberts, K. J.; Ghadiri, M.; Ding, Y. The Breakage Behaviour of Aspirin under Quasi-Static Indentation and Single Particle Impact Loading: Effect of Crystallographic Anisotropy. *Int J Pharm* **2011**, *411* (1–2), 49–63. https://doi.org/10.1016/J.IJPHARM.2011.03.039.
- (159) Ibrahim, S. F.; Pickering, J.; Ramachandran, V.; Roberts, K. J. Prediction of the Mechanical Deformation Properties of Organic Crystals Based upon Their Crystallographic Structures: Case Studies of Pentaerythritol and Pentaerythritol Tetranitrate. *Pharm Res* 2022, 39 (12), 3063–3078. https://doi.org/10.1007/s11095-022-03314-x.
- (160) Winder, C. V.; Kaump, D. H.; Glazko, A. J.; Holmes, E. L. Experimental Observations on Flufenamic, Mefenamic, and Meclofenamic Acids. *Rheumatology* 1966, *VIII* (suppl_1), 7–49. https://doi.org/10.1093/RHEUMATOLOGY/VIII.SUPPL 1.7.
- (161) World, P. P. Pharmaceutical Processing World. Tablet Manufacturing Challenges: Process Inefficiencies and Material Losses. 2019. https://www.pharmaceuticalprocessingworld.com.

- (162) Chattoraj, S.; Daugherity, P.; McDermott, T.; Olsofsky, A.; Roth, W. J.; Tobyn, M. Sticking and Picking in Pharmaceutical Tablet Compression: An IQ Consortium Review. *J Pharm Sci* **2018**, 107 (9), 2267–2282. https://doi.org/https://doi.org/10.1016/j.xphs.2018.04.029.
- (163) Wakai, A.; Roberts, I.; Schierhout, G. Mannitol for Acute Traumatic Brain Injury. *Cochrane Database Syst Rev* **2005**, No. 4, CD001049. https://doi.org/10.1002/14651858.CD001049.pub2.
- (164) Chen, M.; Zhang, W.; Wu, H.; Guang, C.; Mu, W. Mannitol: Physiological Functionalities, Determination Methods, Biotechnological Production, and Applications. *Appl Microbiol Biotechnol* 2020, 104 (16), 6941–6951. https://doi.org/10.1007/s00253-020-10757-y.
- (165) McConnell, J. F.; Company, F. Z. N-(2,3-Xylyl) Anthranilic Acid, C15H15NO2 Mefenamic Acid. Cryst. Struct. Commun 1976, 5, 861–864.
- (166) Fronczek, F. R.; Kamel, H. N.; Slattery, M. Three Polymorphs (α, β, and δ) of D-Mannitol at 100K. Acta Crystallographica Section C 2003, 59 (10), o567--o570. https://doi.org/10.1107/S0108270103018961.
- (167) Leach, A. R. Molecular Modelling: Principles and Applications; Pearson education, 2001.
- (168) Singh, U. C.; Kollman, P. A. An Approach to Computing Electrostatic Charges for Molecules.

 J Comput Chem 1984, 5 (2), 129–145.

 https://doi.org/10.1002/JCC.540050204;WGROUP:STRING:PUBLICATION.
- (169) Řezáč, J.; Hobza, P. Advanced Corrections of Hydrogen Bonding and Dispersion for Semiempirical Quantum Mechanical Methods. *J Chem Theory Comput* 2012, 8 (1), 141–151. https://doi.org/10.1021/CT200751E.
- (170) Brandenburg, J. G.; Maas, T.; Grimme, S. Benchmarking DFT and Semiempirical Methods on Structures and Lattice Energies for Ten Ice Polymorphs. *J Chem Phys* **2015**, *142* (12). https://doi.org/10.1063/1.4916070.

- (171) Price, S. L. From Crystal Structure Prediction to Polymorph Prediction: Interpreting the Crystal Energy Landscape. *Physical Chemistry Chemical Physics* 2008, 10 (15), 1996–2009. https://doi.org/10.1039/B719351C.
- (172) Momany, F. A.; Carruthers, L. M.; McGuire, R. F.; Scheraga, H. A. Intermolecular Potentials from Crystal Data. III. Determination of Empirical Potentials and Application to the Packing Configurations and Lattice Energies in Crystals of Hydrocarbons, Carboxylic Acids, Amines, and Amides. *Journal of Physical Chemistry* 1974. https://doi.org/10.1021/j100609a005.
- (173) Mayo, S. L.; Olafson, B. D.; Goddard, W. A. DREIDING: A Generic Force Field for Molecular Simulations. *Journal of Physical Chemistry* 1990, 94 (26), 8897–8909. https://doi.org/10.1021/j100389a010.
- (174) Brooks, B. R.; Bruccoleri, R. E.; Olafson, B. D.; States, D. J.; Swaminathan, S.; Karplus, M. CHARMM: A Program for Macromolecular Energy, Minimization, and Dynamics Calculations.

 J. Comput. Chem. 1983, 4 (2), 187–217.

 https://doi.org/10.1002/JCC.540040211;PAGE:STRING:ARTICLE/CHAPTER.
- (175) Weiner, S. J.; Kollman, P. A.; Singh, U. C.; Case, D. A.; Ghio, C.; Alagona, G.; Profeta, S.; Weiner, P. A New Force Field for Molecular Mechanical Simulation of Nucleic Acids and Proteins. J Am Chem Soc 1984, 106 (3), 765–784. https://doi.org/10.1021/JA00315A051/ASSET/JA00315A051.FP.PNG V03.
- (176) Clydesdale, G.; Docherty, R.; Roberts, K. J. HABIT a Program for Predicting the Morphology of Molecular Crystals. *Comput Phys Commun* 1991. https://doi.org/10.1016/0010-4655(91)90040-R.
- (177) Saaty, T. L. *The Analytic Hierarchy Process: Planning, Priority Setting, Resource Allocation*; Advanced book program; McGraw-Hill International Book Company, 1980.
- (178) El Alaoui, M. Fuzzy TOPSIS; 2021. https://doi.org/10.1201/9781003168416.

- (179) Ibrahim, S. F. B. Prediction of the Mechanical Properties of Molecular Crystals Based Upon Their Crystallographic Structure. *Doctoral dissertation, University of Leeds* **2016**.
- (180) Garbalińska, H.; Bochenek, M.; Malorny, W.; von Werder, J. Comparative Analysis of the Dynamic Vapor Sorption (DVS) Technique and the Traditional Method for Sorption Isotherms Determination Exemplified at Autoclaved Aerated Concrete Samples of Four Density Classes. *Cem Concr Res* **2017**, *91*, 97–105. https://doi.org/https://doi.org/10.1016/j.cemconres.2016.11.001.
- (181) Nishimura, M.; Ichikawa, K.; Ajima, M. Features and Applications of Hitachi Tabletop Microscope TM3030Plus.
- (182) Turner, T. D.; Gajjar, P.; Fragkopoulos, I.; Carr, J.; Nguyen, T. T. H.; Hooper, D.; Clarke, F.; Dawson, N.; Withers, P. J.; Roberts, K. J. The Flow and Consolidation Behaviour of Alpha and Beta L-Glutamic Acid Powders Studied Using X-Ray Computed Tomography. 2019.
- (183) Inc, C. T. C. Dragonfly 2021.1 [Windows]. Montreal, Canada. https://www.theobjects.com/dragonfly.
- (184) Arfken, G. B.; Weber, H. J.; Boston, A.; London, H.; Oxford, N. Y.; San, P.; San, D.; Singapore, F.; Tokyo, S. MATHEMATICAL METHODS FOR PHYSICISTS SIXTH EDITION, 6th ed.; Elsevier Academic Press.
- (185) Underwood, E. E. Quantitive Stereology. Addison-Wesley, MA, CA, London 1970.
- (186) Harrigan, T. P.; Mann, R. W. Characterization of Microstructural Anisotropy in Orthotropic Materials Using a Second Rank Tensor. *J Mater Sci* **1984**, *19* (3), 761–767. https://doi.org/10.1007/BF00540446/METRICS.
- (187) Rose, H. E.; Robinson, D. J. The Application of Digital Computer to the Study of Some Problems in the Mixing of Powders. *American Institute of Chemical Engineers Symposium Series* **1965**, *10*, 61.

- (188) Chavda, H. V.; Patel, C. N.; Anand, I. S. Biopharmaceutics Classification System. *Systematic Reviews in Pharmacy* **2010**, *I* (1), 62–69. https://doi.org/10.4103/0975-8453.59514.
- (189) McConnell, J. F.; Company, F. Z. N-(2,3-Xylyl) Anthranilic Acid, C15H15NO2 Mefenamic Acid. Cryst. Struct. Commun 1976, 5, 861–864.
- (190) Cesur, S.; Gokbel, S. Crystallization of Mefenamic Acid and Polymorphs. *Crystal Research and Technology* **2008**, *43* (7), 720–728. https://doi.org/10.1002/crat.200711119.
- (191) SeethaLekshmi, S.; Guru Row, T. N. Conformational Polymorphism in a Non-Steroidal Anti-Inflammatory Drug, Mefenamic Acid. Cryst Growth Des 2012, 12 (8), 4283–4289. https://doi.org/10.1021/cg300812v.
- (192) Adam, A.; Schrimpl, L.; Schmidt, P. C.; Kato, F.; Otsuka, M.; Matsuda, Y.; Surov, A. O.; Terekhova, I. V; Bauer-Brandl, A.; Perlovich, G. L.; Panchagnula, R.; Sundaramurthy, P.; Pillai, O.; Agrawal, S. S.; Raj, Y. A.; Abdul Mudalip, S. K.; Abu Bakar, M. R.; Jamal, P.; Adam, F.; Che Man, R.; Sulaiman, S. Z.; Mohd Arshad, Z. I.; Md Shaarani, S.; Bhadra, S.; Kumar, M.; Jain, S.; Agrawal, S. S.; Agrawal, G. P.; Seethalekshmi, S.; Row, T. N. G.; Assafa, S. M.; Khanfar, M. S.; Obeidat, R.; Salem, M. S.; Arida, A. I.; Abdul Mudalip, S. K.; Adam, F.; Abu Bakar, M. R.; Raijada, D.; Bond, A. D.; Larsen, F. H.; Cornett, C.; Qu, H.; Rantanen, J.; Sharma, A.; Gogate, P. R.; Mudalip, S. K. A.; Bakar, Mohd. R. A.; Adam, F.; Jamal, P.; Ramukutty, S.; Ramachandran, E.; Ribeiro, Y. A.; De Oliveira, J. D. S.; Leles, M. I. G.; Juiz, S. A.; Ionashiro, M. Thermodynamic and Structural Aspects of Some Fenamate Molecular Crystals. *Cryst Growth Des* 2009, 9 (7), 3265–3272. https://doi.org/10.1021/cg900002q.
- (193) Romero, S.; Escalera, B.; Bustamante, P. Solubility Behavior of Polymorphs I and II of Mefenamic Acid in Solvent Mixtures. *Int J Pharm* 1999, 178 (2), 193–202. https://doi.org/10.1016/s0378-5173(98)00375-5.
- (194) Fronczek, F. R.; Kamel, H. N.; Slattery, M. Three Polymorphs (α, β, and δ) of D-Mannitol at 100K. Acta Crystallographica Section C 2003, 59 (10), o567--o570. https://doi.org/10.1107/S0108270103018961.

- (195) Gombás, Á.; Szabó-Révész, P.; Regdon, G.; Erös, I. Study of Thermal Behaviour of Sugar Alcohols. *J Therm Anal Calorim* **2003**, 73 (2), 615–621. https://doi.org/10.1023/A:1025490432142.
- (196) Cares-Pacheco, M. G.; Vaca-Medina, G.; Calvet, R.; Espitalier, F.; Letourneau, J. J.; Rouilly, A.; Rodier, E. Physicochemical Characterization of D-Mannitol Polymorphs: The Challenging Surface Energy Determination by Inverse Gas Chromatography in the Infinite Dilution Region. *Int J Pharm* 2014, 475 (1–2), 69–81. https://doi.org/10.1016/j.ijpharm.2014.08.029.
- (197) Surov, A. O.; Terekhova, I. V; Bauer-Brandl, A.; Perlovich, G. L. Thermodynamic and Structural Aspects of Some Fenamate Molecular Crystals. *Cryst Growth Des* **2009**, *9* (7), 3265–3272. https://doi.org/10.1021/cg900002q.
- (198) Tong, B.; Liu, R.-B.; Meng, C.-G.; Yu, F.-Y.; Ji, S.-H.; Tan, Z.-C. Heat Capacities and Nonisothermal Thermal Decomposition Reaction Kinetics of D-Mannitol. *J Chem Eng Data* **2010**, *55* (1), 119–124. https://doi.org/10.1021/je900285w.
- (199) Alskär, L. C.; Porter, C. J. H.; Bergström, C. A. S. Tools for Early Prediction of Drug Loading in Lipid-Based Formulations. *Mol Pharm* 2016, 13 (1), 251–261. https://doi.org/10.1021/acs.molpharmaceut.5b00704.
- (200) BARONE G; DELLA GATTA, G. F. D. P. V. Enthalpies and Entropies of Sublimation, Vaporization and Fusion of Nine Polyhydric Alcohols. *Journal of the Chemical Society.*Faraday Transactions II 1990.
- (201) Clydesdale, G.; Docherty, R.; Roberts, K. J. HABIT a Program for Predicting the Morphology of Molecular Crystals. *Comput Phys Commun* **1991**. https://doi.org/10.1016/0010-4655(91)90040-R.
- (202) Surov, A. O.; Terekhova, I. V; Bauer-Brandl, A.; Perlovich, G. L. Thermodynamic and Structural Aspects of Some Fenamate Molecular Crystals. *Cryst Growth Des* **2009**, *9* (7), 3265–3272. https://doi.org/10.1021/cg900002q.

- (203) Adam, A.; Schrimpl, L.; Schmidt, P. C. Some Physicochemical Properties of Mefenamic Acid.

 *Drug Dev Ind Pharm 2000, 26 (5), 477–487. https://doi.org/10.1081/DDC-100101258.
- (204) Cesur, S.; Gokbel, S. Crystallization of Mefenamic Acid and Polymorphs. *Crystal Research and Technology* **2008**, *43* (7), 720–728. https://doi.org/10.1002/crat.200711119.
- (205) Panchagnula, R.; Sundaramurthy, P.; Pillai, O.; Agrawal, S.; Raj, Y. A. Solid-State Characterization of Mefenamic Acid. *J Pharm Sci* **2004**, *93* (4), 1019–1029. https://doi.org/10.1002/jps.20008.
- (206) SeethaLekshmi, S.; Guru Row, T. N. Conformational Polymorphism in a Non-Steroidal Anti-Inflammatory Drug, Mefenamic Acid. Cryst Growth Des 2012, 12 (8), 4283–4289. https://doi.org/10.1021/cg300812v.
- (207) Romero, S.; Escalera, B.; Bustamante, P. Solubility Behavior of Polymorphs I and II of Mefenamic Acid in Solvent Mixtures. *Int J Pharm* **1999**, *178* (2), 193–202. https://doi.org/10.1016/s0378-5173(98)00375-5.
- (208) Abdul Mudalip, S. K.; Adam, F.; Abu Bakar, M. R. Evaluation of the Intermolecular Interactions and Polymorphism of Mefenamic Acid Crystals in N,N-Dimethyl Formamide Solution: A Molecular Dynamics Simulation and Experimental Study. *Comptes Rendus Chimie* **2019**, *22* (11), 771–778. https://doi.org/https://doi.org/10.1016/j.crci.2019.08.005.
- (209) Abdul Mudalip, S. K.; Abu Bakar, M. R.; Jamal, P.; Adam, F.; Che Man, R.; Sulaiman, S. Z.; Mohd Arshad, Z. I.; Md Shaarani, S. Effects of Solvents on Polymorphism and Shape of Mefenamic Acid Crystals. *MATEC Web of Conferences* 2018, 150, 0–5. https://doi.org/10.1051/matecconf/201815002004.
- (210) Assafa, S. M.; Khanfar, M. S.; Obeidat, R.; Salem, M. S.; Arida, A. I. Effect of Different Organic Solvents on Crystal Habit of Mefenamic Acid. *Jordan Journal of Pharmaceutical Sciences* **2009**.

- (211) Properties of Common Solvents.

 https://www.chemistry.mcmaster.ca/adronov/resources/Common_Solvents_for_Organic_Reac tions.pdf (accessed 2020-05-25).
- (212) Poornachary, S. K.; Parambil, J. V; Chow, P. S.; Tan, R. B. H.; Heng, J. Y. Y. Nucleation of Elusive Crystal Polymorphs at the Solution–Substrate Contact Line. *Cryst Growth Des* 2013, *13* (3), 1180–1186. https://doi.org/10.1021/cg301597d.
- (213) Yang, Y.; Liu, J.; Hu, A.; Nie, T.; Cheng, Z.; Liu, W. A Critical Review on Engineering of D-Mannitol Crystals: Properties, Applications, and Polymorphic Control. *Crystals (Basel)* 2022, 12 (8). https://doi.org/10.3390/cryst12081080.
- (214) Dierks, T. M.; Korter, T. M. Origins of the Relative Stabilities of Anhydrous and Hydrated D-Mannitol Crystals. *J Phys Chem A* **2016**, *120* (33), 6629–6636. https://doi.org/10.1021/acs.jpca.6b05244.
- (215) Kaialy, W. A Review of Factors Affecting Electrostatic Charging of Pharmaceuticals and Adhesive Mixtures for Inhalation. *Int J Pharm* **2016**, *503* (1–2), 262–276. https://doi.org/10.1016/j.ijpharm.2016.01.076.
- (216) Su, W.; Hao, H.; Glennon, B.; Barrett, M. Spontaneous Polymorphic Nucleation of D-Mannitol in Aqueous Solution Monitored with Raman Spectroscopy and FBRM. *Cryst Growth Des* 2013, 13 (12), 5179–5187. https://doi.org/10.1021/cg400304c.
- (217) Cares-Pacheco, M. G.; Vaca-Medina, G.; Calvet, R.; Espitalier, F.; Letourneau, J. –J.; Rouilly, A.; Rodier, E. Physicochemical Characterization of D-Mannitol Polymorphs: The Challenging Surface Energy Determination by Inverse Gas Chromatography in the Infinite Dilution Region.

 Int J Pharm 2014, 475 (1), 69–81. https://doi.org/https://doi.org/10.1016/j.ijpharm.2014.08.029.
- (218) Shishkina, S. V; Vaksler, Y. A.; Konovalova, I. S.; Dyakonenko, V. V; Varchenko, V. V. Quantum Chemical Study on Mefenamic Acid Polymorphic Forms. 2022, 7, 17544–17554. https://doi.org/10.1021/acsomega.1c06967.

- (219) Nguyen, T. T. H.; Hammond, R. B.; Styliari, I. D.; Murnane, D.; Roberts, K. J. A Digital Workflow from Crystallographic Structure to Single Crystal Particle Attributes for Predicting the Formulation Properties of Terbutaline Sulfate. CrystEngComm 2020, 22 (19), 3347–3360. https://doi.org/10.1039/d0ce00026d.
- (220) Ma, C. Y.; Nguyen, T. T. H.; Gajjar, P.; Styliari, I. D.; Hammond, R. B.; Withers, P. J.; Murnane, D.; Roberts, K. J. Predicting the Strength of Cohesive and Adhesive Interparticle Interactions for Dry Powder Inhalation Blends of Terbutaline Sulfate with α-Lactose Monohydrate. *Mol Pharm* 2023, 20 (10), 5019–5031. https://doi.org/10.1021/acs.molpharmaceut.3c00292.
- (221) Turner, T. D.; Dawson, N.; Edwards, M.; Pickering, J. H.; Hammond, R. B.; Docherty, R.; Roberts, K. J. A Digital Mechanistic Workflow for Predicting Solvent-Mediated Crystal Morphology: The α and β Forms of 1 -Glutamic Acid. Cryst Growth Des 2022, 22 (5), 3042–3059. https://doi.org/10.1021/acs.cgd.1c01490.
- (222) Bhadra, S.; Kumar, M.; Jain, S.; Agrawal, S.; Agrawal, G. P. Spherical of Mefenamic Acid. **2004**, No. February.
- (223) Rowe. Mannitol Fact Sheet. Handbook of Pharmaceutical Excipients 7th Edn. 2012, 5-8.
- (224) Gombás, Á.; Szabó-Révész, P.; Regdon, G.; Erös, I. Study of Thermal Behaviour of Sugar Alcohols. *J Therm Anal Calorim* **2003**, 73 (2), 615–621. https://doi.org/10.1023/A:1025490432142.
- (225) Cares-Pacheco, M. G.; Vaca-Medina, G.; Calvet, R.; Espitalier, F.; Letourneau, J. J.; Rouilly, A.; Rodier, E. Physicochemical Characterization of D-Mannitol Polymorphs: The Challenging Surface Energy Determination by Inverse Gas Chromatography in the Infinite Dilution Region.

 Int J Pharm 2014, 475 (1–2), 69–81. https://doi.org/10.1016/j.ijpharm.2014.08.029.
- (226) Umeda, T.; Ohnishi, N.; Yokoyama, T.; Kuroda, T.; Kita, Y.; Kuroda, K.; Tatsumi, E.; Matsuda, Y. No Title. *Chem. Pharm. Bull* **1985**, No. 33, 2079–2078.

- (227) Kumaresan, G.; Velraj, R.; Iniyan, S. Thermal Analysis of D-Mannitol for Use as Phase Change Material for Latent Heat Storage. *Journal of Applied Sciences* **2011**, *11* (16), 3044–3048.
- (228) Descamps, M.; Willart, J. F.; Dudognon, E.; Caron, V. Transformation of Pharmaceutical Compounds upon Milling and Comilling: The Role of Tg. *J Pharm Sci* **2007**, *96* (5), 1398–1407. https://doi.org/10.1002/jps.20939.
- (229) Otsuka, A. Adhesive Properties and Related Phenomena for Powdered Pharmaceuticals. *Yakugaku Zasshi*. 1998. https://doi.org/10.1248/yakushi1947.118.4 127.
- (230) Ribeiro, Y. A.; De Oliveira, J. D. S.; Leles, M. I. G.; Juiz, S. A.; Ionashiro, M. Thermal Decomposition of Some Analgesic Agents. *Journal of Thermal Analysis* **1996**. https://doi.org/10.1007/bf01980770.
- (231) ICH Topic Q 1 A (R2) Stability Testing of New Drug Substances and Products Step 5 NOTE

 FOR GUIDANCE ON STABILITY TESTING: STABILITY TESTING OF NEW DRUG

 SUBSTANCES AND PRODUCTS; 2003. http://www.emea.eu.int (accessed 2020-07-02).
- (232) Anonymous. Characters Section in Monographs. In European Pharmacopoeia 6; 2010.
- (233) Wang, Z.; Shah, U. V.; Olusanmi, D.; Narang, A. S.; Hussain, M. A.; Gamble, J. F.; Tobyn, M. J.; Heng, J. Y. Y. Measuring the Sticking of Mefenamic Acid Powders on Stainless Steel Surface. *Int J Pharm* 2015, 496 (2), 407–413. https://doi.org/10.1016/j.ijpharm.2015.09.067.
- (234) McComiskey, K. P. M.; Tajber, L. Comparison of Particle Size Methodology and Assessment of Nanoparticle Tracking Analysis (NTA) as a Tool for Live Monitoring of Crystallisation Pathways. *European Journal of Pharmaceutics and Biopharmaceutics* **2018**, *130*, 314–326. https://doi.org/10.1016/J.EJPB.2018.07.012.
- (235) ISO 13320:2020 Particle size analysis Laser diffraction methods. https://www.iso.org/standard/69111.html.
- (236) European Directorate for the Quality of Medicine. Powder Flow. *European Pharmacopeia 10.0*2019, 320–323.

- (237) Natoli, D.; Levin, M.; Tsygan, L.; Liu, L. Development, Optimization, and Scale-up of Process Parameters: Tablet Compression; Elsevier Inc., 2017. https://doi.org/10.1016/B978-0-12-802447-8.00033-9.
- (238) Du Hyung Choi, Nam Ah Kim, Kyung Rok Chu, Y. J. J.; Jeong, J.-H. Y. and S. H. Material Properties and Compressibility Using Heckel and Kawakita Equation with Commonly Used Pharmaceutical Excipients. *J Pharm Investig* **2010**, *40* (4), 237–244. https://doi.org/10.4333/kps.2010.40.4.237.
- (239) Pitt, K. G.; Webber, R. J.; Hill, K. A.; Dey, D.; Gamlen, M. J. Compression Prediction Accuracy from Small Scale Compaction Studies to Production Presses. *Powder Technol* 2015, 270 (PB), 490–493. https://doi.org/10.1016/j.powtec.2013.10.007.
- (240) Leane, M.; Pitt, K.; Reynolds, G.; Anwar, J.; Charlton, S.; Crean, A.; Creekmore, R.; Davies, C.; DeBeer, T.; De-Matas, M.; Djemai, A.; Douroumis, D.; Gaisford, S.; Gamble, J.; Stone, E. H.; Kavanagh, A.; Khimyak, Y.; Kleinebudde, P.; Moreton, C.; Paudel, A.; Storey, R.; Toschkoff, G.; Vyas, K. A Proposal for a Drug Product Manufacturing Classification System (MCS) for Oral Solid Dosage Forms. *Pharmaceutical Development and Technology*. 2015. https://doi.org/10.3109/10837450.2014.954728.
- (241) Danjo, K.; Kinoshita, K.; Kitagawa, K.; Iida, K.; Sunada, H.; Otsuka, A. Effect of Particle Shape on the Compaction and Flow Properties of Powders. *Chem Pharm Bull (Tokyo)* **1989**. https://doi.org/10.1248/cpb.37.3070.
- (242) Tan, S. B.; Newton, J. M. Powder Flowability as an Indication of Capsule Filling Performance. *Int J Pharm* **1990**. https://doi.org/10.1016/0378-5173(90)90053-7.
- (243) Paul, S.; Sun, C. C. Gaining Insight into Tablet Capping Tendency from Compaction Simulation.

 *Int J Pharm 2017, 524 (1), 111–120.

 https://doi.org/https://doi.org/10.1016/j.ijpharm.2017.03.073.

- (244) Edge, S.; Steele, D. F.; Tobyn, M. J.; Staniforth, J. N.; Chen, A. Directional Bonding in Compacted Microcrystalline Cellulose. *Drug Dev Ind Pharm* **2001**, *27* (7), 613–621. https://doi.org/10.1081/DDC-100107317.
- (245) Keyser, C. A. Tool and Die Maker's Handbook; 1975.
- (246) Vijayakumar, J.; Goudarzi, N. M.; Eeckhaut, G.; Schrijnemakers, K.; Cnudde, V.; Boone, M. N. Characterization of Pharmaceutical Tablets by X-Ray Tomography. *Pharmaceuticals* 2023, *16* (5), 1–41. https://doi.org/10.3390/ph16050733.
- (247) Joiris, E.; Di Martino, P.; Berneron, C.; Guyot-Hermann, A. M.; Guyot, J. C. Compression Behavior of Orthorhombic Paracetamol. *Pharmaceutical Research*. 1998, pp 1122–1130. https://doi.org/10.1023/A:1011954800246.
- (248) Williams, D. R. Particle Engineering in Pharmaceutical Solids Processing: Surface Energy Considerations. *Curr Pharm Des* **2015**, *21* (19), 2677–2694. https://doi.org/10.2174/1381612821666150416100319.
- (249) Choi, D.-H.; Nam-Ah, K.; Chu, K.-R.; Jung, Y.-J.; Yoon, J.-H.; Jeong, S. H. Material Properties and Compressibility Using Heckel and Kawakita Equation with Commonly Used Pharmaceutical Excipients. *J Pharm Investig* **2010**, *40* (4), 237–244. https://doi.org/10.4333/KPS.2010.40.4.237.
- (250) Desai, Y. A MECHANISTIC STUDY OF FLOW AND COMPRESSION BEHAVIOR OF PHARMACEUTICAL POWDERS. *Open Access Dissertations* **2001**. https://doi.org/10.23860/diss-desai-yogita-2001.
- (251) Charoo, N. A. Critical Excipient Attributes Relevant to Solid Dosage Formulation Manufacturing. *J Pharm Innov* **2020**, *15* (1), 163–181. https://doi.org/10.1007/S12247-019-09372-W/TABLES/1.
- (252) Turner, T. D.; Gajjar, P.; Fragkopoulos, I. S.; Carr, J.; Nguyen, T. T. H.; Hooper, D.; Clarke, F.; Dawson, N.; Withers, P. J.; Roberts, K. J. Measuring the Particle Packing of L-Glutamic Acid

- Crystals through X-Ray Computed Tomography for Understanding Powder Flow and Consolidation Behavior. *Cryst Growth Des* **2020**, *20* (7), 4252–4263. https://doi.org/10.1021/acs.cgd.9b01515.
- (253) Kikuta, J.; Kitamori, N. Evaluation of the Die Wall Friction during Tablet Ejection. *Powder Technol* **1983**, *35* (2), 195–200. https://doi.org/10.1016/0032-5910(83)87009-0.
- (254) Mazel, V.; Guerard, S.; Croquelois, B.; Kopp, J. B.; Girardot, J.; Diarra, H.; Busignies, V.; Tchoreloff, P. Reevaluation of the Diametral Compression Test for Tablets Using the Flattened Disc Geometry. *Int J Pharm* 2016, 513 (1–2), 669–677. https://doi.org/10.1016/J.IJPHARM.2016.09.088.